



**HAL**  
open science

## Thick nematic liquid crystals for ultrafast optics

Vittorio Maria Di Pietro

► **To cite this version:**

Vittorio Maria Di Pietro. Thick nematic liquid crystals for ultrafast optics. Optics [physics.optics]. COMUE Université Côte d'Azur (2015 - 2019), 2019. English. NNT : 2019AZUR4101 . tel-03510378

**HAL Id: tel-03510378**

**<https://theses.hal.science/tel-03510378v1>**

Submitted on 4 Jan 2022

**HAL** is a multi-disciplinary open access archive for the deposit and dissemination of scientific research documents, whether they are published or not. The documents may come from teaching and research institutions in France or abroad, or from public or private research centers.

L'archive ouverte pluridisciplinaire **HAL**, est destinée au dépôt et à la diffusion de documents scientifiques de niveau recherche, publiés ou non, émanant des établissements d'enseignement et de recherche français ou étrangers, des laboratoires publics ou privés.



$$\rho \left( \frac{\partial v}{\partial t} + v \cdot \nabla v \right) = -\nabla p + \nabla \cdot T + f$$

$$e^{i\pi} + 1 = 0$$

# THÈSE DE DOCTORAT

## Cristaux liquides nématiques épais pour l'optique ultra-rapide

Présentée et soutenue par :

**Vittorio Maria di Pietro**

En vue de l'obtention du grade de

Docteur en Sciences

de l'Université de la Côte d'Azur

Discipline : Physique

Laboratoire INPHYNI

---

Thèse dirigée par **Aurélie Jullien**

Soutenue le 12 Decembre 2019

Devant le jury, composé de :

<b>Marc Hanna</b>	Rapporteur	Laboratoire Charles Fabry, Palaiseau
<b>Antoine Monmayrant</b>	Rapporteur	Laboratoire d'analyse et d'architecture des systèmes, Toulouse
<b>Thomas Heiser</b>	Examineur	Laboratoire des sciences de l'ingénieur, de l'informatique et de l'imagerie, Strasbourg
<b>Giovanna Tissoni</b>	Examinatrice	Institut de Physique de Nice, Sophia
<b>Olivier Uteza</b>	Examineur	Laser, Plasma and Procédés Photonique, Marseille
<b>Aurélie Jullien</b>	Directrice de thèse	Institut de Physique de Nice, Sophia
<b>Nicolas Forget</b>	Invité, co-encadrant	Fastlite, Antibes



---

# Abstract

## Version française

Le travail présenté dans cette thèse émane du projet SOFTLITE, une collaboration entre la société FASTLITE (sas) et le groupe Optique des Cristaux Liquides (OCL) de l'Institut de Physique de Nice (INPHYNI). L'objectif principal de cette collaboration est de développer de nouveaux dispositifs à base de cristaux liquides, reposant sur des cellules nématiques biréfringentes en couche épaisses, pour compléter/remplacer les dispositifs actuels de manipulation, façonnage et mesure d'impulsions laser ultra-rapides. Dans le cadre de cette thèse, très expérimentale, nous présentons ainsi une caractérisation avancée des propriétés électro-optiques de cellules nématiques épaisses (de 25  $\mu\text{m}$  à 250  $\mu\text{m}$ ). Nous démontrons également la possibilité de contrôler ces cellules de manière thermo-optique, ce qui débouche sur un nouveau modulateur spatial de lumière (LC-SLM). Ce dispositif innovant dépasse l'état de l'art des LC-SLM traditionnels et permet de moduler en phase des impulsions laser multi-octave. Dans un premier temps, la caractérisation des propriétés optiques d'un mélange cristal liquide inconnu est proposée, basée sur l'interférométrie spectrale large bande, pour mesurer la dispersion chromatique de cristaux liquides. La technique permet de déterminer les coefficients qui régissent la variation des indices et indices de groupe en fonction de la longueur d'onde et de la température. En vue de développer une ligne à retard colinéaire adaptée aux impulsions ultra-rapides, une étude des différentes stratégies de commutation électro-optique des cristaux liquides est proposée. En particulier, une stratégie de commutation ON (excitation par un échelon de tension) est étudiée malgré la présence d'un seuil de tension (transition de Fréedericksz). Une dépendance inattendue de ce seuil avec l'épaisseur des cellules est découverte et deux régimes distincts sont déterminés. Les cellules épaisses ( $\approx 75 \mu\text{m}$ ) peuvent commuter avec une tension de démarrage inférieure à ce seuil, avec un gain remarquable en excursion en biréfringence. Afin de développer les applications dans le proche et moyen infra-rouge, des cellules optimisées pour cette gamme de longueur d'onde ont été fabriquées. Une fois testées, ces cellules montrent une faible absorption laser par l'électrode (ITO), qui contribue à un échauffement local des cristaux liquides. Leur caractère thermotropique induit ainsi un changement des indices de réfraction. Le déphasage induit génère une structure spatiale en anneaux (modulation de phase spatiale). Le déphasage et, par conséquent, l'excursion de biréfringence sont analysés. De là, la température interne de la cellule est également estimée jusqu'à la transition de phase nématique-isotrope. Cette étude sur la thermotropie induite optiquement a permis de développer une approche originale d'adressage thermo-optique des cellules. Cette stratégie innovante aboutit au dimensionnement d'un composant réflectif, dans lequel l'absorption de la lumière d'un faisceau d'écriture chauffe les cristaux liquides, tandis qu'un second (faisceau de lecture) est modulé en phase en passant dans la couche de cristal liquide. Ainsi, un nouveau dispositif optique est développé et breveté : THOR-SLM (modulateur de lumière spatiale thermo-optiquement réflectif). Trois premiers prototypes sont fabriqués afin de trouver la configuration la plus performante. Les déphasages spatial, spectral et temporel de ces prototypes sont mesurés par interférométrie. Les remarquables propriétés optiques du dispositif sont finalement exploitées : une large acceptation spectrale avec un déphasage important et continu sans pixellisation. En guise de démonstration, THOR-SLM est inséré dans une ligne à dispersion nulle pour le façonnage d'impulsions laser dont le spectre couvre plusieurs octaves. Un façonnage

---

arbitraire sans précédent est démontré sur une largeur de bande spectrale allant du visible au moyen IR, introduisant des valeurs positives/négatives de dispersion de phase jusqu'au troisième ordre. Ces résultats ouvrent la voie à des capacités de mise en forme temporelle d'impulsions femtosecondes de durée quelques cycles optiques.

**Mots clés :** Optique ultra-rapides, Cristaux Liquides, modulateur de lumière spatiale, Façonnage spectrale

## English Version

The work presented in this thesis comes from the SOFTLITE project, a collaboration between the company FASTLITE (sas) and the Optical Group of Liquid Crystals (OCL) of the Institute of Physics of Nice (INPHYNI). The main objective of this collaboration is to develop new liquid crystal devices, based on thick layer birefringent nematic cells, to complement/replace current devices for handling, shaping and measuring ultra-fast laser pulses. In the context of this highly experimental thesis, we present an advanced characterization of the electro-optical properties of thick nematic cells (from 25  $\mu\text{m}$  to 250  $\mu\text{m}$ ). We also demonstrate the ability to control these cells thermo-optically, resulting in a new spatial light modulator (LC-SLM). This innovative device goes beyond the *state-of-the-art* LC-SLM traditional and can phase modulate laser pulses multi-octave. Firstly, the characterization of the optical properties of an unknown liquid crystal mixture is proposed, based on broadband spectral interferometry, to measure the chromatic dispersion of liquid crystals. The technique makes it possible to determine the coefficients which govern the variation of the indices and group indices as a function of the wavelength and the temperature. In order to develop a collinear delay line adapted to ultra-fast pulses, a study of the different electro-optical switching strategies of liquid crystals is proposed. In particular, a switching strategy ON (excitation by a voltage step) is studied despite the presence of a voltage threshold (Fréedericksz transition). An unexpected dependence of this threshold with the thickness of the cells is discovered and two distinct regimes are determined. Thick cells ( $\geq 75 \mu\text{m}$ ) can switch with a starting voltage lower than this threshold, with a remarkable gain in birefringence excursion. In order to develop applications in the near and medium infra-red, cells optimized for this wavelength range have been manufactured. Once tested, these cells show low laser absorption by the electrode (ITO), which contributes to the local heating of the liquid crystals. Their thermotropic nature induces a change in the refractive indices. The induced phase shift generates a spatial structure composed by rings (spatial phase modulation). The phase shift and, consequently, the birefringence excursion are analyzed. From these, the internal temperature of the cell is also estimated up to the nematic-isotropic phase transition. This study on thermotropy induced optically allowed to develop an original approach of thermo-optical addressing of cells. This innovative strategy results in the design of a reflective component, in which the absorption of light from a writing beam heats the liquid crystals, while a second (reading beam) is modulated in phase by passing through the liquid crystal layer. Thus, a new optical device is developed and patented: THOR-SLM (thermo-optically reflective spatial light modulator). Three first prototypes are manufactured to find the most efficient configuration. The spatial, spectral and temporal phase shifts of these prototypes are measured by interferometry. The remarkable optical properties of the device are finally exploited: a wide spectral acceptance with a large and continuous phase shift without pixelization. To demonstrate this, THOR-SLM is inserted in a zero-dispersion line to shape a laser pulse with a spectrum span of several octaves. Unprecedented arbitrary shaping is demonstrated over a spectral bandwidth from visible to IR, introducing positive/negative phase-to-third-order values. These results pave the way for temporal shaping capabilities of femtosecond pulses lasting a few optical cycles.

**Key words :** Ultrafast Optics, Liquid Crystal, Spatial Light Modulators, Pulse shaping

---

# Remerciements, Acknowledgements, Ringraziamenti

Mon plus grand remerciement va à Aurélie. Tu m'as pris sous ton aile lorsque j'étais un jeune étudiant et tu m'as formé avec une patience et une disponibilité infinies. Merci pour tout le travail incroyable que t'as fait pour moi, pour tous les corrections et surtout pour le support constant. T'as été bien plus qu'une simple directrice de thèse et je ten serai toujours reconnaissant.

Je voudrais remercier Fastlite pour l'opportunité qui m'a été offerte et pour la grande confiance qu'on m'a accordé. C'était un plaisir de vivre, même si qu'occasionnellement, avec la famille Fastlite et donc je voudrais remercier tout le monde: Anna, Clément, Gaëtan, Hervé, Nicolas T., Olivier, Pascal, Raman, Simen, Stéphanie, Thomas et Yoann.

Un merci spécial à Nicolas F. pour avoir pris en charge le projet de thèse, pour ton soutien constant et pour les conseils scientifiques, entre autres, que tu m'as donné. Egalement, un merci particulier à Simone et Vincent qui ont dû me toléré au bureau comme au laboratoire.

Je tiens à remercier tous les membres de l'équipe d'optique des cristaux liquides du laboratoire. Sans chacun de vous, il aurait été impossible d'en arriver là aujourd'hui. Une pensée particulière pour Gilles, Maxim et Romain: vous avez été plus que des collègues, mais des amis même en dehors de lieu de travail, merci de tout coeur.

Qui me connaît sait combien je participe activement à la vie du laboratoire. Je voudrais donc remercier tous ceux qui ont partagé avec moi un petit café et des blagues pendant ces années. Un remerciement special à Mathilde, pour tous les repas passés ensemble.

Merci à toute l'administration du laboratoire et aux services informatiques: Christian, Isabelle, François-Regis (on parle pas de foot eh!?) et Nathalie.

I would like to thank all my PhD mates. I was so excited to come to work every day because I knew that I would have found the healthy madness that I needed. First, I would like to thank who has introduced me to the lab: Cristina and Axel, but also Aurélien, Jean and Patrice (I will always consider you as PhD student). Then, I would like to thank those who have shared with me those years: Adrian, Alexis, Ana, Amy, Florent, Giovanni, Jesús, Julián, Loïc, and Marius. A special thank goes to *Mon Potó Antonino*: thank you for all your corrections, for our football sessions, for our breaks, for our hangouts, and for all jokes we have made.

One of the best things about a PhD program is that you get to meet many other students, scientists and researchers from other institutes all around the world. Some of them have also

---

participated in this work, so I would like to thank: Aurélien, Bernard, Chiara, Fabian, Florian, Kaloyan, Nicola B., Nicola D., Peter, Philipp, Salvatore, Sebastian, Stefano D., Stefano S., Thomas, Tobias, Victor.

Chi ha vissuto lontano dalla famiglia e dai cari sa cosa significhi avere intorno persone che possano farti sentire a casa anche, e soprattutto, all'estero. In questi anni, ho avuto la fortuna di incontrare, conoscere e legare con ragazzi eccezionali che hanno riempito le mie giornate. Le nostre serate, i nostri pranzi, ma anche le nostre semplici scampagnate o spese in Italia rimarranno per sempre impressi nella mia memoria. Per questo, e per tanto altro ancora, vorrei ringraziare personalmente ciascuno dei membri dei F.I.C.A. :

Grazie Albe, perché le tue parole d'amico mi rimarranno sempre dentro (quali parole?).  
Grazie Aldo, perché sei stato il primo che ho conosciuto e, difatti, dovevo farmi i fatti miei.  
Grazie Anne, perché ci costringi a parlare francese pure nel week-end.  
Grazie Bullo, perché mi hai rubato il compagno di avventure.  
Grazie Felix, perché mi hai confermato che i napoletani sanno fare solo la pizza.  
Grazie Ferro, perché per me rimarrai sempre l'imbucato francese alla festa di Natale.  
Grazie Frigo, perché il tuo essere commmmunista mi ha fatto capire quanto sia fortunato.  
Grazie Giando, perché senza di te avremmo ottenuto, noi tutti, dei risultati migliori.  
Grazie Giova, perché un giorno realizzerai il tuo sogno e ti schiereremo attaccante, ma non oggi.  
Grazie Isa Mo, perché potevi prestarmi il tuo servizio da tavola oggi e non l'hai fatto.  
Grazie Isa Mu, perché, dati alla mano, come voce della coscienza fai abbastanza schifo.  
Grazie Luca, perché nonostante tutto sei ancora in vita, purtroppo.  
Grazie Lore, perché per mia fortuna sono sempre riuscito a evitarti sul 230.  
Grazie Marco, perché il tuo scazzo sui buongiornissimi mi ha fatto raggiungere il Nirvana (cit.).  
Grazie Max, perché seguire il Milan con te lo ha fatto piombare in zona retrocessione, Bedy-law?  
Grazie Pupi, perché mi sono reso conto di quanto ti abbia preso in giro... potevo fare di meglio.  
Grazie Veneta, perché tanto prima o poi ti trovo, tu sai dove.

Anche se lontano da casa, i miei amici storici non mi hanno mai fatto mancare il loro calore e la loro simpatia. Un grazie speciale a Matteo, Simone, Patrizio.

Ci tengo a ringraziare anche chi, non facendo più parte della mia vita oggi, ha comunque permesso che questo giorno arrivasse.

Un ringraziamento va anche ai miei zii e i miei zii acquisiti, i *'Mariucci'*. Grazie per la vostra presenza costante, soprattutto per i tanti chilometri che avete fatto per venire a festeggiare qui oggi.

Un pensiero speciale va alla mia famiglia. Babbo, Bu, Mamma: Voi siete stati il motore che mi ha spinto ogni giorno a mettermi alla prova, a migliorarmi e a puntare in alto. Mi avete supportato in ogni mia decisione, anche la più controversa, e in questo lavoro c'è tanto del vostro. *Da piccolo vi promisi che un giorno sarei diventato 'Dottore' e oggi, in un certo senso, lo sono diventato.*

Un bacio va anche alla mia Nonna, perché so di essere sempre al centro dei suoi pensieri e delle sue preghiere.

Vorrei ringraziare Marika, perché nel momento più buio, mi hai dato occhi nuovi per vedere il Mondo.

And well, thanks to all that I should have mentioned but I forgot.

---

Infine...

...ci siamo lasciati qualche giorno fa con la promessa che avresti fatto di tutto per essere qui oggi. Purtroppo così non è stato, ma so che in qualche modo, mi sei stato vicino fino alla fine, come hai sempre fatto, a partire da quando mi hai insegnato a camminare, o meglio a fare *Hoppe Hoppe*.

Nonno, questo lavoro è per te.



---

---

# Contents

<b>1</b>	<b>Introduction</b>	<b>1</b>
1.1	Femtosecond pulses . . . . .	2
1.1.1	Ultrashort pulses description . . . . .	2
1.1.2	Ultrafast measurement techniques . . . . .	4
1.1.3	Spectral phase and temporal shaping . . . . .	7
1.1.4	Zero-Dispersion-line . . . . .	9
1.1.5	State-of-the-art of ultrafast systems . . . . .	10
1.2	Liquid Crystals . . . . .	12
1.2.1	Introduction to Liquid Crystal features . . . . .	12
1.2.2	Nematic liquid crystals . . . . .	13
1.2.3	Effects of an Electric Field on a Nematic Liquid Crystal . . . . .	15
1.2.4	Nematic Liquid Crystals thermotropicity . . . . .	19
1.2.5	Some liquid crystal mixtures . . . . .	20
1.2.6	LC Cell fabrication . . . . .	21
1.3	Liquid crystals for ultrafast optics . . . . .	23
1.4	SOFTLITE . . . . .	25
1.4.1	A new collaboration for ultrafast pulse shaping with Liquid Crystal . . . . .	25
1.4.2	Thesis Objectives . . . . .	25
<b>2</b>	<b>Characterization of a highly birefringent LC (MLC2132, Merck) with broad-band spectral interferometry</b>	<b>29</b>
2.1	Background . . . . .	30
2.2	Introduction . . . . .	31
2.3	Broadband spectral interferometer for characterization of the LC chromatic dispersion . . . . .	32
2.3.1	Experimental set-up . . . . .	32
2.3.2	Method . . . . .	33
2.3.3	E7 extended Cauchy coefficients validation . . . . .	33
2.3.4	MLC2132 characterization . . . . .	34
2.4	Towards a referenced refractometer . . . . .	36
2.5	LC thermotropic analysis . . . . .	38
2.5.1	Introduction . . . . .	38
2.5.2	Experimental set-up . . . . .	39
2.5.3	Analysis & results . . . . .	39
2.6	Conclusions & Prospectives . . . . .	40
<b>3</b>	<b>Dynamics of electrically driven thick nematic LC cells</b>	<b>43</b>
3.1	Introduction: electrically driven LC tunable delay line . . . . .	44
3.1.1	Background . . . . .	44
3.1.2	Experimental methods . . . . .	45
3.2	LC tunable delay line based on Adiabatic Electrical control . . . . .	47

---

3.3	Transient nematic relaxation addressing . . . . .	48
3.3.1	Principle and response time . . . . .	48
3.3.2	Back-reflexion issues . . . . .	49
3.4	Switch-on addressing . . . . .	51
3.4.1	Fréedericksz transition (FT) . . . . .	51
3.4.2	Dynamical characterization of the Fréedericksz transition . . . . .	52
3.4.3	LC thickness influence on the Fréedericksz transition . . . . .	53
3.4.4	Temporal dynamical features . . . . .	55
3.4.5	LC tunable delay line based on switching-on addressing . . . . .	57
3.4.6	Dynamical characterization of MLC2132 . . . . .	59
3.5	Conclusions & Prospectives . . . . .	59
<b>4</b>	<b>Thermo-optically-induced spatial phase-shift in electrically-driven nematic Liquid-Crystal cells</b>	<b>61</b>
4.1	Electro-optical applications of LC in the IR spectral range . . . . .	62
4.1.1	Motivations . . . . .	62
4.1.2	Background . . . . .	62
4.1.3	Introduction . . . . .	63
4.2	Experimental evidence of absorption in the ITO . . . . .	63
4.2.1	Experimental set-up . . . . .	63
4.2.2	Temporal dynamics . . . . .	64
4.3	Thermo-optically induced self spatial phase modulation . . . . .	64
4.3.1	Principle of thermo-optically induced phase shift . . . . .	64
4.3.2	Enhancement of the thermal effect . . . . .	65
4.3.3	Numerical simulations . . . . .	66
4.3.4	Analysis . . . . .	67
4.3.5	Driving the LC to the isotropic phase transition . . . . .	69
4.3.6	Estimation of the thermal gradient spatial extension . . . . .	71
4.4	Conclusions & Prospectives . . . . .	72
<b>5</b>	<b>An achromatic thermo-optically addressed LC light modulator: THOR</b>	<b>75</b>
5.1	Introduction . . . . .	76
5.1.1	Liquid Crystal SLM and Liquid Crystal Light Valves: an overview . . . . .	76
5.1.2	An innovative LC-SLM: THOR . . . . .	78
5.1.3	THOR-SLM prototypes . . . . .	79
5.2	Characterization of three different THOR-SLM with homogeneous light-addressing	81
5.3	THOR-SLM: Spatial interferometry . . . . .	84
5.3.1	Experimental set-up . . . . .	84
5.3.2	Fringes description . . . . .	84
5.3.3	Spatial phase shift analysis . . . . .	86
5.3.4	Spatial deformations interpretation . . . . .	88
5.3.5	Polarization analysis . . . . .	88
5.3.6	Conclusions . . . . .	88
5.4	THOR-SLM temporal shaping: group delay management . . . . .	89
5.4.1	Experimental set-up . . . . .	89
5.4.2	Results & Analysis . . . . .	90
5.4.3	Scaling with the thickness of the LC layer . . . . .	92
5.4.4	Temporal dynamics . . . . .	93
5.5	THOR-SLM: phase shaping in a 4f-line . . . . .	95
5.5.1	Experimental Set-up . . . . .	95
5.5.2	Estimation of the spectral phase resolution . . . . .	96
5.5.3	Spectral phase shaping . . . . .	98

---

5.6	Conclusions & prospectives . . . . .	101
<b>6</b>	<b>Phase shaping of a multi-octave light source</b>	<b>103</b>
6.1	State-of-the-art of ultra-broadband phase shapers . . . . .	104
6.2	Introduction . . . . .	105
6.3	Estimation of the thermal gradient in THOR-SLM . . . . .	106
6.3.1	Numerical simulations . . . . .	106
6.3.2	New writing beam arrangement: arbitrary control of the writing beam . .	108
6.3.3	Experimental estimation of the thermal gradient . . . . .	109
6.4	Ultra broadband interferometer . . . . .	111
6.4.1	Experimental set-up . . . . .	111
6.4.2	THOR-SLM spectral reflectivity . . . . .	112
6.4.3	Calibration of the interferometer . . . . .	113
6.5	Targeted phase and associated spatial profiles . . . . .	115
6.5.1	Phase shaping algorithm . . . . .	115
6.6	Phase shaping experimental results . . . . .	118
6.6.1	Spatial sensitivity . . . . .	118
6.6.2	Pure quadratic or cubic phase . . . . .	119
6.6.3	Influence of the writing beam power . . . . .	120
6.6.4	Influence of the LC layer thickness . . . . .	120
6.7	Prospectives . . . . .	122
6.7.1	Experimental arrangement improvements . . . . .	122
6.7.2	THOR-SLM conception improvements . . . . .	123
6.8	Conclusions . . . . .	125
<b>7</b>	<b>Annex</b>	<b>129</b>
A.1	Scientific Production . . . . .	129
A.1.1	List of Publications . . . . .	129
A.1.2	Patents . . . . .	129
A.1.3	List of conferences . . . . .	130
B.2.4	HICONO activities . . . . .	130
D.4	THOR-SLM applications . . . . .	131
D.4.1	First applications to femtosecond pulses . . . . .	131
D.4.2	Defocusing tunable lens for IR light . . . . .	134
	References . . . . .	145



---

# General Introduction

The development of femtosecond lasers is maybe one of the most striking facts in the history of lasers since their invention. These ultra-short sources have opened the field to a considerable number of academic and industrial applications such as laser machining, multi-photon microscopy, coherent control of atomic or molecular systems and, more generally, the study and control of ultrafast phenomena. Today, the femtosecond laser is a must-have tool in chemistry, biology, medicine, micro-machining and even archaeology. As underlined by the attribution of the Physics Nobel Prize in 2018, progress have also been spectacular in the research field of ultra-intense lasers, and its applications to particle acceleration and generation of secondary sources in various parts of the electromagnetic spectrum. Indeed, at the dawn of the 2000s, the control of the spatio-temporal quality of energetic pulses has made it possible to reach on target intensities as high as  $10^{21}W/cm^2$ . A couple of years later, the ability to generate intense pulses, whose duration does not exceed a few oscillations of the electric field (few-cycle regime), combined with the stabilization of the phase between the carrier of the field and its envelope, disrupts the temporal landmarks and opens the attosecond physics.

Research topics related to femtosecond sources are extremely varied and under constant development. Among them, the ability to shape the spatial and spectro-temporal properties of the pulses enables to optimize the associated interaction or studied dynamically. Thus, numerous advanced optical instruments and processes to control the temporal profile of femtosecond pulses, and to reduce their duration through new frequencies generation, are the basis of third-generation ultrafast sources architecture.

As for the femtosecond scientific community, research and development of liquid crystal have done some incredible step forward in the last decades. Since the first display, presented in 1968 by Heilmeyer, liquid crystal technology is constantly evolving even in non-display applications such as non-linear optics, optical communication, and data/signal/image processing. Indeed, this huge impact on the society was awarded in 1991 with the Nobel Prize. Nowadays Liquid crystal science permeates almost all segments of the society, from large industrial displays to individual homes and offices. Industrial applications are still dynamic in the field of displays (extra-large field of view or folding screens) and smart windows, just to cite a few. Scientific research, for its part, is still very active in the field of continuous non-linear optics. Moreover, blue phases liquid crystal are opening new prospectives in display performances, meanwhile the biomimetism of chiral mixtures is under study, this phase being widespread in living matter.

It should be noted that liquid crystals have been and are still widely used in optics, but their properties have been barely exploited in the regime of ultrafast optics, except the traditional spatial light modulators including a thin nematic layer. As a matter of fact, none of the existing devices is able to fully exploit their broad transparency and their large tunable birefringence. Nevertheless, the remarkable and configurable properties of liquid crystals make them suitable candidates to provide new and complementary technological solutions for the manipulation of femtosecond sources, especially when the liquid crystal is arranged in thick-layers.

For this reason, the project SOFTLITE has begun in 2015 between the company FASTLITE SAS and the optics of liquid crystal group of the INPHYNI and a new thematic has emerged. The

---

main goal of this collaboration is to create a scientific activity able to merge the ultrafast physics with the liquid crystal one, in order to improve not only the available devices suitable for linear ultrashort pulses manipulation, but also to provide an ultrafast characterization of optical properties of liquid crystal, especially non-linearly induced. In particular, one goal is to skilfully exploit the physical mechanisms behind liquid-crystal-based spatial light modulators, thereby optimizing their conception and operation, and making them more compatible with ultrashort pulse, especially in the infrared spectral range.

In the framework of this collaboration, this thesis, highly experimental, is born. Its goal is to optically characterize thick nematic liquid crystal cells and evaluate their possible implementation for ultrafast manipulation. The characterization firstly involves the liquid crystal mixture itself, developing an original method to analyze its chromatic dispersion. Afterward, a study about the unexpected influence of the liquid crystal thickness on the molecular reorientation for electro-optic applications is disclosed. The attempt to extend the working spectral range to the infrared light is demonstrated to be hampered by yet-IR-optimized materials. Nevertheless, this experiment indicates a new way to control the refractive index of the liquid crystal molecules. Exploiting this new control strategy, an innovative phase-only pulse shaper is developed and patented. This device is finally able to fully take advantage of the unique liquid crystal optical properties opening the way to unprecedented temporal shaping capabilities of few-cycle and single-cycle femtosecond pulses.

---

## List of Acronyms

Acronym	Meaning
FTL	Fourier Transform Limit
GD	Group Delay
GDD	Group Delay Dispersion
TOD	Third Order Dispersion
CEP	Carrier-envelope phase
FTSI	Fourier-Transform Spectral Interferometry
FROG	Frequency-Resolved Optical Gating
D-S	Dispersive scan
SHG	Second Harmonic Generation
CM	Chirped Mirrors
AOPDF	Acousto-optic programmable dispersive lters
LC	Liquid Crystal
SLM	Spatial Light Modulator
LC-SLM	Liquid Crystal based Spatial Light Modulator
CPA	Chirped Pulse Amplification
OPA	Optical Parametric Amplification
LCD	Liquid Crystal Display
CLC	Cholesteric Liquid Crystal
NLC	Nematic Liquid Crystal
FT	Freedericksz transition
ITO	Indium Tin Oxide
PVA	polyvinyl alcohol
E7	cyanobiphenyls mixture
SPM	Spatial Phase modulation



---

Acronym	Meaning
LCOS	Liquid crystal on silicon
LCLV	Liquid Crystal Light Valve
LLCD	Laser-Addressed Liquid Crystal Displays
THOR-SLM	Thermo-optical Reflective Spatial light Modulator
E7-Gold	THOR-SLM prototype based on 50 $\mu\text{m}$ of E7 mixture and Gold mirror
E7-Gold-25	THOR-SLM prototype based on 25 $\mu\text{m}$ of E7 mixture and Gold mirror
E7-Gold-110	THOR-SLM prototype based on 110 $\mu\text{m}$ of E7 mixture and Gold mirror
MLC-Gold	THOR-SLM prototype based on 50 $\mu\text{m}$ of MLC2132 mixture and Gold mirror
MLC-Chrome	THOR-SLM prototype based on 50 $\mu\text{m}$ of MLC2132 mixture, Chrome-Silver mirror
DLP	Digital Light Processor

---

---

# Chapter 1

## Introduction

### Objective

In this Chapter, a brief introduction to the femtosecond science is presented. Some methods to shape and measure an ultrashort pulse are described with a summary of the state-of-the-art of ultrafast systems. The physics of liquid crystal is described as-well. A description of the molecular reorientation and liquid crystal thermotrocipity is proposed.

Finally, the motivations that have led to this work are disclosed with summary of the main achievements.

## 1.1 Femtosecond pulses

### 1.1.1 Ultrashort pulses description

In this section, the general concepts used to describe femtosecond pulses are presented, restricted to the main notions used in the manuscript.

Since the invention of mode-lock lasers in the mid-1960s, ultrafast laser pulses have become key tools for ultrashort phenomena studies, and they are widely used in research nowadays. Laser plasma physics, attosecond science, ultrafast reaction dynamics in chemistry, biomacromolecules solid-state, and two-photon laser microscopy, just to cite a few that require femtosecond pulses as a laser excitation source.

An optical pulse is defined by its electric field:

$$\varepsilon(t) = A(t)e^{(-i\omega_0 t + \Phi_0 + \Phi(t))} \quad (1.1)$$

where  $A(t)$  is the real envelope changing in time,  $\omega_0$  is the fundamental frequencies defining the oscillation of the carrier wave,  $\Phi_0$  the so-called CEP (carrier-envelope phase), and  $\Phi(t)$  the temporal phase. The electric field can be expressed in the spectral domain also through Fourier Transform:  $\tilde{\varepsilon}(t) = \frac{1}{2\pi} \int_{-\infty}^{+\infty} \varepsilon(\omega)e^{-i\omega t} d\omega$ , and  $\tilde{\varepsilon}(\omega) = \int_{-\infty}^{+\infty} \varepsilon(t)e^{i\omega t} dt$ . Thus,  $\tilde{\varepsilon}(\omega)$  can be re-written as:

$$\tilde{\varepsilon}(\omega) = A(\omega)e^{i\varphi(\omega)} \quad (1.2)$$

where  $A(\omega)$  is the spectral amplitude and  $\varphi(\omega)$  the spectral phase. As a consequence, a pulse is completely known, if  $A(\omega)$  and  $\varphi(\omega)$  are known. These two quantities directly contribute to the pulse temporal profile.

The shortest pulse duration is achieved when the spectral phase is flat, and is then so-called

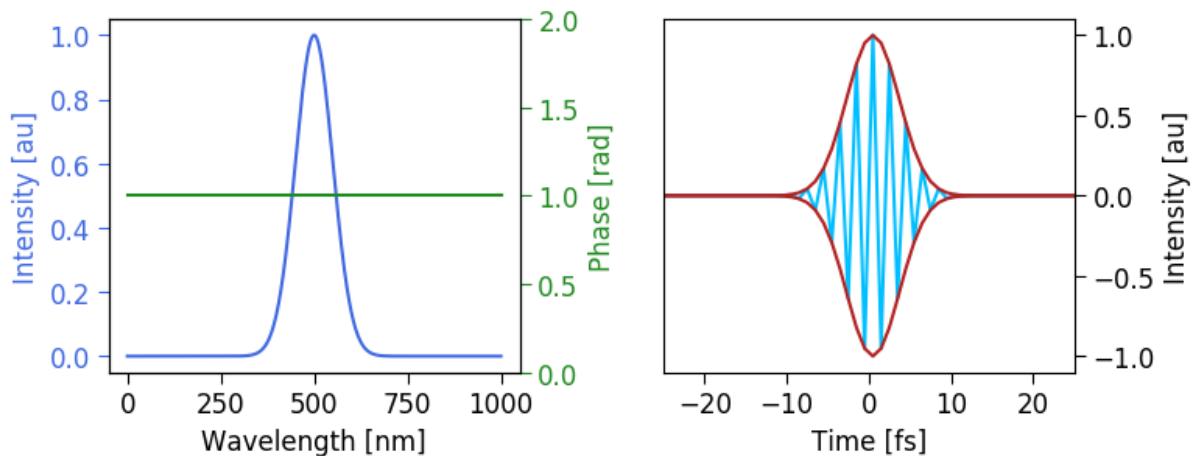


Figure 1: Spectral and temporal representation of a Gaussian ultrashort pulse.

*Fourier Transform Limited (FTL)*. If the pulse is Fourier Limited, its duration is inversely proportional to its spectral bandwidth. Hence, the common way to handle spectral phase functions is to describe them through their Taylor series as:

$$\varphi(\omega) = \varphi(\omega_0) + \frac{d\varphi(\omega)}{d\omega} \Big|_{\omega_0} (\omega - \omega_0) + \frac{1}{2} \frac{d^2\varphi(\omega)}{d\omega^2} \Big|_{\omega_0} (\omega - \omega_0)^2 + \frac{1}{6} \frac{d^3\varphi(\omega, z)}{d\omega^3} \Big|_{\omega_0} (\omega - \omega_0)^3 + \dots \quad (1.3)$$

The so-called phase derivatives, have the following conventional notations:

$$GD \equiv \varphi^{(1)} = \frac{d\varphi(\omega)}{d\omega} \Big|_{\omega_0} \quad (1.4)$$

$$GDD \equiv \varphi^{(2)} = \frac{d^2\varphi(\omega)}{d\omega^2} \Big|_{\omega_0} \quad (1.5)$$

$$TOD \equiv \varphi^{(3)} = \left. \frac{d^3 \varphi(\omega)}{d\omega^3} \right|_{\omega_0} \quad (1.6)$$

Where GD, GDD, and TOD stand respectively for group-delay, group-delay dispersion, and third order dispersion.

A group delay (GD) change simply corresponds to a temporal shift of the pulse without any profile deformation.

The quadratic term, GDD or chirp, describes the fact that the frequency components do not propagate at the same velocity in a dispersive medium, and is responsible for the temporal spreading of the pulse, with a linear temporal distribution of the frequencies.

Third order dispersion (TOD) corresponds to the cubic phase and leads in the temporal domain to pre and post pulses.

The influence of these terms onto the temporal profile of a pulse is shown in Figure 2. Higher spectral orders are not taken into account in this thesis, but they have an important role for ultra-fast pulses.

Fitting algorithms provide the coefficients of the Taylor series to characterize the laser pulse. However, the reconstructed spectral polynomial phase may diverge from the actual spectral phase function at frequencies far from  $\omega_0$ .

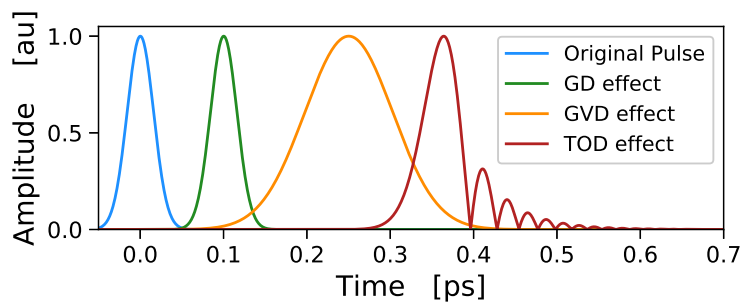


Figure 2: Effect of the first three phase components on the pulse temporal profile.

Any dispersive medium presents a chromatic variation of its refractive index  $n(\omega)$  and modifies the spectral phase of the propagating pulse following:

$$\varphi(\omega, z) = \omega \frac{n(\omega)z}{c} \quad (1.7)$$

Thus, the larger the spectrum of the considered pulse, the more the pulse will be sensitive to the material's spectral phase, which therefore must be quantified and controlled.

To summarize, knowing  $A(\omega)$  and  $\varphi(\omega)$  is the key of pulse temporal measurement while controlling these quantities opens the way to pulse shaping.

Temporal dispersion might be accompanied also by spatial dispersion, e.g. when a pulse refracts at the boundary between media with different dispersions or passes through a prism or a grating (see Figure 3), the propagation is also affected by the so-called angular dispersion. The different spectral components of the original pulse are not only propagating at different velocities but also in different directions. Angular dispersion is practically always accompanied by some pulse front tilt and spatial chirp. One can see easily that spatio-temporal pulse distortions usually arise simultaneously; moreover, they are coupled with each other. A general mathematical analysis of this effect is discussed in (Akturk, Gu, Gabolde, & Trebino, 2005). So, angular dispersion is a tool for pulse shaping, indeed spatial dispersion enables to manipulate independently the spectral components.

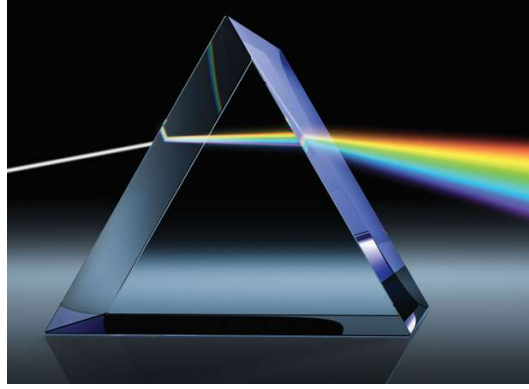


Figure 3: Angular dispersion induced by a dispersive glass prism.

### 1.1.2 Ultrafast measurement techniques

Electrical detectors are obviously too slow to access the temporal dynamic of a femtosecond pulse. Thus, for pulse characterization, optical methods are necessary. Furthermore, it is more convenient to examine the pulse properties in the spectral domain. One can distinguish linear and non-linear methods.

#### A linear method: the spectral interferometry

Spectral interferometry has been introduced in 1973 by C. Froehly (Froehly, Lacourt, & Vienot, 1973). It allows measuring the difference in spectral phase between two coherent polychromatic pulses.

In this thesis, a particular numerical treatment of the spectral interferometry has been used several times: the *Fourier-Transform Spectral Interferometry* technique (FTSI) (Lepetit, Chériaux, & Joffre, 1995). In this section, a general view of the method and numerical treatment, extensively explained in (Grabielle, 2011), is presented.

**The Fourier-Transform Spectral Interferometry FTSI** The pulse that has to be characterized is defined by  $\varepsilon(\omega)$  (eq. 1.2), while the reference one is completely described with  $\varepsilon_0(\omega)$  (Figure4). Both can be represented in the time domain, respectively, by the complex fields  $\varepsilon(t)$  and  $\varepsilon_0(t)$ . If the two pulses coherently interfere with a time delay  $\tau$ , the spectral-fringes pattern

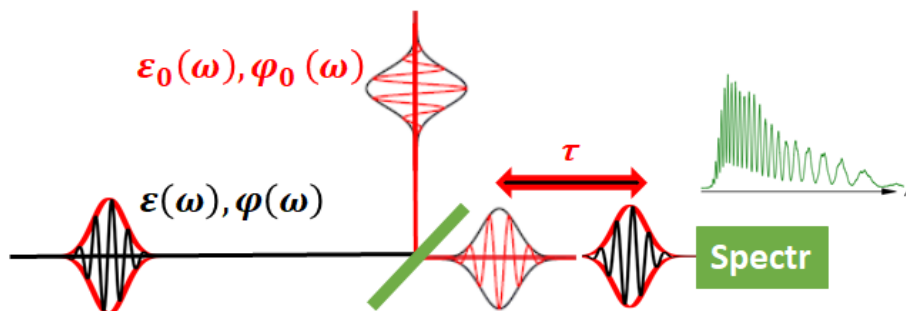


Figure 4: Principle of spectral interferometry.

corresponding to the electric field can be written as:

$$S(\omega) = |\varepsilon_0(\omega) \exp(i\omega\tau) + \varepsilon(\omega)|^2 \quad (1.8)$$

In terms of spectral amplitude and phase, eq.1.1.2 can be re-written as:

$$S(\omega) = |\varepsilon_0(\omega)|^2 + |\varepsilon(\omega)|^2 + 2|\varepsilon_0(\omega)||\varepsilon(\omega)| \cos[\varphi_0(\omega) - \varphi(\omega) + \omega\tau] \quad (1.9)$$

This expression (eq.1.1.2) can be split into two parts:

- Non-interferometric terms which contain no information about the spectral phase difference between the two pulses (first two terms)
- An interferometric term that contains all the information on the spectral phase difference between the two pulses (last term).

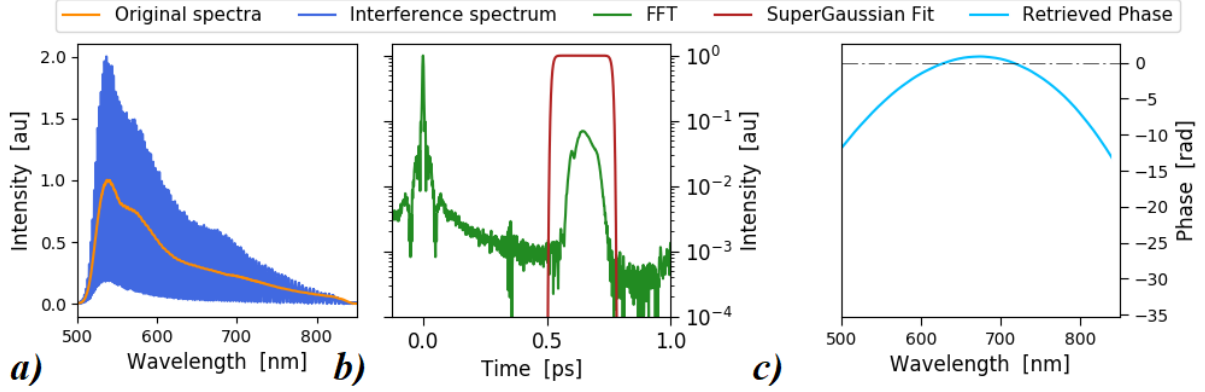


Figure 5: FTSI algorithm: a) Original spectral and its interference pattern. b) AC component filtering, c) Retrieved spectral phase.

Considering  $f(\omega) = \varepsilon^*(\omega)\varepsilon_0(\omega)$  and  $S_0(\omega) = |\varepsilon_0(\omega)|^2 + |\varepsilon(\omega)|^2$ , the interferometric signal of eq.1.1.2 can be also written as:

$$S(\omega) = S_0(\omega) + f(\omega) \exp(i\omega\tau) + f^*(\omega) \exp(-i\omega\tau) \quad (1.10)$$

By Fourier transform, the signal in the time domain is:

$$\tilde{S}(t) = \tilde{S}_0(t) + \tilde{f}(t - \tau) + \tilde{f}^*(-t - \tau) \quad (1.11)$$

where  $\tilde{S}_0(t)$  and  $\tilde{f}(t - \tau)$  are respectively the Fourier transforms of  $S_0(\omega)$  and  $f(\omega)$ . Replacing  $\tilde{S}_0(t)$  and  $\tilde{f}(t - \tau)$  by their relative electric field functions  $\tilde{\varepsilon}_0(t)$  and  $\tilde{\varepsilon}(t)$

$$\tilde{S}_0(t) = \tilde{\varepsilon}_0^*(-t) \otimes \tilde{\varepsilon}_0^*(t) + \tilde{\varepsilon}^*(-t) \otimes \tilde{\varepsilon}^*(t) \quad (1.12)$$

$$\tilde{f}(t - \tau) = \tilde{\varepsilon}_0(t - \tau) \otimes \tilde{\varepsilon}(-t) \quad (1.13)$$

$$\tilde{f}^*(-t - \tau) = \tilde{\varepsilon}_0(t + \tau) \otimes \tilde{\varepsilon}(-t) \quad (1.14)$$

So,  $\tilde{S}_0(t)$  corresponds to the sum of the first order of the auto-correlations of  $\tilde{\varepsilon}_0(t)$  and  $\tilde{\varepsilon}(t)$  (eq.1.1.2) and it is generally defined as the DC component. This term is centered in  $t = 0$  as shown in Figure 5b). The following two terms  $\tilde{f}(t - \tau)$  and  $\tilde{f}^*(-t - \tau)$  correspond to the cross-correlation products of the fields (1.1.2 and 1.1.2) and they are commonly called AC components. The addition of a delay  $\tau$  between the two pulses is crucial in this technique. For a zero-delay no fringes are obtained and the difference of phase cannot be reconstructed. Furthermore, its value has to be accurately chosen so as the component centered at  $t = 0$  and the one centered at  $t = \tau$  do not overlap in time domain.

Therefore, the three steps of the FTSI algorithm are:

1. Fourier transform of the interference spectrum

## 1. Introduction

2. Filtering of the AC components in time domain ( $t = \tau$ )
3. Inverse Fourier transform (returning to the spectral domain) which leads to the phase difference

These three steps represent the FTSI algorithm technique which is illustrated in Figure 5. The signal  $S'(\omega)$  is so obtained after the temporal filtering (Super-Gaussian filter) and an inverse Fourier transform:

$$S'(\omega) = \varepsilon^*(\omega)\varepsilon_0(\omega) \exp(i\omega\tau) = |\varepsilon_0(\omega)||\varepsilon(\omega)| \exp[i(\varphi_0(\omega) - \varphi(\omega) + \omega\tau)] \quad (1.15)$$

Where the module of  $S'(\omega)$  gives the spectral amplitudes product  $|\varepsilon_0(\omega)||\varepsilon(\omega)|$ , while its argument  $\Phi(\omega)$  is:

$$\Phi(\omega) = \varphi_0(\omega) - \varphi(\omega) + \omega\tau \quad (1.16)$$

Subtracting the linear term, determined by a polynomial fit or accurate calibration of the introduced delay, the spectral phase difference between the two pulses is retrieved:

$$\Delta\varphi(\omega) = \varphi_0(\omega) - \varphi(\omega) \quad (1.17)$$

Since the spectral phase  $\varphi_0(\omega)$  of the reference pulse is known, the phase of the pulse to characterize  $\varphi(\omega)$  is reconstructed.

In the framework of this thesis, spectral interferometry is widely used, in self-referenced configuration to characterize spectral phase changes undergone by an ultrashort pulse when propagating through an unknown sample (see Figure 6).

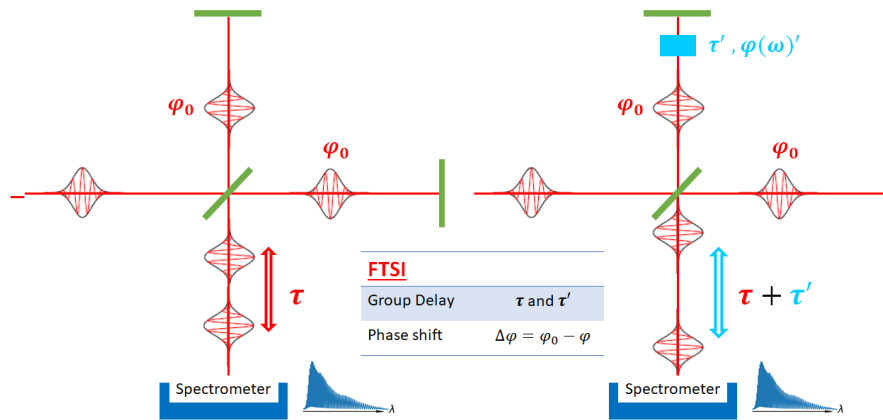


Figure 6: The FTSI technique in self-referenced Michelson configuration.

## Non-linear Methods

Non-linear methods enable to get access to the pulse spectral properties without the need of a reference pulse. Several methods have been proposed, here only two of those are briefly described.

**FROG** Second Harmonic Generation SHG FROG is a spectrally-resolved second-order autocorrelation of the pulse (Trebino, 2012). A typical experimental set-up and spectrogram are shown in Figure 7. The detected intensity autocorrelation signal is emitted as:

$$I_{FROG}(\tau, \omega) = \left| \int \varepsilon(t)\varepsilon(t - \tau) \exp(i\omega t) dt \right|^2 \quad (1.18)$$

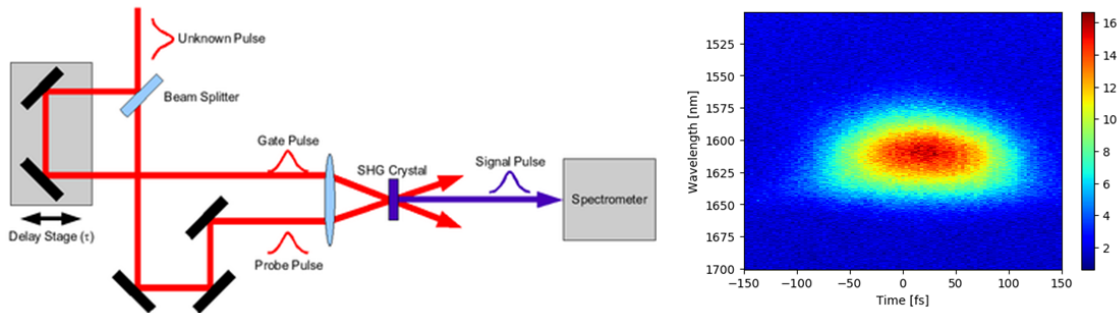


Figure 7: Scheme of a typical experimental SHG FROG setup with a typical spectral map.

Finally, FROG uses a phase-retrieval algorithm to retrieve the intensity and the phase from the measured spectrogram.

FROG devices are relatively easy to implement and existing set-ups (such as an auto-correlator or a cross-correlator) can be adapted to measure FROG traces. The device is suitable for a wide range of pulse durations. The iterative analysis algorithm and the ambiguity on the phase sign are still the main drawbacks of this technique.

### Dispersion-scan

The technique relies on a dispersion scan by mechanical insertion of glass wedges around the optimum compression value, while recording simultaneously spectrum issued from a non-linear process, this one being second-order (SHG<sup>1</sup> (Miranda et al., 2012)) or third-order non-linear process (XPW (Tajalli et al., 2016)).

The phase recovery relies on an iterative algorithm as well. The technique is quite simple and makes use of a dispersive devices already included in the laser chain. However, because of the amount of dispersion necessary, it is usually restricted to sub-10 femtosecond pulses.

#### 1.1.3 Spectral phase and temporal shaping

In parallel to the development of femtosecond pulses characterization tools, large efforts have been pushed towards arbitrary pulse shaping. For linear methods, it consists in modifying in a controlled way the phase relationship between the frequency components of the pulse. None of the existing pulse shapers is universal: different systems are available with various performances in terms of pulse shaping capability, spectral bandwidth acceptance, tunability, ease of use, and cost. In the following, most of the common methods are briefly explained.

### Prisms

Prisms-pairs are one of the first optical components developed for ultrafast pulse phase manipulation. They are well suited to introduce adjustable group delay dispersion. Negative and positive group delay dispersions are obtained via the angular dispersion. By translating one of the prisms along its axis of symmetry it is possible to change the amount of glass crossed and therefore the dispersion inserted. These devices allow a convenient continuous tuning of group delay dispersion from negative to positive values without beam deviation. Large negative GDD can be introduced, however a distance exceeding 1 m is often impractical (Träger, 2012). Those devices are not the most versatile as phase shapers, indeed arbitrary phase management is still cumbersome. Nevertheless, they can handle broadband spectra, sometimes even larger than an octave.

<sup>1</sup><http://sphere-photonics.com/>



## Gratings Pairs

Another historical method to manipulate the phase of an ultra-fast pulse involves diffraction gratings. In a similar way to prisms, gratings provide the spatial dispersion of the pulse spectrum via angular dispersion. This chromatic dispersion is governed by the grating equation:

$$\sin(\gamma) + \sin(\theta) = \frac{\lambda}{d} \quad (1.19)$$

where  $\gamma$  is the angle of incidence,  $\theta$  is the angle of the reflected wavelength component and *grooves/mm* is the grating constant  $d$ .

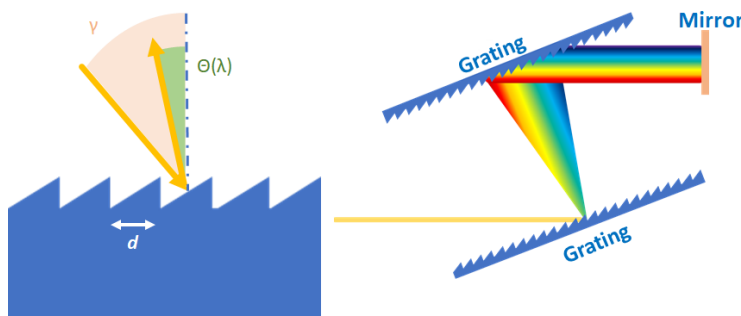


Figure 8: Basic set-up of a phase shaper based on gratings.

The standard grating arrangement consists of two parallel gratings in a double-pass configuration, as pictured in Figure 8. This system provides a longer optical path for the longest wavelength components than the shortest one, therefore pulse compression can be achieved. This system can be considered one of the most dispersive in terms of net phase shape capabilities. The spectral acceptance bandwidth is limited to one octave, with low diffraction efficiency far from their central working wavelength.

## Chirped-Mirrors

Chirped mirrors (CM) are essential elements in the landscape of pulse shaping. These dielectric dispersive mirrors are composed of chirped Bragg-type multi-layers enabling different penetration depth of the different spectral components.

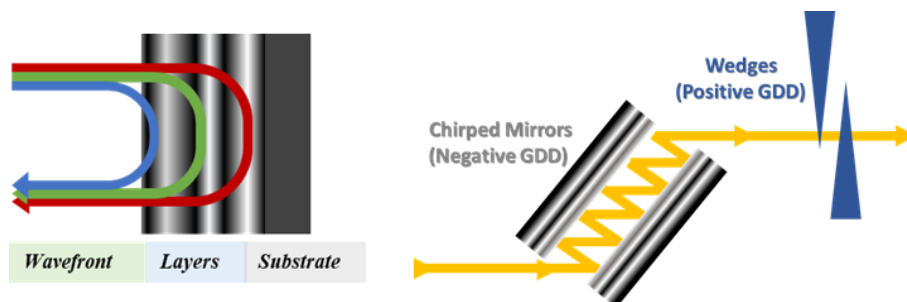


Figure 9: Basic set-up of a phase shaper based on chirped mirrors and dispersive wedges.

In Figure 9 is shown how those mirrors reflect deeper the longer wavelength (red part) than the shorter ones (blue part) inducing a negative group delay dispersion (GDD).

Multiple reflections allow tuning the introduced negative dispersion. Actually, CMs are most of the time accompanied by optical wedges to reach the lowest possible dispersion conditions. Indeed, combining reflections on the CMs (negative GDD) with the fine insertion of wedges (positive GDD) enables to flatten the spectral phase. In this way, few-cycle pulses have been

compressed, also thanks to the CMs large spectral acceptance of such devices. Indeed, mirror with a spectral acceptance of several hundred nanometers (typically 500–600 nm) in the visible or NIR range are nowadays commercially available and quite accessible<sup>2,3</sup>.

## AOPDF

An alternative system was developed at the end of the 1990s called AOPDF (*Acousto-optic programmable dispersive filters*) or Dazzler as its commercial name (Fastlite) (see Figure 10). It is based on the acousto-optic interaction between a controlled acoustic wave and an optical ultrashort pulse (Tournois, 1997). The acoustic-optic crystal is highly birefringent for both the acoustic and the optical waves. In the AOPDF, the acoustic wave creates a longitudinal transient grating which maximizes the interaction length. The crystal shapes the input pulse through diffraction to the other polarization state. The laser pulse amplitude and phase shaping is achieved through control of the acoustic wave.

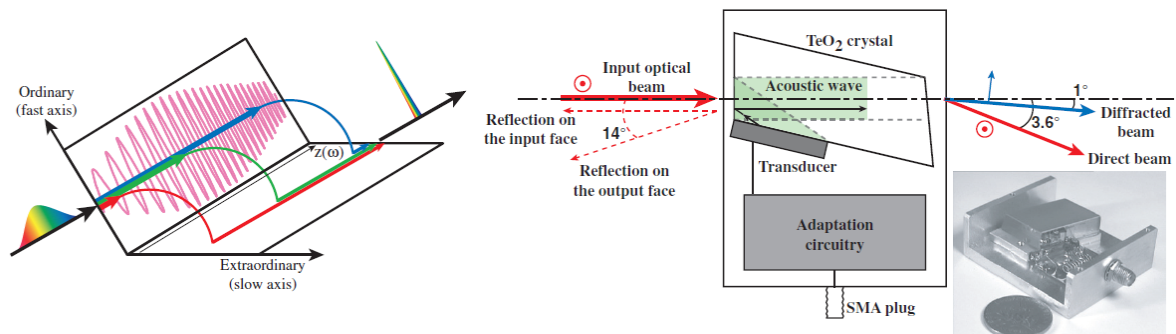


Figure 10: AOPDF principle: by diffraction on the acoustic grating through an acousto-optic interaction, the different spectral components can be diffracted to the extraordinary axis at different positions of the crystal.

The possibility to tune independently positively and negatively up to fourth orders of the spectral phase in a collinear set-up makes AOPDFs one of the most versatile devices in ultrafast laser manipulation. However, the AOPDF nature limits both the spectral acceptance and the repetition rate of the shaped pulse. In more detail, few-cycle pulses cannot be shaped due to the high dispersion of the acoustic-crystal, while the repetition rate is restricted to hundred of kHz because of the launch time of the acoustic wave.

### 1.1.4 Zero-Dispersion-line

In 1983, Froehly proposed a new design of versatile pulse shaper, the so-called zero-dispersion-line or 4f-line (Froehly, Colombeau, & Vampouille, 1983). This last is a particular optical system composed of two diffraction gratings and two lenses arranged in a 4f set-up, with a mask in the Fourier plane, as sketched in Figure 11 (Monmayrant, Weber, & Chatel, 2010). The input light is angularly dispersed by the first grating and then is collimated passing through the first lens. All the spectral components are spatially separated and they can be modified by the mask placed in the Fourier plane.

Finally, a symmetric lens and a grating allow the spatial recombination of the frequencies into a single collimated beam. If nothing is placed in the Fourier plane then the system is dispersion free and the output pulse shape is identical to the input one. By putting a specific mask in the

<sup>2</sup><http://www.ultrafast-innovations.com/>

<sup>3</sup><https://www.layertec.de/en/>

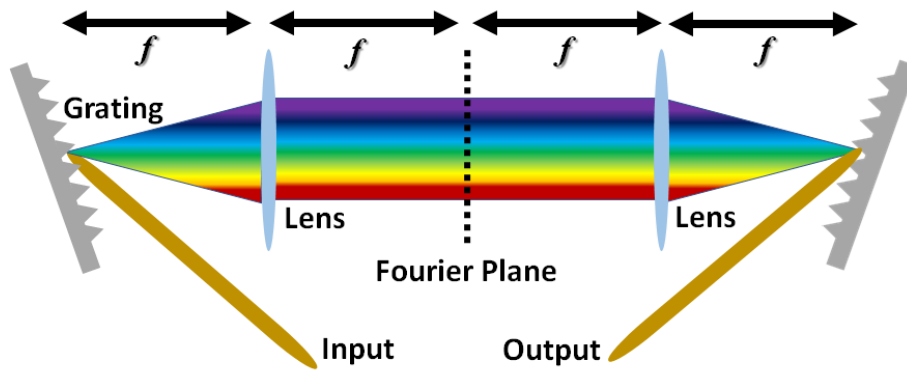


Figure 11: Basic set-up of a 4f-line shaper system.

Fourier plane, each spectral component can be modified independently and thus the temporal properties of the output pulse are modified.

A detailed analysis of the 4f-line is available in (Monmayrant et al., 2010). To summarize, during propagation in the 4f-line each frequency  $\omega_i$  can be associated with a specific spatial coordinate ( $x_i$ ) in the Fourier Plane through  $x_i = \alpha\omega_i$ , with  $\alpha$  is set by the chosen geometry. The output spectral properties are approximated as

$$\tilde{E}_{out}(\omega) = H(\omega)\tilde{E}_{in}(\omega) \quad (1.20)$$

with  $H(\omega)$  a correlation function between the spatial mask and the spatial extension of each spectral component.

This pulse shaping was originally performed by using microlithographic patterning techniques (Weiner, Heritage, & Kirschner, 1988) and only subsequently programmable spatial light modulators (Weiner, 2000; Wefers & Nelson, 1995; Weiner, Leaird, Patel, & Wullert, 1992, 1990), acousto-optic modulators (Dugan, Tull, & Warren, 1997), holographic masks, deformable mirrors (Zeek et al., 1999), and micro-mirror arrays were implemented too. Today, the common technique uses liquid crystal modulator (LC-SLM) arrays. A complete description of this device is discussed in the following sections. Several geometries with varying degrees of compacity and optical aberrations have been also used. Gratings can be replaced by dispersive wedges, meanwhile curved mirrors (concave, cylindrical or spherical) can substitute the flat ones to avoid unwanted dispersion and chromatic aberrations.

Depending on the mask, a 4f pulse shaper controls the phase (Weiner, 2000), both phase and amplitude (Weiner et al., 1988), the polarization (Brixner & Gerber, 2001) and also the transverse spatial profile (Feurer, Vaughan, Koehl, & Nelson, 2002).

### 1.1.5 State-of-the-art of ultrafast systems

Femtosecond technology was born in the 1970s when passively mode-locked dye lasers produced the first pulses shorter than 1 ps. But, ultrafast laser amplification was revolutionized in 1985 when chirped-pulse amplification (CPA) was introduced (Strickland & Mourou, 1985). This technique has been awarded by the Nobel Price in 2018. Through CPA, a pulse from an ultrafast oscillator is first stretched in time and then it is amplified in consecutive amplifier stages. In this way, the peak power can be kept below the threshold of optical damage and pulse distortion. Afterward, the pulse is re-compressed nearly to the original pulse duration, allowing to achieve ultrafast pulses with Terawatt (TW) peak powers (Maine, Strickland, Bado, Pessot, & Mourou, 1988).

Ti:sapphire as laser medium was first proposed in the 80s by Moulton at the MIT Lincoln Laboratory (Moulton, 1986). Ti:sapphire-based lasers systems (Spence, Kean, & Sibbett, 1991; Backus, Durfee, Mourou, Kapteyn, & Murnane, 1997; Nabekawa, Kuramoto, Togashi, Sekikawa,

& Watanabe, 1998) combined with dispersion control techniques paved the way for entirely new research fields and technologies such as attosecond science (Krausz & Ivanov, 2009) and laser-driven particle acceleration (Mourou, Tajima, & Bulanov, 2006). Ti:sapphire lasers operate most efficiently near 800 nm, even though the large spectral bandwidth acceptance makes it possible to generate pulses in the spectral span from 650 nm to 1100 nm. For those reasons, Ti:sapphire-based CPA systems are currently one of the driving lasers for ultrafast-high-intensity experiments with a relative low repetition rate, but with high pulse energy. To date, the corresponding focused peak intensity has already reached multi-petawatt level (4.2 PW and 85 J in (Sung et al., 2017)), in addition with the development of 10-PW lasers (Lureau et al., 2016; Papadopoulos et al., 2016) the focused intensity is reaching  $10^{23} \text{ W/cm}^2$  with more  $> 100 \text{ J/pulse}$  energy.

The physical properties of ytterbium ions combined with some technological aspects pave the way to new diode-pumped ytterbium-doped solid-state lasers. The advantage of this technology mostly resides on the versatile repetition rates and on the remarkable energy stability achievable that made it possible to increase the laser amplification at multi-kHz to MHz repetition rates. With ytterbium-doped lasers, thanks to diode pumping, the typical thermal issues and beam distortions of standard Ti:sapphire-based CPA systems are mitigated, thereby facilitating average power scaling.

Another way to reach such high intensities is to further reduce the pulse duration rather than increase its energy. Nowadays, common ways to generate pulses with duration not exceeding a few optical cycles, make use of a post-compression stage. A well-accepted method consists in adding a non-linear post-compression stage at the output of the CPA system. Post-compression relies on controlled SPM in hollow-core fibers (Brabec & Krausz, 2000; Bohman, Suda, Kanai, Yamaguchi, & Midorikawa, 2010) or self-compressed-filamentation (Hauri et al., 2004; Stibenz, Zhavoronkov, & Steinmeyer, 2006; Mysyrowicz, Couairon, & Keller, 2008). Recently, post-compression of a Ti:sapphire source leads to the generations of TW peak power with a pulse duration of 1.5 times the optical cycle (Ouillé et al., 2019). The method is currently extended to the post-compression of Yb lasers in multi-pass cavities (Lavenu et al., 2018)

Optical-parametric-chirped-pulse amplification (OPCPA) produced another step forward in ultrafast optics giving birth to the so-called 3rd generation of femtosecond sources (Fattahi et al., 2014). Similar to CPA, an ultrashort pulse is first stretched in time, amplified, and re-compressed. However the amplification is not based anymore on stimulated emission (CPA), but on a non-linear parametric process, the optical parametric amplifier (OPA). The amplification spectral bandwidth is large enough that sub10 fs pulse in the visible spectrum can be quite easily generated. One of the main advantages of OPCPA systems is the possibility to shift the central wavelength to more infrared lights, interesting not only in spectroscopy but also for high-field physics. Some recent results show remarkable CEP stability for 15W few-cycle OPCPA pulses in the mid-IR (Thiré et al., 2018).

## 1.2 Liquid Crystals

### 1.2.1 Introduction to Liquid Crystal features

Liquid crystals were first discovered at the end of 19th century, by the Austrian botanist Friedrich Reinitzer (Reinitzer, 1888). Reinitzer observed that when melting a curious cholesterol-like substance (cholesteryl benzoate), it first became a cloudy liquid and then cooling down, the liquid crystallized. This experiment showed some intermediate states, between crystalline solids and isotropic liquids that were defined as *mesomorphes* or *mesophase* by Otto Lehmann. However only eighty years later, in 1968, the first experimental LCD, as we know today, was finally synthesized (Kelker & Scheurle, 1969).

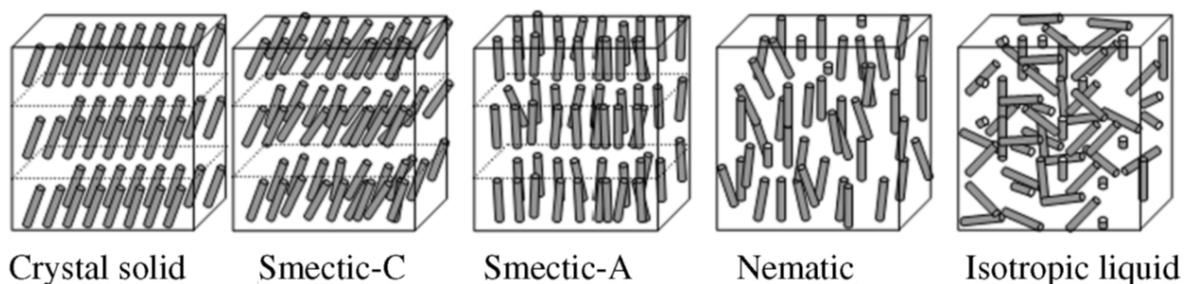


Figure 12: Schematic representation of the mesophases of rod-like molecules (Image from (Yang, 2014)).

LC are organic compounds that can be pictured as several strongly elongated molecules with a quasi-crystalline spatial disposition. Hence, they appear as a collection of rod-like molecules Figure 12. The size of the molecules is typically a few nanometers and the ratio between the length and the diameter about 4 and sometimes even larger. Typical molecules are long about 2 nm with a diameter of 0.5 nm.

An immediate consequence is a spatial anisotropy that implies different properties (optical, dielectric, magnetic, mechanical, etc.) in different directions. In the framework of this thesis, the optical anisotropy is the main characteristic, insofar it induces an optical birefringence. The birefringence is defined as the difference between the refractive indices depending on the optical field polarization and propagation directions. This anisotropy is generally much higher in LC than solid crystals, but above all, the fluid characteristic adds a possibility to control this anisotropy.

There are several types of liquid crystals. In this thesis, the thermotropic ones only are extensively studied. Indeed, they exhibit various molecular organization as a function of temperature: from pure liquid to pure crystalline. There are three main meso-phases of thermotropic liquid crystals: nematic (homeotropic, parallel and twisted), Smectics (A and C), and cholesteric. Nematics are directionally correlated but disordered in position and on average aligned along with a particular director (see next section). Smectics add also a positional ordering with layered structures. Finally Cholesteric (CLC) are chiral nematic liquid in which molecules self-assemble in a helical-manner around a particular axis. In this thesis, only the nematic mesophase is taken into account.

For those ordered LC, the theoretical model describes that mesophase physical properties are close to the one used for standard solid: it is called *elastic continuum theory*. In this case, various terms and definitions typical of solid materials (e.g., elastic constant, distortion energy, torque, etc.) are commonly used (De Gennes & Prost, 1995).

### 1.2.2 Nematic liquid crystals

Nematic comes from the Greek prefix *nemato* meaning threadlike, and it is used here because the molecules in the liquid align themselves into a threadlike shape (see Figure 13). Indeed in this phase, the configuration of lowest energy is reached when all the molecules are, on average, aligned along a single direction defined by a unit vector  $\vec{n}$ , the so-called director axis. This director is characterized by a long-range orientational order, on the contrary to Smectics and Cholesteric (Chandrasekhar, Sadashiva, & Suresh, 1977; De Gennes & Prost, 1995). In addition, molecules do not have a positional order, that is, their centers of gravity are placed randomly in space. Hence, the molecules can *flow* freely on each other and so, in this sense, the nematic phase is considered as a fluid phase. The spacing between molecules in all directions is not uniform.

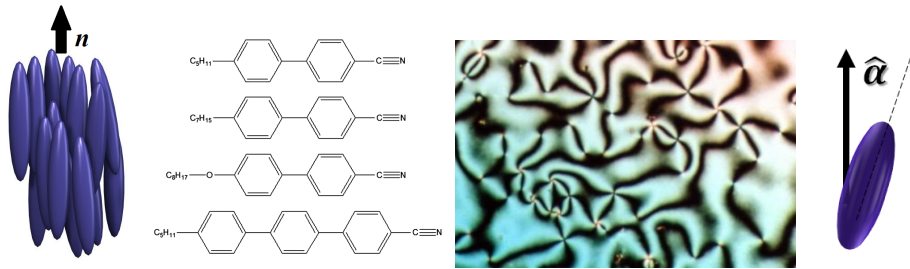


Figure 13: Alignment, chemical components and global texture of E7 Nematic liquid crystal from Merck (Images from Wikipedia).

The elastic intrinsic forces are at the origin of the orientation of the molecules along with the director. This direction can be experimentally specified either by applying an external electric field or by imposing particular boundary conditions at the confining surfaces of the sample, which are the anchoring conditions. When two of these constraints compete, the long-range orientational order may be partially destroyed or modified. Typical anchoring conditions for a liquid crystal sample may be either simple planar ( $\vec{n}$  parallel to the confining plates), twisted (combination of two planar anchoring condition along different directions in the plane of the interface) or homeotropic ( $\vec{n}$  orthogonal to the confining plates), see Figure 14.

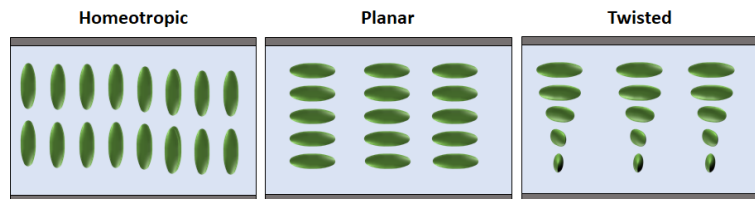


Figure 14: Sketches of the different nematic geometries: Homeotropic, Planer splay, Planar twisted.

The interest of this thesis is only in planar alignment, which is quasi-parallel to substrates (see in the next sections).

From the director axis  $\vec{n}$  the microscopic scalar order parameter  $S$  (De Gennes & Prost, 1995) is defined by analogy with ferro-magnetism:

$$S = \frac{1}{2} \langle 3(\vec{k} \cdot \vec{n})(\vec{k} \cdot \vec{n}) - 1 \rangle = \frac{1}{2} \langle 3 \cos^2 \alpha - 1 \rangle \quad (1.21)$$

Where  $\alpha$  is the angle made by the molecular axis with the director axis and  $\cos \alpha$  is the first-order Legendre polynomial. The average  $\langle \rangle$  is taken over the whole set of molecules. It is called microscopic because it describes the average response of a molecule. So when the fluctuations

of the molecular axis from the director axis orientation are small,  $S$  is close to unity. On the one hand, in a perfectly aligned liquid crystal, as in other crystalline materials,  $\langle \cos^2 \rangle = 1$  and  $S = 1$ ; on the other hand, in a perfectly random system, such as ordinary liquids or the isotropic phase of liquid crystals,  $\langle \cos^2 \rangle = \frac{1}{3}$  and  $S = 0$ . All these order parameters show a critical temperature dependence as was suggested by the name, thermotropic liquid crystal.

**Elastic Continuum theory** Elastic Continuum theory is the model that best represents the dual nature of the liquid crystal (Frank, 1958; Ericksen, 1969; De Gennes & Prost, 1995). The first principle of continuum theory neglects the details of the molecular structures. Indeed, liquid crystals are considered as rigid rods correlated by Coulomb interactions and the entire collective behavior is described only by the director axis  $\vec{n}$ . When an external perturbation distorts a nematic LC crystal, the local optical properties are still pertaining to a uni-axial crystal: only the orientation direction ( $\vec{n}$ ) spatially changes. Twist, splay, and bend are the three principal distinct director axis deformations in nematic liquid crystals (see Figure 15). Following the theoretical formalism first developed by Frank (Frank, 1958), the free-energy densities (in units of energy per volume) associated with these deformations are given by:

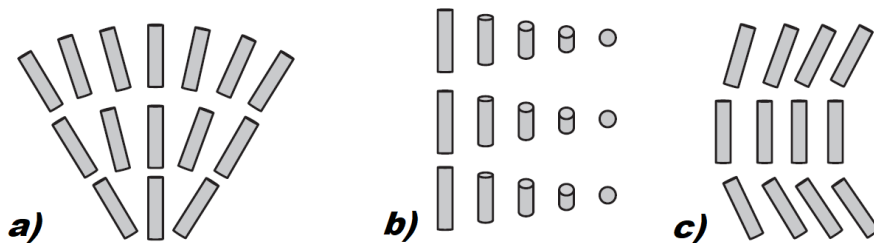


Figure 15: Sketches of the different director axis deformations: (a) splay; (b) twist; and (c) bend (image from (Yang, 2014)).

$$Splay : f_1 = \frac{1}{2} K_1 (\nabla \cdot \vec{n})^2 \quad (1.22)$$

$$Twist : f_2 = \frac{1}{2} K_2 (\nabla \times \vec{n})^2 \quad (1.23)$$

$$Bend : f_3 = \frac{1}{2} K_3 (\vec{n} \times \nabla \times \vec{n})^2 \quad (1.24)$$

where  $K_1$ ,  $K_2$ , and  $K_3$  are the respective Frank elastic constants (Splay, Twist, Bend). In general, more than one form of deformation is induced by an applied perturbation, so the total distortion-free energy density is given by the combination of the previous equations:

$$W_K = \frac{1}{2} K_1 (\nabla \cdot \vec{n})^2 + \frac{1}{2} K_2 (\nabla \times \vec{n})^2 + \frac{1}{2} K_3 (\vec{n} \times \nabla \times \vec{n})^2 \quad (1.25)$$

This expression can be greatly simplified if one makes a frequently used assumption, namely, the one-constant approximation ( $K_1 = K_2 = K_3 = K$ ) (I. Khoo, 2006).

A complete description should also include the surface interaction energy at the nematic liquid crystal cell boundaries. In this thesis, all the cells fabricated have a hard-boundary condition. This means that liquid crystal molecules are strongly anchored to the boundary and close to the surfaces, they do not respond to the applied perturbation fields (see sect. 1.2.6). The surface energy may thus be regarded as a constant and the surface interactions do not enter into the dynamical equations (I. Khoo, 2006). Those deformations play a fundamental role in liquid crystal molecular dynamics, in particular when an electric field is applied (see sect. 1.2.3).

**Optical anisotropy** Nematic liquid crystals present one axis in which the polarizability, the dielectric constant and the refractive index are different from the other two axes (uni-axial medium). The refractive index of the medium will be different according to the direction of propagation of the light, its polarization state, and molecular orientation. So, two preferred optical axis with different refractive index, are defined:  $n_o$  and  $n_e$ , respectively ordinary and extra-ordinary indices. Optical anisotropy can be represented by the index ellipsoid, as shown in Figure 16. Typical nematic liquid crystal values of  $n_e$  is  $\sim 1.7$  and  $n_o$  is about  $\sim 1.5$ , i.e. a positive birefringence  $\Delta n = n_e - n_o = 0.2$ .

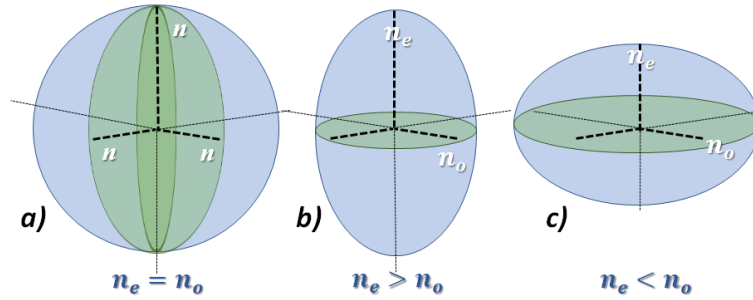


Figure 16: Isotropic and uniaxial index ellipsoids. a) Spherical isotropic index ellipsoid with refractive index  $n$ . b) Uniaxial positive, refractive indices  $n_e > n_o$ . c) Uniaxial negative, refractive indices  $n_e < n_o$ .

The overall index is then a combination of the two main axis according to:

$$n(\theta) = \frac{n_e n_o}{\sqrt{n_e^2 \cos^2(\theta) + n_o^2 \sin^2(\theta)}} \quad (1.26)$$

where  $\theta$  is the angle between the optical axis and the propagation direction of the polarized beam through the LC.

### 1.2.3 Effects of an Electric Field on a Nematic Liquid Crystal

#### Molecular reorientation

One of the main interests of liquid crystals is their response to an externally applied electric field. The nematic director can be easily rotated by applying a few volts across the liquid crystal layer. When the molecules reorient, the optical properties of the LC layer drastically change. When an electric field ( $\vec{E}$ ) is applied to a nematic liquid crystal, it induces a polarization ( $\vec{P}$ ) that depends on the orientation of the liquid crystal director with respect to the applied field direction. The resulting torque generates a rotation perpendicular to  $\sim \vec{E}$ , and centered on the molecule (De Gennes & Prost, 1995). Hence, the molecules will orient themselves to minimize the torque, and balance the electrical energy.

In a birefringent medium, the displacement  $\vec{D}$  generated by a field  $\vec{E}$  results from the projection of  $\vec{E}$  on the proper axes and the corresponding permittivities  $\varepsilon_o$  and  $\varepsilon_e$  (ordinary and extraordinary). The displacement is expressed through (I. Khoo, 1995):

$$\vec{D} = \varepsilon_{\perp} \vec{E} + (\varepsilon_{\parallel} - \varepsilon_{\perp})(\vec{n} \cdot \vec{E}) \vec{n} \quad (1.27)$$

Therefore, the molecular torque produced by the electric field is given by:

$$\vec{\Gamma}_E = \vec{D} \wedge \vec{E} = \Delta\varepsilon(\vec{n} \cdot \vec{E})(\vec{n} \times \vec{E}) \quad (1.28)$$

where  $\Delta\varepsilon = \varepsilon_{\parallel} - \varepsilon_{\perp}$ , and  $\vec{\Gamma}_E$  is hence proportional to the square of the electric field representing the effort of rotation generated by  $\vec{E}$  to push the molecules out of their rest position. If the liquid crystal has a positive dielectric anisotropy ( $\Delta\varepsilon > 0$ ), the molecules tend to align themselves



parallel (or anti-parallel) to the applied field because the (electric) energy is then minimized. Conversely, if the dielectric anisotropy is negative ( $\Delta\varepsilon < 0$ ), then the molecules tend to align themselves perpendicular to the applied field (De Gennes & Prost, 1995).

The use of high frequency alternating current is required to prevent electromigration effects in the liquid crystal occurring with direct current (De Gennes & Prost, 1995). The frequency of the applied electric field can drastically modify the molecular reorientation and the overall dynamic of the liquid crystal. For instance, the so-called Dual-frequency-Liquid-Crystal can eventually inverse the sign of their dielectric anisotropy (De Gennes & Prost, 1995). The crossover frequency ( $f_{co}$ ) is defined as the frequency at which they behave as a pure isotropic medium ( $\Delta\varepsilon = 0$ ) (De Gennes & Prost, 1995). To prevent all those issues, in this thesis the frequency of the electric field is fixed at 1 kHz, so as to consider a quasi-static field for the LC molecules reorientation. Moreover, all the mixtures studied in this work have a positive anisotropy ( $\Delta\varepsilon > 0$ ).

### Fréedericksz transition

Considering a NLC in the planar splay geometry with a  $\Delta\varepsilon > 0$ , the molecules are uniformly aligned along the  $\vec{x}$  axis in rest conditions, as shown in Figure 17a). As discussed above, when a sufficiently high electric field is applied across the cell (in the  $\vec{z}$  direction), the liquid crystal director is distorted toward the cell normal direction, as shown in Figure 17b). Because of the molecules anchoring at the surface, the liquid crystal director in the altered state is not uniform. Indeed, molecules at the border persist in their rest position even under an external electric field. Conversely, the inner molecules can rotate under its effect. This deformation costs elastic energy that works against the rotation. This is expressed as a voltage threshold that has to be overcome to start the reorientation. This threshold is the Fréedericksz transition (FT), named in honor of the Russian physicist Vsevolod Frederiks who observed the effect for the first time in 1927. In (Yang, 2014), it is demonstrated that from the electric torque it is possible to evaluate the effort inside the LC, the tilt angle of the molecules and the consequent voltage threshold.

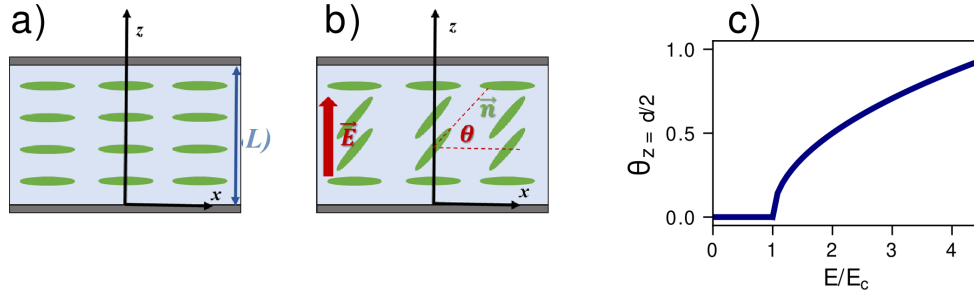


Figure 17: a) LC cell in the steady state. b) Molecular re-orientation induced by the external electric field. c) Tilt angle at the middle plane as function of the external electric field, where  $E_c$  is the threshold.

According to (Yang, 2014), the total free energy (per unit area) can be expressed as:

$$\int_0^L \left[ \frac{1}{2} (K_1 \cos^2 \theta + K_3 \sin^2 \theta) \theta' - \frac{1}{2} \varepsilon_0 \varepsilon E^2 \sin^2 \theta \right] dz = 0 \quad (1.29)$$

where  $K_1$  and  $K_3$  are the splay and the bend constants,  $\theta$  is the tilt angle and  $d$  the LC layer thickness. The first two terms represent the inner elastic forces contrasting the external electric field (last term). Using the Euler–Lagrange method and neglecting second-order terms, eq.1.29 becomes (Yang, 2014):

$$-\varepsilon_0 \Delta \varepsilon E^2 \theta - K_1 \frac{\partial^2 \theta}{\partial z^2} = 0 \quad (1.30)$$

The tilt angle  $\theta$  can be deduced using the boundary conditions:  $\theta_{(z=0)} = \theta_{(z=L)} = 0$ , e.g. strong anchoring. The sinusoidal solution of eq.1.30 is:

$$\sqrt{\frac{\varepsilon_0 \Delta \varepsilon E^2}{K_1}} L = m\pi \quad (1.31)$$

The  $m = 0$  means that no electric field is applied, and  $m = 1$  corresponds to a critical field  $E_c$  at which the tilt angle just begins to change:

$$E_c = \frac{\pi}{L} \sqrt{\frac{K_1}{\varepsilon_0 \Delta \varepsilon}} \quad (1.32)$$

Therefore, the correspondent threshold voltage is

$$V_c = E_c L = \sqrt{\frac{\pi^2 K_1}{\varepsilon_0 \Delta \varepsilon}} \quad (1.33)$$

which is independent of the cell thickness. Thus, liquid crystals are not governed by the voltage, but by the applied electric field (Lee, Lee, & Kim, 1998). In other words, below the critical field strength the director profile is unperturbed and remains uniform, but above this value a distortion occurs. This effect is due to a competition between restoring elastic forces induced by the strong anchoring and destabilizing torques produced by the external field. Below the critical field strength, the destabilizing torques are insufficient to overcome the elastic forces and the director profile remains uniform. However, above it ( $E > E_c$ ), the torque arises due to the electric anisotropies, it overcomes the elastic forces and the nematic director becomes distorted. In (Yang, 2014) the analytical solution of the tilt angle  $\theta$  is demonstrated also at the middle plane of the LC cell ( $z = d/2$ ):

$$\sin \theta_{L/2} = 2 \sqrt{\frac{(E - E_c)}{E_c}} \quad (1.34)$$

So, only when  $E > E_c$  the molecules start to reorient parallel with the respect of the electric field. The evolution of  $\theta$  as function of the applied field is plotted in Figure 17c).

Derfel (Derfel, 1988) showed for the first time that the Fréedericksz transition arises at a pitchfork bifurcation point. Afterward, Blake (Blake, Mullin, & Tavener, 1999) demonstrates that the effect of an electric field can be fully described by the bifurcation theory with its numerical technique including also imperfections such as non-perfect alignment of the liquid crystal, non-parallel plates and even imperfections in the material. This approach has allowed uncovering important details of the mechanisms involved that are difficult to explore in the laboratory, because of the small length scales, or by previous analytic approaches.

The LC thickness does not influence the voltage threshold at which the commutation occurs. This is already well verified for thin cells ( $< 25\mu\text{m}$ ). However, the dynamics and the optical response in more thicker cells are investigated in chapter 3.

### Dynamic of molecular rotation

Up to now, the balance between the elastic forces of the molecules and the external electric one has been considered static. If the external electric field is removed, the molecules are reoriented back in the initial position through a transient relaxation. Indeed, they are driven back by the elastic and viscosity of the medium thanks to the planar anchoring geometry. Therefore, the dynamical analysis should include also the viscous torque, which opposes the director rotation (Jakeman & Raynes, 1972; De Gennes & Prost, 1995). Equations providing a full description of the dynamical rotation have been proposed in the last decades. One of those, the Ericksen-Leslie expression (Ericksen, 1961; Leslie, 1968) can reproduce with high reliability the commutation.

This model has been further simplified in order to get more easily the overall molecular dynamic (Oh-e & Kondo, 1996). The response time comes from the momentum conservation in which the elastic, viscous, and electric torques are expressed respectively as (De Gennes & Prost, 1995):

$$\gamma_1 \frac{\partial \theta}{\partial t} = K_2 \frac{\partial^2 \theta}{\partial z^2} + E^2 \varepsilon_0 \Delta \varepsilon \sin \theta \cos \theta \quad (1.35)$$

where  $\theta$  is the twist angle and  $\gamma_1$  is the twist-viscous coefficient. This last, that has been introduced by Leslie, arises from the molecular rotational inertia composed by a combination of the three deformations (De Gennes & Prost, 1995). Eq. 1.35 can be solved considering the evolution in time and in space of the tilt angle ( $\theta$ ). Spatially, the strong anchoring conditions impose that  $\theta(z = 0) = \theta(z = L) = 0$  and  $\theta(z = L/2) = \theta_m$ , so the tilt angle across the LC layer can be written as (Oh-e & Kondo, 1996):

$$\theta(z) = \theta_m \sin\left(\frac{\pi z}{d}\right) \quad (1.36)$$

where  $\vec{z}$  is the propagation direction and  $d$  the LC thickness.

Temporally, when the electric field is removed at time  $t = t_0$ , the evolution in time of the tilt angle  $\theta$  can be expressed as an exponential decay (Oh-e & Kondo, 1996):

$$\theta(z, t) = \theta_0(z) \exp(-t/\tau) \quad (1.37)$$

where  $\tau$  represents the characteristic switching-off time. This relaxation time  $\tau$  for returning to the initial state of the liquid crystals can be expressed as :

$$\tau_{off} = \frac{\gamma_1 d^2}{\pi^2 K_2} = \frac{\gamma_1}{\varepsilon_0 \Delta \varepsilon E_c^2} \quad (1.38)$$

Therefore, the response time of the switching-off process is independent of the applied electric field. But, it quadratically depends on the LC's thickness  $L$ , e.g. thicker cells are considerably slower.

In the switching-on process, the assumption of small twist deformation can be made, then the torque balance eq.1.35 can be simplified to (Oh-e & Kondo, 1996):

$$\gamma_1 \frac{\partial \theta}{\partial t} = K_2 \frac{\partial^2 \theta}{\partial z^2} + E^2 \varepsilon_0 \Delta \varepsilon \theta \quad (1.39)$$

By solving this derivative expression, the response time for the switching-on process is:

$$\tau_{on} = \frac{\gamma_1}{\varepsilon_0 \Delta \varepsilon E^2 - K_2 \pi^2 / d^2} = \frac{\gamma_1}{\varepsilon_0 \Delta \varepsilon (E^2 - E_c^2)} \quad (1.40)$$

Therefore, by contrast to the switching-off process, the response time for the switching-on process depends on the electric field amplitude. Indeed, the stronger the electric field, the faster the molecules reorient. In the same way, the LC thickness influences both the switching-on dynamics as the switching-off. Indeed, thicker cells result slower again.

The different switching configurations for thin and thick cells are discussed in chapter 3 in view of the femtosecond applications. Applying an electric field to a LC layer is then an efficient way to tune its optical properties. Similar effects have been studied already when a magnetic field is applied instead of the electric one (De Gennes & Prost, 1995).

### 1.2.4 Nematic Liquid Crystals thermotropicity

As stated in section 1.2.1, the LC mixtures studied in this thesis are thermotropic, meaning that the temperature can also modify the mesophase. Landau developed a theory to describe the phase transition (Landau, 1980), in which the order parameter decreases continuously approaching a transition temperature  $T_c$  (also named critical temperature or clearing point). This temperature is defined as the temperature at which  $S$  becomes zero and then the molecules behave as pure isotropic liquid losing their crystalline properties, positional and orientation order (Figure 18). This phase transition affects as well the optical properties of the liquid crystal. Indeed, the anisotropy is reduced for higher temperature with, as a consequence, an overall decrease of the birefringence.

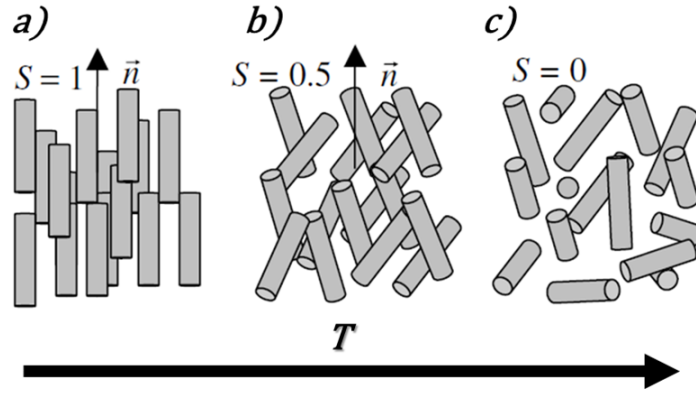


Figure 18: Schematic diagram showing the states with different orientational order parameters (Image from (Yang, 2014)).

From Vuks equation (Vuks, 1966), the temperature-dependent LC refractive indices can be expressed using the average refractive index  $\langle n \rangle$  and birefringence  $\Delta n$  as (Li & Wu, 2004; Li, Gauza, & Wu, 2004):

$$n_e = \langle n \rangle + \frac{2}{3} \Delta n \quad (1.41)$$

$$n_o = \langle n \rangle - \frac{1}{3} \Delta n \quad (1.42)$$

Therefore, the temperature derivatives of eq.1.41 and eq.1.42 are:

$$\frac{dn_e}{dT} = \frac{d\langle n \rangle}{dT} + \frac{2}{3} \frac{d\Delta n}{dT} \quad (1.43)$$

$$\frac{dn_o}{dT} = \frac{d\langle n \rangle}{dT} - \frac{1}{3} \frac{d\Delta n}{dT} \quad (1.44)$$

The  $\langle n \rangle$  variation with the temperature is demonstrated to be linear (Li, Gauzia, & Wu, 2004). At the same time, LC birefringence is linearly proportional to the order parameter  $S$  (Wu, 1986). Through Hallers semi-empirical equation, the order parameter can be approximated as (Haller, 1975):

$$S = (1 - T/T_c)^\beta \quad (1.45)$$

where  $T$  is the operating temperature,  $T_c$  is the clearing temperature of the LC material, and  $\beta$  is a fitting coefficient. Thus,  $\Delta n(T)$  can be rewritten knowing that  $\Delta n_0$  stands for the LC birefringence at  $T = 0K$ :

$$n_e(T) = A - BT + \frac{2\Delta n_0}{3} \left(1 - \frac{T}{T_c}\right)^\beta \quad (1.46)$$

$$n_o(T) = A - BT - \frac{\Delta n_0}{3} \left(1 - \frac{T}{T_c}\right)^\beta \quad (1.47)$$

Although there are four parameters, actually they are obtained by pairs: A and B are obtained by fitting the temperature dependent average refractive index  $\langle n \rangle$ , while  $\Delta n_0$  and  $\beta$  are obtained by fitting the birefringence data (Li, Gauzia, & Wu, 2004). Eq. 1.46 shows that  $n_e$  decreases as the temperature increases, while  $n_o$  has two different regimes. When  $T \ll T_c$ ,  $n_o$  keeps almost constant, but when the temperature approaches the clearing point the refractive index on the ordinary axe suddenly increases.

Eq. 1.46 and eq. 1.47 will be widely used in this thesis to characterize the behaviour of the liquid crystal mixture under different temperature conditions.

### 1.2.5 Some liquid crystal mixtures

#### E7 mixture

The abbreviation E7 stands for a liquid crystal mixture consisting of several cyanobiphenyls with long aliphatic tails merges together and often used commercially in liquid crystal displays. It was demonstrated for the first time in 1974 by Raynes (Castellano, 2005) that has synthesised four different liquid crystals mixtures (5CB, 7CB, 8OCB, and 5CT) in a new eutectic one (Figure 19).

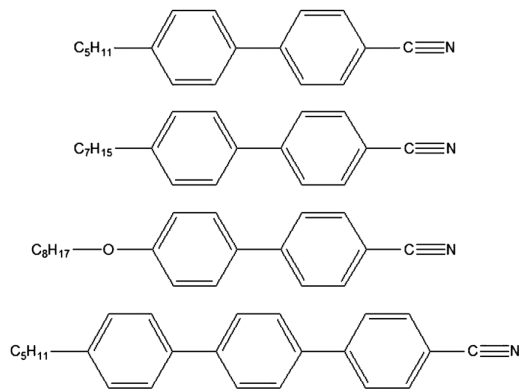


Figure 19: The Four liquid crystal chemical components of the E7 by Merck.

Characteristic	E7 mixture
$\Delta n$	0.2253
$\Delta \epsilon$	13.8
$\Delta h$ [ $m^2/s$ ]	$9 \cdot 10^{-6}$
Clearing temperature [K]	331
$\gamma_1$ [mPa s]	250
$V_{th}$ [V]	1.2
$K_1$ [pN]	11.7
$K_2$ [pN]	8.8
$K_3$ [pN]	19.5

Table 2: Merck E7 datasheet

The large dielectric anisotropy makes a large positive birefringence ( $\Delta n > 0$ ) with  $n_e = 1.73$  and  $n_o = 1.51$ . This birefringence is found almost constant in a really large spectrum range (I. Khoo, 1995) (Figure 20a). This combined with a broadband spectral acceptance makes E7 one of the most used LC mixture in optics. Indeed, from 400 nm to 18  $\mu m$ , few narrow absorption peaks are detected depending on the polarization state. In the extraordinary axis, a first absorption is detected after 3  $\mu m$  and a second one at 13  $\mu m$  (Figure 20). Therefore, all the visible and part of the NIR spectral range can be exploited in the view of novel optics applications. This anisotropy is also transmitted to the thermal conductivity ( $k[W/cm^2]$ ) and the thermal diffusivity ( $\alpha[m^2/s]$ ) with an impact also on the thermal gradient extension. The nematic state is stable in temperature from 283K to 331K where the clearing point is reached. Also the Frank elastic constants (Splay, Twist, Bend) have been deeply studied, therefore the Fréedericksz transition voltage and its dynamic are well-known today ( $V_{th} = 1.2$  V).

Table 2 summarizes the most important features.

#### MLC2132 mixture

Recently, Merck (Southampton, UK) developed and commercialized a new nematic liquid crystal mixture: MLC2132. The interest on this one comes from the larger birefringence than E7, (

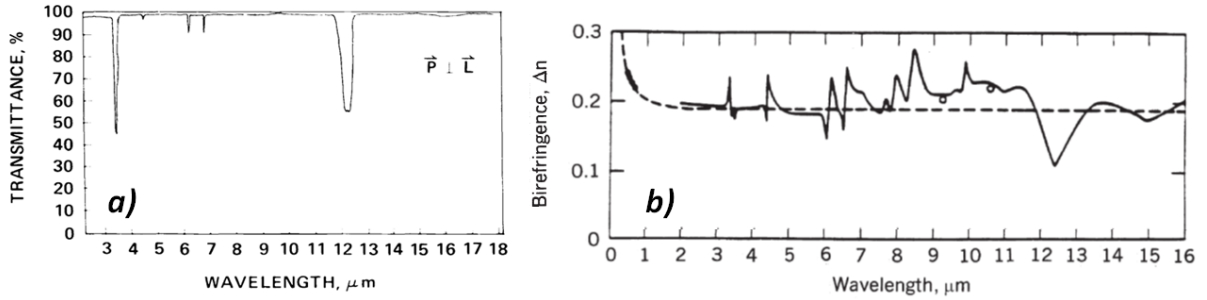


Figure 20: a) E7 transmission on the extraordinary axes and birefringence as function of the wavelength (images from (I. Khoo, 2006)).

$\Delta n = 0.26$ ) in the visible spectral range (589 nm), according to the furnisher data. In addition, an high isotropic transition temperature (386 K) and a large spectral bandwidth acceptance are also expected. However, the mixture is so recent that all the values have to be confirmed experimentally (Humar & Muševič, 2010).

### 1.2.6 LC Cell fabrication

In this thesis, a large number of LC cells are characterized and used for application in optics, in particular for ultrafast pulses phase control. They are all home-made with commercial mixtures and realized keeping constant some features and changing some others depending on the application (table 3).

Constant Features	Variable Features
Meso-phase: Nematic	LC mixtures
Anchoring: Strong	Thickness LC layer
Geometry: Planar	Substrate
Pre-tilt angle $\sim 1$	ITO coating

Table 3: Constant and variable features of the home-made LC cell.

As summarized in table 3, all the LC cells present a splay planar geometry with a strong anchoring and small pre-tilt ( $< 1^\circ$ ) in order to facilitate the director rotation in a single direction. The procedure for fabricating the cells is the following (Residori & Petrossian, 2003; Petrossian & Residori, 2002; McConville, Laurent, Guarino, & Residori, 2005):

1. **Substrates:** transparent substrates are used to confine the LC mixture. They are usually coated with ITO. This ITO layer is the electrode enabling to apply the electric field.
2. **Cleaning:** the glass plates are first cleaned in an ultrasonic bath, at 25 °C, for 15 ~ 20 min with a Micro 90 cleaning solution, then the slides are rinsed in highly purified distilled water ( $R \sim 18M\Omega$ )
3. **Anchoring:** The anchoring consists of trapping the molecules in contact with the surfaces in a chosen direction, in order to maintain all the molecules aligned. For this purpose, several techniques have been proposed, but the most popular consists of depositing an

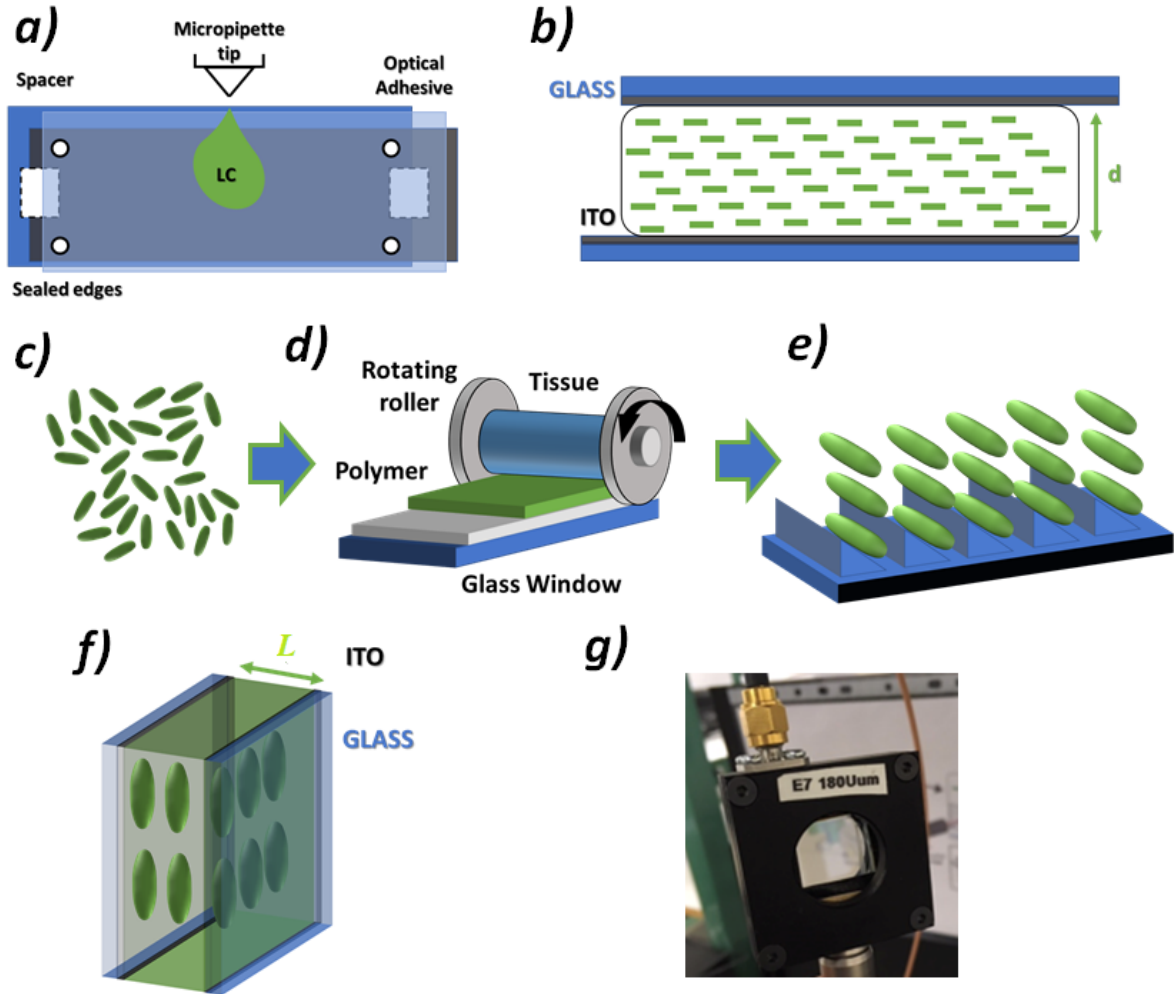


Figure 21: Assembly of the cell: a) first step with positioning of the spacers and polymerization of four glue dots and a second step with sealing the lateral edges. b) lateral view of the finished cell. c) and e) Molecules alignment due to the anchoring induced by the rubbing roll (d). 3D view (f) and photo (g) of the final cell.

insulating layer (usually a polymer) over the glass which is then rubbed by a roll covered with velvet (Takato et al., 2005). This brushing inscribes parallel grooves on the polymer which is then thermally hardened. The nano-relief obtained is shown schematically in the Figure 21d).

As a result of the surface rubbing, a small tilt angle exists for the nematic director. This pre-tilt is very important in molecular reorientation. Indeed, having no polarity, the rod-like molecules can turn in two ways following the electric field. A small tilt angle of the molecular axis would greatly facilitate the molecular reorientation. A uniform tilt angle is provided by the rubbing process.

4. **Cell assembly:** the glass plates are dried with filtered air and then positioned face to face separated by only Teflon spacers in order to be fixed together to make a cell (Figure 21a). Four dots of UV curable NOA 81 (Thorlabs) optical adhesive are placed at the corners of the plates. Once the quality of the assembly is checked, the cell is placed under a UV light source for several minutes to polymerize the optical adhesive. The spacers are then removed and the two lateral edges are sealed with optical adhesive, which is polymerized under the UV light

5. **LC introduction:** the cell is filled with the liquid crystal mixture by capillarity. As depicted schematically in Figure 21, a micro-pipette is used to deposit a drop of liquid crystal at the entrance of the cell, and the liquid crystal flows by capillarity through the spacer gap. During the filling, the liquid crystal director tends to orient parallel to the direction of the flow.
6. **LC cell:** A plastic containment is, finally, fixed as protection and after some hours of resting the cell is ready to be used ( Figure 21 f),g) ).

Through this procedure, numerous cells have been fabricated from  $9\ \mu\text{m}$  to  $250\ \mu\text{m}$ . The process although well controlled remains artisanal and imperfections can be noted. For instance, before any applications, the LC thickness is firstly verified. It was regularly found that the  $25\ \mu\text{m}$ -thick and  $50\ \mu\text{m}$ -thick cells have actually the desired thickness, all the other cells are slightly larger, probably because the spacers are thicker than expected. Nevertheless, high reproducibility of the cell thickness is found when using the given spacer size. All the fabricated cells present a small tilt angle ( $< 0.1^\circ$ ) between the two substrates that make them slightly wedged.

### 1.3 Liquid crystals for ultrafast optics

All the LC properties described so far make LC suitable in optics, and as a matter of fact, they are extensively used in photonics for light manipulation. Furthermore, their exceptional properties make them interesting candidates to handle femtosecond pulses as well. Indeed, optical components with large spectral transparency are needed and LC spectral acceptance is large enough to cover most of the visible and part of the near-infrared spectral range (up to  $3000\ \text{nm}$  for E7 mixture).

In ultrafast optics, birefringent materials are also crucial for pulse shaping and measurements. LC are then suitable thanks to their large difference between the two refractive indices in the whole transparency spectral bandwidth. Finally, this birefringence can be tuned, applying a specific electric/magnetic field. Therefore, this tunable birefringence over thousands of nanometers makes LC an even more interesting material for femtosecond optics.

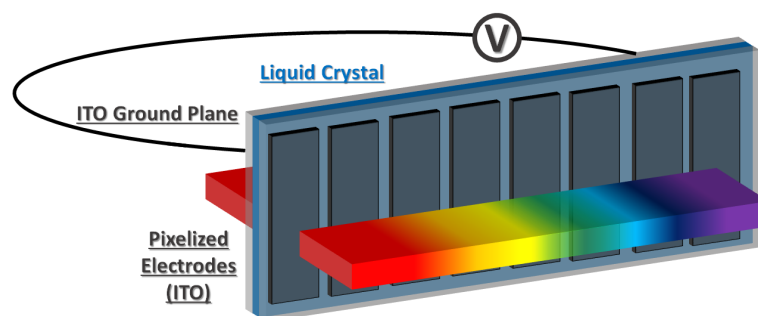


Figure 22: Sketch of a common LC-based SLM.

Despite these remarkable properties, LC cells are rarely used with femtosecond pulses except as spatial light modulators (SLM) for a spatial or temporal shaping.

The common design of those devices is pictured in Figure 22. The architecture of the device provides a thin layer ( $< 25\ \mu\text{m}$ ) of a liquid crystal, generally nematic, sandwiched between two glass plates. In order to apply the required electric field, the inside glass surfaces are coated with a thin, transparent, electrically conducting film. The most used is indium-tin-oxide (ITO). One piece is patterned into a finite number of pixels with the corresponding fan out for electrical connections; the conducting film on the other glass surface is un-patterned and serves as a ground



plane. A typical commercial LC-SLM is configured including between  $500\ \mu\text{m}$  and  $1000\ \mu\text{m}$  pixels, with a pixel pitch of  $36\ \mu\text{m}^4$ . The planar anchoring is generally preferred, e.g. the LC molecules are parallel with the respect to the glass plates. When an electric field is applied across the LC layer, the molecular reorientation induces the desired birefringence change. After the starting voltage threshold (Fréedericksz transition), the refractive index changes rapidly, and eventually saturates as the molecules become aligned along the electric field (longitudinal direction).

As already mentioned, for temporal shaping, the LC-SLM is placed in the Fourier Plane of a zero-dispersion line. Therefore, spectral components can be independently manipulated by changing the amplitude of the electric field of the corresponding pixel. Assuming appropriately designed drive electronics, the masking function may be held nearly constant. Hence, even high repetition rate lasers can be correctly manipulated and successive pulses identically shaped.

When LC-based SLM is placed in the Fourier Plane of a zero-dispersion line, it can arbitrarily control the amplitude, the phase or even the polarization of the dispersed pulse.

The single layer SLM arrangements of Figure 22 are primarily used for phase-only pulse shaping. By using a  $45^\circ$  launch polarization, a single layer device for amplitude only shaping can be also implemented. In order to achieve independent amplitude-phase control, a two layer SLM design is commonly used (Wefers & Nelson, 1995). The layout is similar to that of Figure 22, but with two such SLMs aligned and attached together back to back. This configuration has also been used for polarization pulse shaping. The pulse shaping speed depends on the response time of the SLM, which is limited to milliseconds scale by the dynamics of the liquid crystal itself and partially limited by electronic.

Apart from shaping by LC-SLM in the Fourier plane, only a few studies report on the use of LC cells for the manipulation of femtosecond pulses. Indeed, in 2013 it was demonstrated that the cholesteric mesophase can post-compress a femtosecond pulse as a 1D non-linear Bragg-grating (Song et al., 2013). 2 years later, Cattaneo and co-authors have studied optical Kerr-effect in nematics, on a sub-picosecond time scale (Cattaneo, Savoini, Muševič, Kimel, & Rasing, 2015).

The main limitation that hampered the development of a different LC-based device is probably connected to the commutation time, always considered too slow for ultrafast applications. Thus, to speed-up the reorientation process, the LC thickness has always been limited to a few microns ( $< 25\ \mu\text{m}$ ). This thickness restriction also affects the phase shaping capabilities, typically clamped to  $2\pi$ .

The concern about the LC damage threshold with pulse lasers might also be a reason. However, in 2011 Dorrer e co-Authors have demonstrated that common LC devices (composed by a glass substrate, ITO as electrode and nematic liquid crystals) are permanently damaged if more than  $300\ \text{mJ}/\text{cm}^2$  are applied (Dorrer et al., 2011). Nevertheless, this threshold, although quite high, comes only from the electrode and not from the LC mixture. Indeed, the same study has demonstrated that LC cells without any electrodes can work at high peak intensities and/or high flux without any permanent damage  $30\ \text{J}/\text{cm}^2$ . These measurements were done for nanosecond singles-shot lasers. In the femtosecond regime, some LC-based systems, such as LCos, are specified to work under a few  $\text{W}/\text{cm}^2$  at 1 KHz, here again limited by the electrode. Then, although the electrode is the limiting factor, the damage threshold remains acceptable, especially as other possibilities for LC manipulation can emerge.

---

<sup>4</sup><https://holoeye.com/spatial-light-modulators/lc-2012-spatial-light-modulator/>

## 1.4 SOFTLITE

### 1.4.1 A new collaboration for ultrafast pulse shaping with Liquid Crystal

In 2015 a new collaborative structure LABCOM SOFTLITE between the optics of liquid crystal group of the INPHYNI lab and FASTLITE company (SAS) has begun. The goal of this partnership is to exploit the unique characteristic of LC cells in order to improve the already existing LC based devices, or to create new ones for ultrafast pulse shaping and measurement. The possibility to fabricate versatile and thick LC cells (up to  $250\ \mu\text{m}$ ) by the INPHYNI laboratories combined with the knowledge of ultrafast shaping and measurement techniques of FASTLITE team can lead to new devices.

Since the beginning of this collaboration several results and publications have been achieved:

- The first relevant result was published in 2016. It was shown that thick nematic cells can act as a collinear, tunable femtosecond delay-line at  $\lambda_0 = 800\text{nm}$  (Jullien et al., 2016). Eventually, a cascaded multi-cells configuration also discloses the possibility to modulate independently from positive to negative values the phase and group delay. The device is static with no moving parts and opens interesting prospectives for femtosecond instrumentation.
- The former delay-line system can be extended beyond the femtosecond domain and NIR spectral range. Indeed, the phase management has been also applied to a broadband incoherent white light for Fourier Transform spectrometry, leading to a simple and compact high-resolution hyperspectral imaging instrument (Jullien, Pascal, Bortolozzo, Forget, & Residori, 2017; Jullien, Scarangella, Bortolozzo, Residori, & Mitov, 2019). This system is able to spatially resolve the spectral signature of an image, with the purpose of finding objects, identifying materials, or detecting processes.
- The collaboration also led to changes in the LC cell architecture. A first change concerns the overall geometry. Wedge-cells have been fabricated with a thickness difference between the bottom ( $L=0\ \mu\text{m}$ ) and the top of the cell ( $L=250\ \mu\text{m}$ ) (Laberdesque, Jullien, Bortolozzo, Forget, & Residori, 2017). This thickness gradient produces tunable lateral shearing interferograms from the polarization interference between the ordinary and extraordinary waves propagating into the cell. Thus, this device is suitable for large beam size and tunable shearing interferometry, with some potential and attractive applications in phase sensing, photoalignment or photolithography.
- Finally, in the framework of an additional collaboration with CEMES laboratory in Toulouse, also the nematic mixture has been changed in favor of cholesteric mixture (CLC). In this phase, the helical structure around an axis perpendicular to the local molecular director, with a given pitch and twist sense, confers to the structure a periodic modulation of the refractive index. As a consequence, light propagating through such a layer in the Bragg regime experiences partial reflection, selective in wavelength and in polarization. This remarkable property makes the CLC close to a 1D photonic structure and gives rise to a smooth band-gap. In 2019, these CLC samples have been able to tune positively and negatively the dispersion of femtosecond pulses with a broad spectrum (20 fs) (Neradovskiy, Scarangella, Jullien, & Mitov, 2019).

### 1.4.2 Thesis Objectives

The framework of this thesis emanates from this SOFTLITE collaboration and fits in this novel scientific activity. The objectives are then to exploit the aforementioned SOFTLITE results and

develop new methods and devices to characterize and/or shape broadband femtosecond pulses. A special interest is also to extend the working spectral range to the mid-IR, where common SLMs cannot, or only partially, work. Practically, this thesis can be summarized as the attempt to enlarge the tunable phase shift and, at the same time, extend the working spectral span. Thus:

$$\Delta\varphi(\lambda) = \frac{2\pi}{\lambda}\Delta n(\lambda)L \quad (1.48)$$

can be considered as a reference equation behind this work. Eq. 1.48 expresses the phase shift ( $\Delta\varphi$ ) in terms of birefringence excursion ( $\Delta n$ ), and liquid crystal thickness ( $L$ ). So, distinct ways to increase and control  $\Delta\varphi$  are disclosed in this thesis and here briefly listed.

### **Birefringence increase**

The birefringence excursion  $\Delta n$  is fixed by the nature of the liquid crystal itself. Since it is not possible to manufacture new mixture in the INPHYNI or FASTLITE laboratories, the only way to improve the phase retardation is to try other mixture available on the market.

However, the most interesting mixtures are often the most recent too, thus the informations about them are quite limited or sometimes they are not characterized at all. Therefore a new instrument to characterize the optical properties LC mixture is developed and explained in detail in Chapter 2. This method comes from a well-known and largely used technique in the ultrafast optics community: The Fourier-Transform Spectral Interferometry (FTSI). However, to the best of my knowledge, this technique has never been used to analyze LC mixture. Hence, through broadband white light interferometry, the recent MLC2132 mixture has been characterized and the coefficients for the refractive indices equation are retrieved. Particular attention is also paid to the mixture thermotropicity.

### **Optical properties of thick nematic LC cells**

Another possibility to increase the phase shift is to enlarge the LC thickness ( $L$ ). INPHYNI lab has recently demonstrated that thick-LC ( $> 200 \mu\text{m}$ ) can be fabricated without losing spatial homogeneity. This thickness growth is expected to affect some of the LC properties, for instance, the commutation time, as already mentioned. Nevertheless, experimental studies that confirm this theoretical behavior have never been performed. In addition, for many other properties, its influence is still unknown. Therefore, in Chapter 3 the optical response of thick nematic layers under the application of dynamic voltage steps is studied, with particular attention to the Fréedericksz transition. Actually for the first time, it is experimentally demonstrated that thick cells can be addressed even below this voltage threshold enabling to increase the achievable birefringence excursion.

### **Towards the mid-IR**

Another main goal of this thesis is the extension of the working spectral range towards mid-infrared lights to fit the requirements on Yb and OPCPA sources. Indeed all the existing LC-SLM are limited in this spectral range because of the electrodes. In fact, ITO and the common semiconductor present a strong non-linear behavior or absorption edge that restrict the spectral acceptance.

Thus, some IR-optimized ITO layers have been implemented in the LC cell conception trying to exploit the LC birefringence excursion even for longer wavelengths. However, in chapter 4 it is demonstrated that a femtosecond oscillator at  $1.5 \mu\text{m}$  undergoes a partial absorption even in yet optimized LC-cell. Nevertheless, this absorption drives a change of the refractive index due to the LC thermotropicity. The induced spatial-phase-modulations (SPM) and the generated multiple-ring pattern are analyzed to characterize this thermal effect.

**LC-based femtosecond measurements**

As already mentioned, one of the initial goals was also to develop devices able to characterize ultrashort pulses using the birefringence excursion of the LC molecules. In particular, some FROG measurements can be contemplated managing the group delay. Meanwhile, the control of the higher phase dispersion (GDD) term can also be exploited to perform some Dispersive-scan (D-scan) measurements.

**An alternative method to control the LC birefringence**

However, the difficulties encountered using the common electrical control of the birefringence has driven the investigations towards alternative strategies. As a matter of fact, most of the LC limitations arise from the electrode (spectral acceptance, maximum phase shift, damage threshold), so other ways that do not involve electrical addressing are fascinating and also convenient. All the discoveries made in this work, especially the thermo-optically induced SPM described in chapter 4, finally gave birth to an innovative LC-based phase shaper. A THERMO-Optically Reflective SLM (THOR-SLM) is so developed and patented (FR1910894).

In chapter 5, the conception of the new SLM is disclosed and a complete characterization of the spatial, spectral and temporal phase shift is performed by self-referenced spectral interferometry. In the same chapter different THOR-SLM prototypes have been also compared.

In chapter 6, the best THOR-SLM design is experimentally applied to arbitrary shape the spectral phase of a multi-octave light source. To the best of my knowledge, none of the existing pulse shapers is able to introduce an arbitrary phase shift over such a spectral bandwidth. The total introduced chirp span is large enough to open the way to unprecedented temporal shaping capabilities of few-cycle and single-cycle femtosecond pulses.



## Chapter 2

# Characterization of a highly birefringent LC (MLC2132, Merck) with broadband spectral interferometry

### Objective

The objective of this chapter consists in characterizing a recent birefringent LC mixture, MLC-2132, for which no information can be found in the literature, in view of electro-optical applications. Thus, a novel instrument is developed, based on broadband spectral interferometry. The tool is first validated through the characterization of a well-known liquid mixture. As a result, the refractive indices, the chromatic dispersion and the thermotropic features of MLC-2132 are determined.

## 2.1 Background

The optical properties of the LC cells discussed so far, tunable birefringence and transparency, induce a growing development with constant research in the field of the liquid crystal mixtures. Nevertheless, one of the most used is the E7 mixture: the spectral transparency and the refractive indices at different temperatures (Li, 2005) or under electric field are well-known (De Gennes & Prost, 1995). But the research for more performant mixtures progresses rapidly and new mixtures are coming out every year. Among these, the MLC2132 (produced by Merck, Southampton, UK) has more potential than E7 in the framework of this thesis because of the larger value of birefringence ( $\Delta n = 0.26$ ) and the higher isotropic phase transition temperature (386 K). The mixture is so recent that the only informations available so far are the ones provided by the manufacturers (Humar & Mušević, 2010). For these reasons, a system able to characterize the LC optical properties without breaking or modifying the LC cell is essential for our applications.

The goal of this chapter is to characterize MLC2132, to measure both refractive indices ( $n_e$  and  $n_o$ ) and to verify the birefringence excursion  $\Delta n$  in comparison with E7. The selected spectral range is from 500 nm - 950 nm, due to the larger non-linearity of the refractive indices in this region compared to the IR (Tkachenko et al., 2006) and because most of the laser sources available in the laboratory belong to this spectral range. Spectral phase dispersion terms ( $\varphi^2$  and  $\varphi^3$ ) have also to be determined for their crucial role in the femtosecond pulse manipulation. Moreover, since LC molecules are sensitive to the temperature, the refractive index variation is characterized when LC is heating up.

Several methods have been used to optically characterize the LC. The most common methods are issued from cumbersome bulk characterization instruments:

- Abbe Refractometer
- wedged-cell refractometer method
- Talbot-Rayleigh refractometer
- Jelley-Leitz Refractometer

With Abbe Refractometer precise measurements can be performed in a short time and for both polarization states (Li & Wu, 2004), but the monochromatic measurements and the small working temperature range limit the system (Li, Gauza, & Wu, 2004). Wedged-cell refractometer method (Laberdesque et al., 2017; Brugioni, Faetti, & Meucci, 2003) is recently adopted for precise mid-IR and far-IR measurements (up to 10  $\mu\text{m}$ ), but it requires the fabrication of *'ad hoc'* LC wedges. Also Talbot-Rayleigh refractometer is used for fast polychromatic refractive indices measurement in less than 1 second, but low precision and resolution still limit its applications (Warenghem & Joly, 1991). Finally, Jelley-Leitz Refractometer (Vaz et al., 1991) is also been used to measure liquid crystal drops at different conditions, but without taking into account the difference between the ordinary and extraordinary axis.

Conventional technique to measure the birefringence excursion makes use of a cw laser passing through the LC placed between two crossed polarizers and a detector that acquires the transmitted intensity signal written as (Bortolozzo, Residori, & Huignard, 2013):

$$I(t) = \frac{I_0}{2}(1 - \cos(\Delta\varphi)) \quad (2.1)$$

with  $\Delta\varphi = 2\pi\frac{\Delta n}{\lambda}L$  and  $L$  the nematic thickness. However, this method is not suited for thick cell ( $> 50\mu\text{m}$ ) for which the phase shift is well above  $2\pi$ , with a consequent not negligible error

induced by the  $\arccos(x)$  approximation. Moreover, the system is also affected by the laser intensity fluctuations.

## 2.2 Introduction

In this chapter, a new method to measure the sample refractive index is proposed that does not involve any refractometer or monochromatic laser measurements. Indeed, a broadband referenced FTSI using the Fourier transform is used. This technique is resistant to energy fluctuations and is limited only by the spectral resolution of the spectrometer (Borzsonyi, Kovacs, & Osvay, 2013). Furthermore, as shown below, the method is particularly suited to characterize strongly dispersive samples, as liquid crystals.

Broadband FTSI is performed in a Michelson configuration, with slightly different experimental arrangements. Figure 23 summarizes the experimental set-ups, the used cells, the performed measurements and the obtained results. In this chapter the dispersion relation  $n(\lambda)$  of the MLC2132 is measured in the spectral range 500 nm-950 nm for both polarization states. Furthermore estimation of the MLC2132 refractive index at one specific wavelength  $n(\lambda_0)$  is performed using as reference the E7 LC cell. Finally, the effect of the temperature is studied for both LC mixtures (E7 and MLC2132): the analogy between  $\Delta n_g(T)$  and  $\Delta n(T)$  is verified and the birefringence excursion is completely performed up to the isotropic transition. Therefore, pertinent coefficients of the temperature evolution equation of MLC2132 are determined. So, finally and this new mixture is confirmed to have a larger birefringence excursion than E7 on the extraordinary axis.




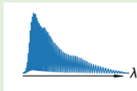
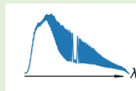
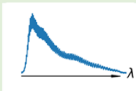
Experimental Set-up			
Interference spectrum			
LC thickness	$L = 180 \mu\text{m}$	$L = 25 \mu\text{m}$	$L = 25 \mu\text{m}$
Measuring	$\varphi(\lambda)$	$n_g(\lambda_0)$	$n_g(T)$
Objective	$n(\lambda)$	$n(\lambda_0)$	$n(T)$

Figure 23: Summary table of the 3 different experimental set-ups (first row, LC cell is highlighted in yellow) with their own interference spectra (second row), the thicknesses of the used cells (third row), with their own results (fourth row), and their own objectives (fifth row).



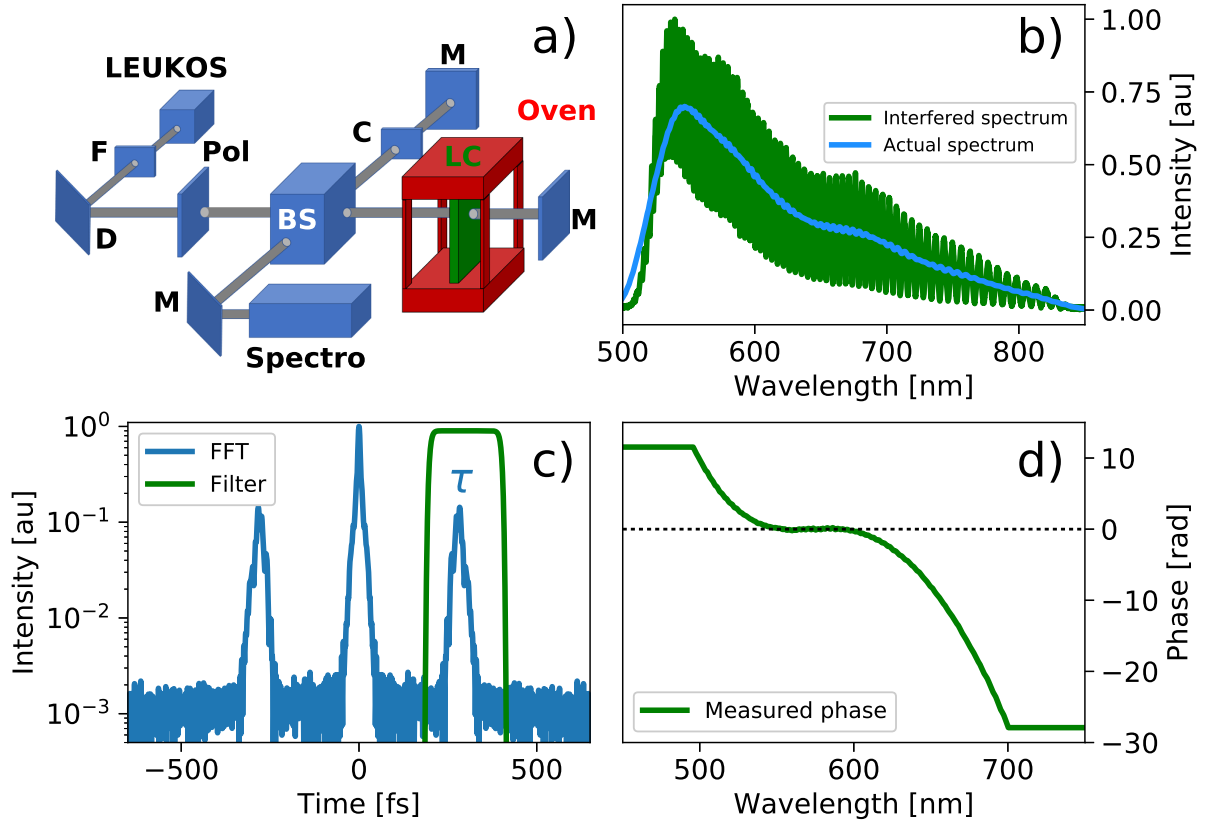


Figure 24: a) Experimental Set Up: a super-continuum fiber laser source from Leukos is used as a source of Michelson interferometer for referenced spectral phase interferometry (FTSI). A polarizer sets the polarization state in order to study both LC axis. The LC cell is placed in one arm, and eventually inside a oven for thermotropy analysis. Figure legend (F: long-pass filter (cut-off:  $530\text{ nm}$ ), D: short-pass dichroic mirror (cut-off:  $950\text{ nm}$ ), M: mirror, BS: beam splitter, C: compensator). b) Input raw spectrum (blue curve) and the interference pattern (green curve) acquired by the Ocean Optics 450 nm-850 nm spectrometers (the other is an Avantes 550 nm-1000 nm). c) Fourier Transform of the acquired spectrum in blue and the Super Gaussian profile used as a filter in green. d) Recovered spectral phase from the FTSI analysis.

## 2.3 Broadband spectral interferometer for characterization of the LC chromatic dispersion

### 2.3.1 Experimental set-up

A Broadband fiber super-continuum from Leukos (Electro-Visir-250-VIS-IR, 650 mW, 450 nm - 2500 nm) is passing through a long-pass filter (cut-off:  $500\text{ nm}$ ) to avoid any light absorption in the LC and a short-pass dichroic mirror (cut-off:  $950\text{ nm}$ ) (Figure 24). A polarizer defines the polarization state and a beam-splitter (50:50) splits the laser to a Michelson interferometer. The interferometer is first balanced in dispersion and then a LC cell is placed in one arm and an empty one on the other (e.g. 2 BK7 windows of  $0.7\text{ mm}$  thickness with ITO conductive layers). As summarized in Figure 23, three different experiments are performed using this configuration: the dispersion of the refractive index over the considered spectral range ( $n(\lambda)$ ), the refractive index measurement at one specific wavelength ( $n(\lambda_0)$ ) and finally the thermotropic analysis ( $n(T)$ ). LC thickness is changing: for the first experiment ( $n(\lambda)$ ) the thickest cell ( $L = 180\mu\text{m}$ ) is used because it introduces the maximum phase shift and so the FTSI technique is more precise. Instead, the refractive index measurement  $n(\lambda_0)$  requires the smallest possible variation between the unknown cell and its reference. Therefore, the better reproducibility fabrication of the  $25\mu\text{m}$  cells is suitable. The same thinner cells are used for the thermotropic analysis.

The generated interference pattern is finally acquired by two different spectrometers in order to increase the fit quality and the spectral bandwidth: an Ocean Optics is used in the range of 450 nm- 850 nm and an Advantes for 550 nm-950 nm (Figure 24b) ).

### 2.3.2 Method

As discussed in chapter 1, from the interference spectrum it is possible to retrieve the spectral phase. The refractive group index ( $n_g(\lambda)$ ) can be deduced from the group delay changes ( $\Delta\tau$ ) of the FFT of the spectrum (Figure 24c) ) with a different precision depending on the LC thickness: in the best case the ambiguity is  $< \Delta n_g = 8 \cdot 10^{-4}$  (for  $L = 180\mu\text{m}$ ), while for the thinnest cell ( $L = 25\mu\text{m}$ ) is  $< \Delta n_g = 5 \cdot 10^{-3}$ . Moreover, the measurements take into account the overall LC layer, thus the retrieved refractive group index is averaged over the nematic thickness.

To measure the chromatic dispersion of the LC it is necessary to measure the higher orders of the spectral phase. As stated in 1.1.2  $\varphi(\omega)$  can be written as:

$$\phi(\omega) = \phi_0 + \phi_1(\omega - \omega_0) + \frac{\phi_2}{2}(\omega - \omega_0)^2 + \frac{\phi_3}{6}(\omega - \omega_0)^3 + \dots \quad (2.2)$$

where  $\phi_1 = (d\phi/d\omega)_{\omega=\omega_0}$ . Hence, the FTSI technique is able to measure the higher order of the polynomial fit and is written as (linear term subtracted, Figure24d) ):

$$\phi_{FTSI}(\omega) = \frac{\phi_2}{2}(\omega - \omega_0)^2 + \frac{\phi_3}{6}(\omega - \omega_0)^3 + \dots \quad (2.3)$$

Here, the two arms of the interferometer are balanced in dispersion. When introducing the LC cell in one arm and the empty cell in the other one, the measured spectral phase difference only arises from the dispersion of the LC mixture. Now, the phase introduced by the LC sample can be expressed as:

$$\phi_{LC}(\omega) = n(\omega)\frac{\omega}{c}L = \phi_{FTSI}(\omega) + \phi_0 + \phi_1(\omega - \omega_0) \quad (2.4)$$

where  $n(\omega)$  is the refractive index and  $L$  is LC thickness. Therefore, combining eq.2.3 with eq.2.4:

$$\phi_{FTSI}(\omega) = n(\omega)\frac{\omega}{c}L - \phi_0 - \phi_1(\omega - \omega_0) \quad (2.5)$$

Thus, with an iterative method,  $n(\omega)$  is fitted until the spectral phase is retrieved. According to Li's study (Li, 2005), the chromatic dispersion of LC mixtures can be fitted for both axes by the extended Cauchy equation, written as:

$$n(\lambda) = A_{e,o} + \frac{B_{e,o}}{\lambda^2} + \frac{C_{e,o}}{\lambda^4} \quad (2.6)$$

where  $A_{e,o}, B_{e,o}, C_{e,o}$  are constants that depends only on the LC mixture and the polarization state (e=extraordinary, o=ordinary axis). Fitting the measured phase enables to determinate the coefficients  $B_{e,o}, C_{e,o}$  and then the chromatic variation of  $n$  is recovered. To complete eq. 2.6  $A_{e,o}$  coefficient has to be defined, hence it is necessary to determinate  $n(\lambda_0)$  for a given  $\lambda_0$  in the considered spectral range (Borzsonyi et al., 2013).

### 2.3.3 E7 extended Cauchy coefficients validation

The spectral phase is measured over two different wavelength ranges, one from 0.45  $\mu\text{m}$  to 0.7  $\mu\text{m}$  and from 0.65  $\mu\text{m}$  to 0.9  $\mu\text{m}$ , in order to have the best fit for all the broadband spectra (Figure 25a),b) ). This method is able to measure only the relative dispersion relations, e.g. it is necessary to know the actual refractive index at one specific wavelength in order to get the actual  $n(\lambda)$ . From the extensive E7 study of Li, the values of  $n_e = 1.7390$ ,  $n_o = 1.5222$

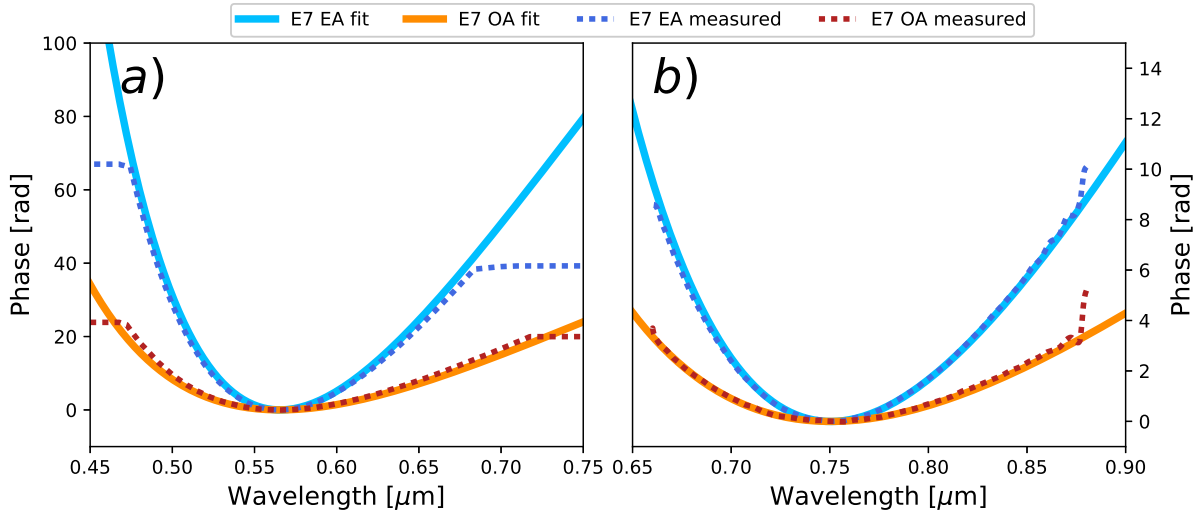


Figure 25: E7 measured spectral phase (dotted lines) and their fit (solid lines) for the 2 different wavelength ranges ( $0.45 \mu\text{m}$ - $0.7 \mu\text{m}$  and  $0.65 \mu\text{m}$ - $0.9 \mu\text{m}$ ) and for the 2 LC axis.

at  $0.55893 \mu\text{m}$  and  $20^\circ$  are taken. The dispersion relation is found and the fitting coefficient  $A_{e,o}, B_{e,o}, C_{e,o}$  are shown in table 4 (Li, 2005). The resulting curves are plotted in Figure 27. The determined values are consistent with the theoretical studies and previous measurements: therefore the broadband interferometer is validated. The refractive index is recovered with two measurements over a broad spectral bandwidth, with good accuracy.

From this index chromatic dependence, the GVD and TOD values of E7 are extracted, required when using LC in ultrafast optics (Table 4).

E7 LC	Extended Cauchy coefficients			Dispersion at 800nm	
	A	B	C	$\Phi^2 (fs^2/mm)$	$\Phi^3 (fs^3/mm)$
EA	1.6933	0.0078	0.0028	300	290
EO	1.499	0.0072	0.0003	120	65

Table 4: E7 Extended Cauchy coefficients (A,B,C) and its dispersion at 800nm.

### 2.3.4 MLC2132 characterization

After this validation, the next experimental step consists in characterizing MLC2132. The measured spectral phase is plotted in Figure 26a),b) (dotted lines) with the relative polynomial phase fit (solid curves) for both polarization states. However, the ambiguity of  $n(\lambda_0)$  still remains. Merck provides the following data:  $n_e = 1.7657, n_o = 1.5094, \Delta n = 0.2563$ , measured at  $589.3 \text{ nm}$  at  $20^\circ$ . So, it is possible now to fit the dispersion curves and propose some values for the extended Cauchy coefficients, summarized in table 5. Then according to eq. 2.6 the chromatic dependence of both indices for both LC mixtures is plotted in Figure 27.

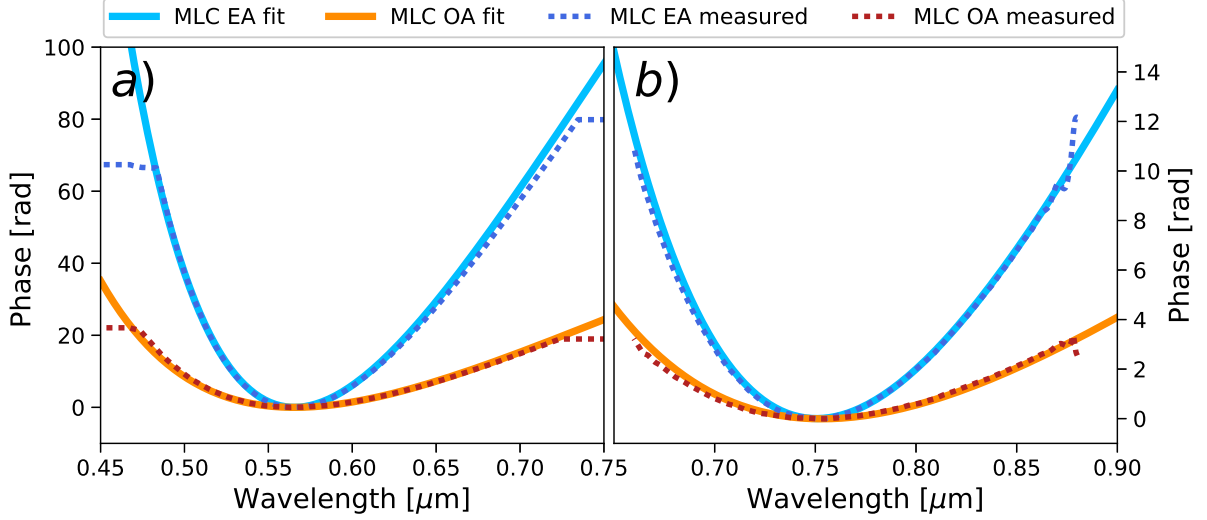


Figure 26: MLC2132 measured spectral phase (dotted lines) and their fit (solid lines) for the 2 spectral ranges (0.45  $\mu\text{m}$ -0.7  $\mu\text{m}$  and 0.65  $\mu\text{m}$ -0.9  $\mu\text{m}$ ) and for the 2 LC axis.

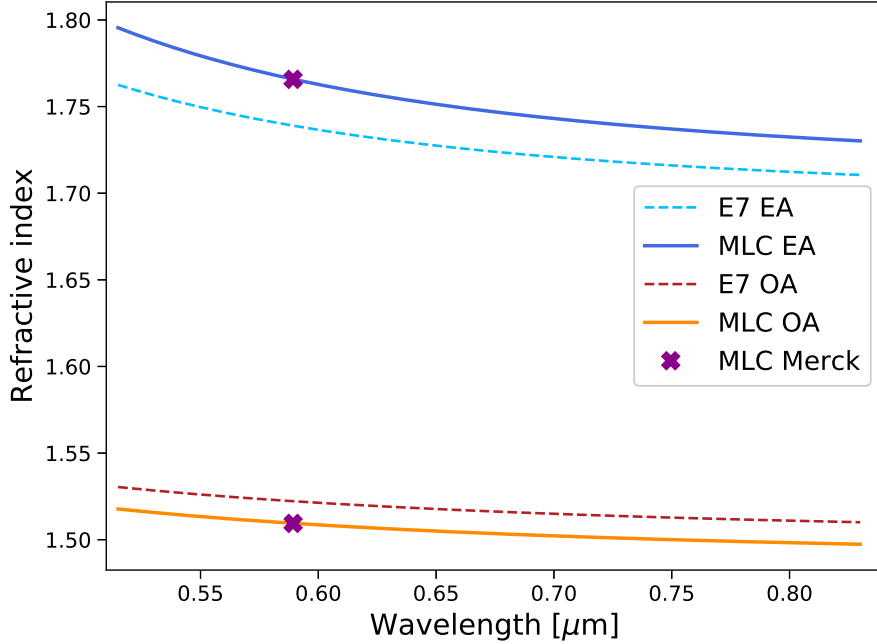


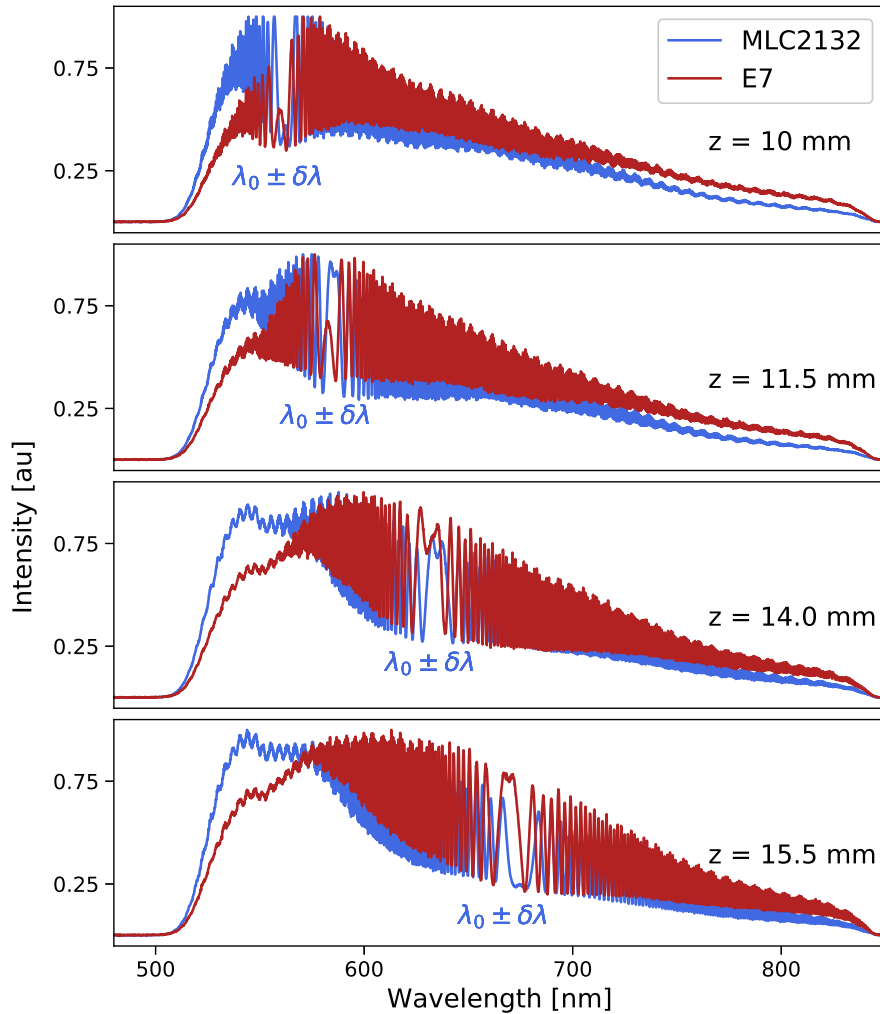
Figure 27: Refractive index as function of wavelength: E7 (dotted lines) and MLC (solid lines) in both polarization directions (Extraordinary axis in blue and Ordinary axis in red). Purple crosses are the official data from the manufacturer.

The birefringence excursion on the extraordinary axis of the MLC2132 is measured ( $\Delta n = 0.223$ ) and it is confirmed to be larger than the E7 one ( $\Delta n = 0.1943$ ). Therefore, the new mixture is more suitable for applications that require a large tunable phase shift. At the same time, MLC2132 is more dispersive, hence the introduced phase has to be taken into account, in an experiment involving femtosecond pulses. In particular, some values of Group Velocity Dispersion (GVD) and Third Order Dispersion (TOD) for a central wavelength of 800 nm are reported in table 5.

MLC2132	Extended Cauchy coefficients			Dispersion at 800nm	
	A	B	C	$\Phi^2$ ( $fs^2/mm$ )	$\Phi^3$ ( $fs^3/mm$ )
<i>EA</i>	1.710	0.0093	0.0034	350	340
<i>EO</i>	1.487	0.0072	0.0003	120	70

Table 5: E7 Extended Cauchy coefficients (A,B,C) and its dispersion at 800nm.

## 2.4 Towards a referenced refractometer


 Figure 28: MLC2132 (blue) and E7 (red) acquired interference spectra for different position of the delays stage. The excursion of  $\lambda_0 \pm \delta\lambda$  shows the index shift between the two mixtures.

The measurements done so far show a new and accurate method for LC mixture characterization. Nevertheless, the technique suffers from some limitations due to the nature of the self-referenced interferometer. More specifically, the FTSI algorithm can give only the derivatives of chromatic index variation and it is always necessary to know the refractive index at one specific wavelength

in order to reconstruct the whole excursion: in section 2.3.4 the data given by the manufacturer are used as reference points. In the absence of this data, an additional measurement is then needed. Therefore, in this section is proposed an experimental method to estimate the group refractive index of an unknown LC cell using another one as a reference. The two cells must have the same thickness. A large group delay is introduced in the interferometer in order to increase

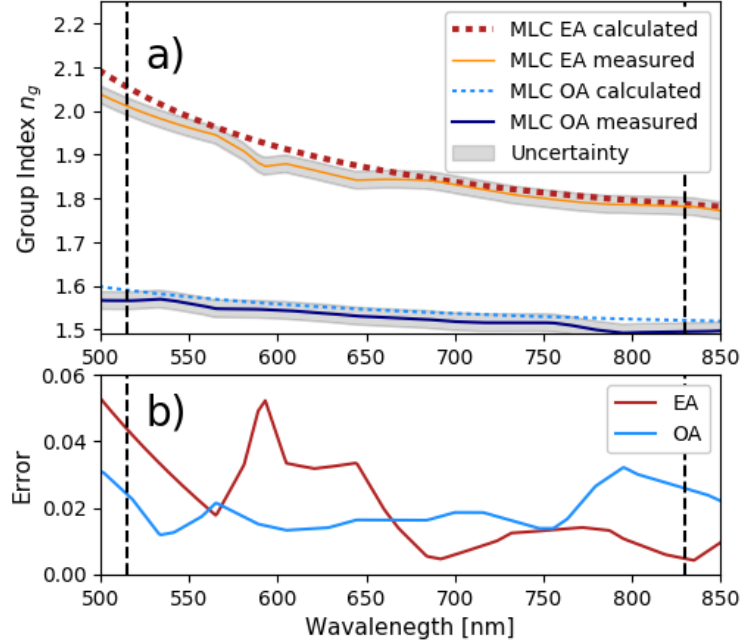


Figure 29: MLC2132 Group indices  $\Delta n_g$  measured (solid lines) and calculated from section 2.3.4 (dashed lines) for both polarization states. An uncertainty of  $2\mu\text{m}$  on  $\Delta z$  is considered (grey span). b) Absolute error.

the number of fringes. Then, a dispersive bulk is added in order to increase the GDD (group delay dispersion) difference between the two arms. As a consequence, the zero group delay presents an important chromatic variation and it is visible in the interference spectrum as the center of the largest fringe (Dou et al., 2010; Forget, Crozatier, & Tournois, 2012). The method then consists in measuring the different translation stage positions leading to zero group delay for different  $\lambda$  and for the two LC mixtures. For this purpose, a z-scan excursion is performed for both LC cells with a position error of  $\pm 1\mu\text{m}$ . Typical fringes pattern is shown in Figure 28, where at the same stage position a spectral shift of the zero group delay is visible. Indeed at each wavelength  $\lambda_i$  corresponds a position  $z_i$  where the group delay excursion is zero: hence the refractive group index ( $n_{gMLC}$ ) of the unknown sample is retrieved from the reference one ( $n_{gET}$ ) using the path difference  $\Delta z$ :

$$n_{gMLC} = \frac{\Delta z}{L} - n_{gET} \quad (2.7)$$

As already mentioned, cells of  $L = 25\mu\text{m}$  are used because this thickness shows the best reproducibility during the fabrication process, hence the main difference between them is only the liquid crystal mixture.

A referenced estimation of the actual group refractive index is obtained. The group index  $n_g(\lambda)$  calculated from previous section is compared with the new measurement in Figure 29a) for both axes. The data agrees with an error deviation of  $\sim 4 \cdot 10^{-3}$  at 830nm, but larger in the blue part of the spectral range. This system still suffers from different uncertainties: the accuracy of the wavelength span or the precision of the z position can be improved for further investigations, but a small shift in the LC fabrication process, small misalignments and interferometer stability have still to find a solution.

## 2.5 LC thermotropic analysis

### 2.5.1 Introduction

Liquid crystals are sensitive to temperature and present a large thermal non-linearity: several analysis about the behavior of the molecules changing the inner temperature have been published so far (Li, 2005; Li, Gauza, & Wu, 2004; di Pietro, Jullien, Bortolozzo, Forget, & Residori, 2018). The temperature variation is interesting for this thesis because the fluctuations occurring in the laboratory have some impact on the LC optical response, but more importantly, a thermal control of the LC cell is developed in the next chapters.

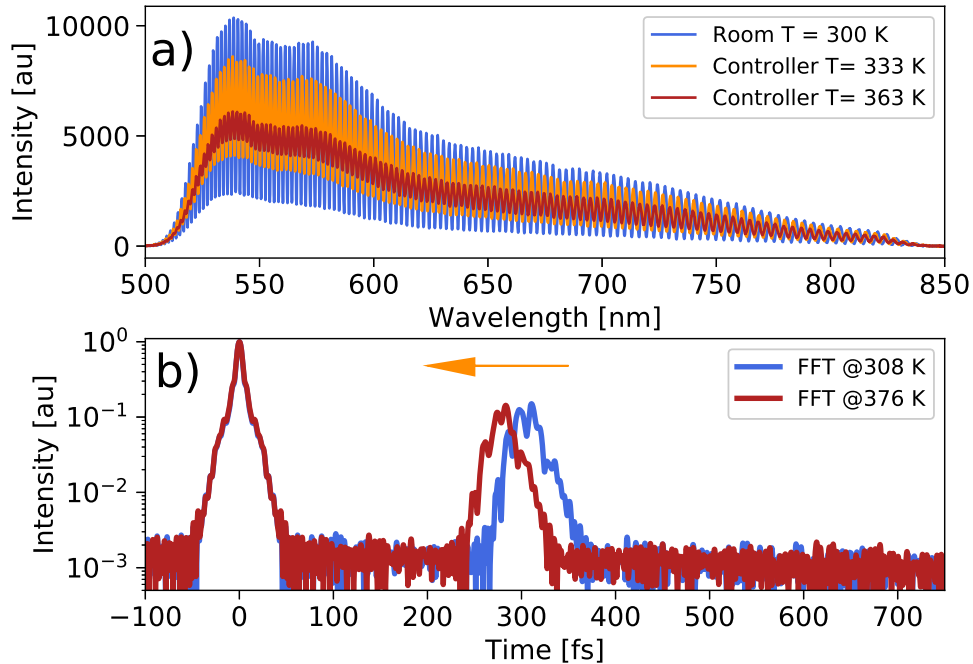


Figure 30: a) Interference spectra for MLC2132 at different values of temperature approaching the isotropic phase transition. b) FFT at different temperature. The temperature increase leads a decrease of  $\Delta n_g$ .

When the temperature increases, the order parameter  $S$  defined in section 1.2.2, decreases leading to a reduction of the overall birefringence up to the clearing point.  $T_c$ , the isotropic phase temperature is defined as the temperature at which the LC phase is fully converted to an isotropic medium. There are few physical models in the literature describing the temperature effect on both refractive indices at the same time up to the isotropic transition. Indeed, Hallers equation and Vuks model (Vuks, 1966; Haller, 1975) disclose the relationship between the birefringence and temperature, but not for the individual refractive indices. More recently, a *4 parameter parabolic model* describing the temperature effect has been developed that includes also the birefringence excursion (Li, 2005):

$$n_e(T) = A - BT + \frac{2\Delta n_0}{3} \left(1 - \frac{T}{T_c}\right)^\beta \quad (2.8)$$

$$n_o(T) = A - BT - \frac{\Delta n_0}{3} \left(1 - \frac{T}{T_c}\right)^\beta \quad (2.9)$$

where coefficients  $A$ ,  $B$ ,  $\Delta n_0$  are constants for a specific mixture and  $T_c$  the temperature transition. E7 coefficients are already reported in the extensive thesis:  $A = 1.7546$ ,  $B = 5.361 \cdot 10^{-4}$ ,  $T_c = 331$ ,  $\beta = 0.2391$ ,  $\Delta n_0 = 0.3768$ . It can be used to check the reliability of the interferometer.

### 2.5.2 Experimental set-up

The Michelson interferometer described so far is also suitable for temperature excursion studies: indeed the LC can be placed on the oven<sup>5</sup> with a thermometer as a checker (Figure 24a). Heating up the cell, the LC order parameter  $S$  decreases and at the same time a spatial deviation and modifications occurs: the combination of both effects reduces the transmitted signal and the fringes contrast decreases as well (Figure 30a). The experiment is performed in two steps. First, the LC cell is heated up until the fringes disappear and the acquired signal starts to have huge fluctuations, suggesting that the isotropic phase is reached (Singh, 2000). Then, several interference spectra are acquired cooling down the cell with a  $5^\circ$  decreasing step every 20min. The only evolving experimental parameter is the LC index due to the inner change of the temperature. This process is preferred to the heating up because of the shorter time needed to reach the thermal stability.

### 2.5.3 Analysis & results

The group index variation  $\Delta n_g(T)$  is then easily recovered from:

$$\Delta n_g = c \frac{\Delta \tau}{L} \quad (2.10)$$

where  $\Delta \tau$  is the group delay change obtained by the FTSI technique (Figure 30b) and  $L$  is the LC thickness ( $25\mu\text{m}$ ). E7 measurements are first performed: the transition temperature is found at  $331\text{ K}$  in excellent agreement with the previous studies (Li, 2005; di Pietro et al., 2018). Group delay excursion with temperature is measured while cooling down the cell. The acquired data agrees with the theoretical thermotropic birefringence over the whole nematic range (Figure 31). Moreover,  $\Delta n(T)$  and  $\Delta n_g(T)$  have the same evolution with  $T$  on the considered spectral range (500 nm- 950 nm). Several spectra are acquired at the same temperature to estimate the uncertainty of the measurement: the error bars are  $< 10^{-3}$ , not distinguishable in Figure 31, but they increase approaching the transition. In Figure 31 are reported the experimental data and the theoretical predictions for both axes, changing the polarization direction of the laser source (Li, 2005). The good agreement between the experimental data and the theoretical curves validate the interferometer.

Therefore, the MLC2132 cell can be characterized using the same process. The transition temperature is found higher than E7, around  $386\text{ K}$ , confirming the manufacturers data. Afterward, the refractive group index evolution with the temperature is plotted in Figure 31, using as reference points the  $n_e$  and  $n_o$  values determined at room temperature in the previous section. The overlap of the two refractive indices at  $386\text{ K}$  confirms the nematic-to-isotropic transition. Finally, coefficients of eq. 2.8 for the MLC2132 are proposed through a two steps fitting process of the experimental data. The coefficients  $A$  and  $B$  are retrieved from the averaged refractive index  $\langle n \rangle$ , defined in chapter 1. Afterward,  $\beta$  and  $\Delta n_0$  are found fitting the experimental data.

The birefringence excursion on the extraordinary axis  $\Delta n_e(T)$  is also found larger than E7, with larger error bars due to the higher clearing point (lower oven stability). Hence, MLC2132 can be contemplated as a substitute for E7 mixture.

<sup>5</sup><https://www.hcphotonics.com/accessories>



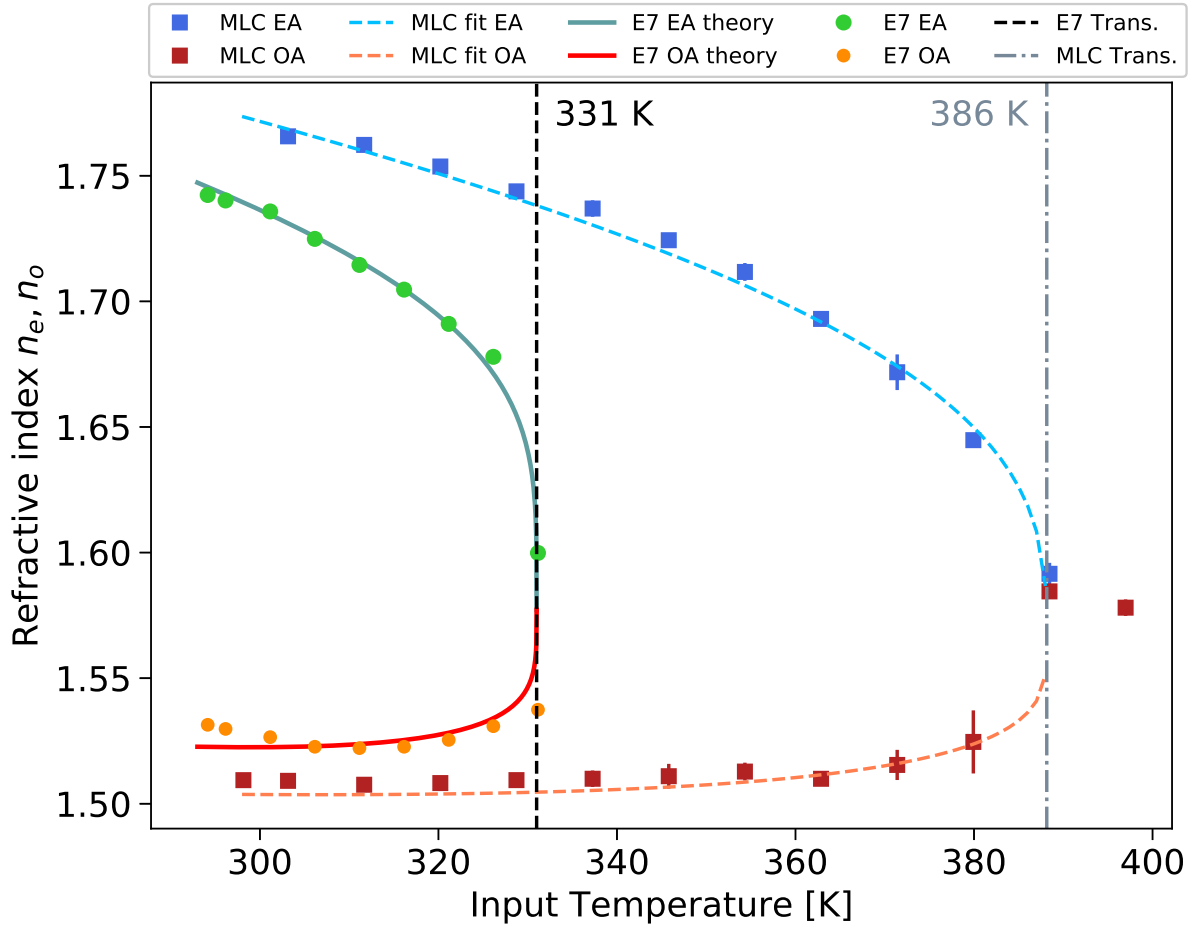


Figure 31: Refractive index variation with the temperature. The E7 theoretical curves  $n_{e,o}$  (solid lines) is in agreement with the  $\Delta n_{g_{e,o}}$  experimental data (dots). The MLC2132  $\Delta n_{g_{e,o}}$  data are also plotted (squares) with the coefficient determined in this work for  $n_{e,o}$  (dashed lines). The phase transition temperatures for both mixture are also indicated. The spectral range is 550-1050 nm.

LC	A	B	$\Delta n_0$	$\beta$	$T_c$
E7	1.7546	$5.36 \cdot 10^{-4}$	0.3768	0.2391	331
MLC	1.7127	$3.8072 \cdot 10^{-4}$	0.4550	0.3559	386

Table 6: E7 and MLC2132 coefficients for the 4 parameter parabolic equation.

## 2.6 Conclusions & Prospectives

In this chapter, a broadband spectral interferometer is used for the first time for LC cell characterization, using the Fourier-transform spectral interferometry (FTSI) technique. This method is innovative for those kinds of applications and it allows to measure the dispersion relation of the whole LC cell in a faster way and with higher resolution compared to the common refractometers or birefringence measurements. To my knowledge, it is the first time that such technique is used for this purpose. The precision and accuracy of the measured chromatic dispersion are first validated for a well-known mixture (E7). Then, a completely unknown mixture (MLC2132) is characterized for the first time and the coefficients for the Extended Cauchy equation are proposed. A method to evaluate the actual refractive index at one specific wavelength is also

developed using E7 mixture and exploiting the high quality cell reproducibility. An ambiguity of  $< 10^{-4}$  is estimated.

Finally, the thermotropicity of the LC mixtures is also studied increasing the inner temperature up to the isotropic phase transition. Once again, measurements are first validated for a well-known mixture (E7) and consequently, the MLC2132 is studied determining the fitting coefficients for the theoretical curves.

To conclude, MLC2132 can be preferred to E7 when a larger phase shift (or group delay or GDD phase shift) is required, for instance, a LC based dispersion scan. MLC2132 can also be selected when the environment has some temperature fluctuations. Conversely, E7 can be preferred when less dispersive materials or high temperature sensitivity are necessary. The optical response of these two LC mixtures to an electric field is studied in the next chapter.

## Summary tables

The following tables summarize the optical coefficients useful for ultrafast applications, for E7 and MLC2132

LC	A	B	C
$E7_E$	1.6933	0.0078	0.0028
$E7_O$	1.499	0.0072	0.0003
$MLC2132_E$	1.709	0.00936	0.0036
$MLC2132_O$	1.4865	0.0072	0.00034
Error	$\pm 10^{-3}$	$\pm 10^{-4}$	$\pm 10^{-4}$

Table 7: E7 and MLC2132 Extended Cauchy coefficients.

at 20° 740nm	$\Delta n$	$\Delta n_g$	$\Phi_e^2$	$\Phi_o^2$	$\Phi_e^3$	$\Phi_o^3$
$E7$	0.2037	0.2393	350 ( $fs^2/mm$ )	130 ( $fs^2/mm$ )	300 ( $fs^3/mm$ )	300 ( $fs^3/mm$ )
$MLC$	0.2377	0.2868	420 ( $fs^2/mm$ )	125 ( $fs^2/mm$ )	250 ( $fs^3/mm$ )	250 ( $fs^3/mm$ )

Table 8: E7 and MLC2132 Dispersion coefficients.

LC	A	B	$\Delta n_0$	$\beta$	$T_c$
$E7$	1.7546	$5.36e^{-4}$	0.3768	0.239	331
MLC-2132	1.7127	$3.8072 \cdot 10^{-4}$	0.4550	0.3559	386

Table 9: E7 and MLC2132 Li's coefficients.

## Chapter 3

# Dynamics of electrically driven thick nematic LC cells

### Objective

In this chapter, the dynamics of electrically driven thick nematic cells are studied in view of a particular application: the ultrafast tunable delay line. The most common strategies to control the molecular reorientation are first described: the adiabatic voltage control and the transient relaxation. A faster alternative method is proposed (dynamic switching-on) despite the voltage threshold limitations. Thus, the *Fréedericksz transition* is qualitatively and quantitatively studied during this commutation and the influence of different starting voltages and different LC thicknesses are analyzed. The unexpected influence of the LC thickness on the *Fréedericksz transition* is demonstrated for the first time. Therefore an improvement of the tunable group delay control of the LC is proposed.

### 3.1 Introduction: electrically driven LC tunable delay line

#### 3.1.1 Background

As discussed in chapter 1 the LC molecules can be orientated applying an external electric field. The related birefringence excursion is then used to modify the characteristics of a laser beam passing through the cell. Indeed, a continuously tunable ultrafast delay-line has been recently developed (Jullien et al., 2016). The outline of the system is the following (Figure 32): An ultrafast laser pulses train is passing through the LC with a polarization direction at  $45^\circ$  with respect to the nematic director. In the birefringent layer, the pulses are divided into the two optical axes, creating two replicas. Thus, phase and group delays acquired in the LC mixture for each polarization directions are respectively:

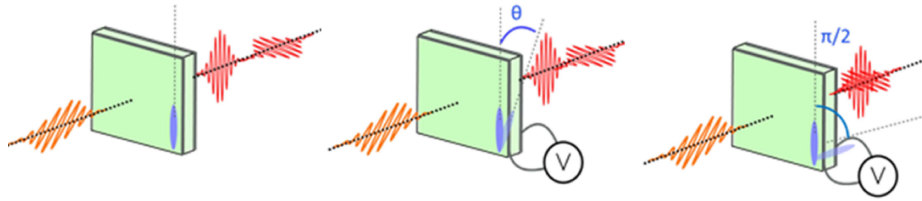


Figure 32: a) Principle of the ultrafast LC (group) delay line. Green : LC cell, blue: molecular orientation.

$$\tau_{(\phi)o,e} = n_{o,e} \frac{L}{c} \quad (3.1)$$

$$\tau_{(g)o,e} = n_{g,o,e} \frac{L}{c} \quad (3.2)$$

with  $n_{(g)o,e} = n_{o,e} + \omega_0(dn_{o,e}/d\omega)$ . So,  $n_o$  (resp.  $n_e$ ) is the ordinary (resp. extraordinary) refractive index of the LC mixture,  $n(g)_o$  (resp.  $n(g)_e$ ) is the ordinary (resp. extraordinary) group index,  $L$  is the LC thickness and  $\omega_0$  is the central laser frequency. In the rest state, the horizontal-polarized pulse propagates through a purely extraordinary medium. The refractive index difference with the vertical-polarized ordinary wave is maximum and it can be expressed as  $\Delta n_g = n_{g,e} - n_{g,o}$  ( $\Delta n_g = 0.23$  for E7 at 770nm). Therefore, the two sub-pulses consequently emerge out of the cell with a temporal delay proportional to the LC thickness:

$$\Delta \tau_g = \Delta n_g \frac{L}{c} \quad (3.3)$$

where  $\Delta n_g$  is the group index difference between the extraordinary and ordinary directions, and  $c$  is the speed of light in vacuum.

As stated in chapter 1, when an external electric field is applied, the molecules tend to follow the  $\vec{E}$  orientation, as the employed liquid crystal presents a positive dielectric anisotropy. Therefore, the extraordinary index is then progressively changed as:

$$n(\theta) = \frac{n_e n_o}{\sqrt{n_e^2 \cos^2(\theta) + n_o^2 \sin^2(\theta)}} \quad (3.4)$$

with  $\theta$  the local angle formed between the nematic director and the original alignment axis. It is important to remind that  $\theta$  depends on the voltage and is not uniform across the LC thickness, as reorientation occurs mostly in the middle of the cell, while closer to the substrates the anchoring conditions dominate (Yang, 2014).

This configuration constitutes an optical delay line that is continuously tunable, compact, and with no moving parts.

To tune the delay line, 3 different strategies can be contemplated as illustrated in Figure 33 :

1. **Adiabatic control:** several consecutive voltage steps are applied until the full reorientation is achieved. LC stabilization has to be reached between each step.
2. **Switching off:** One dynamic voltage step is applied, the birefringence scan occurs when the electric field is turned-off and molecules are driven back to their rest position (transient relaxation).
3. **Switching on:** One dynamic voltage step is applied and the birefringence excursion occurs during the transient nematic effect (e.g. orientation of the molecules under the action of an external electric field).

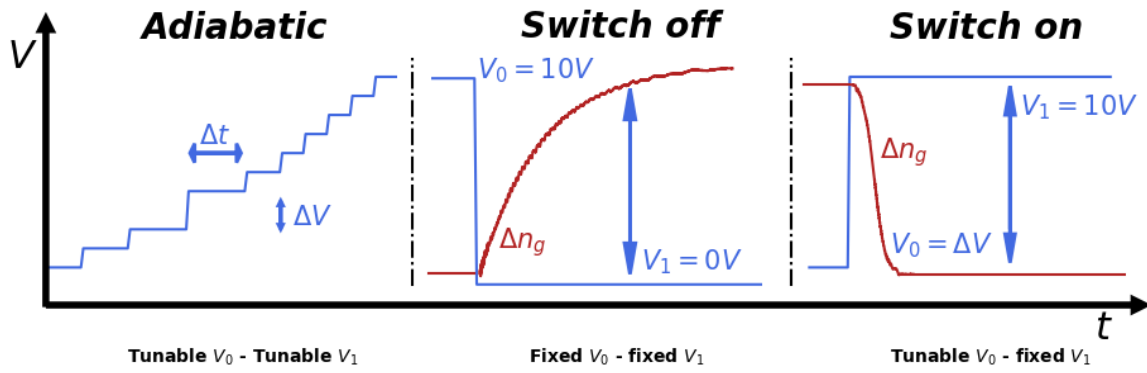


Figure 33: Illustration of the considered three driving options and associated experimental tunable parameters.

Targeted applications require to get the largest birefringence excursion (e.g. the largest group delay change) together with the fastest acquisition time.

These three options are characterized and compared in the following.

### 3.1.2 Experimental methods

Two different experimental set-ups are installed (Figure 34) and several cells have been fabricated to study the effect of the LC thickness on the molecular commutation.

- LC cells fabrication and driving conditions:  
 Different thicknesses ( $L$ ) of the cell gap, from  $9\ \mu\text{m}$  to  $250\ \mu\text{m}$ , are used, keeping constant the planar splay geometry and strong anchoring conditions. The LC mixture is E7 ( $V_{th} = 1.2V$ , see chapter 1), except in the last section (3.4.6) where a  $180\ \mu\text{m}$  cell composed by MLC2132 is also fabricated.  
 All the LC-cells are connected to a waveform generator producing a sinusoidal AC voltage with variable amplitude, enabling the control of the average molecular orientation ( $\theta$ ). The maximum voltage (peak to peak) is  $10V$ . To prevent low-frequency electro-convection phenomena, the frequency of the electric field is fixed at  $1kHz$ , to consider a quasi-static field for the LC molecules reorientation.
- Group delay experimental set-up:  
 The first experimental setup, shown in Figure 34a), allows the measurement of the phase

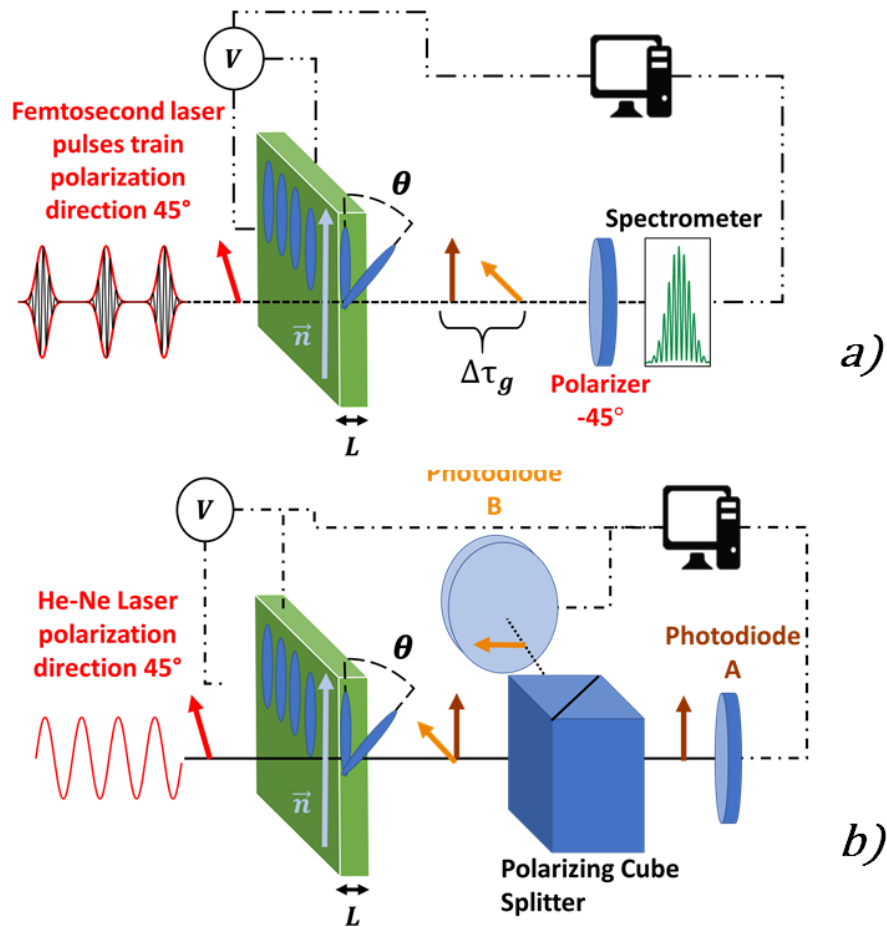


Figure 34: Experimental set-ups: a) A femtosecond laser (30 fs, repetition rate 80 MHz, spectrum centered at 770 nm) produces a 30mW beam. A half-wave plate and a polarizer orientate the input polarization at  $45^\circ$  with respect to the initial director of the LC-cell ( $L=180 \mu\text{m}$  fixed) to generate two cross-polarized sub-pulses delayed by  $\Delta\tau_g = \Delta n_g \frac{L}{c}$  after the propagation in the LC. A polarizer placed at the output of the cell projects the two polarization components onto the same polarization direction in order to generate a spectral interference pattern. A spectrometer acquires the dynamical spectral map. (b) The dynamical characterization of the FT. A 5mW light beam from a Helium-Neon laser ( $\lambda = 633 \text{ nm}$ ) is sent onto the LC-cell after a half-wave plate and a polarizer that orientate its polarization direction at  $45^\circ$  with respect to the initial nematic director  $\vec{n}$ . The cube beam-splitter separates the two components of polarization at the output of the cell, each component is, then, sent to a photodiode. The photodiodes and the voltage generator are connected to the oscilloscope to acquire the polarization signals and a copy of the applied voltage.

shift undergone by a polychromatic pulsed light when passing through the LC-cell. The method relies on the broadband spectral interferometry technique with femtosecond pulses (FTSI), see chapter 1.1.2. A fs laser, emitting pulses with a spectrum centered at 770 nm (120nm full width) and with 30 mW average power is sent through the LC-cell. A half-wave plate and a polarizer set the linear polarization direction at  $45^\circ$  with respect to the LC anchoring direction. A second polarizer is placed at the exit of the LC-cell at  $90^\circ$  with respect to the first one. The resulting interference pattern is registered in the spectral domain where wavelength-dependent constructive and destructive interferences occur over the whole bandwidth. The interferogram is dynamically acquired by an OceanOptics spectrometer (2ms integration time, 5ms acquisition span, 0.3nm spectral resolution). The FTSI technique recovers the group delay  $\Delta\tau_g$  (the harmonic position in the Fourier domain) and, thus, the group index difference  $\Delta n_g$ , with a precision only limited by the

spectral resolution (see eq. 3.3). Here, the precision on  $\Delta\tau_g$  is  $\pm 0.1\text{fs}$ , e.g.  $\Delta n_g$  is recovered with a precision better than one part in a thousand ( $10^{-3}$ , (Jullien et al., 2016)).

- Optical transmission experimental set-up:

The polarization-dependent and the disorder-induced optical losses during the FT are studied using the experimental setup shown in Figure 34b). A Helium-Neon laser emits a continuous radiation at  $\lambda=633\text{ nm}$  with 5 mW average power. A half-wave plate and a polarizer set the linear polarization direction at  $45^\circ$  with respect to the LC anchoring direction. This polarization alignment is done prior to any set of measurements and under a constant 10V bias voltage applied to the LC-cell. Then, the laser beam passes through a polarizing cube splitter that separates the two components of polarization, S (resp. P), parallel (resp. orthogonal) to the LC anchoring direction. Finally, each polarization component is recorded by a photodiode and the two respective signals are acquired by an oscilloscope. This experimental set-up is used for switch-on dynamics characterization described in section 3.4.2.

### 3.2 LC tunable delay line based on Adiabatic Electrical control

The first strategy consists in applying consecutive voltage steps to the LC cell in order to induce a progressive molecular rotation. Using this technique, a tunable femtosecond delay device based on liquid crystal has been already developed (Jullien et al., 2016). The voltage is regularly increased by several steps: 50 mV between 1.3 V and 3 V, 100 mV otherwise, up to 10V. The resting time, e.g. time to reach the stability, between two consecutive steps changes according to the LC thickness and to the applied voltage (see chapter 1).

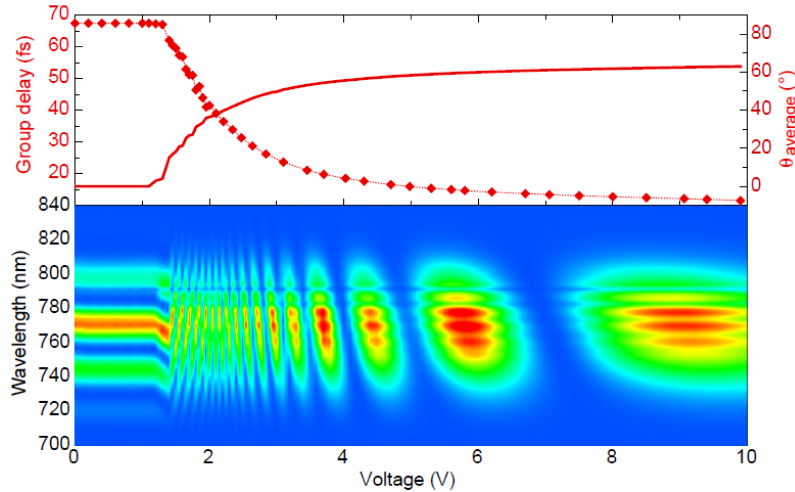


Figure 35: a) Retrieved group delay (points) and corresponding molecular tilt angle  $\theta$  (solid line) averaged over the cell thickness as a function of the applied voltage. b) Interference spectrum map measured as a function of the voltage, for a  $88\ \mu\text{m}$ -thick LC cell. Image from (Jullien et al., 2016).

An illustration extracted from (Jullien et al., 2016) is shown in Figure 35. The group delay excursion and deduced tilt angle  $\theta$  are plotted as a function of the applied voltage for a  $88\ \mu\text{m}$ -thick cell (Figure 35a) using the first experimental set-up (group delay measurement). The spectrogram is also shown in Figure 35b), and the table 10 indicates the response time and



Voltage		136 $\mu\text{m}$	88 $\mu\text{m}$
2V	$\delta t$ ( $f\text{s}/50\text{mV}$ )	2.3	1.3
	$\tau$ (s)	20	10
4V	$\delta t$ ( $f\text{s}/100\text{mV}$ )	0.7	0.4
	$\tau$ (s)	3	1
6V	$\delta t$ ( $f\text{s}/100\text{mV}$ )	0.7	0.4
	$\tau$ (s)	0.1	0.01
8V	$\delta t$ ( $f\text{s}/100\text{mV}$ )	0.1	0.07
	$\tau$ (s)	0.001	0.001

Table 10: Temporal resolution ( $\delta t$ ) and response time ( $\tau$ ) for different voltages (2V, 4V, 6V, 8V) and thicknesses (88, 136  $\mu\text{m}$ ).

the temporal resolution for several voltage ranges. Group delay is continuously tuned between  $70fs(\text{max})$  and  $10fs$ , with a sub-cycle resolution and response time depending on the bias voltage.

This scheme has enabled to characterize the LC cells behavior in the femtosecond regime and to scan their birefringence. It has also been proven to be efficient to realize independent control of phase and group delay. However, the main drawback of this strategy is the time required to complete the molecular reorientation and, therefore to get the maximum phase shift. As mentioned in the introduction, the molecules response time to an applied electric field is (1.40):

$$\tau_{on} \propto \frac{Const.}{(E^2 - E_c^2)} \quad (3.5)$$

Hence,  $\tau_{on}$  is proportional to the amplitude of the electric field, to the characteristic of the mixture and cell thickness ( $E_c \sim 1/L^2$ ). Therefore for the first steps of the process, the time necessary to reach the stability is about several seconds ( $\sim 20\text{sec}$ , (Jullien et al., 2016)). Considering the small voltage steps close to threshold (50 mV), the full commutation requires several hours. This effect is even enhanced with thicker cells. Therefore another strategy to speed up the commutation is suitable.

### 3.3 Transient nematic relaxation addressing

#### 3.3.1 Principle and response time

To speed up the molecular reorientation, a dynamic process can be contemplated to exploit the transient molecular motion. Instead of several small voltage steps, a higher electric field is applied that drives the LC molecules out of the equilibrium. Once the excursion is complete, the voltage is turned off, and LC molecules are dynamically driven back to their rest position. The birefringence scan occurs during this relaxation. If during the switching-on process the commutation cannot be exploited because of the Fréedericksz transition, during the switching-off this issue does not affect the molecular commutation. The time required to go back to the rest position depends only on the characteristic of the LC cell, e.g. the used mixture and its thickness (eq.1.38,  $\tau_{off} \sim L^2$ ). To verify this, several cells with different thicknesses have been tested using the switching-off strategy (from 10V to 0V). A typical interference pattern is shown

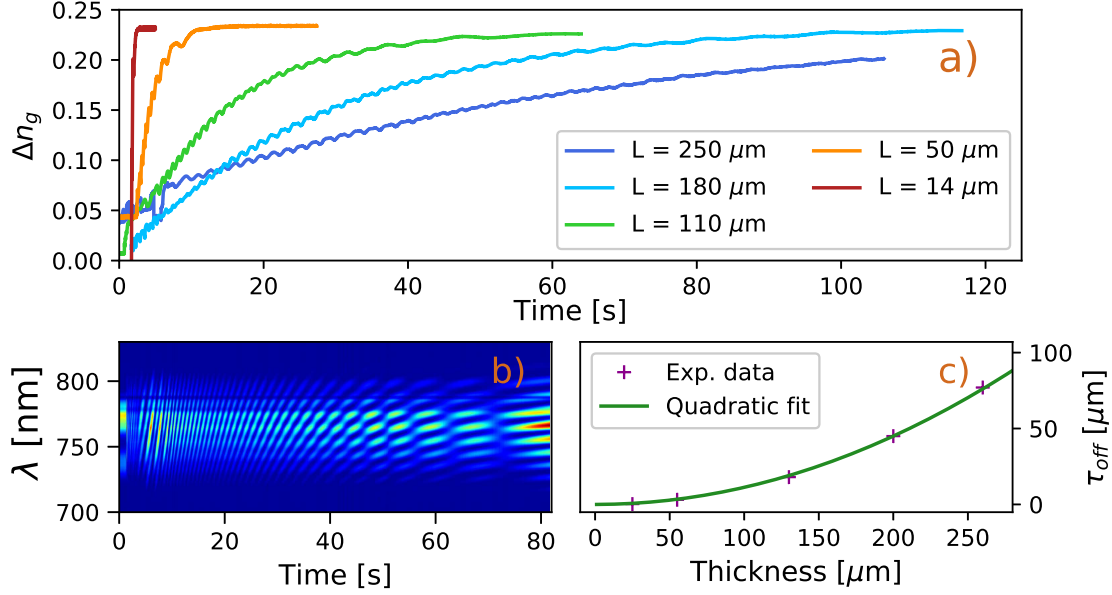


Figure 36: a) Group index variation as a function of time for different LC thicknesses ( $L = 14, 50, 110, 180, 250 \mu\text{m}$ ). b) Spectrogram of  $180 \mu\text{m}$  thick cell during the transient nematic relaxation. c) Time coefficient ( $\tau_{off}$ ) as a function of effective LC thickness (crosses) which slightly differs from the size of the spacers (see chapter 1), and its quadratic fit (green curve).

in Figure 36b) using the group delay experimental set-up (first arrangement). Five different cells have been studied from  $14 \mu\text{m}$  to  $250 \mu\text{m}$ . In Figure 36a), the relative group delay excursions are plotted as a function of time. The influence of the thickness is clear, and the  $180 \mu\text{m}$  thick-cell needs more than 100 s to drive back the molecules. Nevertheless, for comparable introduced group delay (100 fs), transient relaxation speeds up the evolution comparing with the adiabatic control. The commutation time is fitted using an exponential decay, and the  $\tau_{off}$  as a function of LC-thickness is plotted. As expected, the switching-off dynamic follows a quadratic dependence (Figure 36c).

### 3.3.2 Back-reflexion issues

Although the transient relaxation speeds up the molecular reorientation, some dampened oscillations on the group delay excursion are always detected whatever the LC thickness (Figure 36a)). Indeed, the only exponential decay cannot reproduce these fluctuations on the measured data. Moreover, a temporal dependence of these oscillations is always measured: larger in amplitude and frequency at the beginning of the relaxation. The first suggestion about their origin comes from the fluctuations of the nematic director during the commutation.

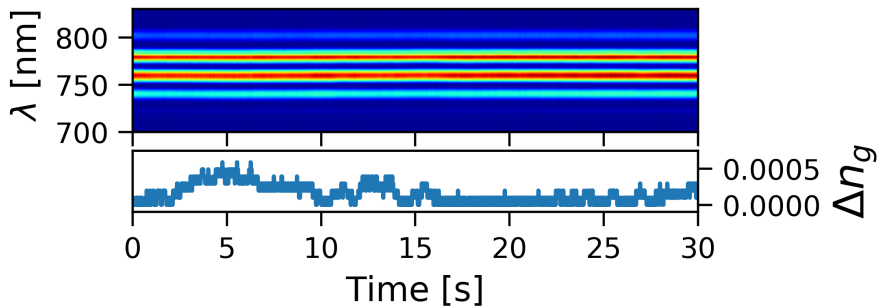


Figure 37: Spectrogram as a function of time for the  $180 \mu\text{m}$  LC cell under a constant bias voltage of 2V. The relative group index is plotted below (note the narrow scale).

Thus, spectrograms are monitored keeping constant the bias voltage for a given cell to verify the molecular stability under the effect of an external electric field. In Figure 37) the interference pattern induced by the 180  $\mu\text{m}$  thick-cell at 2V is plotted. The group index variation ( $\Delta n_g$ ) measured is smaller than  $5 \cdot 10^{-4}$  (Fourier Transform noise level), more than three orders of magnitude lower than the commutation oscillations. Therefore, the nematic director does not fluctuate in time, even for such thick layer and a driving voltage close to the FT threshold. Therefore the reason for those oscillations has to be found somewhere else.

In particular, the multilayer configuration of the LC cell (BK7-ITO-PVA-LC) can lead to Fabry-Perot interferences that modulate the laser in phase and amplitude (Clarke, 2004). This effect was deeply studied even in LC-SLM (Wittenbecher & Zigmantas, 2019; Vargas, del Mar Sánchez-López, García-Martínez, Arias, & Moreno, 2014) considering also different geometries and configurations (Bock et al., 2008). The phenomenon consists of an interference effect between the main beam and the partial reflections occurring at the interfaces between successive layers that have two different refractive indices. In particular, along the extraordinary polarisation direction, a back-reflection at the LC-ITO interface adds a modulation component, whose temporal evolution depends on  $n_e(t)$ . Indeed, the reflectivity decreases during the transient relaxation ( $n_e$  increases) (Figure 38a) according to:

$$R(t)^2 = \frac{n_{ITO} - n_e(t)}{n_{ITO} + n_e(t)} \quad (3.6)$$

The induced phase shift can be written as (Bock et al., 2008):

$$\Phi(t) = \arctan\left[\frac{(1 - R(t)) \sin(\delta(t))}{2\sqrt{R} - (1 + R) \cos(\delta(t))}\right] \quad (3.7)$$

Where  $\delta$  is:

$$\delta = \frac{\pi}{\lambda} 2Ln_e(\lambda, t) \quad (3.8)$$

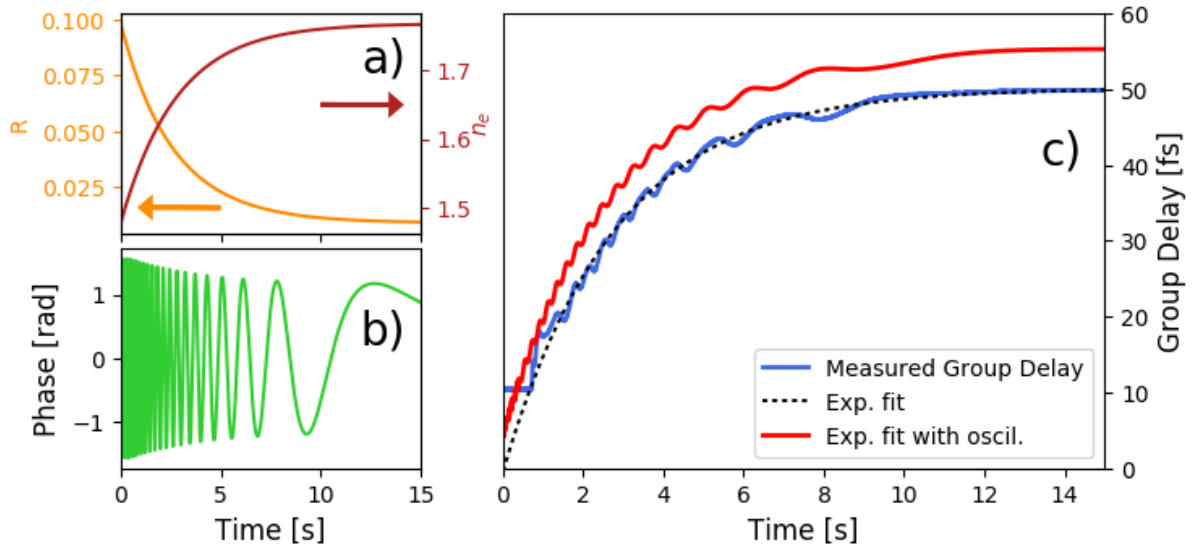


Figure 38: a) Refractive index (orange curve) and Reflectivity at ITO-E7 boundaries (red curve) are plotted as a function of time. b) The related oscillations. c) Group delay excursion of a 50  $\mu\text{m}$  cell: raw data (blue solid curve), exponential fit (black solid curve), and exponential fit with oscillations (red dotted curve).

Therefore, from eq. 3.7 a dumping oscillating phase shift is calculated (Figure 38b) and afterwards its related group delay (fs). So, this last term is added to the exponential decay fit ( $\tau_{off}$ ). The results are plotted in Figure 38c) for a 50  $\mu\text{m}$  thick-cell with artificial temporal

offset for sake of the visibility. The fit quality is considerably improved, the measured oscillations are reproduced including the dumping effect in amplitude and frequency. However, some uncertainties are still visible, and the fit has to be further improved. These ambiguities might come from several approximations:

- The reflections are assumed between the LC and ITO layers as always done in the literature (Wittenbecher & Zigmantas, 2019; Vargas et al., 2014; Bock et al., 2008). Actually, between these two layers, a really thin film of PVA is placed but neglected here.
- The ITO refractive index changes considerably ( $n_{ITO} = 1.8 \pm 0.3$ ) following its thickness and the quality of the manufactures<sup>6</sup> (Kondilis, Aperathitis, & Modreanu, 2008; Yan et al., 2009).
- The interference effect has a remarkable spatial dependence, as already demonstrated by (Wittenbecher & Zigmantas, 2019).
- The layers assembly is slightly wedged.

Nevertheless, a qualitative explanation of the oscillations is enough for the interest of this thesis, but all this uncertainty have to be solved in the future for more precise studies.

To conclude, transient relaxation is demonstrated to be a better strategy to address LC molecules without reducing the birefringence excursion. The required time to commute is drastically reduced, in particular for very thick cells ( $180\mu\text{m}$ ). However,  $> 2\text{min}$  are still necessary to drive back the molecules, which remains quite slow for applications. Therefore, another strategy has to be contemplated. Moreover, the oscillations due to the back-reflections affect the phase addressing capabilities and need to be taken into account.

Nevertheless, if well-calibrated, this transient relaxation has been already applied to high resolution hyperspectral imaging (Jullien et al., 2017, 2019).

## 3.4 Switch-on addressing

### 3.4.1 Fréedericksz transition (FT)

The switch-on dynamics inverse the process of the transient relaxation and the molecular re-orientation is exploited when the external electric field is applied. If the voltage amplitude is large enough, the time to address the molecules is reduced to a few seconds (typically  $3/4$  sec). However, the birefringence excursion is drastically affected by the Fréedericksz transition (see section 1.2.3). Indeed, the competition between the inner elastic forces and the external electric torque results as a pitchfork bifurcation instability (Derfel, 1988; Blake et al., 1999). The control parameters are: the field strength and the voltage threshold above which the molecules start to reorient, Fréedericksz threshold voltage ( $V_{th}$ ). This last value depends on the elastic constants (bend, twist, and splay) introduced in section 1.2.2.

Several experimental methods to measure  $V_{th}$  of a given LC have been proposed so far. As a complement to capacitance measurement, optical methods are mainly based on transmission measurement between cross-polarizers, or the direct measurement of the phase shift due to the birefringence changes, or diffusion and optical scattering observation (Raynes, Brown, & Strmer, 2003; Orihara, Sakai, & Nagaya, 2001; Nespoulous, Blanc, & Nobili, 2010). Besides, FT has been the subject of numerous theoretical and experimental papers, including twisted nematic cells (Gerritsma, Van Doorn, & Van Zanten, 1974), strong and weak anchoring conditions (Napoli, 2005), turbulence around the phase transition (Manneville, 1981), just to cite a few.

<sup>6</sup><https://www.filmetrics.com/refractive-index-database/ITO/Indium-Tin-Oxide-InSnO>

Molecular disorder and/or defect formation in LC-cells during the FT are of interest as they might induce significant optical losses, especially in the framework of this thesis. A microscopic model based on molecular-dynamics simulation of a nematic liquid crystal under the application of an electric field has been proposed by Tian and Co. (Tian, Bedrov, Smith, Glaser, & Maclennan, 2002). In this study, it was shown that the order parameter  $S(t)$  decreases monotonically when an electric field is applied. Reaching a minimum value  $S_{min}$  at time  $\tau_{Smin}$  (corresponding to the maximum disorder),  $S(t)$  presents an exponential recovery time that restores the nematic order. In homeotropic thin cells, a disordered switch-on dynamics has been confirmed through depolarization measurements during the application of a small voltage step around the Fréedericksz threshold voltage (Vena, Versace, Strangi, DELia, & Bartolino, 2007). In this particular configuration, a maximum depolarization related to the FT was attributed to disorder and defect formation at the reorientation onset. These studies are restricted to LC-cells with a thickness below  $30 \mu\text{m}$ , and the scaling to larger nematic layers has not been studied so far. In the next sections, an experimental study about the switch-on dynamics and disorder-induced losses during FT in planar nematic cells is presented. The goal is to define the best switch-on dynamics that can be used in view of femtosecond applications. A real-time optical measurement is performed during the transient molecular rearrangement.

- By quantifying the optical transmission on both polarization directions and its characteristic time-scale, the FT is dynamically pictured and LC-thickness influence is measured for the first time. The results qualitatively agree with the predicted microscopic disorder model (Tian et al., 2002).
- The analysis is then extended to a fast measurement of the transient birefringence of a thick cell, reporting on the optimum electrical control for the ultrafast tunable group delay line. The qualitative and quantitative influence of the initial conditions on the FT are investigated on the basis of the dynamical measurements performed before.
- Finally, MLC2132 is compared to E7.

#### 3.4.2 Dynamical characterization of the Fréedericksz transition

In order to characterize the FT, several steps of voltage are applied to the LC-cells using the second experimental set-up, as shown in Figure 34b). All the voltage steps have different starting voltage ( $V_0$ ), with  $V_0$  higher or lower than  $V_{th}$ , but the same final voltage ( $V_1 = 10 \text{ V}$ ), so that the influence of passing through the FT threshold is probed for the same final ordered state (Figure 39a). To avoid any memory effects, 4 minutes of rest time is respected between any two successive measurements.

The polarization-dependent dynamical behaviour of the cells under the application of different voltage steps (setup of Figure 34b) ) is studied. As an example, in Figure 39b) are plotted the signals acquired by photodiodes A and B during the cell switch-on for the two voltage steps given by  $V_0 = 0\text{V}$  and  $V_0 = 1.3\text{V}$  for a  $L = 14\mu\text{m}$ -thick cell.

When  $V_0$  is smaller than  $V_{th}$  ( $V_0 = 0\text{V}$ ), a large optical transmission loss is detected on the extraordinary axis (photodiode A, blue curve) while no loss occurs on the ordinary axis (photodiode B, light blue curve). The sum of both signals is not constant over time, indicating an overall loss of transmission, rather than a simple energy exchange between polarizations. This transmission decrease by optical scattering is due to the induced molecular disorder. Indeed, as predicted in (Tian et al., 2002), the electrical switch-on of a LC-cell is associated with a reduction of the nematic order, following three stages: initiation, orientation, and relaxation. This behavior is here qualitatively observed when  $V_0 = 0\text{V}$ . Consistently, the optical transmission losses are thus supposed to be induced by the molecular rearrangement, characterized by

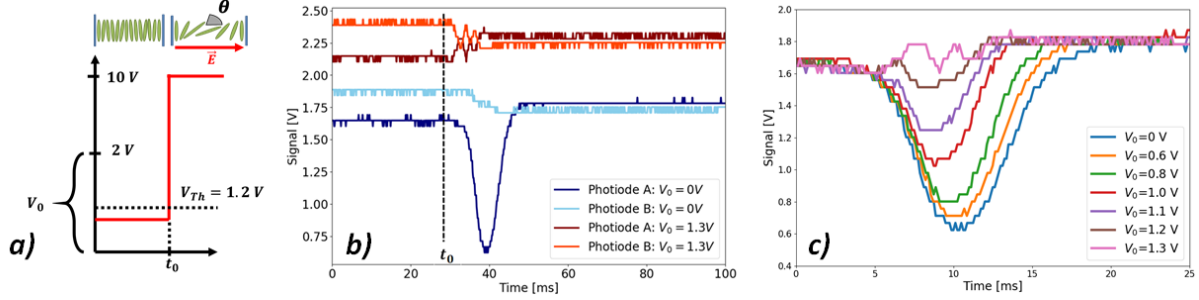


Figure 39: a) Voltage step applied to the LC-cells during the switch-on dynamics.  $V_0$  varies from 0V to 2V, while the final voltage is fixed at 10V. b) Transmitted signals along with the extraordinary (A, blue and red) and ordinary (B, light blue and orange) axis, acquired for a voltage step  $V_0 = 0V - 10V$  and a voltage step  $V_0 = 1.3V - 10V$  ( $L=14 \mu\text{m}$ ). An artificial offset (0.5V) is added between the two sets of data for a better visibility. c) Transmitted signal from photodiode A (extraordinary axis) for the same cell ( $L=14 \mu\text{m}$ ) and for different starting voltages  $V_0$ . All the measurements start from the same  $t_0$  (not indicated in the plot for the sake of better visibility).

a strong disorder when passing through the FT. Losses are found in the extraordinary plane, indicating a minor contribution of the twist elastic constant to the transient molecular disorder. Conversely, when  $V_0$  is higher than  $V_{th}$  practically no losses are detected (photodiode A and B for the red, respectively, orange curve). Only a relative energy exchange between A and B as a result of the overall reorientation is observed. These observations show a clear disorder dependence on whether or not  $V_{th}$  is included in the voltage step. The projections on ordinary and extraordinary polarizations are slightly different before and after  $t_0$  because the reorientation movement described by the average director angle tilt  $\theta(t)$ , is not perfectly confined on the  $xz$  plane (see Figure 34c). Figure 39c) shows the signals measured by photodiode A (extraordinary axis) for the same cell ( $L=14 \mu\text{m}$ ) and for different starting voltages,  $V_0$  from 0 to 1.3V. All the measurements start from the same  $t_0$ . As it can be clearly appreciated from the different curves, increasing  $V_0$  from 0V to 1.3V induces a progressive reduction of the disorder losses. This set of measurements enables to figure out a reduction of the order parameter when the LC-cell is driven through the FT, in a qualitative agreement with the predictions provided by (Tian et al., 2002). When the starting voltage is above  $V_{th} = 1.2V$ , practically no losses are detected, and the molecular rearrangement occurs smoothly in this case.

### 3.4.3 LC thickness influence on the Fréedericksz transition

Thin LC cell ( $14\mu\text{m}$ ) is used in the previous section in order to visualize the effect of the Fréedericksz Transition. To study the LC thickness influence on the optical losses several cells with different LC layer thicknesses are tested with different starting voltage.

Indeed, for the same applied voltage step ( $V_0 = 0V$ ), a significant dependence on the LC thickness is observed. This is shown in Figure 40a), where the signal transmitted on the extraordinary axis and measured by photodiode A is plotted for a fixed voltage step ( $V_0 = 0V$ ) and for different thicknesses of the LC-cell ( $9 \mu\text{m}, 11 \mu\text{m}, 25 \mu\text{m}, 75 \mu\text{m}, 180 \mu\text{m}$ ). The measurements show that thin cells present fast and huge losses (up to 60% for the thinner cells). Conversely, thicker cells exhibit lower maximum losses (higher minimum of the transmission dip), but these losses spread over a much longer time scale. Increasing the LC layer thickness, therefore, reduces the value of the maximum losses occurring close to the center of the transmission dip but also stretches the temporal scale for the complete switch-on to occur and over which the losses take place.

In order to quantify the optical transmission losses, that mainly occur along the extraordinary axis, a *transient transmission* is defined as:

$$T = \frac{I_{MIN}}{I_0} \quad (3.9)$$

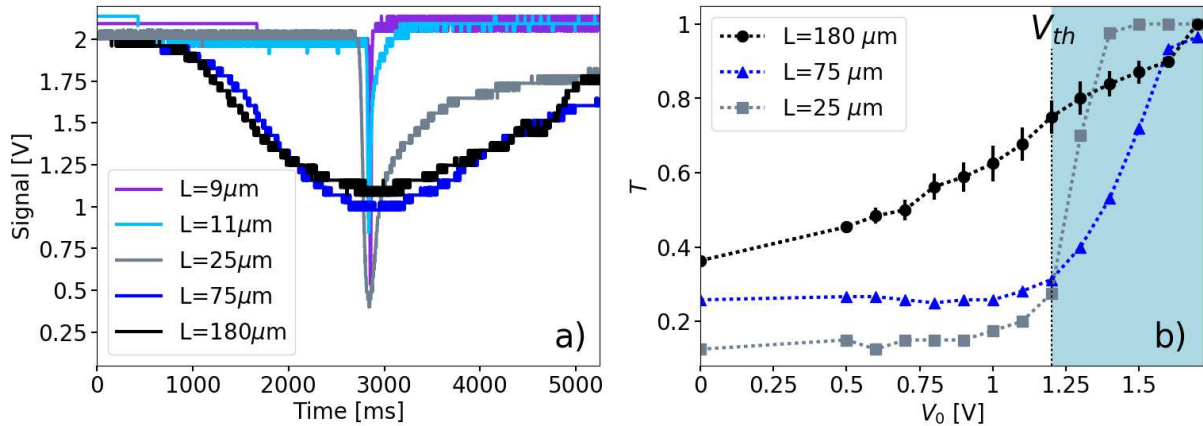


Figure 40: a) Transmitted signal along the extraordinary axis (photodiode A) acquired during the cell switch-on for the same voltage step ( $0V - 10V$ ) and for different LC thickness. Data are normalized and presented with an arbitrary temporal offset in order to compare the maximum losses (lowest value of the transmission dip). b) Transient transmission (see definition in the text) measured along the extraordinary axis during the cell switch-on for an applied voltage step  $V_0-10V$  by changing the starting voltage  $V_0$  and for different cell thicknesses. The area beyond  $V_{th}$  ( $1.2V$ ) is highlighted in blue.

where  $I_{MIN}$  represents the minimum value reached by the signal, thus the time of maximum disorder and  $I_0$  is its initial value.  $T = 1$  means that no losses are detected on the extraordinary axis, i.e. the molecular arrangement occurs homogeneously. Instead,  $T = 0$  represents a minimal transmission and, therefore, corresponds to the maximal disorder. The measured transient transmission evolution as a function of  $V_0$  is plotted in Figure 40b) for some cells of different thicknesses ( $25, 75, 180 \mu\text{m}$ ).

The  $T$  value corresponding to the  $0V - 10V$  step is changed accordingly to the cell thickness, as underlined in Figure 40a). Note that the  $25\mu\text{m}$  cell has the most regular behavior, with a transmission as low as 0.1 when  $V_0 < 1V$ . Then, starting from  $V_0 = 1.1$  V,  $T$  increases rapidly up to 0.95 for  $V_0 > 1.3$  V. It is worth noting that the curve is a visualization of the FT, in compliance with the expected steep phase transition occurring at  $V_{th}$ . The proposed analysis thus represents an original dynamical method to evaluate the FT voltage threshold.

However, the transition is largely spread out for the thickest cell ( $180\mu\text{m}$ ). In that case, increasing  $V_0$  also increases  $T$ , even for  $V_0$  below the threshold. The  $75\mu\text{m}$  cell has an intermediate behavior: an increase of  $T$  is noted for  $V_0 = 1.1V$ , but the slope is smoother than for the  $25\mu\text{m}$ -thick cell. For the thickest cell of  $180\mu\text{m}$ , several identical measurements have been made (with the same  $V_0$ ) in order to estimate the reproducibility. The data dispersion is also function of the FT: in particular when  $V_0$  is smaller than  $1$  V or greater than  $1.4$  V the measurement is repeatable with a maximum uncertainty of 3%. Conversely when  $0.9 < V_0 < 1.3$  V the error bar can reach a maximum of 9.5%. These fluctuations may be explained with the bifurcation theory: the statistical repartition of molecules in the two states of the pitchfork might change for successive measurements.

The above measurements demonstrate that the cell thickness affects the FT manifestation. Particularly, the transient molecular dynamics at the onset of the transition is characterized by optical losses on the extraordinary axis, which can be attributed to the microscopic spatial disorder, and whose features change when passing from thin to thick LC-cells. While thin cells present the expected step-like FT, with strong ( $T \sim 0$ ) and localized in time molecular disorder, thick cells show a rounding of the transition, a phenomenon typically affecting bifurcations in the presence of noise (see (Moss & McClintock, 1989) and references therein, and (Agez, Clerc, Louvergneaux, & Rojas, 2013) for a more recent review). In the considered case, the inner molecules of the cell are less affected by the anchoring strength than the molecules close to the cell surfaces, therefore, more affected by the disorder occurring at the transition point.

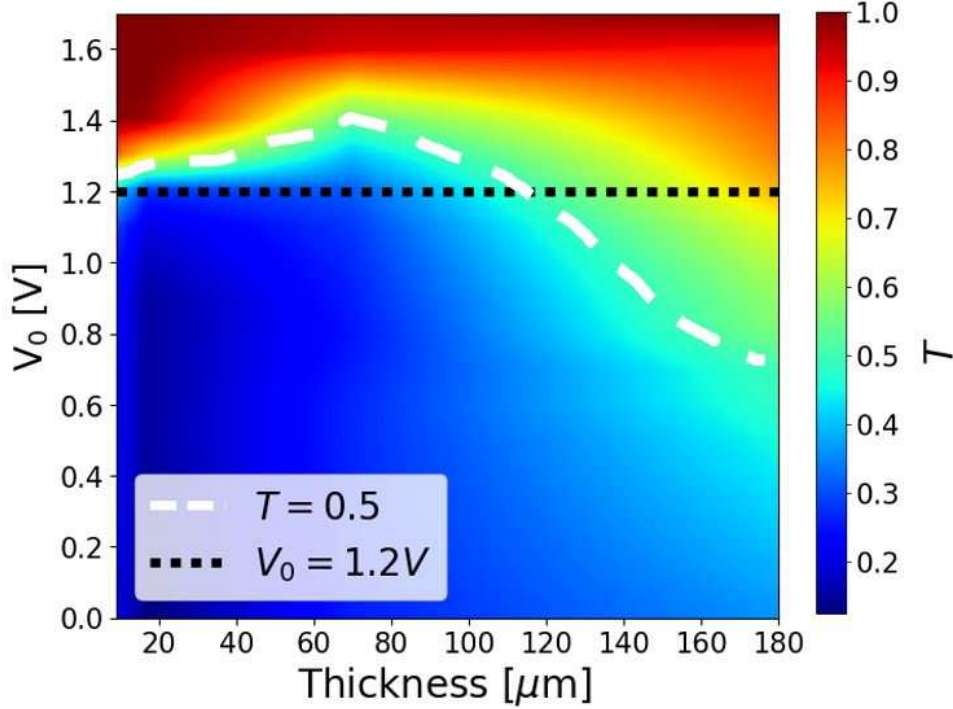


Figure 41: Transient transmission (color-coded) as function of  $L$  and  $V_0$ , extrapolated from our experimental data. The dotted white line features  $T = 50\%$ .

Because several bifurcating modes are simultaneously excited and amplified by the transient disorder, this effect is expected to be enhanced for thick cells, where the inner molecules experience more degrees of freedom to reorient, adding some noise to the bifurcation. Consequently, the transition rounding induces a larger molecular disorder when integrated over time, but simultaneously a lower maximum transient disorder around the threshold, because inner molecules tend to realign themselves more easily. Thus, when a voltage step is applied, although with  $V_0$  below  $V_{th}$ , precursor modes with a non-zero projection along the extraordinary axis maintain the transient transmission value above 0. This realizes a pre-ordered state for which a significant transmittance is obtained below  $V_{th}$ , even though the finally reoriented state is not reached yet. These findings draw different types of applications for LC-cell switch-on, depending on the nematic layer thickness. Indeed, based on the measured data, obtained with cells with various thicknesses, an operating area of nematics as a function of their thickness and of the driving voltage can be proposed. This is illustrated in Figure 41, featuring the transient transmission as a function of  $V_0$  and  $L$ . According to this map, the optimum starting voltage for switch-on can be easily deduced from the tolerable losses for any cell thickness. Two noticeable features emerge out. On the one hand, for thin cells ( $L=20 \mu\text{m}$  or less), the transient transmission is maximum once  $V_{th}$  has been reached. On the other hand, thick cells ( $L > 100 \mu\text{m}$ ) can be driven well below the FT threshold with a transmission still above 50%. The transition between thin and thick cells can be located at  $75 \mu\text{m}$ , when the slope of the 50% transmission is changed.

#### 3.4.4 Temporal dynamical features

Another signature of the FT resides in the time scale of the dynamical optical transmission losses. In order to characterize the temporal dynamical features,  $\tau_{min}$  is defined as the time span between the launch of the electric field ( $t_0$ ) and the moment of minimum transmission, e.g. the instant of the maximum molecular disorder. In the same way, a precursor time  $\tau_{prec}$  is defined as the span between  $t_0$  and the start of the decrease of the transmission, as illustrated



### 3. Dynamics of electrically driven thick nematic LC cells

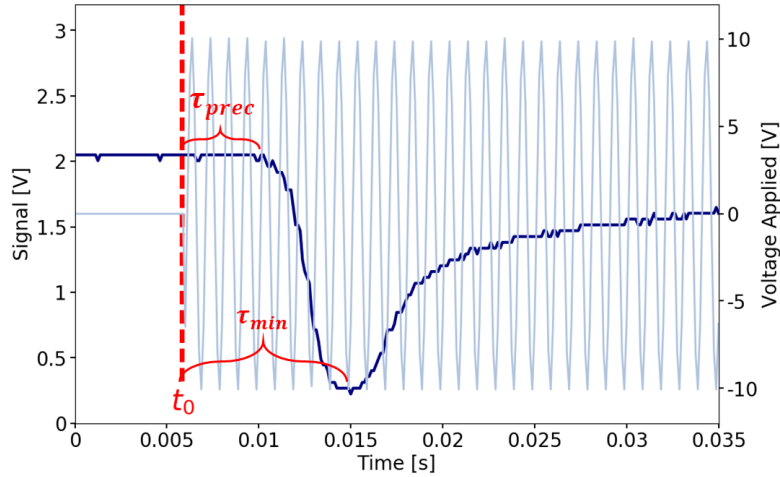


Figure 42: Transmitted signal along the extraordinary axis from a  $L=9\mu\text{m}$  cell at  $V_0 = 0\text{V}$  (blue line). Grey line represents the electric field applied.  $\tau_{min}$  and  $\tau_{prec}$  are indicated.

in Figure 42.  $\tau_{prec}$  can be seen as the initiation of the FT. By following this procedure,  $\tau_{min}$

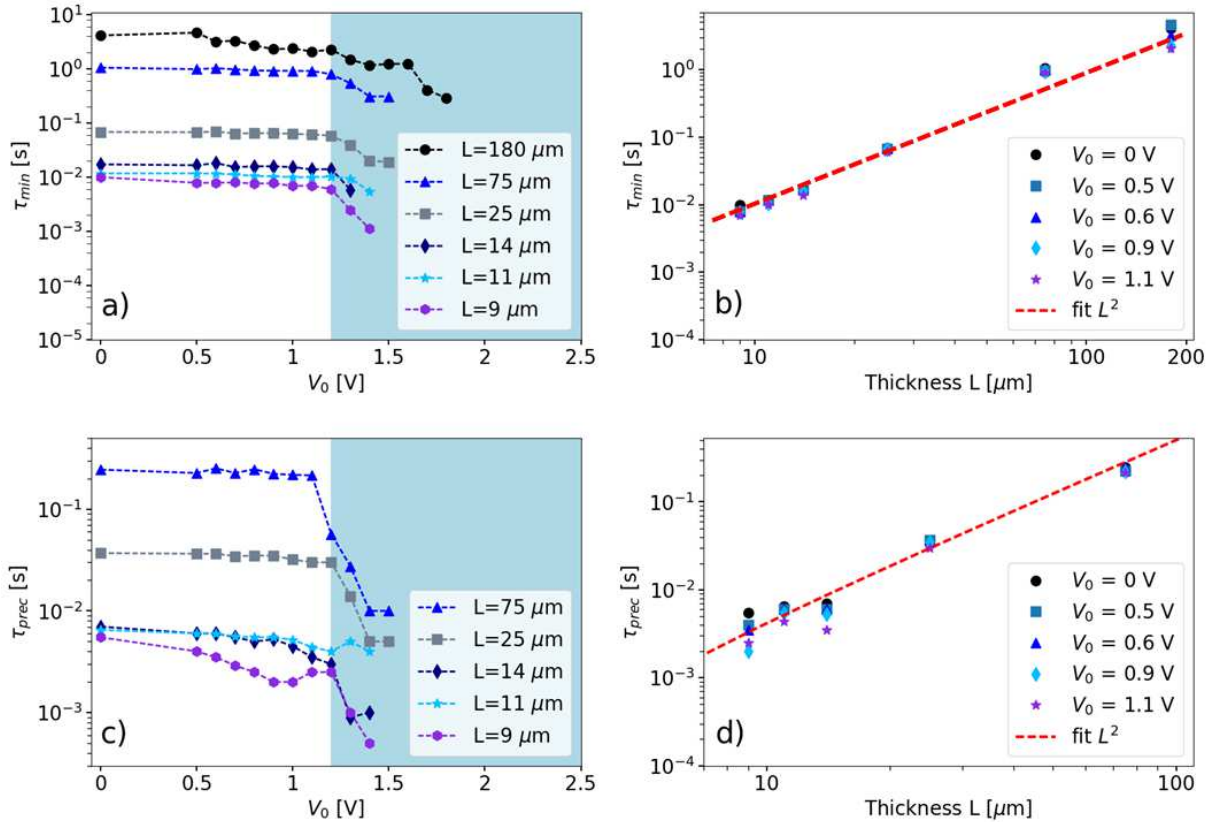


Figure 43: Temporal dynamical features of the Fréedericksz transition.  $\tau_{min}$  evolution as a function of  $V_0$  and thickness (a, b),  $\tau_{prec}$  as a function of  $V_0$  and thickness (c, d). The area beyond the  $V_{th}$  (1.2V) is highlighted in blue (a,c) and the red line (b,d) indicates a quadratic fit of the data.

and  $\tau_{prec}$  are registered as a function of  $V_0$  for all cells (Figure 43a)-Figure 43c). Both values are strongly affected by  $V_0$  and by the cell thickness, and both exhibit similar trends. For thin cells,  $\tau_{min}$  remains nearly constant with  $V_0$  until  $V_0 \sim V_{th}$ , after which the temporal span for minimum transmission strongly decreases. This abrupt slope change is precisely localized to  $V_0 = 1.2\text{V} = V_{th}$ , establishing a dynamical measurement of the FT. This trend remains valid for all LC-cells, except the  $180\mu\text{m}$ -thick cell, for which the shortening of  $\tau_{min}$  starts for

$V_0 > 0.5V$ , well below the threshold. The curve then exhibits only a slight slope change over the threshold value. For very thick cells, as underlined in the previous section, the steepness of the phase transition has vanished. This is explained by the different strength imposed by the anchoring on the LC molecules, whether they are confined in a thin cell (in that case strong anchoring conditions dominate until  $V_{th}$ ) or in a thick one (inner molecules undergo weaker anchoring constraints and reorient themselves faster). Measuring  $\tau_{prec}$  is less precise, especially for thick cells. Indeed, the measurement for the thickest cell was even not possible (Figure 43c). Nevertheless, the precursor time has the same qualitative behavior than  $\tau_{min}$ .

The time scale of these values changes from hundreds of milliseconds to a few seconds, depending on the LC thickness. Figure 43b) (resp. Figure 43d) ) shows  $\tau_{min}$  (resp.  $\tau_{prec}$ ) as a function of the LC thickness for different values of  $V_0$ . Both the precursor delay and the time of maximal disorder depend quadratically on the thickness  $L$  of the nematic layer. Therefore, they both follow the characteristic switch-on time for LC displays (Yang, 2014). Those measurements indicate that the dynamical steps of the FT are all stretched with a quadratic dependence on  $L$  when increasing the LC-thickness. A recent study has confirmed the quadratic influence of the thickness for LC switch-on dynamic, identifying a thin-cell and thick-cell regime (Melnyk, Garbovskiy, Bueno-Baques, & Glushchenko, 2019). Over  $50\mu\text{m}$  of thickness, LC cells start to change their molecular reorientation dynamic, corroborating the results of this thesis.

### 3.4.5 LC tunable delay line based on switching-on addressing

From the study of the dynamical FT and the results presented in the previous sections,  $V_0$  has to be carefully determined in order to find the adequate balance between the FT-induced disorder losses and the reduction of the birefringence excursion due to a pre-ordered state ( $V_0 > V_{th}$ ). Nevertheless, with the switch-on dynamic the commutation time is reduced to a few seconds ( $< 5s$ ) even for thick-cell. Therefore, the characterization of the induced birefringence scan is now necessary.

The experimental set-up is schemed in Figure 34 (see section 3.1.2). The broadband spectral interferometry technique (FTSI) is used to measure the  $\Delta\tau_g$  and  $\Delta n_g$  induced during the switching-on. For all measurements, the thickest cell ( $L=180\ \mu\text{m}$ ) is used.

When no voltage is applied, the LC tilt angle  $\theta = 0^\circ$  and the birefringence is maximum, e.g.  $\Delta n_g = \Delta n_{g_{max}} = 0.23$  for E7 (Li, 2005). Just as in the previous experiments, a  $V_0 - 10V$  voltage step is applied to the cell at  $t = t_0$  ( $V_0 = 0V, 1V, 1.3V, 1.5V$ ). The spectral maps acquired during the dynamical switch-on following  $t_0$  are shown in Figure 44, while the retrieved temporal delay and birefringence as a function of acquisition time are displayed in Figure 45a). When  $V_0 = 0V$ , the FT is clearly visible on the spectral map and the disorder losses on the signal are so strong that it is not possible to follow the trend of the interference fringes. As a consequence, the Fourier analysis is not possible in this case (highlighted blue zone in Figure 45a) ). Only the initial and final  $\Delta n_g$  values can be measured, when the nematic order is restored. Conversely, when  $V_0$  is 1 V, 1.3 V and 1.5 V, the spectral fringes are distinctly visible, despite an overall loss of the contrast of the fringes.. A group delay of 170 fs can be finally introduced from  $V_0 = 1\ \text{V}$  in a few seconds. This is a remarkable step forward compared to the adiabatic process and the transient relaxation. The temporal shortening of the transition is also visible. The birefringence dynamics are, then, correctly retrieved and all the measurements converge correctly towards the same value (0.053), i.e.  $\Delta n_g$  for  $V = 10\ \text{V}$ . These results are in accordance with the conclusions of section 3.4.2 and section 3.4.3. For thick cells ( $180\ \mu\text{m}$  in this case) the FT is not steep, but there is a gradual decrease in disorder losses when increasing  $V_0$ .

Some oscillations of the group delay excursion are detected, as during the transient relaxation. The dumping in amplitude and frequency of the oscillations are recovered. Unlike the relaxation, the oscillations are stronger at the end of the commutation. Indeed, the reflectivity (resp. refractive index on the extraordinary axis) is larger (resp. smaller) when the molecules are

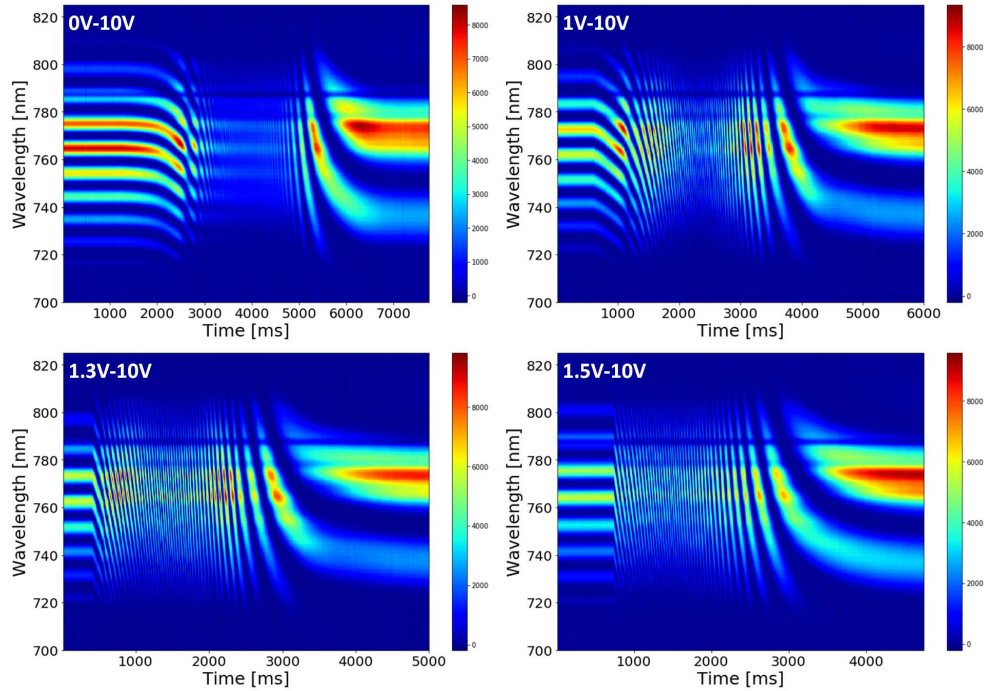


Figure 44: Dynamical spectral maps obtained by using the experimental setup shown in Figure 34b); data are acquired at  $t = t_0$  for different  $V_0$ -10 V voltage steps  $V_0 = (0 \text{ V}-1 \text{ V}-1.3 \text{ V}-1.5 \text{ V})$ .

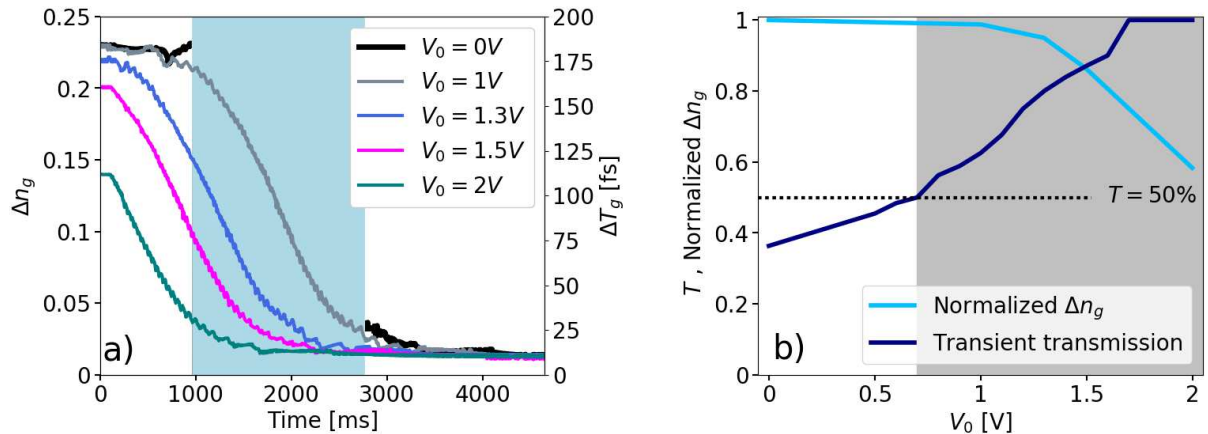


Figure 45: a)  $\Delta n_g$  and  $\Delta \tau_g$  plotted as a function of acquisition time for different  $V_0$  (0V, 1V, 1.3V, 1.5V); the blue area is associated to the  $V_0 = 0$  measurement and indicates that for this voltage step the Fourier Transform is not possible in this time interval. b) Comparison between  $\Delta n_g$  normalized and the transient transmission  $T$  as a function of  $V_0$  (the curve is extrapolated from the experimental data). In gray the condition of  $T = 50\%$ .

out of the rest position but parallel with the electric field. Therefore the oscillations are more intense when the molecules are almost completely reoriented. This is a further confirmation of the Fabry-Perot effect explained in the previous section.

In particular, the 1 – 10 V scan, although  $V_0 < V_{th}$ , provides a full birefringence excursion and an overall group delay tuning of 170 fs in less than 4 s. According to Figure 40b), the transient transmission is not lower than 60% on the extraordinary axis, making this configuration admissible for several applications. It should be noted that the applied bias voltage ( $V_0 = 1 \text{ V} < V_{th}$ ) enables to reduce the losses but not through a measurable pre-orientation of the inner molecules, as  $\Delta n_g(t_0) = \Delta n_{gmax}$ . This indicates a subtle change of the elasticity of the LC as a precursor state to the FT. Increasing  $V_0$  naturally decreases the FT-induced losses, but the  $\Delta n_g$  excursion is decreased as well, as shown in Figure 44b). This figure features the normalized

birefringence change and the transient transmission as a function of  $V_0$  for the 180  $\mu\text{m}$ -thick cell. It can help to find out the compromise between the optical transmission losses and the overall birefringence scan for any application.

### 3.4.6 Dynamical characterization of MLC2132

Up to now, the only mixture studied is E7, however, the same characterization can be performed for other LC mixtures. As discussed in chapter 2, MLC2132 is an interesting candidate to replace E7 due to the largest  $\Delta n$  that makes it favorable for tunable birefringence applications. Therefore, the switching-on dynamics, the Fréedericksz transition, and the transient transition can be all evaluated even for this new mixture.

The MLC2132 birefringence excursion is analysed using the first experimental set-up ( Figure 34a ). In Figure 46a) the group delay is plotted as function of time for the two mixtures using 180 $\mu\text{m}$  thick-cells. The starting voltage is below the FT for both mixtures ( $V_0 = 1 \text{ V}$ ), while the final voltage is 10 V. The relative group index excursions ( $\Delta n_g$ ) are plotted. MLC2132 introduces a larger group delay (185  $fs$ ) compared to E7 (155  $fs$ ) when the molecules are in their own rest position ( $t = 0$ ) because of the higher birefringence. This different delay is in agreement with the refractive indices difference measured in the previous sections (MLC2132  $\sim 1.2$  higher). Applying the external electric field, the commutation starts for both cells, however MLC2132 requires almost double time to complete the molecular reorientation (8 s). Therefore, the viscous-elastic forces require more time to reach the ordered nematic state (see Chapter 1). This could be a way to measure the Leslie coefficient ( $\gamma_1$ ) in the future, because as already mentioned,  $\tau_{on}$  depends on the difference ( $E - E_c$ ) and, as consequence, on this coefficient.

Afterward, the Fréedericksz voltage threshold of the new mixture is retrieved through the second experimental set-up ( Figure 34b ). Using a thin cell (25  $\mu\text{m}$ ), a large step-like growth of the transient transmission is measured around  $V_0=1.8 \text{ V}$ . Therefore, this value can be considered as the Fréedericksz transition voltage for MLC2132.

Nevertheless, the same measurements are performed on the thicker-cell (180 $\mu\text{m}$ ), in order to verify the rounding of the transition even for MLC-2132. As for E7, a continuous increase of the transient transmission is measured even below the threshold.

## 3.5 Conclusions & Prospectives

To conclude, the different electrical driving strategies are presented with their own merits and drawbacks.

The adiabatic way can introduce and control a group delay of 100fs. However, the really slow response in time of thick cells requires several hours to perform just one scan. In the same way, transient relaxation speeds up the molecular reorientation dynamic, but more than 2 minutes are still too much and back-reflections affect the signal. Finally, the switching-on strategy is preferred, even if the presence of a starting voltage threshold reduces the birefringence excursion. Indeed, the Fréedericksz transition is studied for different LC thicknesses and the behavior of really thick cells ( $> 75 \mu\text{m}$ ) is observed for the first time from this point of view. The transient transmission is defined to quantify these losses. By contrast to the common step-like function of thin cells, the thicker ones show a rounding of the transition. Therefore, thick cells can be used even below the voltage threshold with an overall group delay tuning of 170  $fs$  in less than 4  $sec$ . A comparison with the new LC mixture (MLC2132) is also performed. The phase shift is confirmed 1.2 times larger compared to E7 starting from the same voltage, however, the commutation time is doubled due to the different nature of the mixture. This is a remarkable step forward, when compared with the previous strategies, and it paves the way to develop LC-base ultrafast instrumentations. The table 11 summarizes the results of the chapter.

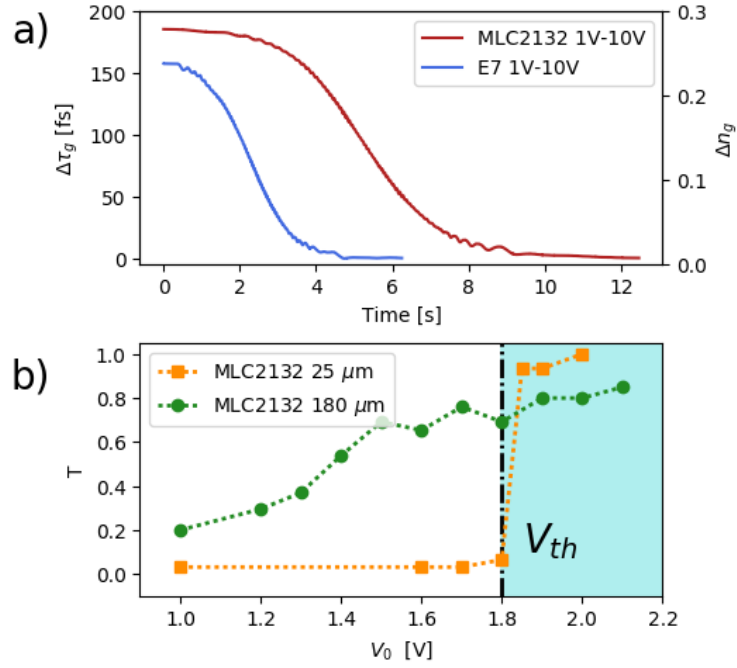


Figure 46: a) Retrieved group delay as a function of time for E7 (blue curve) and MLC (red curve) using  $180\mu\text{m}$ . Starting voltage is 1V and final one is 10V. b) Transient transition ( $T$ ) as function of the starting voltage  $V_0$  for a thin- $25\mu\text{m}$  (orange curve) and thick- $180\mu\text{m}$  MLC2132-based cells.

180 $\mu\text{m}$ thick-cell	$\Delta n/\Delta n_{max}$	$\Delta t(\text{acq.})$	$\delta t$
Adiabatic	1	hours	1 – 0.1 fs
Relaxation switching-off	1	Minutes	0.3 – 0.1 fs
dynamic switching-on	0.5-1	seconds	0.6 – 0.8 fs

Table 11: Summary table of the birefringence excursions, evolution time and temporal resolutions for the three different voltage strategies for a  $180\mu\text{m}$  thick-cell based on E7 mixture.

## Chapter 4

# Thermo-optically-induced spatial phase-shift in electrically-driven nematic Liquid-Crystal cells

### Objective

In this chapter, the possibility to use electro-optic LC-cells in near-IR range ( $\lambda_0 = 1.55\mu\text{m}$ ) is investigated involving yet-IT-optimized electrodes (optimized-ITO). However, above a given power threshold, residual light absorption in the ITO layer is able to generate a thermal gradient that induces spatial phase modulation with a ring-pattern typical of thin non-linear media. The generated patterns are analyzed in order to study the internal birefringence excursion and the established thermal gradient, up to the nematic-to-isotropic phase transition.

## 4.1 Electro-optical applications of LC in the IR spectral range

### 4.1.1 Motivations

Most of the ultrafast measurement techniques require, among others, control of the group delay (FROG (Trebino, 2012)) or group delay dispersion (dispersive scan (Miranda et al., 2012)). Both of them can be achieved by thick, electrically-driven LC cells, as described in the previous chapters. In this way, mechanical actions are not anymore necessary, with a significant economic impact and a easier collinear single beam setup configuration. A greater interest could be contemplated if those applications would be demonstrated in the IR spectral range. In this sense, the broadband spectral transparency of the LC molecules is interesting (I. Khoo, 1995). As already mentioned in Chapter 1, E7 shows a large spectral anisotropy and transmission for a bandwidth of more than 2000 nm. Thus, this mixture is suitable for those kinds of purposes. Therefore, in principle, ultrafast tunable delay line based on E7 mixture can be developed in the near-infrared spectral range.

### 4.1.2 Background

The LC-based devices with electrical control are still strongly affected by the spectral transmission of the conductor. In particular, most of the commercial electrodes used in LC cells present some limitations in the IR and NIR spectral ranges. ITO (Indium-Thin-Oxide) represents the best compromise between price, conductivity, and transparency in the visible spectral range and for those reasons it is widely used. However, standard ITO exhibits strong absorption and non-linear behavior around  $1.55 \mu\text{m}$  (Alam, De Leon, & Boyd, 2016). Although some optimized versions of ITO are available in this spectral range (Figure 47) with a remaining weak absorption that might have a significant impact on the LC optical response.

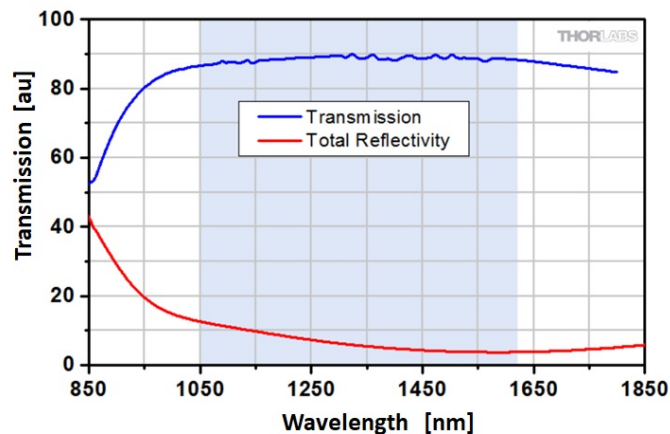


Figure 47: ITO spectral transmission and reflectivity for optimized-AR-ITO layer (Image from Thorlabs).

Indeed, some theoretical studies about the interaction between a femtosecond laser and an ITO based LC-cell employed for optical beam steering have already been published (He et al., 2017). These simulations consider a KHz laser with  $10 \text{ W/cm}^2$  average power density and 5% of absorption in the ITO layer. This configuration heats up the LC layer and induces a phase shift through thermal lensing. The performed simulations show a well-confined thermal gradient due to the large difference between the heat transfer coefficients of the three cell components (BK7, ITO, and E7). Moreover, a linear increase of the temperature with the laser intensity is demon-

strated up to 80 K.

### 4.1.3 Introduction

In this chapter, it is demonstrated that even IR-optimized ITO layer cannot be used if the laser flux is higher than  $5 \text{ W/cm}^2$  at  $1.5 \mu\text{m}$ . Indeed, the laser absorption induces the LC layer heating and then birefringence excursion of the LC refractive indices. Polarization-dependent ring-patterns, typical of spatial self-phase modulation (SPM) in thin media, are analyzed. Spectral, spatial and temporal analysis is then performed demonstrating that a thermal equilibrium is reached and so the inner thermal gradient is stable in time and spatially well-confined. So, from the measured phase shift, the liquid crystal birefringence excursion is retrieved and the inner temperature is estimated. Finally, increasing the input flux the nematic-isotropic phase transition is reached and the whole E7 birefringence excursion ( $\Delta n = 0.23$ ) is performed. This effect was fortuitously discovered during the investigations to develop a LC-based ultrafast delay line in the NIR spectral range. It greatly influenced the rest of the thesis.

## 4.2 Experimental evidence of absorption in the ITO

### 4.2.1 Experimental set-up

For the experiment,  $180 \mu\text{m}$  of nematic mixture E7 is inserted between two ITO thin layers optimized for the spectral range 1050-1650 nm (Figure 48). The 5mm BK7 substrates present an AR coating in order to fabricate a transparent cell to infrared light. Although the first goal was to study electro-optical applications of such a cell, no voltage is applied for all the following experiments.

The employed source is a fiber-based femtosecond oscillator (TOPTICA) delivering 40 fs pulses train at 80 MHz and average power of 150 mW. The spectrum is centred at  $\lambda_0 = 1.55 \mu\text{m}$  and the spectral bandwidth is 200nm ( $1/e^2$  width). A typical spectrum is shown Figure 48 with the experimental set-up. The collimated femtosecond laser, with tunable linear polarization, propagates through the cell. In order to detect the spatial deformation, an iris is then used to select the central part of the beam after  $> 10 \text{ cm}$  of laser propagation. The transmission is then measured by a photodiode.

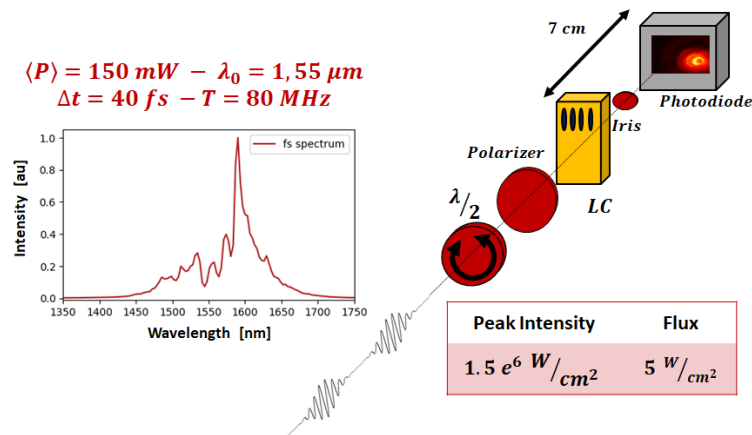


Figure 48: A half-wave plate and a polarizer set the laser polarization and pulse energy. The laser is collimated and an iris selects the central part of the beam after propagation in the LC cell. In the inset the laser spectrum is plotted.



### 4.2.2 Temporal dynamics

When the pulse, polarized on the extraordinary axis (E.A.), propagates through the ITO-coated LC-cell, beam depletion occurs after some propagation ( $> 10$  cm), as shown in Figure 49a). The experimental arrangement described in the previous section enables to monitor the temporal features of this depletion (Figure 48). The transmitted signal decreases in a few hundreds of milliseconds (Figure 49b): the time scale of the process suggests a thermal effect. To rule out intensity-dependent non-linear effects, the laser pulse duration is changed by adding more than  $\pm 1500$  fs (i.e. roughly a factor of 4 on the pulse duration) and no noteworthy variation with respect to the original signal is detected. This demonstrates that the generated effect depends only on the laser flux rather than the peak intensity: hence, non-linear processes induced by the laser electric field are excluded. At first, the same measurement performed on another LC-cell with the same thickness but no ITO layer shows a constant transmitted signal in time whatever the laser polarization (Figure 49b). This proves the significant role of the electrode on the process and rules out pure laser-induced molecular reorientation. The remaining explanation resides in light absorption in both ITO layers creating a thermal index gradient in the LC cell. The full absorption of the LC cell is then measured: more of the 75% (89% per window, as provided by the furnisher) of the signal is transmitted. Increasing the incoming flux results in a faster exponential decay of the transmission, with a linear dependence, as shown in Figure 49c), which is an additional indication of the absorption-induced thermal nature of the effect.

When the laser beam is polarized along the ordinary axis (O.A.), almost no change of the

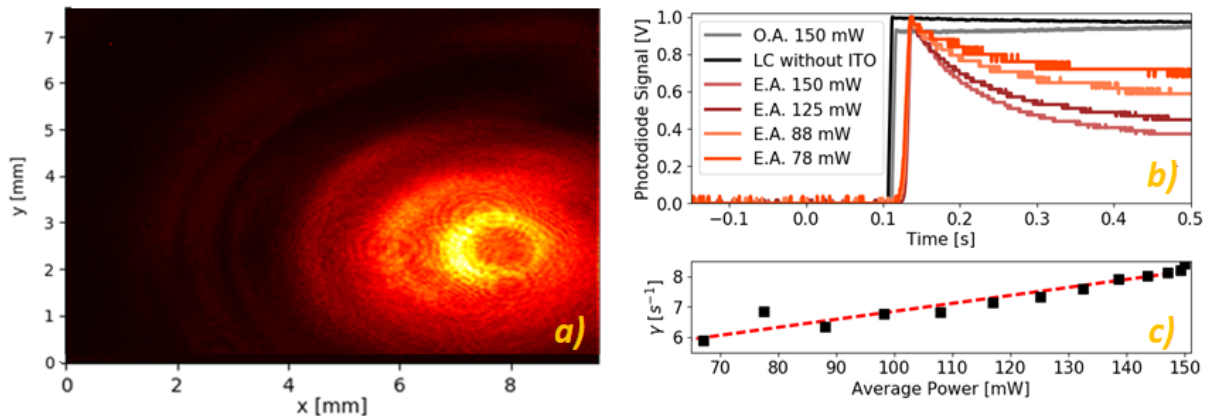


Figure 49: a) Transmitted beam profile after  $> 10$  cm of propagation for an average input power of  $5\text{ W/cm}^2$ . b) Signal transmitted through a central iris in different configurations (O.A. = ordinary axis, E.A. = extraordinary axis, see text). c) Characteristic decay rate  $\gamma$  ( $\text{s}^{-1}$ ) of an exponential fit of the signal decreases as a function of laser average power. The dashed line indicates a linear fit.

transmission is detected even at the maximum flux.

Finally, the current experimental conditions (e.g.  $5\text{ W/cm}^2$ ) can be estimated as the threshold of the studied thermally-induced non-linear effects.

## 4.3 Thermo-optically induced self spatial phase modulation

### 4.3.1 Principle of thermo-optically induced phase shift

Excluding peak intensity related non-linear effects, the only explanation that can reproduce this effect resides in thermo-optical phase modulation. In more detail, the femtosecond laser drives a change of the refractive index of the LC through temperature rising because of absorption in the ITO layer. Indeed, the thermal conductivity of the LC is two orders of magnitude lower than the electrode and one order of magnitude lower than the glass (He et al., 2017) (see Table 12), thus the heat remains confined in the LC, enabling the establishment of a thermal gradient.

Large sensitivity of the thermotropic LC with temperature, as studied in chapter 2, generates the observed refractive index changes. The spatial distribution is Gaussian, then the refractive index changes are expected to follow this spatial variation. The phase-shift depends on the LC thickness, thus here strong dephasing is expected. Nevertheless, similar results were obtained with a  $50 \mu\text{m}$ , with a lower overall dephasing.

Layer	Transfer Coefficient
<i>E7</i>	$0.13 \text{ W/mK}$
<i>BK7</i>	$1.11 \text{ W/mK}$
<i>ITO</i>	$11 \text{ W/mK}$

Table 12: Heat transfer coefficient for the different layers constituting the LC-cell (BK7, ITO, E7).

### 4.3.2 Enhancement of the thermal effect

The collimated set-up of the previous section produced a limited phase-shift on the extraordinary, and no detectable change on the ordinary axis. In order to enhance the phase shift, the laser is focused ( $d = 2 \text{ mm}$ ,  $f = 40 \text{ mm}$ ) into the LC, reaching a maximum flux of  $7 \text{ kW/cm}^2$ . The experimental arrangement is then changed as shown in Figure 50. The LC cell is placed on a translation stage and a camera replaces the photodiode acquiring the spatial beam profiles after  $11 \text{ cm}$  of propagation.

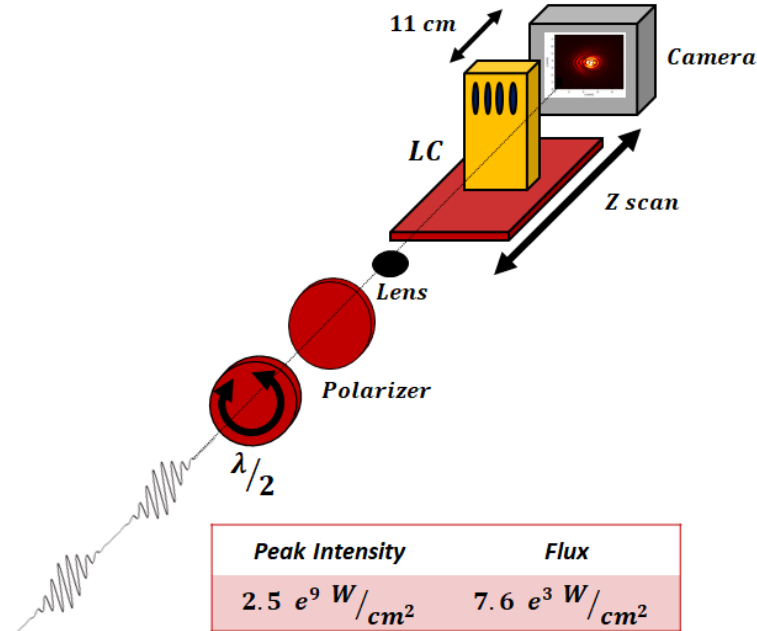


Figure 50: The laser is focused onto the LC cell and the beam profile is acquired after propagation (Goldeye ALLIED vision P-008 SWIR). Maximum peak intensity is  $2.5e^9 \text{ W/cm}^2$  while the maximum average flux is  $7.6e^3 \text{ W/cm}^2$

The effect is now significantly stronger and a pattern of multiple concentric rings is observed. A central hot-spot when the laser is polarized along the nematic director or, conversely, a black spot when the laser is polarized along the ordinary axis is observed (Figure 51 a), b). This

pattern is typical of spatial self-phase modulation (SPM) in thin media when the dephasing across the beam profile is larger than  $2\pi$  (Gaussian case (Ramirez, Carrasco, Otero, Cerda, & Castillo, 2010)). SPM refers to the spatial phase-shift accumulated when a laser-beam with a Gaussian transverse distribution illuminates a thin non-linear medium. When the overall phase is larger than  $2\pi$ , for a given spatial coordinate undergoing a phase-shift  $\varphi_1$ , there is another coordinate with a phase-shift  $\varphi_2 = \varphi_1 + k\pi$  ( $k = \text{integer}$ ), giving rise to constructive or destructive interferences in the far-field. Given the cylindrical symmetry of the laser beam, concentric rings are there observed.

Thin layers of liquid crystals (LC) are particularly suited to induce such effects ((Choon Khoo, 2009)) and multiple-ring patterns are reported in numerous studies (I. Khoo et al., 1987)-(De Luca, Nersisyan, & Umeton, 2003). The process can be instantaneous Kerr-effect (Kerr, 1875), photoinduced in a biased nonlinear photorefractive crystal (Boughdad, Eloy, Mortessagne, Bellec, & Michel, 2019), but also due to field-induced molecular orientation with high-power cw-laser in homeotropic cells (Durbin, Arakelian, & Shen, 1981) or dye-doped LC to enhance the non-linearity (Ara, Bahramian, Mousavi, & Abolhasani, 2009; Ono, Igarashi, & Harato, 1998).

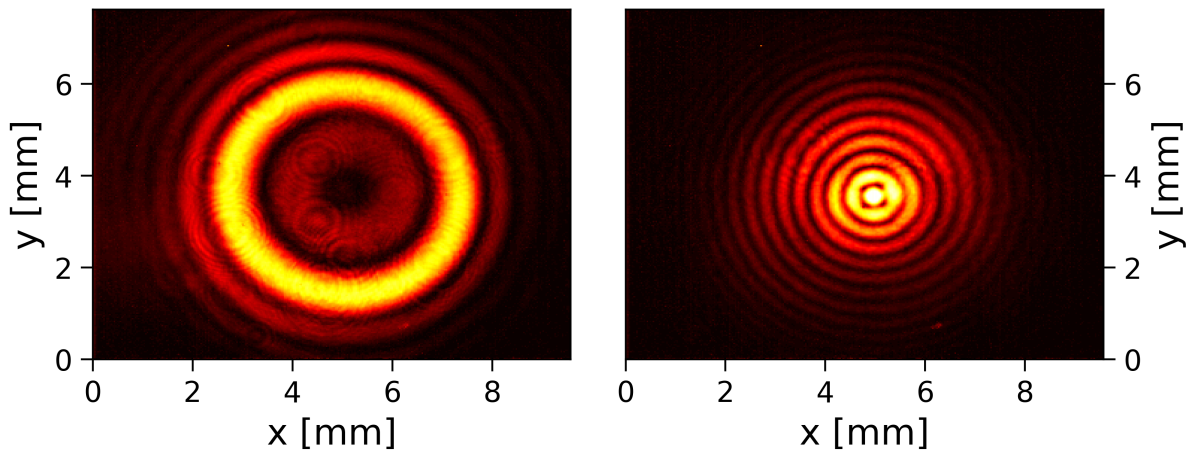


Figure 51: Typical multiple-ring pattern when the laser is polarized along the LC ordinary axis in a) and along the extraordinary axis in b).

### 4.3.3 Numerical simulations

In order to reproduce the phenomenon, some laser propagation simulations are performed using the MIRO software (Morice, 2003). This well-known simulation code allows solving equations governing the propagation of broadband laser pulses. The modulation phase is the selected calculation mode from the MIRO library. The spatial-temporal frame is set considering a temporal window of 300 fs composed by 64 distinct points and a spatial grid of 128x128 points (the full size of 6 mm).

The thermal defect is considered as a static, local phase variation of a thin medium featuring the LC, encountered during propagation. The radial phase variation  $\Delta\varphi(r)$  in this medium plane is defined following Ramirez's model (Ramirez et al., 2010), who has proposed a complete numerical study of spatial self-phase modulation in thin non-local and non-linear media:

$$\Delta\varphi(r) \approx \Delta\varphi_0 e^{-mr^2/w^2} \quad (4.1)$$

where  $r$  is the radial coordinate,  $w$  laser beam width,  $\Delta\varphi_0$  the maximum on axis phase shift and  $m$  is the non-locality, e.g. the difference between the phase defect (here the thermal gradient) and laser beam width. For  $m < 2$  the non-linear phase change extends beyond the incident intensity distribution, while for  $m > 2$  it is narrower. In the presented simulations, the  $m$  is

taken equal to 2, e.g. it follows the laser intensity distribution as intuited by previous studied thermally-induced non-linear effects (Callen, Huth, & Pantell, 1967; Dabby, Gustafson, Whinnery, Kohanzadeh, & Kelley, 1970; Harrison, Dambly, Yu, & Lu, 1997). A collimated Gaussian beam of 2 mm (FWHM) is simulated to pass through a LC-cell introducing  $\pm 10rad$  arbitrarily chosen as maximum phase shift. Figure 52 shows the spatial profile after 40cm of propagation as a function of the sign of the phase-shift: a black (resp. bright) spot surrounded by rings with a positive refractive index variation (resp. negative). The simulations are found in good agreement with the experimental data. In particular, different patterns observed in Figure 52 for the two polarization directions come from the different signs of the thermally-induced index variation (negative for extraordinary polarization, positive for ordinary polarization).

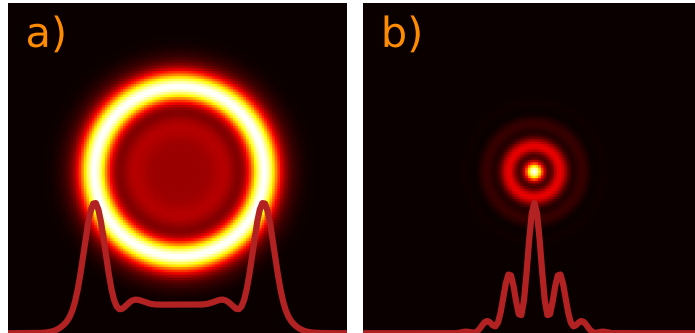


Figure 52: MIRO simulations of the spatial profile after long propagation induced by a Gaussian pulse encountering a phase change with the same spatial extension: a) positive phase shift ( $+10rad$ ) and b) negative phase shift ( $-10rad$ ).

#### 4.3.4 Analysis

##### Thermal equilibrium

The induced phase-shift evolution is characterized in order to verify the stability of the thermal gradient inside the LC-cell and to check if an equilibrium is reached (Figure 53a)). Several images are acquired for a given rings number  $N$  ( $N = 15$  rings) and, over more than one hour, the number and spatial position of the rings keep constant. In a given observation plane, the ring size is found constant ( $250 \mu m$  in this case) and no variation of the spatial dephasing is measured within the resolution of the camera ( $30 \mu m$ ), e.g. the stability is estimated better than  $\pi/5$  for a maximum phase shift of  $30\pi$  (Figure 53b) ) (Durbin et al., 1981). Therefore the refractive index variation is temporally stable, the thermal equilibrium is verified and the thermal gradient is well-confined.

##### Spectral analysis

The spectrum of each ring is also analyzed (Figure 53c) ). As a matter of fact, the spectral distribution of each ring is found constant and unchanged with respect to the original laser spectrum (last figure on the right). This is original compared with the usual spatial non-linear phenomena achieved with femtosecond pulses, where the longer non-linear length thus generates strong self-focusing or defocusing, preventing to acquire such high spatial phase shift without beam collapse.

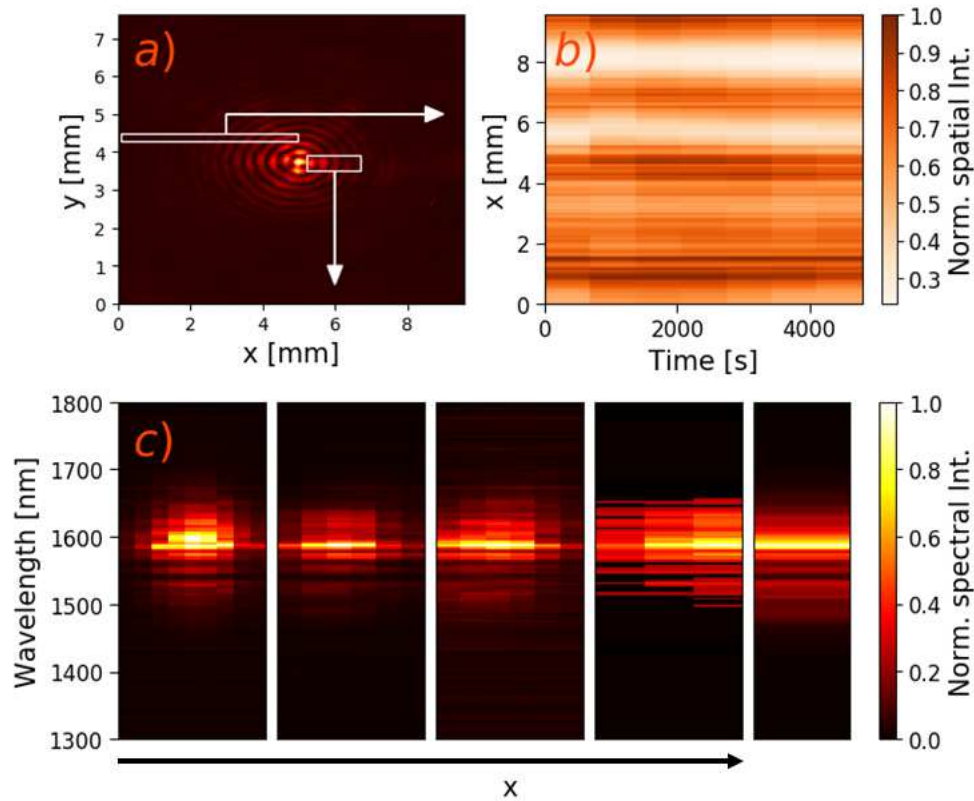


Figure 53: a) Acquired multiple-ring pattern (laser polarized along EA). b) Horizontal spatial distribution as a function of time for a pattern composed by 15 rings. c) Horizontal spectral distribution. Each sub-plot is related to one-ring. The last image on the right represents to reference laser spectrum.

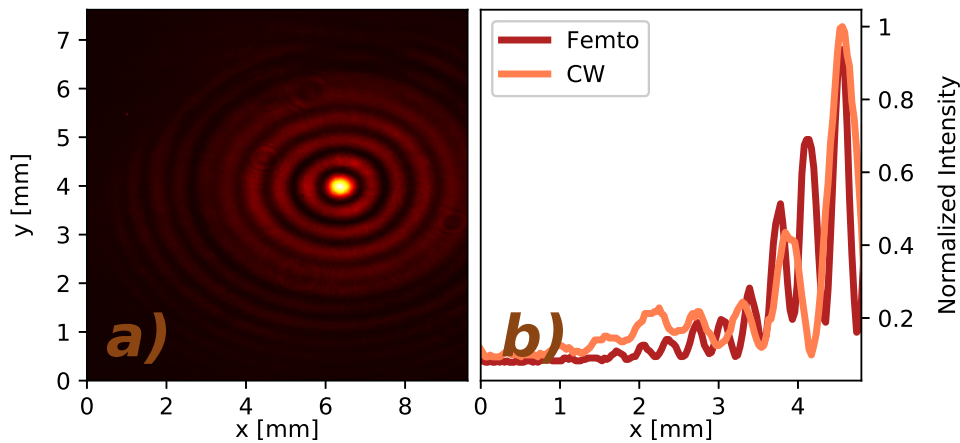


Figure 54: a) Typical multiple-ring pattern on the extraordinary axis induced by a cw laser. Normalized intensity horizontal profiles (for  $N \sim 10$ ) for the femtosecond laser (dark red curve) and cw laser (orange curve).

### Thermo-optically induced SPM from other laser sources

The results have been also reproduced with a cw laser of 60  $mW$  at  $\lambda_0 = 1.5 \mu m$  focused into the LC-cell. The thermal gradient is established again and several rings appear, but for the same number of rings (e.g. similar thermal gradient) the pitch and overall shape appear to be slightly different and in the CW case the beam profile is closer to a Bessel function (Figure 54b) ). This is attributed to the broad spectrum of the femtosecond pulses, that blurs slightly the interference pattern. The same experiment is performed also with a 100  $mW$  femtosecond oscillator with

$\lambda_0 = 1.06 \mu m$  in order to verify the contribution of other wavelengths to the effect. Self-phase modulation is generated as well, but for the same average power the number of generated rings is smaller, e.g. phase shift is lower. The explanation resides in the spectral dependence of the ITO absorption (Alam et al., 2016), far from the central wavelength  $\lambda_0 = 1.55 \mu m$ , the ITO absorbs less, so a smaller thermal gradient is established.

#### 4.3.5 Driving the LC to the isotropic phase transition

In this section, images are acquired while increasing the input flux (Figure 49b) ), rotating the half-wave plate to change the power (P-scan) and moving the cell with the respect to the focus (z-scan) with a maximum value of  $7 kW/cm^2$ .

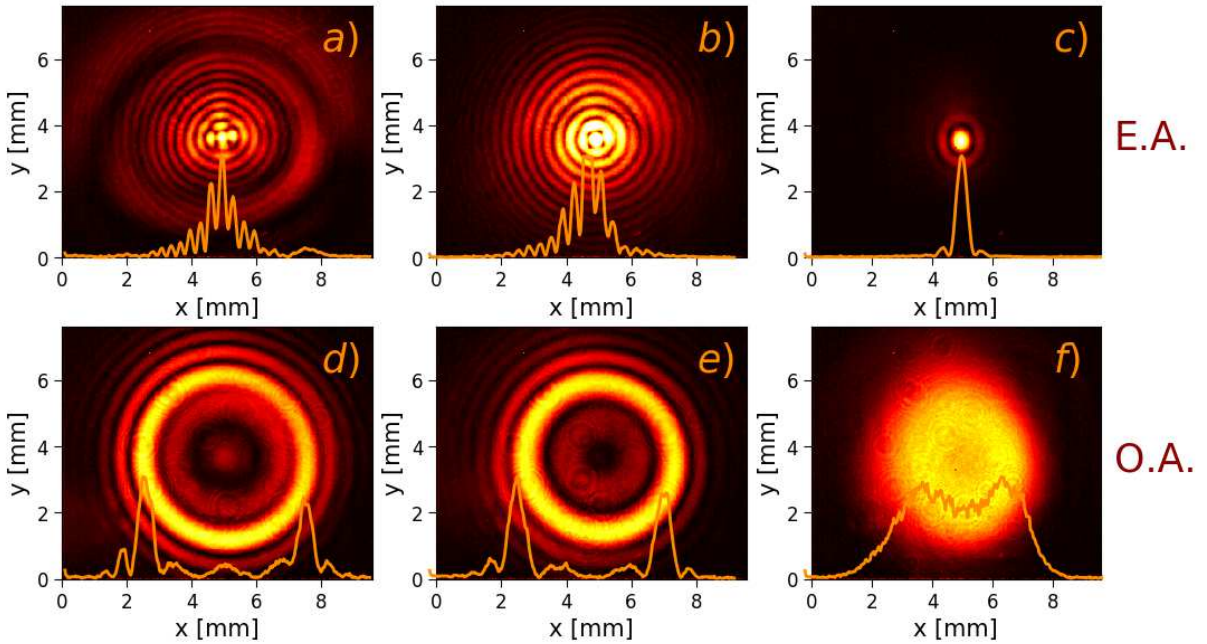


Figure 55: Ring pattern formation. First line: the laser is extraordinary polarized ( $a= 150mW$ ,  $b= 132mW$ ,  $c= 108mW$ ). Second line: the laser is ordinary polarized ( $d= 150mW$ ,  $e= 143mW$ ,  $f= 108mW$ ).

Some typical images are shown in Figure 55 for both extraordinary ( $a, b, c$ ) and ordinary ( $d, e, f$ ) polarization directions. As suggested by (Ramirez et al., 2010), increasing the intensity the number of the rings around the central hot spot increases when the laser is polarized along with the nematic director. Conversely, on the ordinary axis, the black spot remains, while the first ring intensity increases and, at the same time, more rings appear around it.

Polarization state and intensity are not the only parameters that play a crucial role in the ring-pattern generation: as deeply studied in (Ramirez et al., 2010), also the radius of the laser curvature and the non-locality of the induced phase will influence the spatial pattern according to these simulations. The position of the LC cell, with the respect to the focus, determinates the constant presence of a black (resp. bright) central spot on the ordinary axis (resp. extraordinary), while the non-locality ( $m$  factor in eq.4.1) changes the ring-pattern global shape and only weakly affects the number of the generated rings.

In particular, an ambiguity of  $\pm 1$  ring is found between the local and non-local case ( $m = 2$  and  $m = 1$ ) when the phase shift is larger  $> 12\pi$  (Ramirez et al., 2010).

During the P-scan, the radius of curvature is kept constant, therefore the non-locality can be estimated comparing the patterns of the performed experiments with Ramirez's simulations. After this qualitative comparison, the considered phase variation can be related to  $m < 2$ , hence a thermal gradient extending slightly beyond the laser spot. This is intuitively in agreement

#### 4. A thermo-optically induced spatial phase shift

with the expectations about the thermal nature of the effect and with measurements done in the next section (4.3.6).

Therefore, to quantify the inner thermal gradient, the following assumption is used:

$$N \simeq \frac{\Delta\varphi}{2\pi} = \frac{\Delta n L}{\lambda}. \quad (4.2)$$

Figure 56 represents the measured refractive index variation, deduced from the number of rings, as a function of the average power (the cell is slightly out-focus) (a) and as a function of the position with respect to the focus, for the maximum power (b). The two cases of an extraordinary ( $n_e$ ) and ordinary ( $n_o$ ) polarized laser beam are considered, while the error bars come from uncertainty of  $\pm 1$  ring for each measurement.

As expected from the thermotropic character of the LC birefringence, the average power excursion shows a constant and nonlinear decrease (resp. increase) of  $n_e$  (resp.  $n_o$ ) (I. Khoo, 1995). The z-scan confirms this trend until the extraordinary and ordinary axis are no longer distinguishable: the laser power density is high enough to approach the phase transition ( $331K$ ) around the focus. Experimentally the phase transition is visualized as background blurring and fluctuations in the center of the ring pattern. The beam waist evolution is plotted as well in b) in order to picture the beam size changes together with the index evolution.

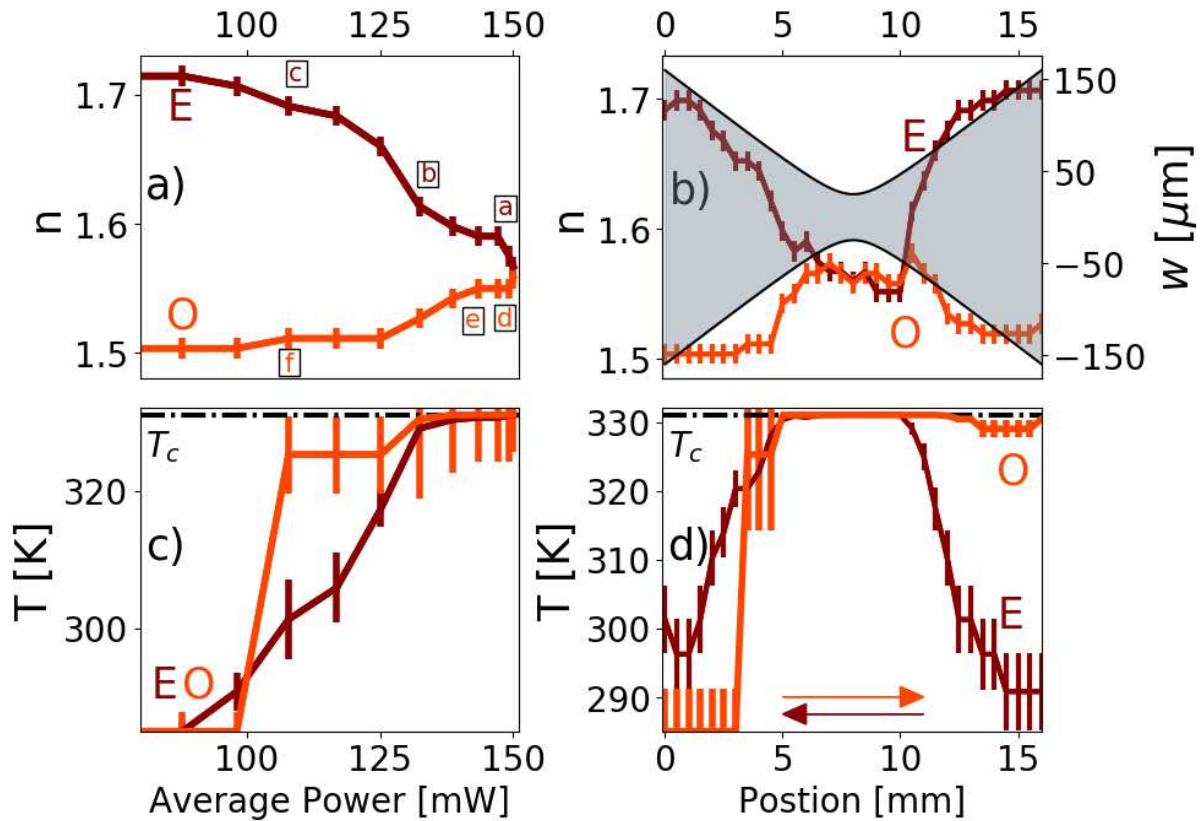


Figure 56: Refractive index  $n$  variation as a function of the average power and the position around the focus (a, b respectively). The red (resp. orange) line refers to an extraordinary (resp. ordinary) laser polarization direction. In a), the labels refer to Figure 55. The beam as a function of  $z$  appears in gray in panel b). In c), d) are plotted the maximum LC temperature  $T$  as function of the average power (c) and the position (d), deduced from a) and b) (see text). Again, the red (resp. orange) line refers to an extraordinary (resp. ordinary) laser polarization direction. Critical temperature ( $T_c = 331K$ ) is indicated. Arrows show the z-scan direction.

Following the extensive work of Li and coauthors, who have characterized E7 thermotropy for several spectral ranges including near-infrared ( $\lambda_0 = 1.5\mu\text{m}$ ), it is possible to recover  $\Delta T$ , the

LC temperature elevation across the laser spot, from  $\Delta n$ . Considering the two laser polarization directions, the refractive index evolution is written as (see chapter 2):

$$n_e(T) = A - BT + \frac{2\Delta n_0}{3} \left(1 - \frac{T}{T_c}\right)^\beta \quad (4.3)$$

$$n_o(T) = A - BT - \frac{\Delta n_0}{3} \left(1 - \frac{T}{T_c}\right)^\beta \quad (4.4)$$

where  $A = 1.723$ ,  $B = 5.24 \cdot 10^{-4}$ ,  $T_c = 331$ ,  $\beta = 0.2542$ ,  $\Delta n_0 = 0.3768$  (constants for E7 liquid crystal mixture) (Li, 2005). Thermal gradient  $\Delta T$  is calculated, considering an initial temperature of 285 K. The maximum temperature  $T_o$  (resp.  $T_e$ ) then refers to the laser polarized along the ordinary (resp. extraordinary) axis and it is plotted in Figure 56 c), d). Strong non-linearity of the index evolution affects the error bars when approaching  $T_c$ .

In the P-scan (Figure 56 c) ), a difference between the temperature of the two polarization states is visible, indeed for a given fluency,  $T_o > T_e$  due to the anisotropy of the thermal conductivity coefficients. According to (Mercuri, Marinelli, Zammit, & Scudieri, 1998; I. C. Khoo, 2014), this coefficient is nearly two times lower in the ordinary direction, confining even more the transferred heat. It can be further noticed that, although the index variation is strongly non-linear, the temperature  $T_e$  increases linearly with the power, before reaching saturation close to the transition. For the lower thermal gradients, this linear dependence was predicted in (He et al., 2017).

The Z-scan temperature evolution (Figure 56d) ) is not symmetric around the focus, because of the scan acquisition direction (opposite for both polarization directions). Just after getting close to the transition, recovery time of the LC molecules is considerably increased and the initial order parameter, e.g. molecular orientation, is finally recovered after a few minutes.

### 4.3.6 Estimation of the thermal gradient spatial extension

Within the context of beam shaping, it is important to estimate the spatial extension of the thermal gradient. The presented experiments tend to suggest that the non-linear effect, although thermally-induced, can be considered nearly localized to the laser size. The measured stability with a focused beam, the changes observed around the 50  $\mu\text{m}$  focal spot during z-scan (Figure 56b) ), the theoretical predictions of (He et al., 2017), where the gradient does not extend beyond the finite laser dimension, all tend to point toward a spatial extension of around 100  $\mu\text{m}$ .

In addition, a self-diffraction experiment in a two-wave configuration is performed, using a 0.5 W, continuous laser at  $\lambda_0 = 1.06 \mu\text{m}$  (Figure 57a) ). The principle is the following:

lateral shearing interferometry is applied to the laser, so as to produce spatial interferences in the LC plane with tunable fringes period. This spatial pattern induces a periodic modulation of the index, following the investigated thermal effect. The induced grating then generates self-diffraction with an efficiency depending on the index modulation depth.

Here, the goal is to determine the smallest fringe period giving rise to self-diffraction. The period is progressively decreased meanwhile the occurrence of a self-diffracted beam is monitored. With a grating period of 140  $\mu\text{m}$  (Figure 57b) ) self diffraction generated beams are still detected and indicated with arrows in (Figure 57c) and d) ). Therefore a spatial modulation of 140  $\mu\text{m}$  gives rise to a still detectable index modulation, which then provides an estimation of the process spatial extension. The estimated spatial resolution is here smaller than LC thickness (180  $\mu\text{m}$ ). This value is also expected to be enhanced for a thinner LC cell and establishes an upper threshold for the actual spatial resolution at the optimum wavelength ( $\lambda_0 = 1.55 \mu\text{m}$ ).



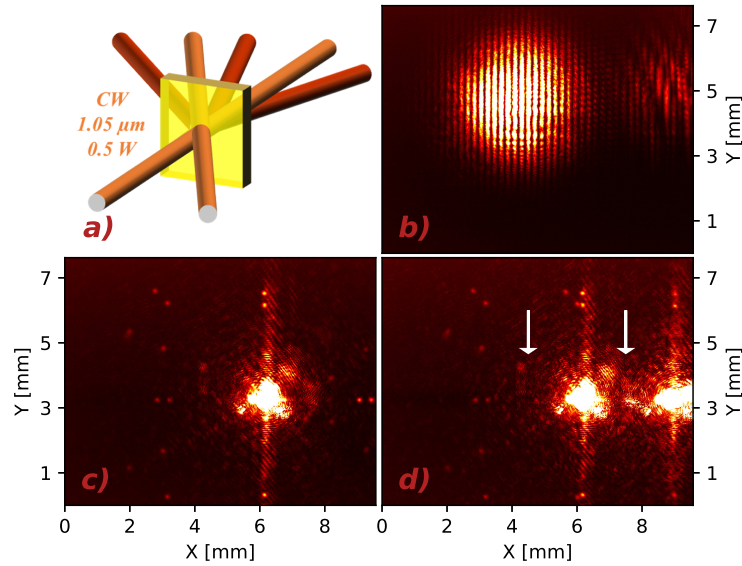


Figure 57: a) Experimental Set-up: self-diffraction experiment in a two-wave configuration with a 500 *mW* cw laser at ( $\lambda_0 = 1.06 \mu\text{m}$ ): red beams are the diffracted beams. b) Image of the fringes with a period of  $140 \mu\text{m}$ . c) The spatial pattern when blocking one beam: the image is taken as reference. d) Diffraction pattern when the two beams interfere onto the LC: the generated diffracted beams are highlighted by arrows.

#### 4.4 Conclusions & Prospectives

In this chapter, it is demonstrated that electro-optical applications of LC cell based on IR-optimized ITO are still limited in the NIR spectral range, because of the residual absorption.  $5 \text{ W/cm}^2$  is the flux threshold for applications and for the tested optimized ITO layer at  $\lambda_0 = 1.55 \mu\text{m}$ .

The characterization of this thermo-optically induced birefringence is presented. Above that threshold, temperature rising of the LC layer occurs, the refractive index variation is stable in time and therefore a thermal equilibrium is reached with a well-confined thermal gradient, up to the transition corresponding to a phase shift  $> 100 \text{ rad}$  for  $7 \text{ kW/cm}^2$ .

The common spatial non-linear effects achieved with femtosecond lasers always generate self-focusing (or defocusing) and therefore precludes high spatial phase shifts. Here, the thickness of the non-linear medium avoids any beam collapse and therefore represents a novel insight for ultrashort optical pulses.

The obtained results confirm the previous and theoretical studies showing a non-linear decrease (resp. increase) on the extraordinary axis (resp. ordinary) without any permanent damage during and after the phase transition of the LC molecules (331 K). Therefore, the temperature excursion is studied as well up to a maximum of 40K (limited by the phase transition), with a not-negligible spatial anisotropy due to the different magnitude of the heat transfer coefficient. However, this study suffers from some approximations. The phase shift calculation considering only the number of rings is a valid approximation, according to the bibliography, but it suffers from some uncertainties. Thus, further analysis still has to be performed, among the others a proper wavefront measurement to better describe the thermal gradient spatial profile. Moreover, a good modelization of the ITO absorption has still to be performed.

The study demonstrates that at the state of art, it is not possible to develop temporal measurements with a working flux  $> 5 \text{ W/cm}^2$ , with electro-optic LC-cell. However, in chapter 2 it has been demonstrated that a temperature control can be an alternative to voltage control to tune the birefringence of the thick LC cell. This is summarized again in the Figure 58, showing that equal GDD excursion can be achieved with the application of a dynamic voltage step or

by turning off the oven after LC heating of the LC cell. Nevertheless, overall and slow heating of the cell in an oven limits a bit the applications. Then, the thermo-optically induced effect in absorbing layers described here opens some new LC-cell addressing possibilities. Among them, spatial shaping, beam measurement and spatio-temporal shaping of femtosecond pulses can be contemplated. This is the subject of the next chapter.

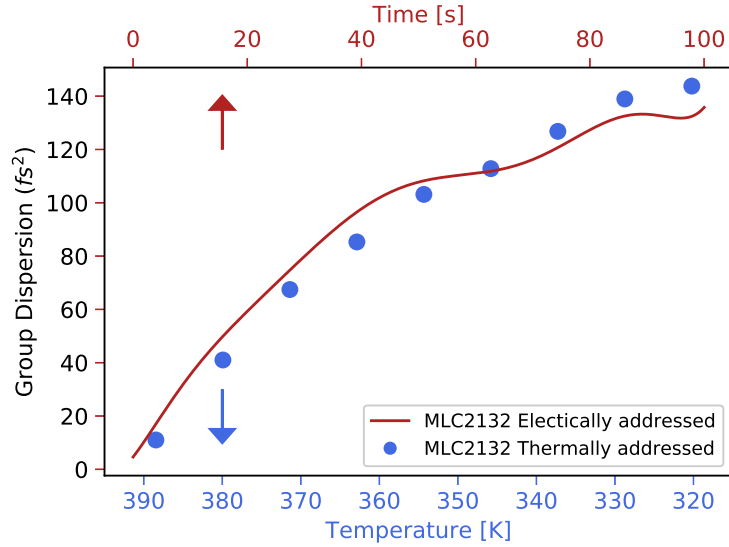


Figure 58: Group Delay Dispersion ( $fs^2$ ) introduced by a  $180\mu m$  thick NLC. In red, GDD as a function of time following a 10v-0v voltage step in an electrically-driven Lc-cell. In blue, GDD variation as a function of the inner temperature. Note the decreasing temperature scale.



## Chapter 5

# An achromatic thermo-optically addressed LC light modulator: THOR

### Objective

In this chapter, a new thermo-optical phase shaper is presented. The new device overcomes some of the limitations of a common LC-based light modulator. In particular, the spectral bandwidth is extended to multi-octave scale. A novel thermo-optical addressing in a writing-reading reflective configuration is demonstrated.

Three different prototypes are proposed, studied and compared measuring the spatial, the spectral and the temporal phase shaping capabilities.

## 5.1 Introduction

### 5.1.1 Liquid Crystal SLM and Liquid Crystal Light Valves: an overview

Spatial light modulators (SLMs) are well-known technological devices enabling to modify the intensity, the phase or the polarization of the light. Phase modulation capabilities present a particular interest when the SLM is inserted in the Fourier-plane of a zero-dispersion line. The resulting device is a so-called pulse shaper. Reflective SLMs are particularly suited as they enable to fold the zero-dispersion line (see chapter 1).

Liquid crystals, thanks to their remarkable and versatile optical properties, are already part of the framework of light modulators, through electrical control of their birefringence (Weiner et al., 1990). In that case, the modulated light has to be polarized along the extraordinary axis. The structure of main LC-SLM devices is sketched in Figure 59.

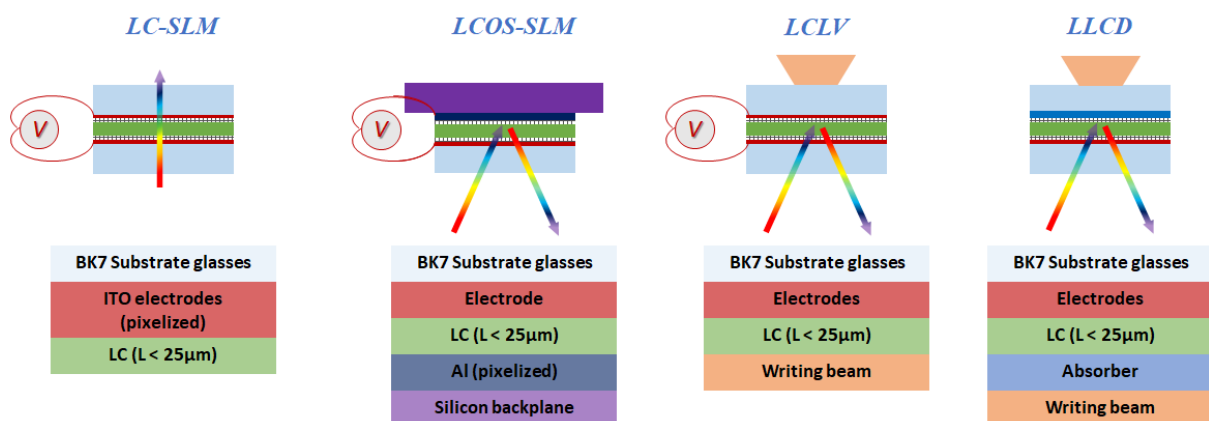


Figure 59: Common LC based light modulators (LC-SLM, LCOS, LCLV, LLCD).

**LC-SLM** A LC-SLM consists of a thin layer of nematic liquid crystal placed between two glass substrates. Over each substrate a transparent electrode matrix is deposited, generally ITO (indium tin oxide), which allows the application of independent voltages to each pixel. Through electrically-controlled molecular orientation, each pixel then acts as a programmable waveplate. Thus, if placed in the Fourier-plane of a zero-dispersion 4f-line, they are able to arbitrarily modulate the input beam. Thus, the incident light polarization state has to be parallel with the molecular reorientation plane. In general, electrically-addressed devices can independently control light properties over a limited number of points, equal to the number of actuators or electrode segments. Typical electrode matrix of commercial LC-SLM are composed by  $1024 \times 768$  pixels with a pitch of  $36 \mu\text{m}$ <sup>7</sup>. In addition, the gap between two actuators is inactive and can induce discontinuity of the modulated signal properties. Furthermore, for most of these LC-based devices, mainly to reduce the commutation time, the LC layer thickness is between  $10 \mu\text{m}$  and  $20 \mu\text{m}$ , thus limiting the overall phase-shift to  $2\pi$ . An additional drawback of the LC-SLM technology is the optical behavior of the required electrode (ITO, most of the time), typically transparent over spectral the visible range, which strongly reduces the spectral acceptance of the device, by comparison with the LC mixture itself. The electrode is also the limiting factor for damage threshold (Dorrer et al., 2011).

**LCOS** LC-SLMs have been gradually replaced by LCOS (Liquid crystal on silicon) technology developed for many years for image and video display applications and now also adapted for

<sup>7</sup><https://holoeye.com/spatial-light-modulators/lc-2012-spatial-light-modulator/>

phase shaping (Zhang, You, & Chu, 2014; Vettese, 2010). The architecture of LCOS is similar to conventional LC-SLM described so far except that a silicon backplane (CMOS) constitutes one of the substrates (second sketch of Figure 59). This CMOS layer consists of the electronic circuitry that is buried underneath pixel arrays. Once again, the phase modulation is achieved applying a different voltage on each pixel controlling the LC birefringence. The pixels are aluminium mirrors deposited on the surface of the silicon backplane, generally smaller compared to the ones used in common LC-SLM. Commercial high resolution LCOS are composed by a matrix of (3840 x 2160) pixel, with a pixel pitch of  $3.75 \mu\text{m}$ <sup>8</sup>. Phase-only modulating LCOS devices have a wide range of applications based on the spatial modulation of coherent lights (Hussain, Martínez, Lizana, & Campos, 2013; Hussain, Martínez, & Campos, 2013), including real-time holography (Reichelt et al., 2012) optical correlators (Zeng, Bai, Hou, & Yang, 2011), wavelength selective switches (Robertson et al., 2013), reconfigurable optical add-drop multiplexers and diffractive optical components (Robertson, Zhang, Yang, et al., 2012; Robertson, Zhang, Redmond, et al., 2012). Despite a higher spatial resolution than common LC-SLM, LCOS are still affected by pixelization. In addition, the phase retardation is always limited to  $2\pi$  and the required electrode still limits the spectral acceptance bandwidth.

**LCLV** A particular type of LC-SLM is the Liquid Crystal Light Valve (LCLV) (third sketch of Figure 59). In these devices, the matrix of electronically driven pixels is substituted by a continuous photosensitive layer. Therefore, the electric field that controls the molecular reorientation does not come from an external voltage generator, but it is optically induced by the beam itself or by an auxiliary extra one in a writing-reading configuration. The writing laser is absorbed by a photoreceptor, generally a semi-conductor thin layer, meanwhile the reading light is modulated passing through the liquid crystal layer. However, in order to able the spreading of electric charges, a bias external voltage has to be applied.

Several optical functions have been shown in the last decades, such as non-linear wave mixing (Brignon, Bongrand, Loiseaux, & Huignard, 1997), spatial beam shaping of femtosecond pulses (Sanner et al., 2005), optical pattern formation (Bortolozzo, Residori, Petrosyan, & Huignard, 2006), phase conjugation (Bortolozzo, Residori, & Huignard, 2007), non-linear optical cavities (Bortolozzo, Montina, Arecchi, Huignard, & Residori, 2007), dynamic holography (Peigné et al., 2015), manipulation of singular beams (Lenzini, Residori, Arecchi, & Bortolozzo, 2011), and interferometry (Bortolozzo, Residori, & Huignard, 2010; Bortolozzo, Residori, & Howell, 2013). LCLV have been also inserted in a 4f zero-dispersion line (Dorrer, Salin, Verluise, & Huignard, 1998) to shape narrow-band femtosecond pulses.

A retro-reflective scheme has been also proposed recently (Onokhov et al., 2000). In this configuration, a dielectric mirror is the photoreceptor and writing-reading process occurs in the two sides of the mirror. In more detail, on one side the writing laser induces the electric field, meanwhile on the other one the light is modulated in its double passage through the LC layer. In both configurations (transmissive or reflective), the presence of the photosensitive layer removes the pixelization issue but does not solve the other electrode-related restrictions, such as the accepted spectral bandwidth. Light-Valves based on thin thin mono-crystalline BSO ( $\text{Bi}_{12}\text{SiO}_{20}$ ) crystal are preferred in the visible spectral range (Brignon et al., 1997; Aubourg, Huignard, Hareng, & Mullen, 1982), while *GaAs* has recently been demonstrated in the spectral range from  $1 \mu\text{m}$  to  $1.55 \mu\text{m}$  (Bortolozzo, Residori, & Huignard, 2013; Peigné et al., 2015). Again, the LC layer is usually  $< 25 \mu\text{m}$ .

<sup>8</sup>[https://www.thorlabs.com/newgrouppage9.cfm?objectgroup\\_id=10378&gclid=CjwKCAjw2qHsBRAGEiwAMBp0DFp000bhnG1d3T39xvUMeXeq9wEYqZz05HTMXUH3AFZn45frR0S0xhoCnOEQAuD\\_BwE](https://www.thorlabs.com/newgrouppage9.cfm?objectgroup_id=10378&gclid=CjwKCAjw2qHsBRAGEiwAMBp0DFp000bhnG1d3T39xvUMeXeq9wEYqZz05HTMXUH3AFZn45frR0S0xhoCnOEQAuD_BwE)

**LLCD** LC-based former devices have numerous issues related to the electrical driving, as also confirmed in this work. Among them, the chromatic restrictions, the phase modulation limitations and the damage threshold reduction can be all related to the presence of a conductive layer. Thus, other addressing strategies have been developed in the past to try to fully exploit the LC characteristics. One of these is the LLCD technology (Laser-addressed Liquid Crystal Displays) that has been investigated in the '80s for LC displays (Dewey, 1984). It consists in replacing the electric addressing with a thermo-optical control in a writing-reading configuration. A cw Nd:YAG (writing beam) is absorbed in a smectic liquid crystal layer itself generating a thermal gradient. This rise of temperature induces the Smectics-to-isotropic phase transition with a consequent amplitude modulation through the nucleation of transient diffusion centers. A He-Ne laser (reading beam) coaxial with the respect to the writing beam is then modulated in intensity.

To improve the overall modulation capabilities several experimental geometries have been reported. For instance, different writing laser beams have been tested, but also the LLCD cell itself has been modified inserting an additional absorbent layer to enhance the light absorption. ITO was one of them. Finally, even a retro-reflective scheme has been demonstrated with the absorption process on one side and the modulation on the other one of the LC layer.

Inexplicably, this technology has been used only with Smectic mixtures and for light intensity modulation, and afterward it has been forgotten in favor of common LCD. But still, the advantages of this technology, if optimized for phase shaping using nematic LC could solve some of the electrode-related limitations discussed so far.

### 5.1.2 An innovative LC-SLM: THOR

The idea of a new LC-based phase shaper comes from the presented LLCD, combined with all the results obtained so far in this thesis. Indeed, the thermally induced refractive index excursion has been demonstrated close to the electrically induced birefringence, even for thick nematics ( $\Delta n > 0.2$  for  $180 \mu\text{m}$  E7 mixture). In chapter 2, an oven was used, but the long time required to elevate the inner temperature is not attractive, while in chapter 4 it is verified that the temperature rising can be optically induced by the ITO layer absorption at  $\lambda_0 = 1.5 \mu\text{m}$  with a response time of few seconds.

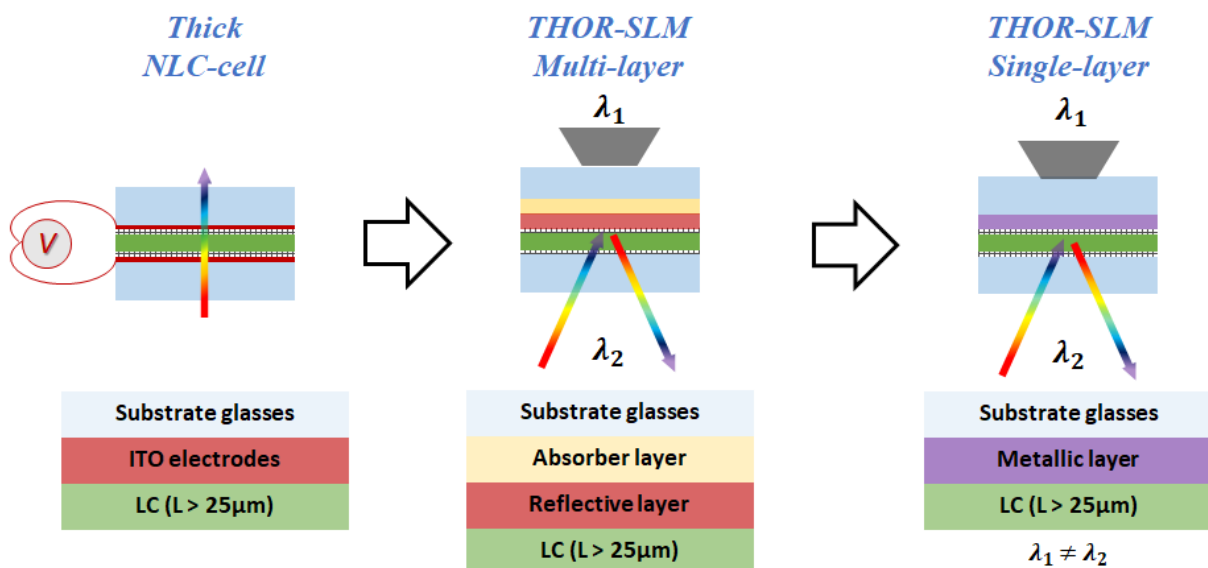


Figure 60: Evolution of the LC devices used in this thesis: from the transmissive LC cells (left) to the retro-reflective multilayer THOR-SLM (center) until the final single-layer THOR-SLM (right).

The new device is thermo-optically addressed, and it is an evolution of the former LC cell used in Chapter 4 (Figure 60 left), with several conceptual differences.

- In the initial LC device, the birefringence excursion is self-induced, e.g. the laser beam generates the thermal gradient and, at the same time, undergoes the induced phase modulation. As demonstrated by the LCLV and LLC, a writing-reading configuration is preferred in pulse shapers to separate the two functions. Hence, one beam induces and controls the refractive index change, while the other one is phase modulated.
- In chapter 4, the absorption takes place into the ITO layer at  $1.55 \mu\text{m}$ . Since the new device aims to be thermo-optically addressed, the electrode can be removed because no electric field is necessary. Instead, a specific *absorbent* layer in contact with the LC layer can be introduced. The main feature of this layer must be a high absorption of the writing laser, whatever is its wavelength span.
- To configure the writing-reading configuration, a physical isolation of the two beams must be achieved. The division is possible using an additional reflective layer in contact with the absorbing layer. This layer must have a large spectral reflectivity for the reading beam, and also large thermal conductivity to correctly spread the heat. On this layer has to be also possible to spin coat the PVA film necessary for the NLC molecules anchoring.
- Finally a glass window is needed to confine the LC mixture and fix its thickness. Obviously, this window has to be compatible with the LC mixture and at the same time transparent to the reading beam light.

This defines the general structure of the new LC-SLM, as represented in Figure 60 (central sketch). In this retro-reflective configuration, it is expected that the writing light illuminates the absorbent layer on one side of the device. The heat propagates through the reflective layer and increases the temperature of the LC layer. The thermal equilibrium is then reached generating a stable in time and spatially well-confined thermal gradient as demonstrated in chapter 4. LC thermotropy induces a local refractive index change that corresponds to a given phase-shift that is transferred to the reading beam.

A further evolution is the fusion of the absorbent layer and the reflective one in a single-layer configuration (Figure 60 right). Thus, this layer absorbs the writing beam on one side and, at the same time, it reflects the reading light on the other one. Obviously, in this arrangement the two laser beams has to be spectrally different ( $\lambda_1 \neq \lambda_2$ ).

Following these considerations a new *Thermo-Optically Reflective addressed Spatial Light Modulator* (**THOR-SLM**) is manufactured and now patented (FR1910894).

### 5.1.3 THOR-SLM prototypes

Considering this last single-layer configuration, the absorbent-reflective layer must endorse three critical features:

- Broadband reflectivity for the reading beam
- High absorption for the writing beam



- Local heating of the LC

In order to have a broadband reading beam spectrum, a large reflectivity wavelength span of the absorbent-reflective layer is necessary: in this sense, metallic surfaces are suitable (such as silver or gold). At the same time, high absorption at one specific wavelength is required in order to maximize the writing laser absorption.

A good compromise is gold. The high reflectivity ( $> 90\%$ ) from  $500\text{ nm}$  to  $8\ \mu\text{m}$  (Ciesielski et al., 2018) and at the same time, a strong absorption around  $450\text{ nm}$  (Johnson & Christy, 1972) makes it suitable for this device. Thus, using gold surfaces, multi-octave spectra can be handled using a relatively cheap blue writing diode laser ( $\lambda_0 = 465\text{ nm}$ ).

Silver has the largest reflectivity spectrum span (from  $300\text{ nm}$  to  $8\ \mu\text{m}$ ), therefore the spectral acceptance can be further extended to the shorter wavelengths part of the visible spectrum. However, the most intense absorption is in the UV range, thus writing lasers that could deposit a few  $W/cm^2$  would be too expensive.

Nevertheless, this reflectivity can be exploited in the multi-layer configuration. Indeed a thin silver film can be deposited over another absorbent layer. Chrome is suitable for this role due to its broadband spectral absorption in all the visible spectrum<sup>9</sup>, despite a lower absorption at  $\lambda_0 = 465\text{ nm}$  compared to gold.

E7 and MLC2132 are the two considered LC mixtures, because of their large value of  $\Delta n_e(T)$ , as measured in chapter 2. In particular, as already mentioned, E7 has a smaller birefringence excursion and a lower isotropic phase transition temperature compared to MLC2132. Eventually, MLC2132 is suitable when a large and precise phase shift is required, while E7 is convenient because it should require less pump energy.

BK7 is the standard glass used to confine the LC mixture and fix its thickness. Thus,  $1\text{ mm}$  of BK7 is chosen as a window. At the same time, an optically-polished BK7 of  $6\text{mm}$  is also used as a substrate to deposit the metallic surface.

To fabricate this device, a thin film of polyvinyl alcohol (PVA) is spin coated on both surfaces (metallic reflective layer and BK7) and then rubbed. The consequent strong anchoring of the LC molecules is reached to fix a planar geometry parallel with the respect of the substrates (see Chapter 1).

The thermal conductivity of each material<sup>10</sup> are shown in table 13. The different orders of magnitude between metallic surface, LC layer and glass windows suggests that a stable in time and spatially well-confined thermal gradient is achievable.

Layer	E7	BK7	Gold	Silver	Chrome
<b>Thermal conductivity</b> $W/mK$	0.13	1.14	317	428	80

Table 13: Heat transfer coefficients for the different layers constituting the THOR-SLM (BK7, ITO, E7, Gold, Silver, and Chrome).

Therefore, three main different THOR-SLM prototypes are developed and characterized:  $50\ \mu\text{m}$  of E7 LC mixture with a Gold reflective layer, a second identical one with MLC2132 mixture

<sup>9</sup><http://mbwhitaker.com/htm/cr.htm>

<sup>10</sup>[https://www.engineeringtoolbox.com/thermal-conductivity-metals-d\\_858.html](https://www.engineeringtoolbox.com/thermal-conductivity-metals-d_858.html)

instead of E7. Eventually, a third device is fabricated with MLC2132, but inserted in a multi-layer configuration with a first Chrome layer (writing side) ( $100\text{ nm}$ ) and a second thin silver layer ( $100\text{ nm}$ ) (reading side). In this way, it is possible to compare the effect of the LC mixture only (comparing E7-Gold with MLC-Gold) and of the reflective layer only (comparing MLC-Gold with MLC-Chrome). All the three studied SLMs have the same LC layer thickness:  $50\text{ }\mu\text{m}$ . Other two extra E7-Gold devices are fabricated with a different LC thickness in order to evaluate its influence: one with a  $25\text{ }\mu\text{m}$  layer and another one at  $110\text{ }\mu\text{m}$  are fabricated in addition, only used in section 5.4. Table 14 summarizes the developed new THOR-SLMs with their names and own features.

THOR-SLM	E7-Gold	MLC-Gold	MLC-Chrome	E7-Gold-25	E7-Gold-110
LC mixture	E7	MLC2132	MLC2132	E7	E7
LC Thickness	$50\mu\text{m}$	$50\mu\text{m}$	$50\mu\text{m}$	$25\mu\text{m}$	$110\mu\text{m}$
Metallic layer	Gold	Gold	Chrome	Gold	Gold
Goal	Low pump power required	Large phase shift	Other diode pump	thinner LC behaviour	thicker LC behaviour

Table 14: Five THOR-SLM developed and characterized in the next sections.

The overall THOR-SLM dimensions are:  $25\text{ mm} \times 25\text{ mm} \times 7\text{ mm}$ , with an aperture of  $2\text{ cm}^2$ . It has to be noted that the lateral dimensions can be easily increased without any limitations or particular issues. Therefore, devices with larger surfaces can be fabricated in the future.

## 5.2 Characterization of three different THOR-SLM with homogeneous light-addressing

In this section, the THOR-SLM characterization is presented. The proposed device is characterized using a spatially homogeneous writing beam laser. Several features of the device are analyzed, among which particular attention is paid to the writing beam requirement. In more detail, the threshold at which the thermal gradient is established and the flux ( $W/\text{cm}^2$ ) that induces the isotropic phase transition are estimated. These two values enclose the working range for the flux for the writing laser.

The writing laser is a blue fibre diode emitting  $650\text{ mW}$ , with  $\lambda_0 = 465\text{ nm}$  and  $d = 6\text{ mm}$  (by Thorlabs) with a Gaussian spatial shape.

The reading beam is either a CW He-Ne laser, either the super-continuum fiber laser from Leukos. Moreover, potential applications are disclosed on femtosecond lasers with various spectral ranges (from  $500\text{ nm}$  to  $1500\text{ nm}$ ).

Three different interferometer schemes are employed to characterize the phase shaping modulation abilities in the spatial, temporal (group delay) and spectral (GDD) domains. The spatial phase shift is measured by a Michelson on the lateral shearing interferometer, while group delay and group delay dispersion (GDD) are measured by spectral interferometry.

Table 15 summarizes the experimental characterizations presented in this chapter.

	Spatial phase control	Delay control	Group Delay Dispersion control
Experimental set up	Spatial Michelson Interferometer	Group delay Michelson Interferometer	4f-line Michelson interferometer
Reading Laser source	He-Ne (633 nm)	Leukos Electro-Visir250 (500nm – 850nm)	Leukos Electro-Visir250 (550nm – 950nm)
Spatial writing-laser configuration	Collimated beam	Collimated beam	Cylindrical (150 mm) lens Convex (200mm) lens
THOR-SLM	E7-Gold MLC-Gold MLC-chrome	E7-Gold E7-Gold 25 $\mu$ m E7-Gold 110 $\mu$ m MLC-Gold MLC-chrome	E7-Gold MLC-Gold MLC-chrome
Detector	CCD Camera (Win Cam)	Spectrometer (Ocean Optics) (350 nm-850 nm)	Spectrometer (Advantes) (500 nm-1050 nm)
Goal	<i>OPD</i> Depolarization	$\Delta n_g(W/cm^2)$ $\Delta n_g(t)$ $L$ influence	Spectral phase shaping GDD control Spectral phase resolution
Application	Tunable IR lens	//	Spectro-temporal shaping of fs pulses

Table 15: THOR-SLM characterization: experimental set-ups, configurations, achieved measurements and disclosed applications

### 5.3 THOR-SLM: Spatial interferometry

#### 5.3.1 Experimental set-up

To characterize the phase-shift introduced by THOR-SLM in the spatial domain, a He-Ne ( $\lambda = 633 \text{ nm}$ ,  $P = 5 \text{ mW}$ ) is used as a reading laser. The polarization state is set by a polarizer and the laser beam diameter is expanded by a telescope in order to cover all the SLM surface ( $d > 1 \text{ cm}$ ). A Michelson interferometer introducing a lateral shearing is installed, with a mirror on one arm and THOR-SLM on the other (Figure 61). The two reflections are laterally separated by a small tilt angle  $\theta$ . The overlap of the two reflected beams shows interference fringes separated by  $d_f = \lambda/2\theta$ , where  $d_f$  is the spacing perpendicular to the shear, and  $\theta$  the tilt angle. This fringe pattern is acquired by a camera placed in the image plane in  $2f$ - $2f$  configuration ( $f = 75 \text{ mm}$ ) in order to relay-image the THOR-SLM. A typical fringe pattern is shown in Figure 62a). The writing laser is a blue fibre-coupled diode ( $\lambda_0 = 465 \text{ nm}$ ,  $P = 650 \text{ mW}$ ) that addresses the rear of the LC-SLM with a smaller spot ( $d = 0.6 \text{ cm}$  at  $1/e^2$ ) and a maximum of flux  $2.25 \text{ W/cm}^2$ . Vertical and horizontal cuts of the spatial profile of the writing beam are also pictured in the figure. The induced spatial phase shift is then visible from the fringes shift and deformation on the camera.

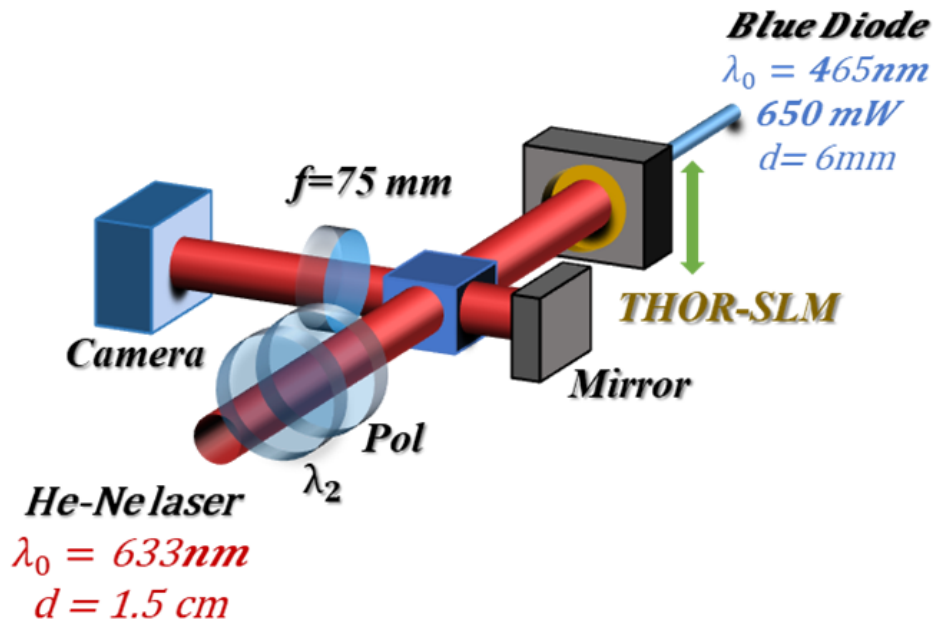


Figure 61: Spatial Interferometer: a half-wave plate and a polarizer set the He-Ne laser polarization and energy. The THOR-SLM is placed on the transmitted arm of a and its spatial profile is imaged onto a camera ( $2f$ - $2f$ ). The rear of the device is illuminated by a blue fibre diode by Thorlabs ( $d = 2 \text{ mm}$ ,  $650 \text{ mW}$  max,  $\lambda = 465 \text{ nm}$ ). The number and position of the fringes are set by the reference mirror. The green arrow indicates the extraordinary axis of THOR-SLM.

#### 5.3.2 Fringes description

**E7-Gold** The first tested SLM is the E7-Gold. When addressing the device with  $0.6 \text{ W/cm}^2$  a complete fringe shift is visible on the camera (Figure 62) indicating a phase shift of more than  $2\pi$ . When increasing the writing beam flux, an unusual *finger print pattern* is established ( $1.3 \text{ W/cm}^2$ ), suggesting a large phase shift. Above  $> 2.1 \text{ W/cm}^2$  a chaotic and unstable feature replaces the finger print pattern followed by an abrupt loss of signal. This chaotic pattern enlarges when the writing beam further increases. Indeed, at  $> 2.25 \text{ W/cm}^2$  (maximum flux

reachable by the writing beam), the chaotic spot becomes a ring with a partial recovery of the transmission on its center (last sub-plot of Figure 62).

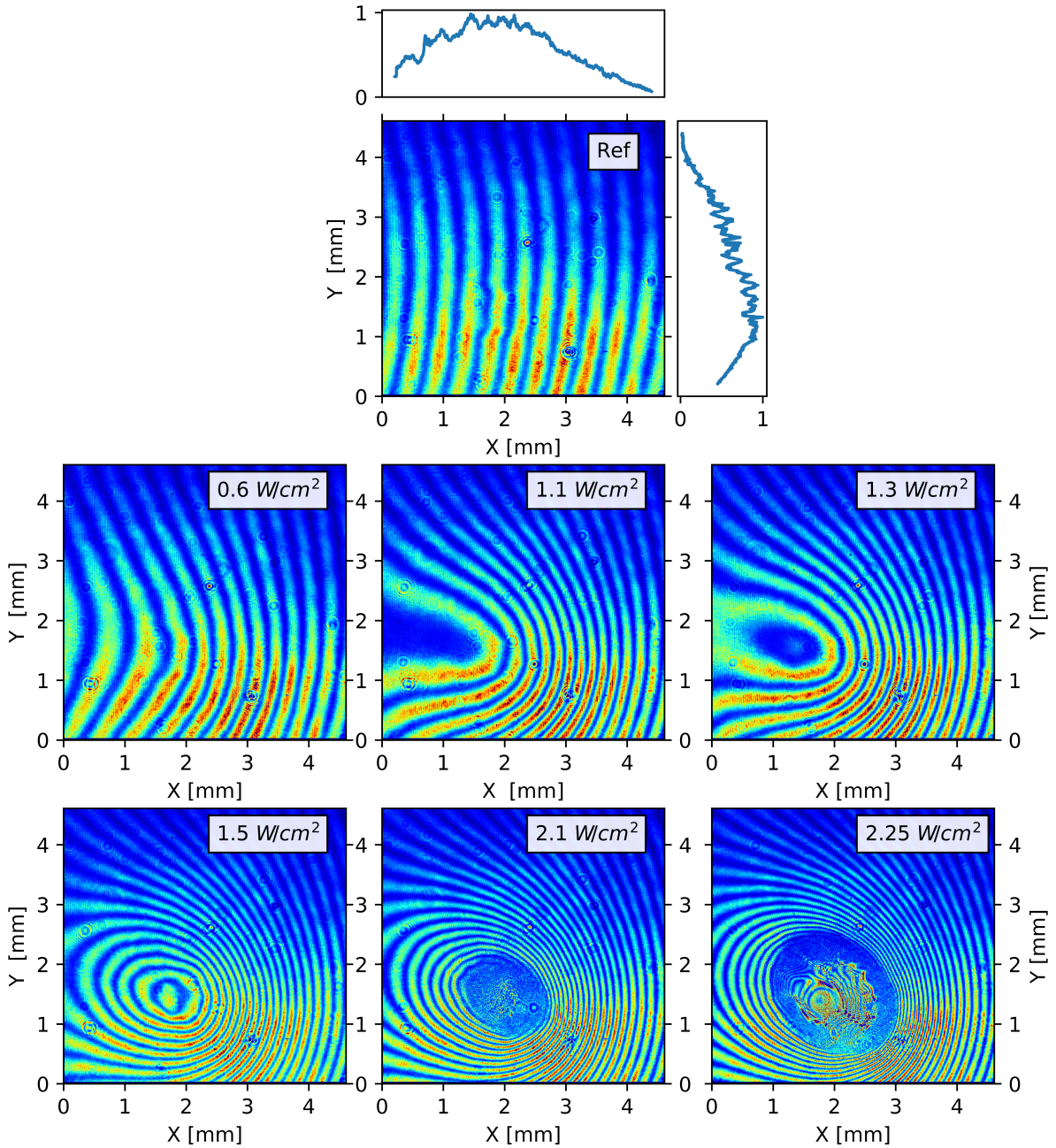


Figure 62: Acquired interference patterns increasing the writing laser flux for the E7-Gold. The blue light spatial profile is plotted close to the reference on the top of the graph. The chaotic transition pattern is visible on the last two graphs ( $2.1\text{-}2.25\text{ W/cm}^2$ ).

**MLC-Gold** MLC-Gold is then tested. The same fringe shift is visible increasing the writing beam flux. For its maximum value, the *finger print* pattern is recovered as for the E7-Gold (see Figure 63). However, the chaotic pattern is not generated.

**MLC-Chrome** Finally, the last prototype is tested. The overall fringe shift is lower than MLC-Gold. Indeed the *finger print* pattern is not reached, not even at  $2.25\text{ W/cm}^2$  (Figure 63). Therefore, a smaller phase shift is expected.

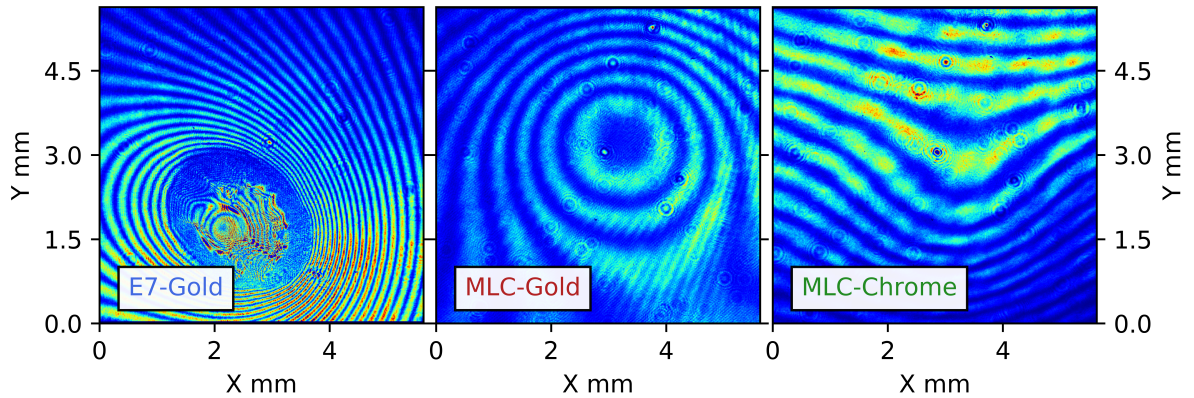


Figure 63: Fringes patterns addressed with the maximum writing flux  $2.25 \text{ (W/cm}^2\text{)}$ : E7-Gold on the left, MLC-Gold on the center, MLC-Chrome on the right.

### 5.3.3 Spatial phase shift analysis

To quantify the introduced phase, the fringes pattern is analysed by 1D Fourier Transform along  $x$  direction of Figure 62. The induced spatial phase shift  $\Delta\varphi$  is then recovered by subtracting a reference phase, e.g. acquired when the THOR-SLM is not illuminated. The measured phase shift is considered as negative, because it has already been demonstrated that the refractive index on the extraordinary axis decreases with the temperature. In addition, a linear temperature rising with the writing beam flux is assumed for these first analyses. Nevertheless, this assumption is verified in the following. Furthermore, the index change is deduced from the retrieved phase shift using:

$$\Delta\varphi = 2\pi \frac{\Delta n L}{\lambda_0} \quad (5.1)$$

where  $\Delta\varphi$  is the phase shift,  $L$  the LC thickness ( $100 \mu\text{m}$ ,  $50 \mu\text{m}$  double pass),  $\lambda_0 = 633 \text{ nm}$ , and  $\Delta n$  is the change of the refractive index. This variation can be also expressed in terms of Optical Path Difference (OPD) defined as:

$$OPD = \frac{\Delta\varphi \lambda_0}{2\pi} = \Delta n L \quad (5.2)$$

**E7-Gold** To quantify the introduced spatial phase shift in E7-Gold, a Y-cut of the recovered phase map is extracted and shown in Figure 64a). Different profiles are plotted increasing the writing beam flux up to  $1.53 \text{ W/cm}^2$ . One can appreciate the gradual increase of the phase gradient, exhibiting a smooth Gaussian-like shape, with a spatial extension comparable to the writing beam. Over this flux value, the analysis is partially affected by the *finger print* pattern. Nevertheless, the introduced phase is still retrieved, even if the uncertainty is considerably increased. The measured phase shift, the relative refractive index change ( $\Delta n$ ) and the OPD are then plotted as a function of the input writing beam flux ( $\text{W/cm}^2$ ) in Figure 64b),c). The phase shift can be continuously retrieved up to  $1.53 \text{ W/cm}^2$ , where a phase shift as high as  $80 \text{ rad}$  is measured. Above  $1.7 \text{ W/cm}^2$ , the *finger print* pattern partially affects the analysis, but the maximum phase shift can still be estimated larger than  $120 \text{ rad}$  ( $\Delta n = 0.125$ ,  $OPD = -12.4 \mu\text{m}$ ).  $200 \text{ rad}$  is the maximum phase shift measured before the chaotic pattern makes the FFT analysis inefficient. The maximum birefringence excursion is then  $\sim 0.2$  with an OPD equal to  $-19.9 \mu\text{m}$ .

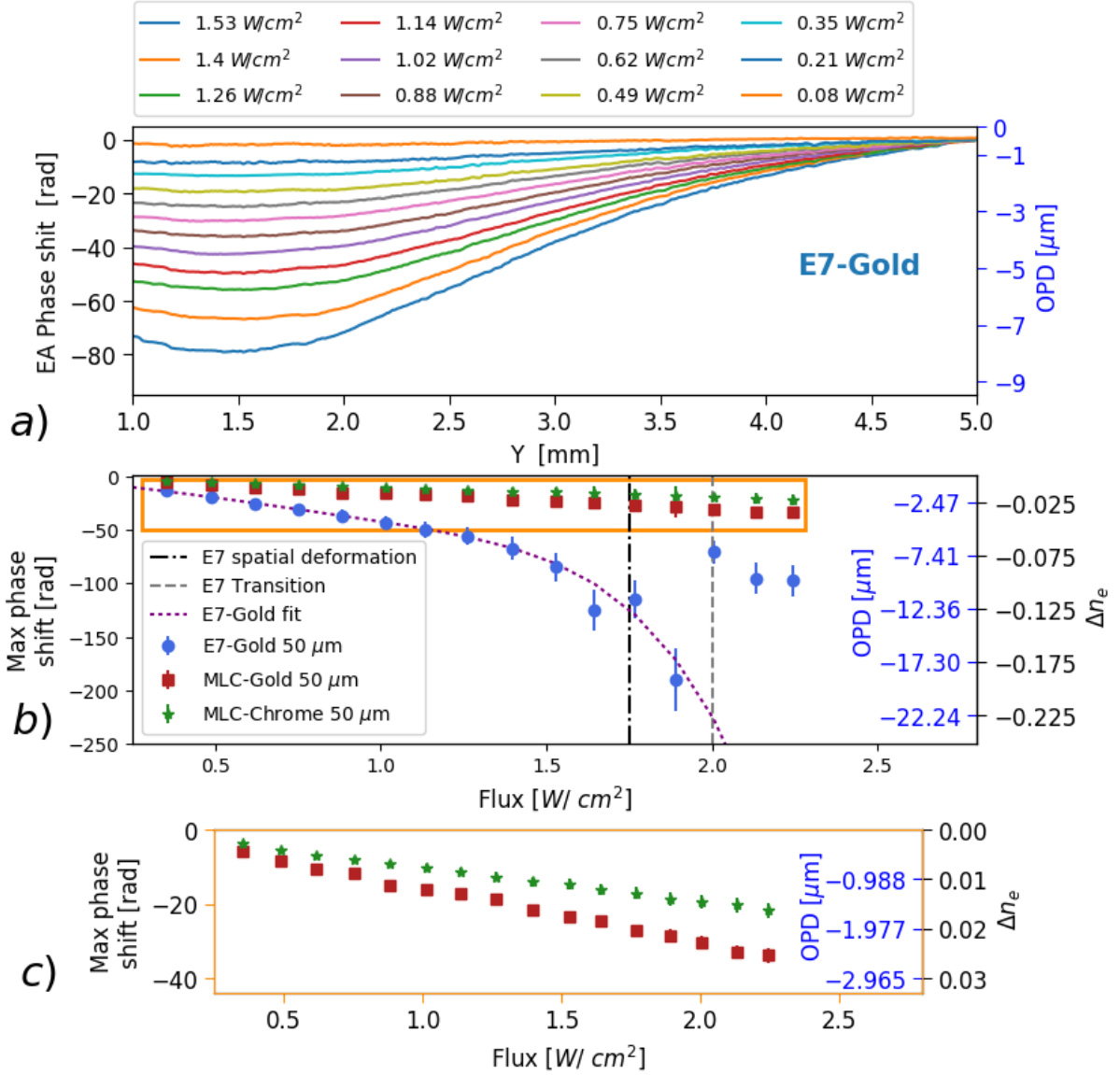


Figure 64: a) Introduced spatial phase shift on the extraordinary axis for E7-Gold: each plot represents a different writing flux. b) Maximum phase shift (left black scale),  $\Delta n_e$  (right black scale) and  $OPD$  (right blue scale) as a function of the writing laser flux ( $W/cm^2$ ) for the three THOR-SLM prototypes. E7-Gold isotropic phase transition is plotted in grey and an exponential fit of the experimental points in blue (dotted) to indicate non-linearity of  $\Delta n_e$  with the writing laser flux. c) (orange frame in b) Zoom of MLC-Gold and MLC-Chrome phase-shift.

**MLC-Gold** MLC-Gold is then analyzed: smooth and linear continuous phase-shift can be induced. The maximum phase shift reached at  $2.25 W/cm^2$  is  $\sim 32rad$  ( $\Delta n = 0.034$ ,  $OPD = -1.9 \mu m$ ) lower than E7. In order to reach the isotropic-transition and to scan the whole nematic range, a more powerful writing laser is necessary.

**MLC-Chrome** Finally, MLC-chrome is studied. It introduces an even smaller phase shift ( $22rad$ ,  $\Delta n = 0.021$ ,  $OPD = -1.2 \mu m$ ), due to the lower chrome absorption of the blue light. Further investigations with a more powerful writing laser at  $465 nm$ , to reach the isotropic state of MLC2132 mixtures will be needed. Eventually, also different wavelengths span can be considered to fully exploit the chrome absorption.



### 5.3.4 Spatial deformations interpretation

The finger print pattern introduced by E7-Gold and MLC-Chrome is not unusual in spatial interferometry. When a large and localized phase shift generates a spherical wavefront, the fringe pattern collapses and produces rings around the central part. The induced phase overcomes the initial lateral phase-shift of the interferometer. This effect is well-known and deeply used to measure the lens sphericity or spatially characterize optical components using the Twyman-Green interferometer (Malacara, 2007).

Conversely, the chaotic pattern generated at high flux is still not fully understood.

A first hypothesis is that this pattern comes from the nematic to isotropic transition of the LC mixture. This possibility is corroborated by the induced birefringence excursion measured ( $\Delta n \sim 0.2$ ) when the chaotic pattern starts to appear. Moreover, the  $\Delta n_e$  trend with the flux (see Figure 64b) reminds the refractive index variation with the temperature already seen in this work (chapter 2 and 4) indicating the vicinity of the isotropic transition. Close to this transition, a LC isotropic droplet could be generated where the molecular order is sufficient to recover the fringes pattern. Therefore, the ring of Figure 62 would then corresponds to the junction between this isotropic droplet and the nematic phase.

Another hypothesis is that the induced phase shift causes a strong spatial change in the beam (divergence) and then some parts of the beam are missing because not collected by the imaging system.

For MLC-Gold and MLC-Chrome, the linear phase shift implies a linear refractive index variation, so a consequent linear temperature elevation. Thus, the linear dependence of the temperature with the flux for both MLC-based prototypes is strengthened.

In addition, the temperature inside the device is estimated lower than 360 *K*. Indeed, above this temperature, the ML2132 refractive index decreases non-linearly with the temperature.

### 5.3.5 Polarization analysis

In this section, the potential depolarization occurring during heating of the LC molecules is estimated. Indeed, the parameter order *S*, introduced in chapter 1, is progressively reduced with increasing inner temperature. This molecular induced disorder could potentially induce a laser beam depolarization.

A similar experimental set-up is used: a second polarizer is added, crossed with respect to the first one, and a photodiode replaces the camera (Figure 61): the transmitted signal is acquired turning-on and turning-off the writing blue laser at its maximum power. The ratio between the signal acquired before and after the switch quantifies this depolarization. MLC-Gold depolarizes a bit less ( $5 \cdot 10^{-3}$ ) compare to the E7-Gold ( $4 \cdot 10^{-3}$ ) and no remarkable difference is found between the switching-on and switching-off dynamics. The polarization degree can be therefore considered preserved during the process.

### 5.3.6 Conclusions

To conclude, the thermo-optically induced spatial phase shift has been measured at 632.8 *nm* for all the SLM prototypes using a shearing interferometer. E7-Gold prototype introduces the largest phase shift (200 rad) and the isotropic-transition is reached for a writing flux around 2 *W/cm<sup>2</sup>*. MLC-Gold and MLC-Chrome introduce smaller phase shift, as expected, because of the higher transition temperature of the MLC2132 mixture. A lower absorption by the Chrome layer is found. From the phase shift, the maximum refractive index excursion is retrieved: a  $\Delta n = 0.22$  is measured for E7-Gold reaching the isotropic transition. MLC-Gold introduces

only  $\Delta n = 0.032$ , but with a linear and smooth dependence to the writing beam flux.

These experiments indicate that the SLM may act as an efficient thermo-optical deformable mirror, with competitive performances with MEMS technology<sup>11</sup> and the recent TDM (Thermally Deformable Mirror) in terms of maximum OPD and available aperture (Kasprzack, 2014). In the annex an application of this spatial phase shift is described: THOR-SLM is applied as a tunable lens for infrared femtosecond pulses (Appendix D.4.2).

Device	OPD	Clear Aperture
MEM by Thorlabs	$3.5 \mu\text{m}$	4.4 mm x 4.4 mm
TDM by (Kasprzack, 2014)	$1.5 \mu\text{m}$	2.6 mm x 4.4 mm
THOR	$-19.9 \mu\text{m}$	25 mm x 25 mm (not limited)

Table 16: Comparison of a few performances between commercial MEMs, TDM and THOR-SLM

## 5.4 THOR-SLM temporal shaping: group delay management

### 5.4.1 Experimental set-up

The goal in this section is to estimate the thermo-optically induced group index change for both polarization axes. This is achieved by broadband spectral interferometry as described in former chapters.

Furthermore, the thermo-optical tuning of the birefringence is compared to the homogeneous temperature addressing (chapter 2) and to the electrical-driving (chapter 3) of classical LC cells.

The induced group delay change is measured using a broadband fiber super-continuum source from Leukos (Electro-Visir-250-VIS-IR, 650 mW, 2 mm, 450-2500 nm) (Figure 65a) ). A long-pass filter (cut-off: 500 nm) and a short-pass dichroic mirror (cut-off: 950 nm) narrow the bandwidth to 500-950 nm and the light is polarized with a polarizer to study both LC axes. The optical set-up includes a dispersion-balanced interferometer: a broadband beam-splitter BS (50:50)<sup>12</sup> splits the input beam in two arms. A phase compensator plate (2mm of UVFS) is added on one arm to balance the optical dispersion of the BS and a metallic mirror placed on a translation stage regulates the group delay. THOR-SLM, placed in the other one, is relay imaged (2f-2f configuration with  $f = 150 \text{ mm}$ ) into an Ocean Optics spectrometer (450-850 nm, resolution of 0.3 nm). The writing laser is a collimated blue fiber-coupled diode ( $d = 6 \text{ mm}$ , 650 mW max,  $\lambda = 465 \text{ nm}$  by Thorlabs). Here, the reading beam size is three times smaller than the writing, hence a spatially homogeneous heating is considered (Figure 65) ).

As introduced in chapter 1 and in chapter 2, Fourier analysis of the spectral interference fringes enables to retrieve the group delay changes ( $\Delta\tau_g$ ). Then, from the group delay excursion, the refractive group index change ( $\Delta n_g$ ), averaged on the LC thickness, is deduced using:

$$\Delta n_g = c \frac{\Delta\tau_g}{L} \quad (5.3)$$

<sup>11</sup>[https://www.thorlabs.com/newgrouppage9.cfm?objectgroup\\_id=3258](https://www.thorlabs.com/newgrouppage9.cfm?objectgroup_id=3258)

<sup>12</sup>[https://www.thorlabs.com/newgrouppage9.cfm?objectgroup\\_id=6265&pn=BSW26R](https://www.thorlabs.com/newgrouppage9.cfm?objectgroup_id=6265&pn=BSW26R)

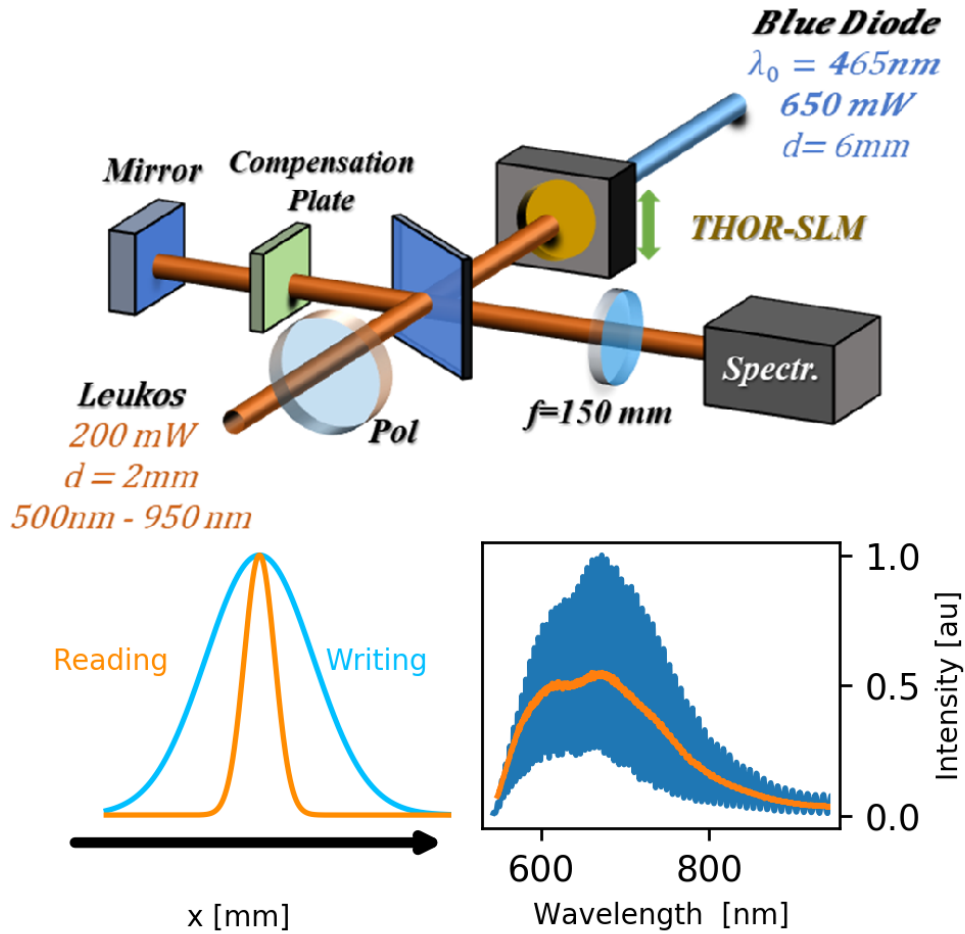


Figure 65: Experimental Set-up: a broadband Michelson interferometer is installed with a super-continuum white light source (LEUKOS, 200 mW, 450-850 nm). A long-pass filter (cut-off: 500 nm) with a short-pass dichroic mirror (cut-off: 950 nm) select the spectral range. The polarization state is set using a polarizer. Bulk materials are added on one interferometer arm to compensate the THOR-SLM dispersion placed in the other one. The device is imaged ( $f = 150$  mm) into a spectrometer (Ocean Optics 450-850 nm). The extraordinary axis of the LC molecules is indicated with a green arrow. The fibre diode ( $d = 6$  mm, 650 mW max,  $\lambda = 465$  nm by Thorlabs) is the addressing writing laser. The two gaussian spatial profiles are also plotted: reading beam (orange curve;  $d=2$  mm) and writing beam (blue curve,  $d=6$  mm). The raw spectrum (orange) and the interference one (blue) are also plotted.

The difference in spectral phase between successive acquisitions enables to follow the GDD excursion simultaneously.

#### 5.4.2 Results & Analysis

**E7-Gold** E7-Gold is first characterized (Figure 66a). The writing flux is increased from 0 to  $2.5$  W/cm<sup>2</sup> monitoring the refractive group index on the extraordinary axis. The non-linear trend of  $\Delta n_{ge}$  with the writing beam flux reminds the dependence of the refractive index variation with the temperature already measured in this work (see chapter 2 and chapter 4). The maximum group delay excursion is 65 fs ( $\Delta n_{ge} = 0.217$ ). GDD is measured on the extraordinary axis between no addressing flux and  $2.2$  W/cm<sup>2</sup> and is found equal  $\sim 30$  fs<sup>2</sup>. At  $2.5$  W/cm<sup>2</sup>, the fringes contrast and the whole signal level are considerably reduced. As already measured in

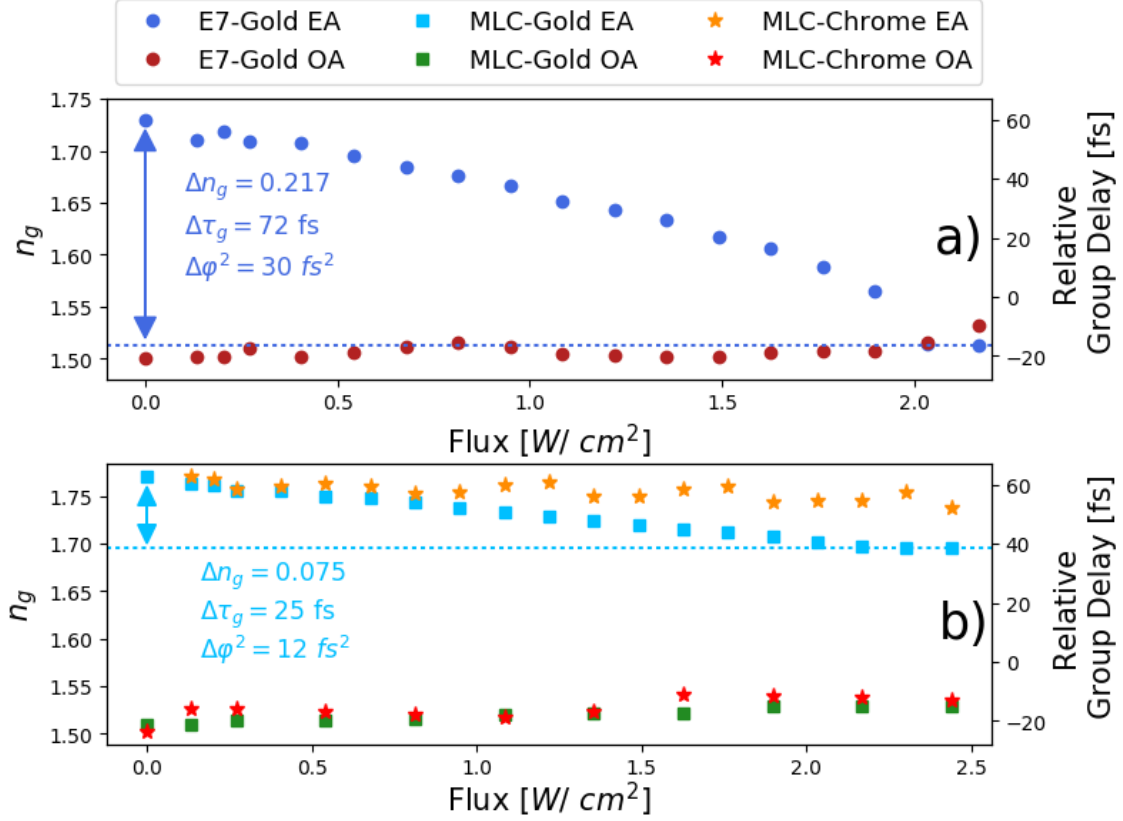


Figure 66: a) E7-Gold refractive group indices  $n_{g_e}$  (green spots) and  $n_{g_o}$  (orange spots) as a function of the addressing flux ( $W/cm^2$ ). b) Same graph but for MLC2132-Gold (squared) and MLC2132-Chrome (stars). The relative introduced group delay scale is plotted on the right axis.

chapter 2, the order parameter  $S$  decreases with the inner temperature, therefore above  $2 W/cm^2$  the isotropic transition is approaching, confirming the results of section 5.3 .

**MLC-Gold** MLC-Gold is then tested. As expected, a smaller phase shift is induced and the transition is not reached which is a further confirmation of the results of section 5.3. Only 25 fs of group delay excursion ( $12 fs^2$  of GDD) is measured at  $2.5 W/cm^2$ , which corresponds to a refractive index excursion of  $\Delta n_g = 0.075$ . This value is actually three times larger than the one measured spatially in section 5.3 ( $\Delta n = 0.02$ ). Nevertheless, the group delay measured using the broadband spectral interferometry is a more precise way to determine the refractive index variation compared to the spatial Fourier Transform of section 64.

**MLC-Chrome** As expected, the MLC-Chrome has an even smaller phase shift ( $\Delta \tau_g = 10$  fs,  $\Delta n = 0.032$ ,  $GDD = 6 fs^2$ ).

**Ordinary axis excursion** To complete the study, the LC ordinary axis is also analyzed for all the prototypes. Despite a small variation with the temperature (as already demonstrated in chapter 2,  $n_o(T)$  is found almost constant, except for E7-Gold close to the isotropic transition (Figure 66a) ). For this prototype, a sudden increase of the group index is measured when the flux is larger than  $2 W/cm^2$ . The clearing point is then confirmed. For the other two devices no noteworthy group index variation are measured even at  $2.5 W/cm^2$  (Figure 66b) ).

In the next section, the ordinary axis will not be taken into account anymore.

**Temperature analysis** The LC refractive index has been studied as a function of the temperature in chapter 2 for both mixtures. Therefore, a calibration of the inner temperature as a function of the writing flux can be performed. Indeed, from the birefringence excursion ( $\Delta n_g$ ) the inner LC temperature inside the device can be estimated. Figure 67 shows the inner temperature as a function of flux for E7-Gold and MLC-Gold prototypes. As a matter of fact, two different regimes can be distinguished. When the flux is below  $1 \text{ W/cm}^2$ , the temperature inside THOR-SLM increases linearly with the writing beam flux, e.g. writing beam power. This agrees with the expected linear gold absorption of the blue light. In addition, the difference between the two prototypes is lower than 2.5 K. Thus, the temperature elevation is only partially affected by the LC nature itself, and the unknown MLC2132 thermal conductivity coefficient must be close to the E7 one ( $0.13 \text{ W/cm}^2$ ).

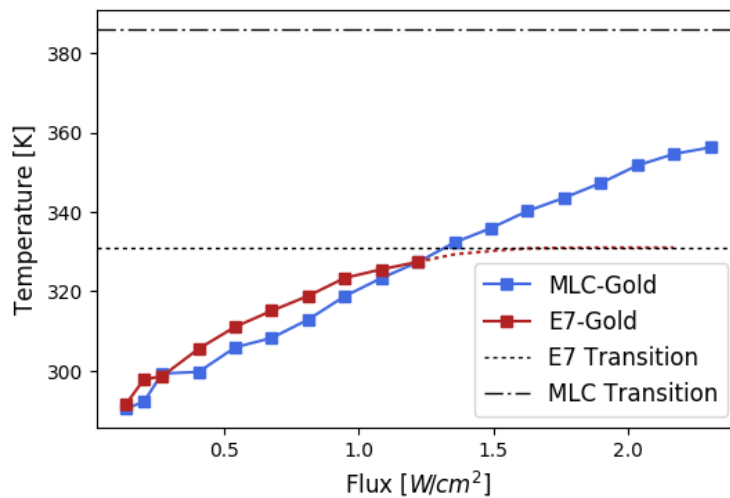


Figure 67: E7-Gold (red curve) and MLC-Gold (blue curve) inner temperature as a function of applied writing flux. E7 isotropic transition temperature is also plotted. Writing beam size of 6 mm.

Conversely, when the flux applied is larger than  $1 \text{ W/cm}^2$ , an horizontal threshold for E7-Gold is found close to 331 K (E7 mixture isotropic phase transition temperature). Indeed, approaching the transition, this calibration has not the resolution to disclose the inner temperature. Indeed, for large  $\Delta n$ , the temperature variation  $\Delta T$  is too small to be differentiated. In addition, the LC properties are strongly altered approaching the transition. Therefore, for E7-gold this temperature calibration is valid only up to 325 K, e.g. before the non-linear regime has started. Nevertheless, MLC-Gold, having a LC mixture with a higher clearing point temperature, indicates that the temperature still increases linearly with the flux, up to 360 K, for this writing beam size (6 mm).

### 5.4.3 Scaling with the thickness of the LC layer

Previously in this thesis, it has already been demonstrated that liquid crystal thickness is a crucial parameter. For this reason, its impact on the optical response has to be taken into account. E7-Gold prototype has been fabricated with two different LC thicknesses: 25  $\mu\text{m}$  to verify the dynamics in the most common thin cell, and 110  $\mu\text{m}$  to increase the induced phase-shift. Both of them are compared to E7-50 $\mu\text{m}$ . The set-up of section 5.4.1 is used to get group delay shift and refractive group index excursion. Several spectra ( $> 10$ ) are acquired for the same writing beam flux in order to estimate also the uncertainty of the measurement: the error bars that come out are so small that are not distinguishable in Figure 68 ( $< 10^{-3}$ ). The group delay excursion  $\Delta\tau$  for 25  $\mu\text{m}$  and 50  $\mu\text{m}$  is in agreement with the results obtained in the previous

sections and homogeneous with the LC different thicknesses. In more detail, 16 fs (resp. 35 fs) are measured for 25  $\mu\text{m}$  (resp. 50  $\mu\text{m}$ ) for 2  $W/cm^2$  that corresponds to a refractive index variation of  $\Delta n = 0.11$ (resp. 0.12). Nevertheless, the isotropic phase transition is not reached due to the lower writing beam flux applied compared to section 5.4.1.

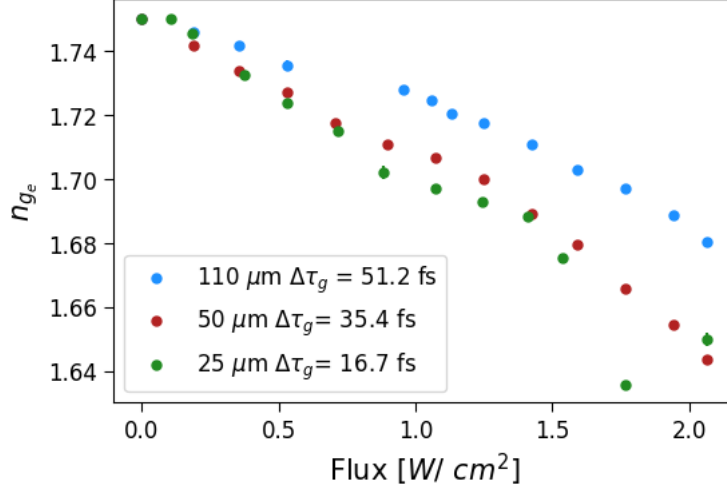


Figure 68: Refractive group index as a function of the writing beam flux on the extraordinary axis. Different LC thicknesses are plotted, E7-Gold: 25  $\mu\text{m}$  (Green spots), 50  $\mu\text{m}$  (Red spots) and 110  $\mu\text{m}$  (Blue spots). In the legend are shown the relative max group delay excursions  $\Delta\tau$ .

Conversely, a thicker cell introduces a larger  $\Delta\tau_g$  variation than the thinner cells, but the corresponding  $\Delta n_g$  is lower than expected. A volume effect is reducing the overall efficiency of the heating process. Hence, a larger flux is necessary to address homogeneously all the molecules in thicker cells. Thus, thicker THOR-SLM can be interesting for some applications but may also require higher writing flux.

#### 5.4.4 Temporal dynamics

Up to now, all the performed measurements are studied adiabatically and do not take into account the dynamic of the process, e.g. how the phase evolves in time when the writing laser is turning on and how long is required to reach the steady state. As explained in chapter 3, the optical response of the device has to be as fast as possible in order to be interesting for potential applications.

In this section, the refractive index evolution in time is measured for E7-Gold and MLC-Gold using the experimental set-up of section 5.4.1. Figure 69(a,b,c) shows the interference spectra as a function of time when the blue writing light is turned on. The abrupt discontinuities in the fringes evolution in all the interferograms are due to the dead time between two consecutive acquisitions.

**E7-Gold** E7-Gold is first characterized applying 2.5  $W/cm^2$  (Figure 69a) ): the beginning of the excursion is visible by the fringe shift (after few hundred ms). The sudden loss of signal and contrast after 20 s corresponds to the isotropic phase transition. The same experiment is performed with 1.75  $W/cm^2$  (Figure 69b) ) in order to avoid the transition. In that case, the fringes pattern can be resolved until the equilibrium is reached.

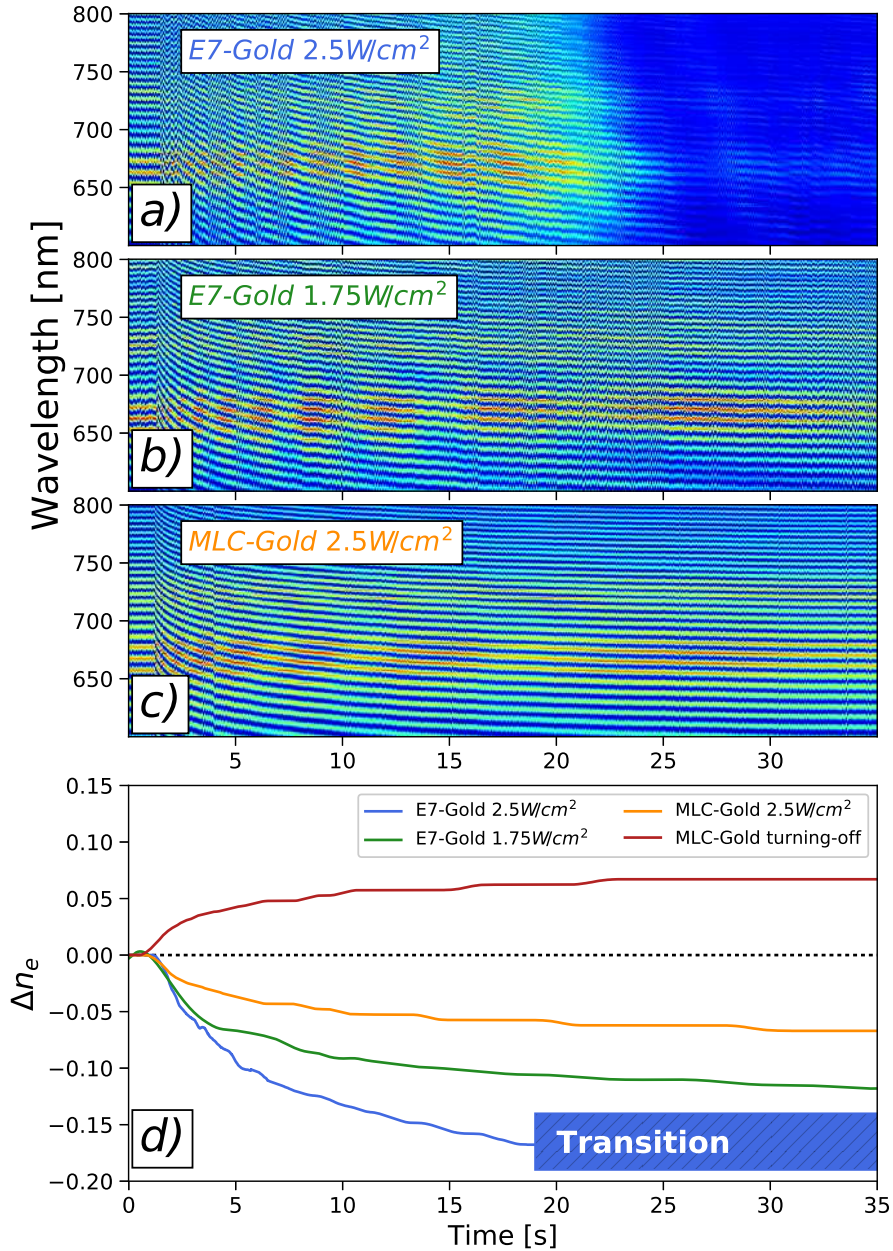


Figure 69: Interferogramm as a function of acquisition time for E7-Gold (a,b) and MLC-Gold (c): approaching the nematic-to-isotropic transition the signal drops suddenly in (a). At lower flux ( $1.75 \text{ W/cm}^2$ ) the full excursion is visible (b). MLC-Gold shows a smaller fringes shift due to the lower dephasing (c). (d) Recovered  $\Delta n_g$  excursion during the turning-on (E7-Gold in blue and green, MLC-Gold in orange) and turning off (MLC-Gold in red).

**MLC-Gold** MLC-Gold is also tested at full writing beam power,  $2.5 \text{ W/cm}^2$  (Figure 69c). As shown above, the transition is not reached for this cell and the fringes pattern is also resolved up to the equilibrium.

The relative refractive index excursion  $\Delta n_{ge}(t)$  is plotted in Figure 69d). Addressing E7-Gold with  $2.5 \text{ W/cm}^2$ , the phase is measurable until the transition affects the spectra. The  $\Delta n_{ge}$  is getting closer to 0.2 as expected. At lower writing beam flux ( $1.75 \text{ W/cm}^2$ ), the full birefringence excursion is 0.13 in agreement with previous measurements. MLC-Gold confirms the smaller phase transition ( $\Delta n_g = 0.06$ ) even at the maximum writing beam power. In red is plotted the MLC-Gold turning-off dynamic. Interestingly no noteworthy difference in the turning-on and turning-off is found in terms of time-scale.

The required acquisition time necessary to perform the 80% of the full excursion ( $t_{80}$ ) is smaller than 15 s: in particular 12.3 s for E7-Gold and 13.5 s for MLC-Gold. Finally, the difference between two consecutive points ( $\tau_1 - \tau_2$ ) in the steeper part of the curve is evaluated. As mentioned in chapter 3, this difference can be related to the temporal resolution of the scan ( $\delta t$ ). A slope of 1.1 fs and 1.5 fs each 5 ms is measured, respectively for E7-God and MLC-Gold.

THOR-SLM is an advantageous alternative for group delay manipulation, compared to electrically-driven cells described in chapter 3. In particular, it is considerably faster compared to the electric-switching-off dynamics (minutes scale for thick cells) and a bit slower compared to the electric-switching-on (few seconds). However, all the issues connected to the molecular reorientation (Fréedericksz transition, local defects, long stabilization time, and so on) are solved. In addition, no remarkable differences between the E7-Gold and the MLC-Gold are found, to the contrary of what measured in chapter 3 where MLC2132 mixture needs double of time to reorient the molecules.

To conclude,  $\Delta n_g$  dynamic excursion is found as high as 0.17 for E7, for 100  $\mu\text{m}$  effective LC layer with a good signal quality, a commutation time below the 15 s, and a temporal resolution of 1.1 fs. Furthermore similar behaviors of turning-on and turning-off drastically reduces the stabilization time needed between successive measurements.

## 5.5 THOR-SLM: phase shaping in a 4f-line

### 5.5.1 Experimental Set-up

In this section, the capabilities of THOR-SLM for ultrafast pulses shaping is demonstrated by inserting THOR-SLM in a 4f-line.

The laser source used as reading beam is the same as in section 5.4.1, e.g. a broadband fiber super-continuum from Leukos (Electro-Visir-250-VIS-IR, 650 mW, 450-2500 nm) spectrally reduced by a long-pass filter (cut-off: 500 nm) and a short-pass dichroic mirror (cut-off: 950 nm) to select the spectral range 550 – 950 nm (Figure 70). A polarizer sets the polarization state parallel with respect to the LC extraordinary axis. This white light seeds a Michelson interferometer balanced in dispersion.

On one arm a 4f-line is installed using a transmissive grating (300 Grooves/mm, 31.7° blaze Angle) which disperses the reading light spectrum. A THOR-SLM is placed in the Fourier plane of a  $f = 75$  mm lens where the beam spatial extension is 7 mm.

On the other arm, the light is passing through 3 mm of sapphire and 2 mm of  $\text{BaF}_2$  mm in order to compensate the phase dispersion introduced by the BS, the gratings and the lens. The group delay is also controlled using a translation stage. A future improvement of this 4f-line is to use a reflective grating and concave mirror. In this way, the phase compensation plates are no more necessary.

An Advantes spectrometer (550-950 nm) acquired the interferogram (Figure 70c). The FTSI technique is used to retrieve the relative spectral phase and to extract the polynomial fit coefficients with particular attention to the GDD coefficient ( $fs^2$ ).

The writing laser used is a blue fiber-coupled diode 650mW,  $\lambda_0 = 465\text{nm}$ ,  $d = 6\text{mm}$  focused in 3 different arrangements, schemed in Figure 70b):

1. Concave spherical lens ( $f=200$  mm) to generate a round focal spot of  $d=400$   $\mu\text{m}$  .
2. Cylindrical lens ( $f=150$  mm) focusing on the center of the dispersed light generating a Gaussian profile ( $\sigma = 1\text{mm}$ ) .
3. A beam splitter and cylindrical lens ( $f=150$  mm) form 2 gaussian profiles both  $\sigma = 1\text{mm}$ .



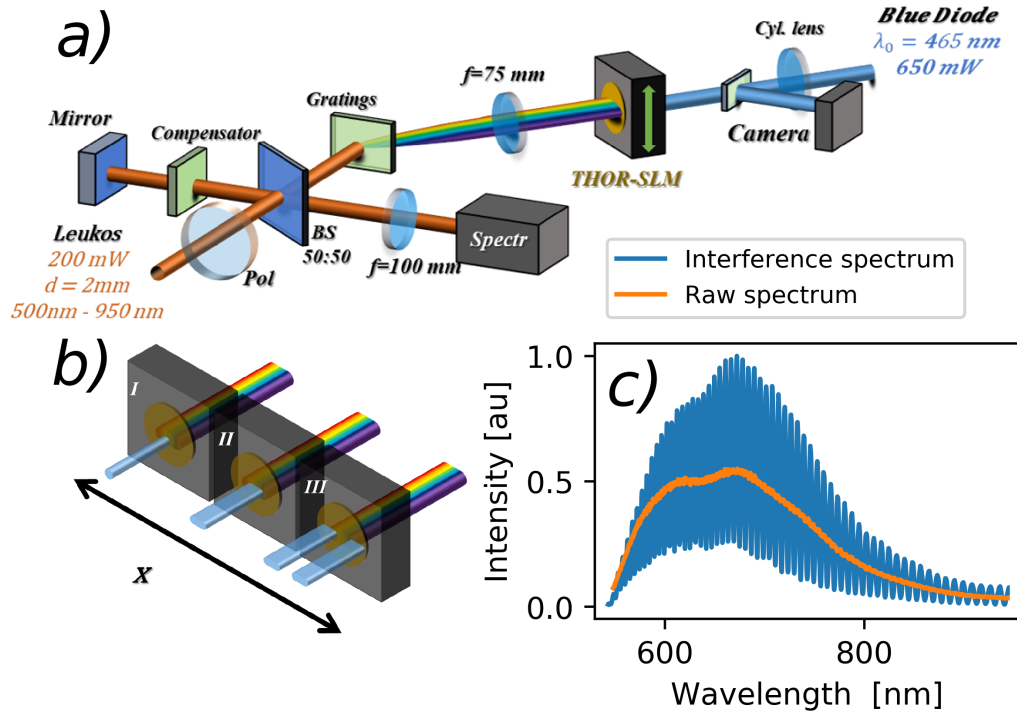


Figure 70: a) Experimental Set-up: a broadband Michelson interferometer is installed with a supercontinuum white light source (LEUKOS, 200 mW, 450-950 nm). A grating (300 Grooves/mm,  $31.7^\circ$  blaze angle) disperses the spectrum and the SLM is placed in the Fourier plane of  $4f$ -line in a folded configuration ( $f=75\text{mm}$ ). Writing laser is a blue fibre diode  $650\text{mW}$ ,  $\lambda_0 = 465\text{nm}$ ,  $d = 6\text{mm}$ . The three spatial addressing configurations (different focusing conditions) are shown in b). c) Raw spectra: one arm in orange, fringed spectrum in blue.

The phase shaping induced by these three configurations is discussed in the following. To estimate the THOR phase shaping capabilities, the un-modulated phase, e.g. the relative phase of the interferometer without blue light, is considered as a reference and subtracted in the following.

### 5.5.2 Estimation of the spectral phase resolution

The goal of this section is to estimate the spectral resolution of the  $4f$ -line, and therein the spatial resolution of the THOR-SLM, using tight addressing beam configuration (1). The writing beam diameter is then focused to  $0.4\text{ mm}$  over a partial part of the spectrum (around  $640\text{ nm}$ ). As Figure 71a) shows, unresolved fringes occur when the writing beam is turned-on (green curve). Here, the introduced phase is larger than  $\gg 2\pi$ , so the fringes pattern has an abrupt discontinuity. For such small writing beam size, the addressing flux applied is much higher (hundred of  $\text{W}/\text{cm}^2$ ) than the ones used in the previous sections (only a few  $\text{W}/\text{cm}^2$ ). A P-scan of the writing laser is performed to analyze the effect of such flux on the introduced phase. The experiment is performed with E7-Gold and MLC-Gold, MLC-chrome is not taken into account because of its low blue absorption. So, phase spectral maps are pictured in Figure 71 for E7-Gold(b) and MLC-Gold(c) as a function of wavelength and flux ( $\text{W}/\text{cm}^2$ ).

The maximum introduced phase and its related spectral width can be estimated from the spectral maps (Figure 71d) ). A linear dependence of the phase shift with the writing beam flux is measured for both prototypes. Hence, the temperature at which the LC refractive index starts to decrease non-linearly is not reached. So, the flux applied is not able to reach neither  $325\text{ K}$ ,

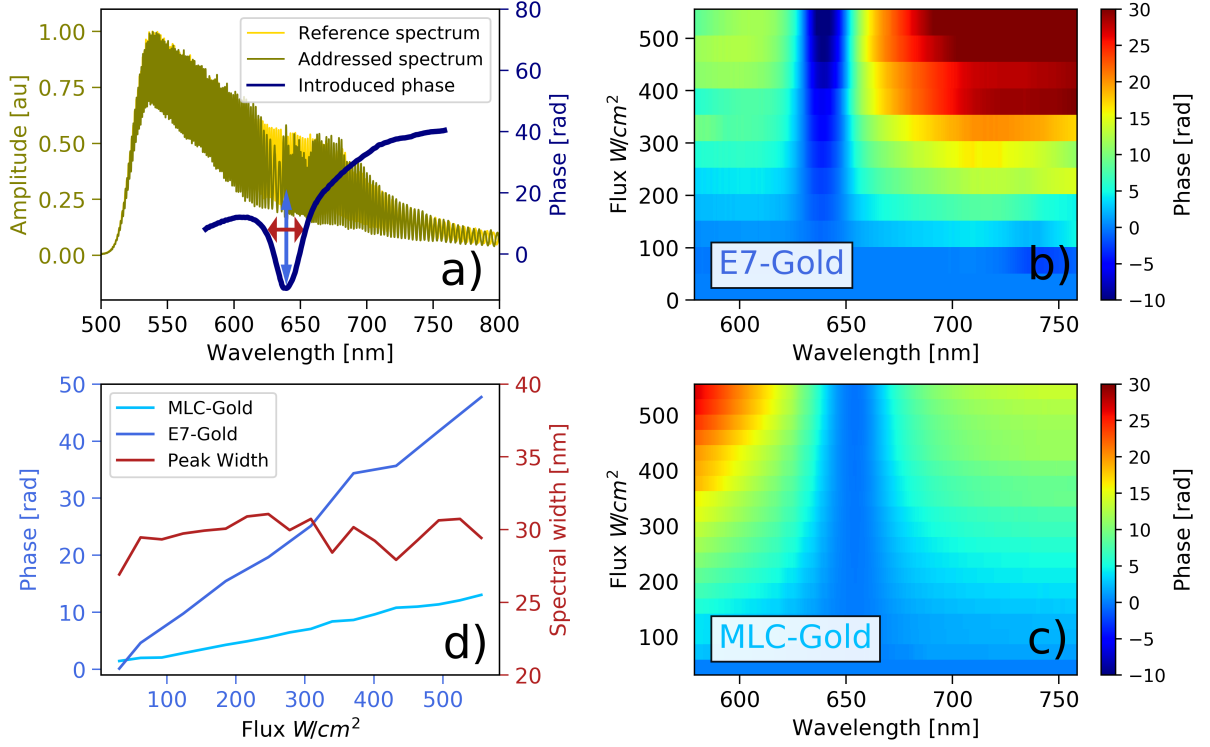


Figure 71: Estimation of the introduced phase resolution: a) Reference (gold) and addressed spectrum (green) with the relative phase shift (blue). The arrows indicates the phase amplitude peak (light blue) and its width (red). Spectral phase map as function of wavelength and writing flux for E7-Gold (b) and MLC-Gold (c). d) The maximum phase introduced for both SLMs (in blue) and the relative width (in red).

where this non-linearity appears for E7 mixture.

At  $500 \text{ W/cm}^2$  almost  $50 \text{ rad}$  are measured for E7-Gold, more than three times larger compared to MLC-Gold ( $14 \text{ rad}$ ). Nevertheless, the related refractive index variation ( $\Delta n$ ) is moderate: 0.051 for E7-Gold and 0.017 for MLC-Gold. Despite the high flux reached, no permanent damage is detected on THOR-SLM. Indeed, turning-off the writing light, the unresolved fringes disappear quickly, excluding any LC melting or metallic surface deterioration. Therefore, the expected high damage threshold of the LC mixtures is experimentally confirmed.

On the contrary, the peak width is found almost constant ( $30 \text{ nm}$ ) for both prototypes increasing the writing flux, hence the thermal gradient does not spread when the inner temperature increases. In Figure 71d), the width variation for E7-gold is also plotted (MLC-Gold is not shown for sake of visibility).

From the lateral extension of the full dispersed spectrum, it is possible to estimate the spatial size of the introduced phase shift and then of the thermal gradient. The spatial extension of the reading beam on the Fourier plane is  $7 \text{ mm}$ , which also corresponds to a spectrum of  $\sim 300 \text{ nm}$ . Therefore the unresolved fringes of  $30 \text{ nm}$  of Figure 71 spatially correspond to  $0.7 \text{ mm}$ . Thus, from a writing beam of  $0.4 \text{ mm}$  a phase shift of  $0.7 \text{ mm}$  is obtained, hence the thermal gradient spatially spread with a 2-fold factor compared to writing beam.

Despite the high flux reached, no permanent damage is detected on THOR-SLM. Indeed, turning-off the writing light, the unresolved fringes disappear quickly, excluding any LC melting or metallic surface deterioration. Therefore, the robustness of the device is experimentally

confirmed.

### 5.5.3 Spectral phase shaping

In this section, the remarkable ability of the THOR-SLM to introduce and shape the spectral phase in the range of 550-850  $nm$  is demonstrated, in particular a continuous control of the Group Delay Dispersion (GDD) with more 1600  $fs^2$  of chirp span. E7-Gold, MLC-Gold, and MLC-Chrome are tested in order to compare the effect of the Liquid Crystal and of the reflective layer.

With this purpose, second and third focusing configurations of section 5.5.1 are taken into account inducing a gaussian-like thermal gradient. The second configuration (single gaussian spot focused on the center of the spectrum) generates a higher temperature on the center of the dispersed spectrum. Therefore the negative variation of the LC refractive index makes a positive group delay dispersion. Conversely, when the writing beam is split in two and focused on the edges of the dispersed spectrum, a negative GDD is induced. A power-scan for each configuration and prototype is also performed to have continuous control of the phase and tune the group delay dispersion from negative to positive values.

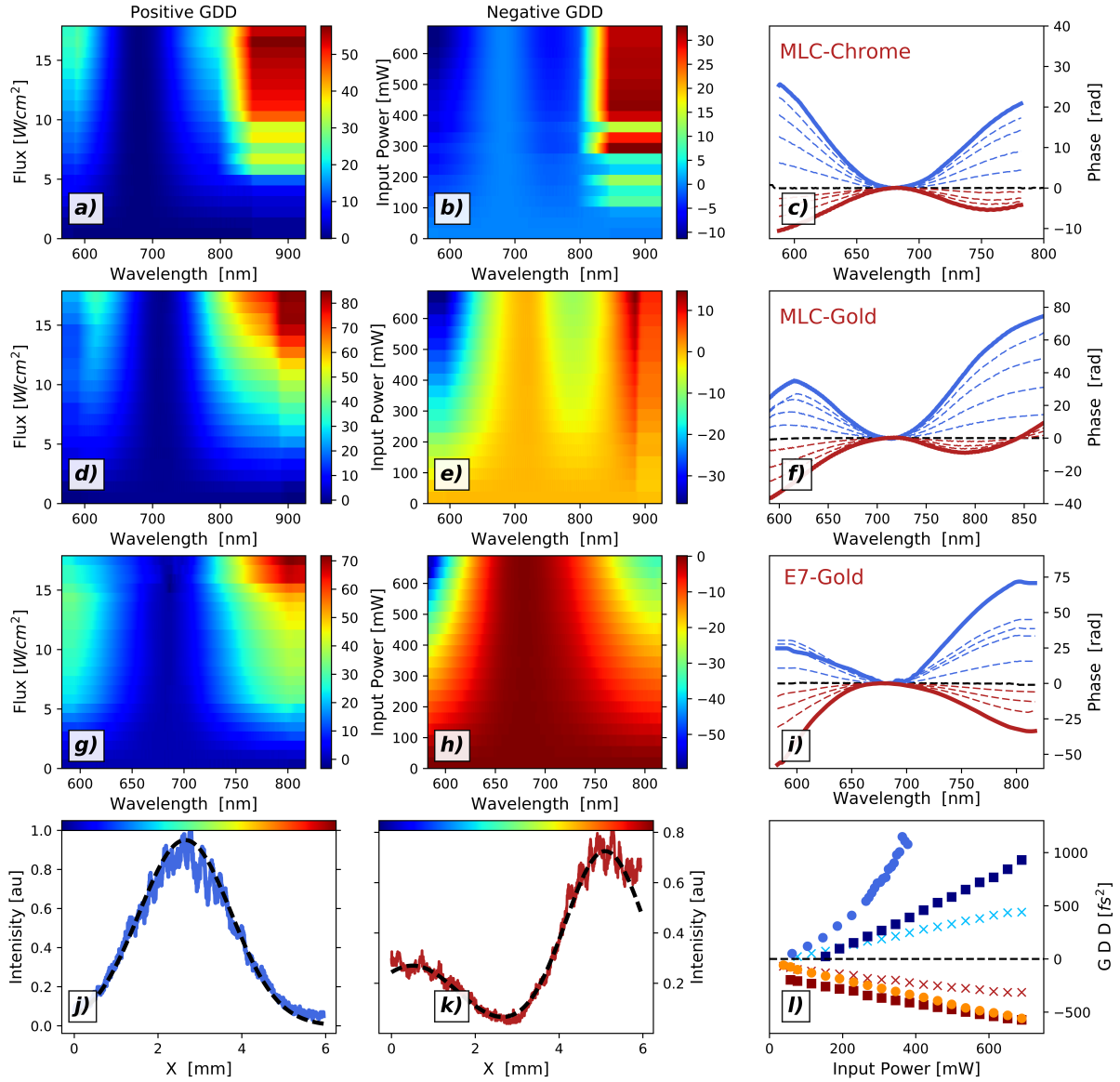


Figure 72: Phase maps for all the prototypes and for both configurations: MLC-Chrome in the first row (a,b,c), MLC-Gold in the second one (d,e,f) and E7-Gold in the last one (g,h,i). The first column (a,d,g) is related to a positive group delay excursion (second focusing arrangement), the second column (b,e,h) shows the spectral maps introducing a negative phase shift (third focusing arrangement). Some positive and negative spectral phase variation are plotted in the third column (c,f,i) for each prototype. In the last row, the relative spatial writing beam intensity profiles are plotted for the second configuration (j) and for the third one (k). Dotted black curves are the gaussian fit ( $\sigma = 1\text{mm}$ .) The colorbar features the chromatic reading beam spatial repartition. In the last graph (l), the GDD coefficients are plotted as a function of the blue writing power. In blue scale the positive variation, in red scale the negative one. The same mark is used to identify the prototype (spot E7-Gold, Squares MLC-Gold, Crosses MLC-Chrome).

Figure 72 summarizes the results for both configurations and for the three prototypes. Each row of the image is related to one of the prototype: first row to MLC-Chrome, second row to MLC-Gold and third row to E7-Gold. The columns, instead, represents the results for the different focusing arrangement: positive phase shifts are pictured in the first column as a function of the writing beam flux ( $W/cm^2$ ), negative GDD in the second one. For this last configuration, the spectral phase is pictured as a function of the writing beam power ( $W$ ) and not as a flux ( $W/cm^2$ ) because of the uncertainty about the blue spot areas. The last column shows some spectral phase profiles from the two different set-ups for better visibility of the continuous tunability. In the last row are plotted the relative intensity writing laser spatial profiles: one centered spot (j) and two spots on the edges (k). The last graph (l) shows the GDD fit coefficient ( $fs^2$ ) as a function of the writing light power for all the prototype and for both configurations.

**MLC-Chrome** MLC-chrome (first row of Figure 72) is the first prototype tested. The low absorption of the chrome induces the smaller phase shift, but almost a pure quadratic phase. The GDD span is about  $750 fs^2$ , with  $+400 fs^2$  in one configuration and  $-300 fs^2$  in the other one.

**MLC-Gold** MLC-Gold (second row of Figure 72) has a larger GDD excursion, with more than  $1000 fs^2$  span (respectively  $+930 fs^2$  and  $-500 fs^2$ ). The phase profiles induced are not perfectly parabolic due to the higher phase order, in particular the presence of some third-order dispersion (TOD) (Figure 72f).

**E7-Gold** The best results are achieved using E7-Gold (third row of Figure 72) with more than  $1600 fs^2$  of phase span.  $1050 fs^2$  (resp.  $-550 fs^2$ ) can be introduced focusing on the center (resp. on the edges) of the dispersed spectrum. This large phase span drastically would change the temporal duration of a laser pulse of  $300 nm$  bandwidth (e.g.  $6.3 fs$  at  $750 nm$ ). Indeed, it corresponds to more than 30 times the FTL<sup>2</sup> (*Fourier Transform Limited*): applying  $+1000 fs^2$  (resp.  $-500 fs^2$ ) the pulse duration passes from  $\sim 6 fs$  to  $460 fs$  (resp.  $230 fs$ ), e.g. more than 70 times longer.

The remarkable ability to control the GDD by the THOR-SLM is so then demonstrated in the last graph of Figure 72. Moreover, the non-linearity of the refractive index variation with the temperature is also found in the GDD excursion of E7-Gold (blue spot points of Figure 72l). For the other two SLM based on MLC2132 mixture, the group delay dispersion is still linear with the writing beam power.

The spectral phase asymmetry, not due to the isotropic transition, comes from the higher phase order introduced (TOD and FOD). They come mainly by the low "hand" control of the writing beam that can induce small dis-alignments on the writing-reading beams overlap.

In addition, the spectral phase is not only function of the birefringence excursion ( $\Delta n$ ) and LC thickness ( $L$ ) but also of the wavelength ( $\lambda$ ) ( $\Delta\varphi = L\frac{\Delta n}{c}$ ). Therefore the phase introduced at  $550 nm$  is 1.5 times larger compared to the one at  $850 nm$  for the same SLM and for the same birefringence excursion. For this reason the intensity spots to introduce a negative GDD have not the same intensity. In particular, the red part has to be addressed with more power in order to get the same phase shift than the blue one. In the presented case the ratio between the amplitudes plotted is 0.37. This study is deepened in chapter 6 where a broader spectrum requires more precise addressing.

Nevertheless, this configuration is applied to phase correction of an ultrafast laser pulse ( $\lambda_0 = 1028 nm$ ,  $400 fs$ ,  $80 MHz$ ). The results are described in Appendix (D.4.1).

## 5.6 Conclusions & prospectives

To conclude, all the results achieved so far have led to a new phase only pulse shaper based on LC: THOR-SLM. The new device is presented with its innovations and potentialities with respect of the traditional LC-SLM. The innovative thermo-optical addressing configuration using a writing-reading arrangement overcomes the common issues related to the Electrical-driven SLM. In particular:

- Without any electrodes the LC spectral acceptance is finally fully exploited. Therefore broadband spectral light can be addressed continuously.
- Pixelation induced by the electrodes matrix is completely solved.
- THOR-SLM is compatible with thick nematic layers. Furthermore, the reflective configuration enables to double the effective thickness.
- No limitations to THOR-SLM lateral dimensions can improve the spectral resolution of the pulse shaper.
- The dynamical change of birefringence is workable during both turning-on and turning-off, reducing the resting time between two consecutive excursions.
- The time to perform the excursion is comparable with the ultrafast group delay line presented in chapter 3. THOR-SLM is considerably faster than the electric switching-off or adiabatic control, but a bit slower than the electric switching-on dynamic.

Three different prototypes (E7-Gold, MLC-Gold and MLC-Chrome) are designed and developed in order to find the best LC mixture and, at the same time, the best reflective layer. Spatial and spectral phase shifts are measured in different configurations for all the prototypes highlighting merits and drawbacks for each of them. Table 17 summarizes these results. E7 is found more accessible than MLC2132 because of its lower clearing point temperature, while Gold is confirmed as the best reflective layer in terms of absorption.

Several THOR-SLM applications are also disclosed in the appendix: A defocusing tunable lens exploiting the spatial phase shift is demonstrated at  $1.5 \mu\text{m}$ . Moreover, THOR-SLM shaping capabilities are validated when inserted in a 4f-folded line configuration. The phase management of broadband light ( $300 \text{ nm}$ ) or a narrower femtosecond pulse ( $300 \text{ fs}$ , e.g.  $11 \text{ nm}$  centered at  $1030 \text{ nm}$ ) is also demonstrated.

Nevertheless, all the potentialities of THOR-SLM have not been expressed. In fact, the achromaticity has been shown only between  $500\text{-}1500 \text{ nm}$ , but it can be largely extended to infrared wavelengths, a priori up to  $3000 \text{ nm}$ . Similarly, the LC isotropic-transition is not always reached, therefore the full birefringence excursion is not performed.

Therefore an even broader spectrum can be phase modulated if some limitations encountered are solved. In more details:

- The spatial profile of the thermal gradient inside the THOR-SLM and the propagation of the heat in the different components have to be studied and simulated.
- THOR-SLM spectral/spatial resolution must be measured with better accuracy.
- An improvement of the writing beam control must be integrated into the arrangement.

All these limitations have been solved in Chapter 6 leading to a multi-octave phase-only pulse shaper.

THOR SLM results		E7-Gold	MLC-Gold	MLC-Chrome	E7-Gold-25	E7-Gold-110
<b>Spatial Phase Shift</b>	$\Delta\varphi$ [rad]	200	32	22	//	//
	$\Delta n$	0.2	0.034	0.021	//	//
	$OPD$ [ $\mu\text{m}$ ]	-11.65	-1.9	-1.2	//	//
<b>Group Delay Adiabatic</b>	$\Delta n_g$	0.217	0.075	0.032	0.12	0.07
	$\Delta\tau_g$ [fs]	72	25	10	16	51
	$\Delta\varphi^2$ [ $f s^2$ ]	30	12	6	12	20
<b>Group Delay Dynamics</b>	$\Delta n_g$	0.2	0.06	//	//	//
	$\Delta\tau_g$ [fs]	40	23	//	//	//
	$Time_{80\%}$ [s]	12.25	13.75	//	//	//
	$\delta\tau$ [fs]	1.1	1.5	//	//	//
<b>GDD</b>	Positive [ $f s^2$ ]	+1050	930	450	//	//
	Negative [ $f s^2$ ]	-560	-500	-300	//	//

Table 17: Summary table of the different prototypes performances.

## Chapter 6

# Phase shaping of a multi-octave light source

### Objective

In this chapter, the spectral phase shaping capabilities of THOR-SLM are demonstrated from 540 nm to 2500 nm, which is a frequency bandwidth larger than 450 THz, modulating a multi-octave light source. The introduced phase is measured using FTSI technique in a Michelson configuration. The writing laser is spatially modulated by a digital processing mirror to improve the phase control. Therefore, continuous, smooth, arbitrary and large phase modulation is demonstrated over more than 2000 nm. The total chirp span ( $> 20fs^2$ ) is large enough to significantly shape single-cycle pulses or even transient electric fields.



## 6.1 State-of-the-art of ultra-broadband phase shapers

As introduced in chapter 1, pulse shaping is a key element to reach and develop ultrashort laser pulses. The growing development of few-cycle and even multi-octave light sources (Marcus, 2019; Wang et al., 2019; Dubietis, Couairon, & Genty, 2019; Vasilyev et al., 2019) requires innovating pulse compression scheme with adequate spectral bandwidth.

As mentioned in the introduction, several advanced optical devices enable ultrafast pulse shaping, among them gratings and grisms combinations (Walmsley, Waxer, & Dorrer, 2001), zero-dispersion line (Froehly et al., 1983), AOPDF (Tournois, 1997), and chirped mirrors (Pervak, Naumov, Krausz, & Apolonski, 2007).

Spectral acceptance bandwidth of such devices has been extended to handle large bandwidths and even few-cycle pulses for some of them.

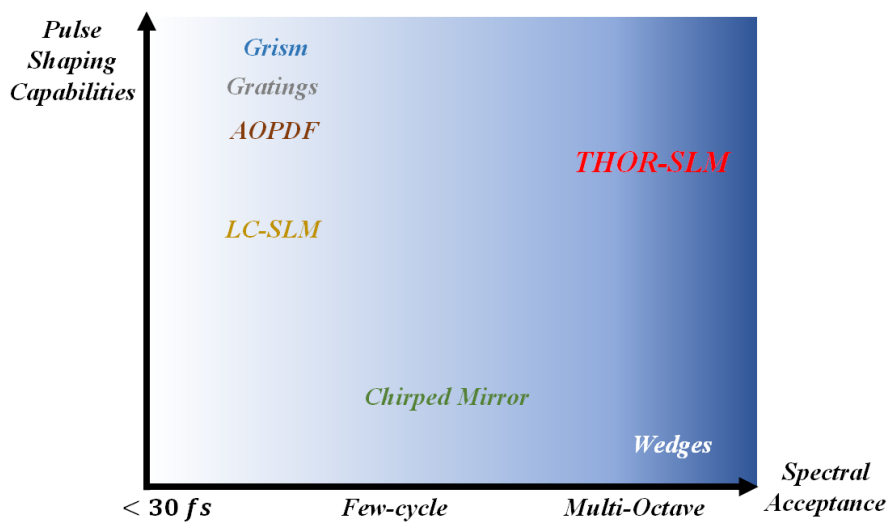


Figure 73: Scheme of the common ultrafast pulse shaper in terms of spectral phase tunability and spectral acceptance.

However, as shown in the scheme of Figure 73, an increase of spectral acceptance is generally accompanied by a decrease in pulse shaping capabilities. Not all of them can handle multi-octave pulses. For instance, AOPDF, although very versatile in terms of spectral shaping, cannot modulate pulses shorter than 10 fs at 800 nm (Tavella, Marcinkevičius, & Krausz, 2006; Tavella et al., 2007).

In the few-cycle regime, most recent results in pulse compression are all obtained by a combination of bulk plates, wedges, and chirped mirrors (Lavenu et al., 2019).

Commercial chirped mirrors present a maximum spectral bandwidth of 500-600 nm in the visible or NIR spectral range (Pervak, Ahmad, Trubetskov, Tikhonravov, & Krausz, 2009), but their tunability is possible only through multiple reflections, hence quite limited. At the forefront of the technical state of the art, chirped mirrors able to extend the spectral acceptance have been demonstrated using the channel parametric synthesizer technique (Huang et al., 2011). In particular, a continuous control of more than 100 fs of group delay (GD) has been reached over  $> 2$ -octave spectral bandwidth (530 nm- 2200 nm) in (Chia et al., 2014) (Figure 74a). More recently, a even broader spectral bandwidth of 3-octave span (370-2700 nm) has been phase modulated, with net discontinuities in group delay (Figure 74b) (Razskazovskaya, Krausz, & Pervak, 2017). However, those results have been reached using a complex system that first divides and then recombines several adjacent optical bandwidths. In addition, those mirrors can shape the group delay only, with also strong oscillations due to the Gires-Tournois effect (Gires

& Tournois, 1964) (see Figure 74a) ).

So, to the best of my knowledge, no phase modulators able to arbitrary shape a light of 2000 nm (450 THz) spectral bandwidth has been ever demonstrated. In this sense, THOR-SLM can be one of the pioneers, showing for the first time that such short pulses can be continuously compressed or stretched with a unique single stage.

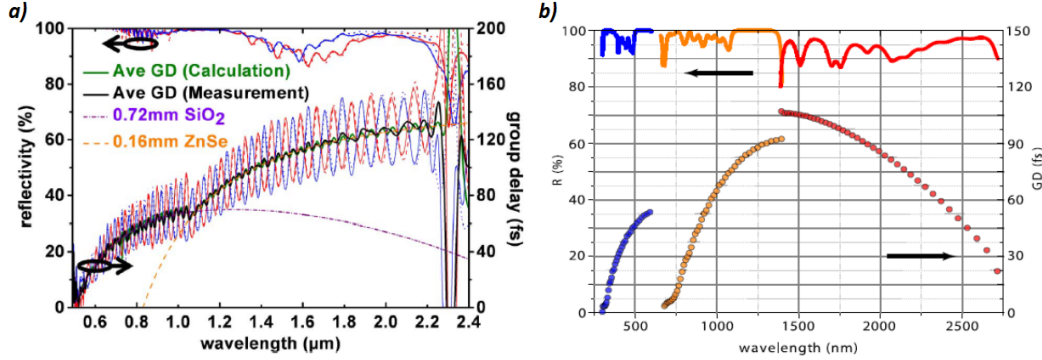


Figure 74: State of art of the best chirped mirrors in terms of spectral acceptance: left continuous Group Delay control by (Chia et al., 2014), right discontinuous phase control over  $> 3$ -octave span by (Razskazovskaya et al., 2017)

## 6.2 Introduction

In chapter 5, the spectral acceptance of the THOR-SLM has already been demonstrated from 500nm to 1  $\mu\text{m}$ . Nevertheless, all its capabilities have not been completely disclosed yet. Indeed, according to the spectral acceptance of THOR-SLM components (E7 mixture, Gold mirror, and BK7 substrate), the device can phase modulate spectrum that extends up to the near-infrared wavelengths. In particular, THOR-SLM can *a priori* handle light spectrum up to 3000 nm: this limitation comes from E7 resonance absorption and from the spectral transmission of the BK7 window<sup>13</sup>. Therefore, the goal of the chapter is to demonstrate the phase shaping ability of the device over such a broad bandwidth. Thus, it is more convenient to quantify the spectral components in frequency (THz) rather than wavelength.

On the other hand, some limitations in the writing beam management were identified in the previous chapter.

To improve the phase management some issues found in chapter 5 have to be solved:

- The thermal gradient characterization
- The pump laser control

The spatial profile and the amplitude of the thermal gradient inside the device are calculated in this chapter. Numerical simulations are performed in order to characterize the heating process of the LC layer to improve the control of the phase modulation. From these simulations, the spatial resolution of the device can be also estimated.

In addition, after these developments, a new writing beam arrangement involving a digital mirror is developed. Multi-octave ( $\sim 450\text{THz}$ ) phase shaping is demonstrated, with pure quadratic or cubic phase shifts. Finally, in section 4, the effect of the writing laser energy and of the LC layer thickness are analyzed showing future step forwards in phase shaping performances.

The prototype used for all these experiments is E7-Gold because of its larger phase dynamics, as demonstrated in chapter 5.

<sup>13</sup><https://refractiveindex.info/?shelf=glass&book=BK7&page=SCHOTT>

## 6.3 Estimation of the thermal gradient in THOR-SLM

### 6.3.1 Numerical simulations

Despite the analysis disclosed so far, the thermal gradient inside THOR-SLM is not yet completely characterized. To get a numerical simulation of the thermal gradient inside the LC layer, the heat equation has to be solved. The following hypothesis are then considered.

The device, sketched in Figure 75, is described with a cylindrical symmetry where the different

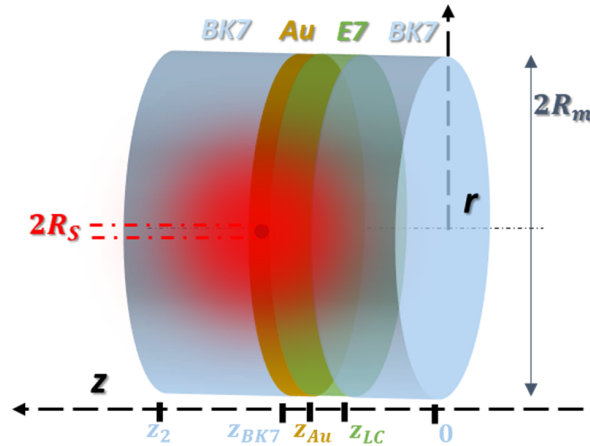


Figure 75: Scheme of the THOR-SLM for thermal calculations. Grey area refer to the glass substrates, yellow to Gold layer, and green to LC layer.  $r$  is the radial coordinate and  $R_m$  the maximum source diameter.  $z$  is the propagation direction and  $z_i$  delimits the thickness of medium  $i$ .

THOR-SLM elements succeed each other along the  $z$  direction. Along the radius (cylindrical coordinates  $r$ ) all the components are considered isotropic. The PVA layer, for LC molecules anchoring, is neglected. Therefore a direct contact between the Gold Mirror (heat source) and the LC is assumed during the heat transfer. The environment temperature ( $T_0 = 298K$ ) is kept constant in time and the heat source is spatially characterized by a function  $P(r, z)$ . At the thermal equilibrium and with no internal heat generation, the temperature  $T(r, z)$  is governed by (baron Fourier, 1822; Kasprzack, 2014; He et al., 2017):

$$\alpha_m \nabla^2 T(r, z) + \frac{P(r, z)}{\rho_{Au} C_p(Au)} = 0 \quad (6.1)$$

$$\alpha_m = \frac{\kappa_m}{\rho_m C_p(m)} \quad (6.2)$$

where  $\alpha_m$  is the thermal diffusivity of the medium  $m$  ( $\kappa_m$  is the thermal conductivity,  $\rho_m$  the volumic density,  $C_p(m)$  the specific heat). Hence, it is assumed that all the heat generated in the gold layer is spread through the device. Table 18 summarizes the thermal properties of the different layers involved in the heat transfer.

The heat equation (6.1) is numerically solved with *Mathematica* (Wolfram, 1999) by taking into account the following boundaries conditions, according to Figure 75:

- if  $r = R_m$ , then  $T = T_0$  (Dirichlet condition)
- if  $z = 0$  and  $z = z_{s2}$  (Neumann condition), then:

$$-h \frac{\partial T}{\partial z} = \kappa_{air} (T(r, z) - T_0) \quad (6.3)$$

where  $R_m$  is the cylinder radius,  $T_0$  the environment temperature,  $z_{s2}$  localizes the BK7-Air surface, and  $\kappa_{air}$  is the air convection exchange coefficient fixed to  $10W/m^2K$ . The maximum

Layer	Material	$\kappa_m$ [W/(mK)]	$\rho$ [g/cm <sup>3</sup> ]	$C_p$ [J/(gK)]	$\alpha$ [m <sup>2</sup> /s]	$L$ [mm]
Substrate 1	BK7	1.14	2.51	0.858	$5.1 \cdot 10^{-5}$	6
Metal	Au	317	19.3	0.129	$1.27 \cdot 10^{-4}$	$1 \cdot 10^{-3}$
LC	E7	0.13	1	0.67	$1.93 \cdot 10^{-7}$	$50 \cdot 10^{-3}$
Substrate 2	BK7	1.14	2.51	0.858	$5.1 \cdot 10^{-5}$	6

Table 18: List of relevant parameters of different layers.  $\kappa_m$  is the thermal conductivity,  $\rho$  the volumic density,  $C_p$  the specific heat,  $\alpha$  the thermal diffusivity,  $L$  the thickness.

flux is  $1W/cm^2$  for  $R_S = 2$ . Furthermore,  $P(r)$  is described by a SuperGaussian profile (m=20).

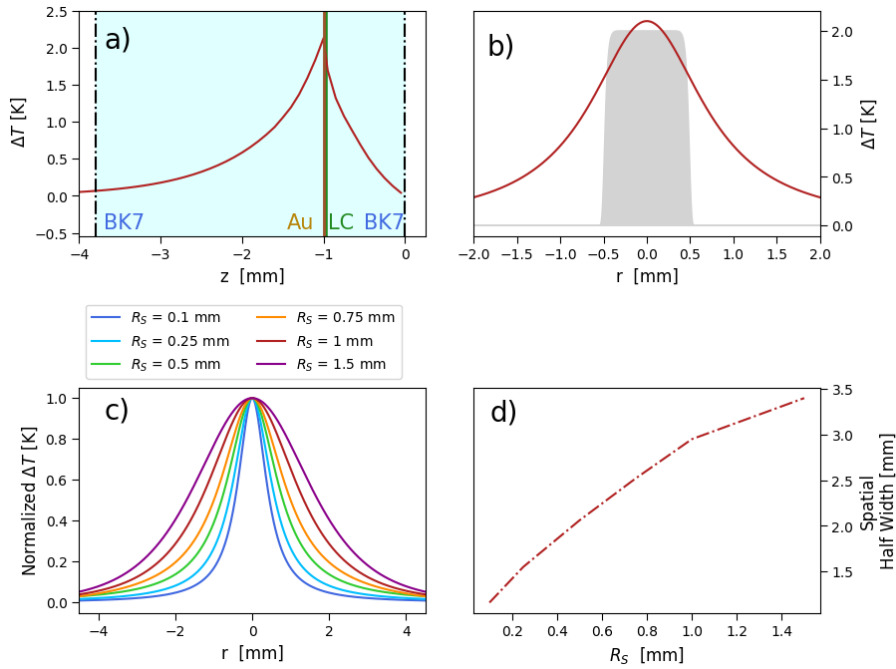


Figure 76: a) Temperature profile along  $z$  direction crossing THOR-SLM layers for  $r=0$ , and  $R_S = 0.5$  mm. b) Increase of the temperature  $\Delta T$  at  $z = z_{Au}$  as a function of  $r$  (orange) for  $R = 0.5$  mm (illumination source spatial profile indicated in grey). c) Normalized Increase of the temperature  $\Delta T$  at  $z = z_{Au}$  as a function of  $r$  for various  $R$  values. d) Thermal gradient width (at  $1/e^2$ ) as a function of the writing beam radius.

Some results are plotted in Figure 76. In a) the temperature profile along the  $z$  direction (at  $r = 0$ ) is plotted crossing the different materials. From this figure comes out that both windows surrounding the LC layer are heated as well, especially the thick mirror substrate. This has a clear contribution to the overall heating of the LC.

Figure 76b) features the spatial distribution of the temperature at the interface LC-Gold (eg  $z = z_{Au}$ ), for  $R_S = 500\mu m$ . The temperature increases of  $2K$  and the thermal gradient exhibits a Lorentzian shape, expanding well beyond the illumination source (shown in grey). This is further investigated by changing the source radius ( $R_S$ ), as shown in Figure 76c). This figure displays the normalized increase of temperature for  $R_S$  ranging between  $100\mu m$  and  $1.5$  mm.

This broadening is quantified in Figure 76d) where the half spatial width of the thermal gradient (at  $1/e^2$ ) is plotted for each  $R_S$ . The progressive broadening and rounding of the thermal gradient when the beam diameter increases is so visible. This demonstrates that the flux of the writing laser is not the only parameter governing the thermal excursion, but also the beam size affects the thermal gradient spatial profile. This has to be taken into account in the following.

### 6.3.2 New writing beam arrangement: arbitrary control of the writing beam

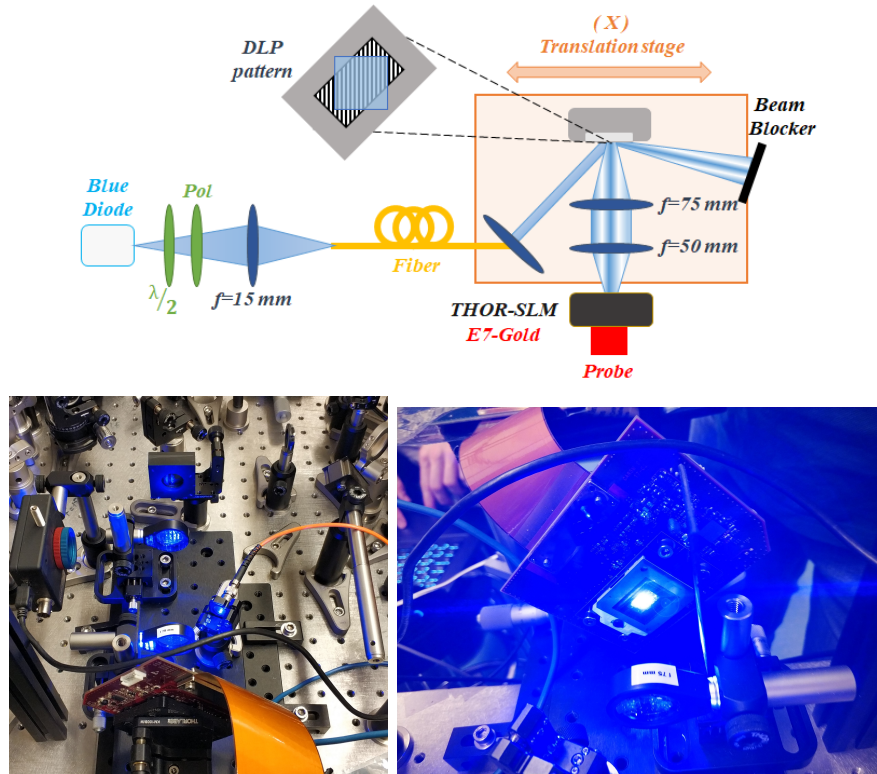


Figure 77: New writing arrangement: a blue diode is passing through a polarizer, a half-wave plate and is focused into a square-core fiber. The writing beam is then reflected on a Digital mirror (DLP) and imaged onto the rear of THOR-SLM. Fiber output, DLP and lenses are all placed on a translation stage. A sketch of the blue spatial profile over the DLP is also shown.

The main experimental limitations in the phase shaping results found in chapter 5 come from the writing laser. Indeed the manual spatial control of the blue beam has to be improved in order to get more degrees of control onto the spectral phase modulation. A more powerful diode is also needed to efficiently address THOR-SLM. Therefore, a new writing laser arrangement is proposed, involving a more powerful writing diode and a digital processing mirror. The set-up is the following (Figure 77).

The new writing light is a blue diode ( $\lambda_0 = 450 \text{ nm}$ ) delivering an uncollimated beam of  $2.5 \text{ W}$ <sup>14</sup>. A half-wave plate combined with a polarizer tune the writing beam power. The beam is then focused ( $f=15\text{mm}$ ) into a multi-mode square-core fiber ( $150\mu\text{m} \times 150\mu\text{m}$ ). The fiber transmission is 70% and at the output a collimated beam illuminates a Digital Light Processor (DLP6500, by Texas Instrument)<sup>15</sup>. This device comprises more than 2 million controllable micromirrors with a high spatial resolution ( $1920 \times 1080$ ) and a modular surface of  $117 \text{ mm}^2$ . Dedicated python code is developed in order to introduce an arbitrary 2D pattern and so modify the spatial profile of the writing beam. To maintain the reflected beams in the propagation plane, the DLP is

<sup>14</sup>[https://www.banggood.com/LA03-3500-450nm-3.5W-Blue-Laser-Module-TTL-Modulation-Fan-Heat-Sink-for-EleksMaker-DIY-Engraver-p-1103261.html?rmmids=search&cur\\_warehouse=CN](https://www.banggood.com/LA03-3500-450nm-3.5W-Blue-Laser-Module-TTL-Modulation-Fan-Heat-Sink-for-EleksMaker-DIY-Engraver-p-1103261.html?rmmids=search&cur_warehouse=CN)

<sup>15</sup><http://www.ti.com/tool/DLI-3P-DLI6500>

rotated at  $45^\circ$ , as illustrated in Figure 77. One reflection is relay-imaged with short focusing lenses ( $f=75\text{ mm}$  and  $f=50\text{ mm}$ ). The DLP pattern is then imaged on the rear of THOR-SLM. However, a consistent part of the power ( $> 50\%$ ) is lost and in the best of the case, e.g. no pattern uploaded,  $600\text{ mW}$  are then available on the rear of the SLM. The fiber output, the DLP, and the lenses are all placed on a translation stage that can move transversally, along ( $x$  direction) to spatially overlap writing-reading beams (see Figure 77).

Since the writing laser spatial profile is not any more homogeneous spatially, in the following the writing laser power replaces the flux as relevant experimental parameter.

### 6.3.3 Experimental estimation of the thermal gradient

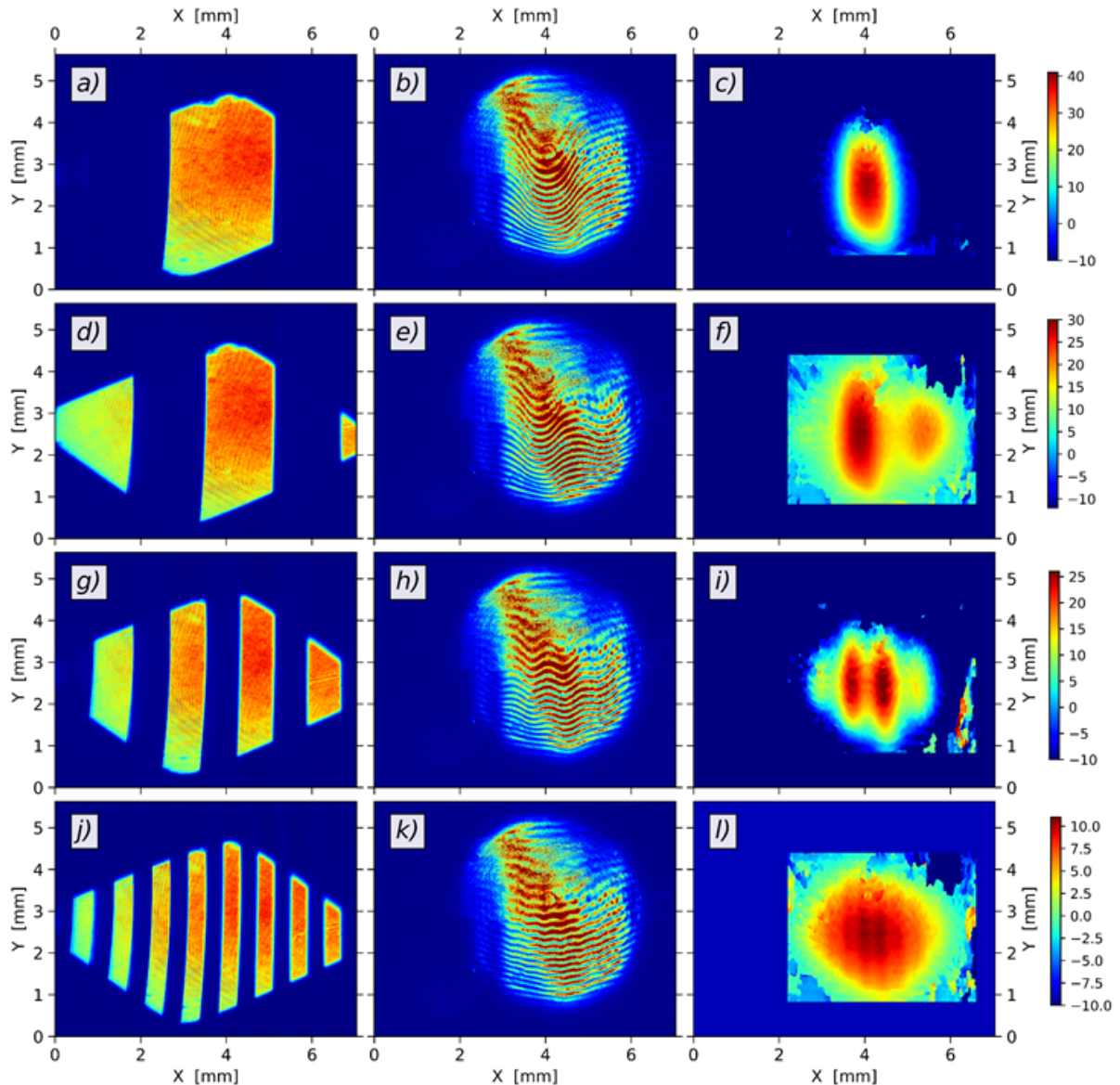


Figure 78: Addressing patterns (first column), measured fringes shift (second column) and spectral map (third column) changing the period step of the stripes. Each row represents a different number and periodic step: from 1 stripe of  $3.75\text{ mm}$ , to 8 stripes of  $0.5\text{ mm}$  thick (last row).

As in Chapter 5.3 a He-Ne based Michelson interferometer is implemented and the spatial fringes

## 6. Phase shaping of a multi-octave light source

patterns are analyzed using a CCD. The experiment consists in uploading on the DLP several images composed by some vertical periodic binary stripes with a duty cycle of 50%. The step period, defined as the distance between two consecutive maxima, is progressively decreased. The spatial phase shift induced by this inhomogeneous light addressing is then analyzed using a 2D-FFT analysis. This characterization is summarized in Figure 78.

In the first column are shown the blue light patterns measured in the THOR-SLM plane. The second column represents the acquired images, showing the shift of the fringes because of the introduced phase. Finally, on the last column, the spectral maps retrieved by 2D-FFT are pictured. Each row of Figure 78 shows a different pattern uploaded on the DLP, from a single stripe of 3.75 mm width up to 8 narrower stripes of 0.5 mm width spaced by the same distance.

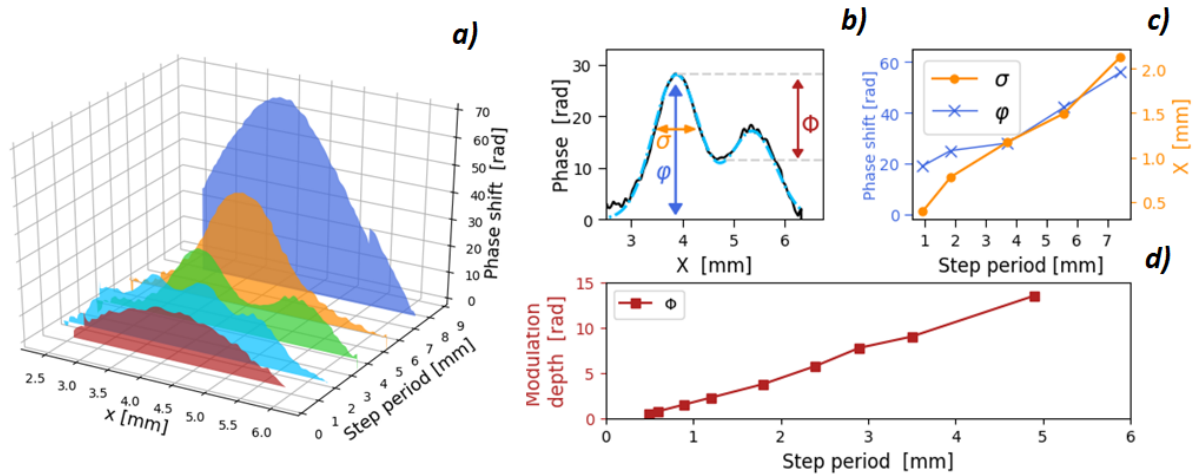


Figure 79: a) Horizontal cut of the phase map for different periodic steps (blue = 7.44 mm, orange = 5.58 mm, green = 3.72 mm, light-blue = 1.86 mm, red = 0.93 mm). b) Introduced phase of 3.72 mm (black curve) with its multi-gaussian fit (light blue dotted curve). The arrows refer to the maximum phase introduced ( $\varphi$  blue), the phase width ( $\sigma$  orange) plotted with the same colour in c) as function of the step period. The modulation depth ( $\Phi$  red arrow in b)) is plotted in d).

Several informations about the DLP addressing, but also about the spatial resolution of THOR-SLM can be estimated thanks to this characterization. The fringe shift visible in the second column, suggests a large phase shift ( $2\pi$ ) introduced by the stripes. Those deformations are still distinguishable even in the last row. To quantify the introduced phase, in Figure 79a) some horizontal plot profiles of the phase maps (last column of Figure 78) are shown. The global shape of the induced phase varies considerably when the step period is decreased. When a single stripe is used, an intense Gaussian-like phase profile is measured (blue and orange curves). The intensity and the lateral extension increase with the stripe width. This agrees with the conclusions of section 6.3.1, e.g. with large writing beams the inner thermal gradient is found even larger, with a Gaussian-like profile.

Loading more stripes, the overall phase shift is smaller due to a lower power deposited on the rear of the device. More interestingly, the periodicity of the pattern is translated to a sinusoidal modulation super-imposed to a large radial phase gradient. The full phase profile can be actually fitted using a multi-Gaussian like profile as shown in Figure 79b), e.g. the linear combination of narrower Gaussians corresponding to a single thermal gradient generated by a single stripe. At the highest spatial frequencies a thermal gradient that is not anymore Gaussian, but closer to a Lorentzian profile is induced. Phase peaks are still detectable even for the closest fringes pattern, however, their size and relative distance are too short to be fitted.

The maximum phase shift and the lateral extension of the phase peaks can be estimated. Both are plotted in as a function of the step period Figure 79c). The phase width evolves linearly with the pattern width. Therefore, the theoretical prediction of section 6.3.1 about the thermal

gradient broadening and rounding are experimentally confirmed.

In addition some useful informations about THOR-SLM spatial resolution can be retrieved. The influence of several addressing stripes can disclose some indications about the thermal gradient spreading in the device. The modulation depth, e.g. the difference between the maximum and the local minimum between two consecutive maxima (red arrow of Figure 79b) ) increases linearly with the step period, as shown in Figure 79d). A periodic pattern of  $0.5\text{ mm}$  can introduce still distinguishable phase peaks, however the modulation drops to  $\sim 1\text{rad}$  with an overall phase shift of  $15\text{rad}$ . It means that the thermal gradient spreading will strongly affects the spatial resolution of the device, in agreement with the theoretical section 6.3.1. For the current prototype, a compromise between the phase dynamic and the desired spatial features have to be determined, depending on the applications.

To conclude, in this section a new writing laser arrangement is proposed and developed to improve the THOR-SLM phase shaping capabilities. A new powerful diode and a digital mirror (DLP) are installed, although the overall useful blue light power is still  $\sim 600\text{ mW}$ . This new implementation provides an arbitrary control of the spatial profile of the writing beam. Finally, as expected by its thermal nature, THOR-SLM spatial resolution has to be balanced with the required phase modulation, in agreement with device based on thermal processes such as deformable mirrors (Kasprzack, 2014).

## 6.4 Ultra broadband interferometer

### 6.4.1 Experimental set-up

The goal of the next sections is to demonstrate that THOR-SLM can modulate the phase of an ultra-broadband light from visible to infrared spectral range. Therefore, an ultra-broadband Michelson interferometer is installed using the fiber super-continuum from Leukos (Electro-Visir-250-VIS-IR,  $650\text{ mW}$ ,  $2\text{ mm}$ ,  $120\text{-}550\text{ THz}$ ). Laser beam is split in two, using a broadband beam splitter. On one way the spectrum is dispersed passing through few mm ( $\sim 5.5\text{ mm}$ ) of a thin glass wedge ( $11^\circ$ ) (Figure 80a) ).

THOR-SLM is placed in the Fourier plane of a folded  $4f$ -line including a  $f = 500\text{ mm}$  concave mirror. The device is optically addressed with the arrangement described in the previous sections. On, the other arm, the broadband spectrum is passing through a phase compensator stage composed of  $3\text{ mm}$  of Sapphire,  $2\text{ mm}$  of *UVFS*, and  $2\text{ mm}$  of *BaF2* to balance the large dispersion introduced by the glass wedge. This phase compensation is necessary for this proof-of-conceptual experimental in order to measure the actual phase introduced by THOR-SLM and so demonstrate its phase shaping capabilities. Nevertheless, in the future this phase compensation must be removed if a multi-octave pulse aims to be compressed or stretched. Other ways to disperse such broadband spectrum, which can be easily phase compensated by THOR-SLM itself, are discussed in the last section of this Chapter (Prospectives).

The broadband interference pattern is then analyzed using three different spectrometers to collect the full spectral bandwidth (Advantes  $300\text{-}545\text{ THz}$ , Advantes  $300\text{-}330\text{ THz}$ , NIRQuest Ocean Optics  $120\text{-}300\text{ THz}$ ) (Figure 80b) ) shows the recovered interference spectra for a group delay of  $120\text{ fs}$  between the two arms. The measurement of all the spectral components enables to recover the overall spectral phase without discontinuity. The spectral relative phase is measured by FTSI technique and subtracting the phase without thermo-optical addressing, used as a reference. The residual first-order term of the spectral phase, if any, is also subtracted.



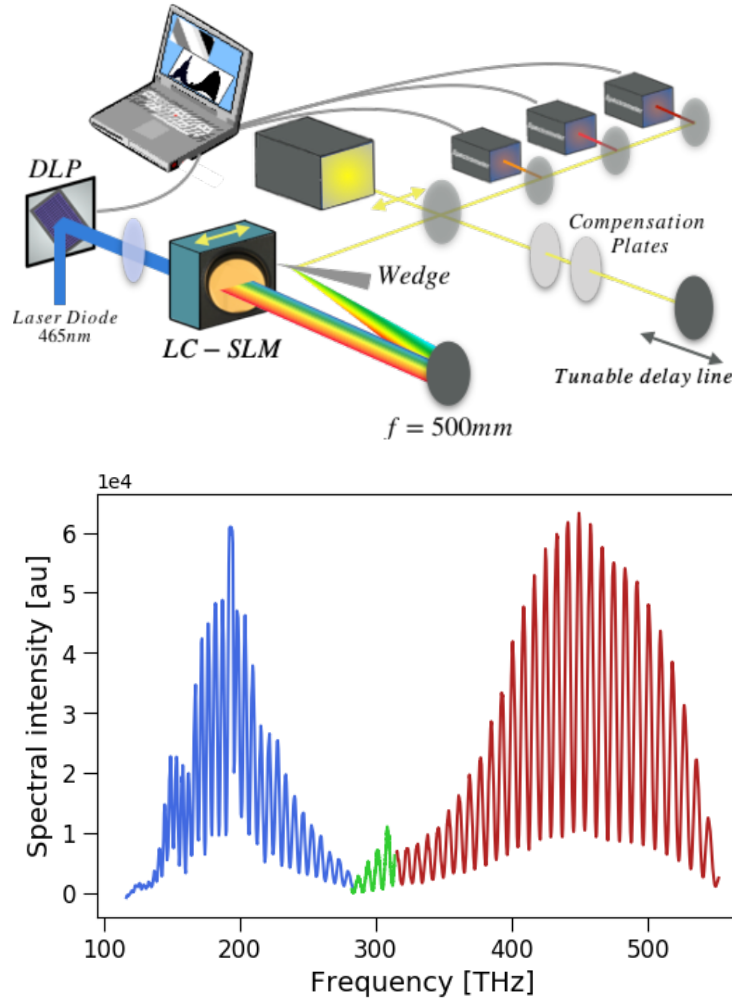


Figure 80: Experimental setup: a) the ultra-broadband light source seeds a Michelson interferometer for referenced phase shaping measurement. The THOR-SLM is inserted in a 4f-line in a folded configuration ( $f=500\text{ mm}$ ). Yellow arrow indicates the laser polarization direction and the extraordinary axis of the LC layer. b) Typical acquired spectra. Different color lines refer to the three different spectrometers.

#### 6.4.2 THOR-SLM spectral reflectivity

The first test concerns the THOR-SLM spectral acceptance bandwidth. Up to now, it is assumed large enough to cover such broadband spectra, however, it has never been verified. In Figure 81, the reflectivity of E7-Gold and MLC-Chrome are plotted. As a matter of fact, the broadband spectral acceptance is verified larger than an octave, from  $120\text{ THz}$  to  $550\text{ THz}$ .

The limitation in the visible edge comes from the source. However, E7-Gold reflectivity is limited for higher frequencies because of the gold layer. Conversely, MLC-Chrome does not have this restriction, hence, devices with a silver reflective layer can be fabricated in the future to further extended the spectral acceptance.

On the other edge, the light source limits again the measurements to  $120\text{ THz}$ , even if the LC application could be extended, in principle, until  $100\text{ THz}$  (Lin, Wu, Chang, & Hsu, 2004; Wu, 1987). Nevertheless, an overall decrease of the reflectivity is measured for both prototypes below  $250\text{ THz}$ . This is probably due to the BK7 window spectral absorption<sup>16</sup>. Thus, one solution to increase the reflectivity is to replace it with a  $\text{CaF}_2$  or Sapphire window, both transparent even at those wavelengths.

A difference between the two prototypes is measured between  $120\text{-}200\text{ THz}$ . In particular, the

<sup>16</sup>[https://www.thorlabs.com/NewGroupPage9.cfm?ObjectGroup\\_ID=1117](https://www.thorlabs.com/NewGroupPage9.cfm?ObjectGroup_ID=1117)

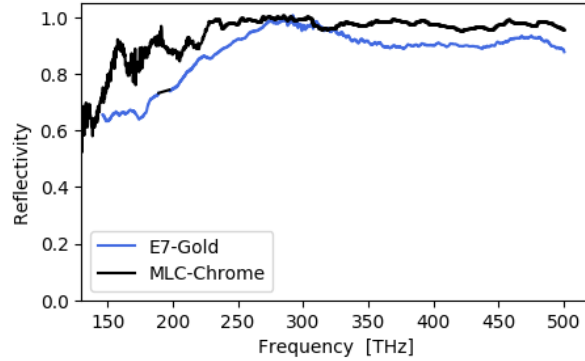


Figure 81: THOR-SLM spectral reflectivity. In blue E7-Gold prototype, in black the MLC-Chrome one.

reflectivity of E7-Gold is 15% lower than MLC-Chrome. The resonance vibration bands of E7 at 100 THz probably start to affect the spectral transmission. So, MLC2132 seems more transparent in the IR than E7, but further characterizations of this new mixture must be performed at those wavelengths in the future.

However, the low efficiency for phase-shifting of MLC based prototypes, demonstrated in chapter 5, makes E7-Gold the chosen prototype used for the next experiments. However, the new mixture and the multi-reflective layers may represent an interesting base for a forthcoming optimized version of THOR-SLM.

To conclude, the ultra-broadband THOR-SLM spectral acceptance is confirmed and multi-octave spectrum can be potentially addressed.

### 6.4.3 Calibration of the interferometer

Working with such large spectrum requires an accurate calibration. First, the angular dispersion generated by the prism has to be measured. Second, a given birefringence excursion ( $\Delta n$ ) leads to a larger phase shift for the highest frequencies compared to the lowest. Therefore two calibrations must be performed.

The spectral distribution of the dispersed light in the Fourier plane is first studied. 6mm is the full spatial extension in this plane. An optical fiber<sup>17</sup>, connected to the spectrometer, is transversally displaced along the x- axis (x-scan), see Figure 80a). Several spectra are acquired from 550 THz up to 136 THz (2200 nm) (limited by the spectral acceptance of the optical fiber) and their center of mass is retrieved. The spectra are shown in 82a), while the central frequencies are plotted as a function of the transversal position  $x$  in b). The expected linear dispersion in frequency is confirmed, and the relationship between a specific spectral component  $\nu_i$  and its spatial  $x_i$  is then determined.

The ability to modulate the phase over the full spectral range is then checked, by positioning THOR-SLM in the Fourier-plane. The writing light arrangement is modified for this calibration. The writing laser used is a blue diode (550mW,  $\lambda_0 = 465\text{nm}$ ,  $d = 250\mu\text{m}$ ,  $Flux = 50\text{W}/\text{cm}^2$ )<sup>18</sup>. The writing laser is directly focused on the rear of THOR-SLM. The beam diameter is reduced to 0.27 mm. Afterward, the writing beam is laterally displaced along  $x$  direction. The measured spectral phase is plotted in Figure 83a) for 7 different positions of the blue focal spot. The ability to continuously address the full spectral range ( $> 450\text{THz}$ ) is demonstrated, with a maximum phase shift as high as 35rad in the visible range (465THz), meanwhile it is limited to 7rad for the infrared edge of the spectrum (130THz). As matter of fact, the introduced phase follows a linear trend  $\propto \nu$ , demonstrating a constant induced refractive index variation

<sup>17</sup><https://www.thorlabs.com/thorproduct.cfm?partnumber=M101L02>

<sup>18</sup>[https://www.thorlabs.com/newgrouppage9.cfm?objectgroup\\_id=7](https://www.thorlabs.com/newgrouppage9.cfm?objectgroup_id=7)

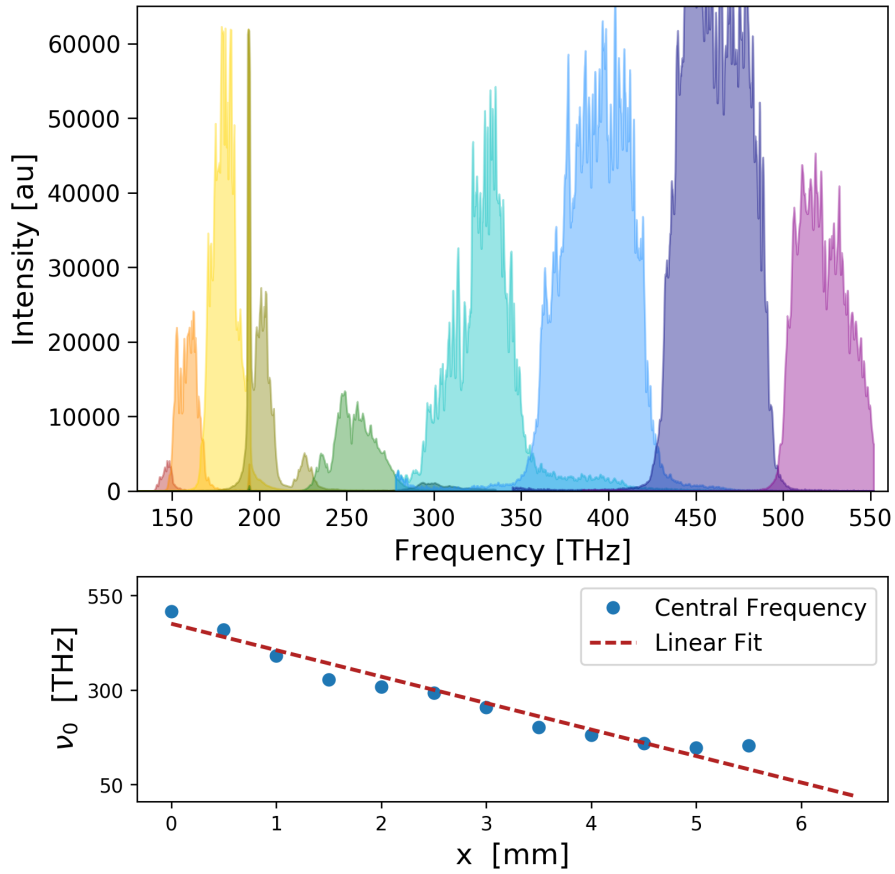


Figure 82: 4f-line calibration through X-scan: in a) the acquired spectra are pictured displacing along  $x$  the optical fiber. b) Retrieved central frequencies  $\nu_0$  as function of the lateral position.

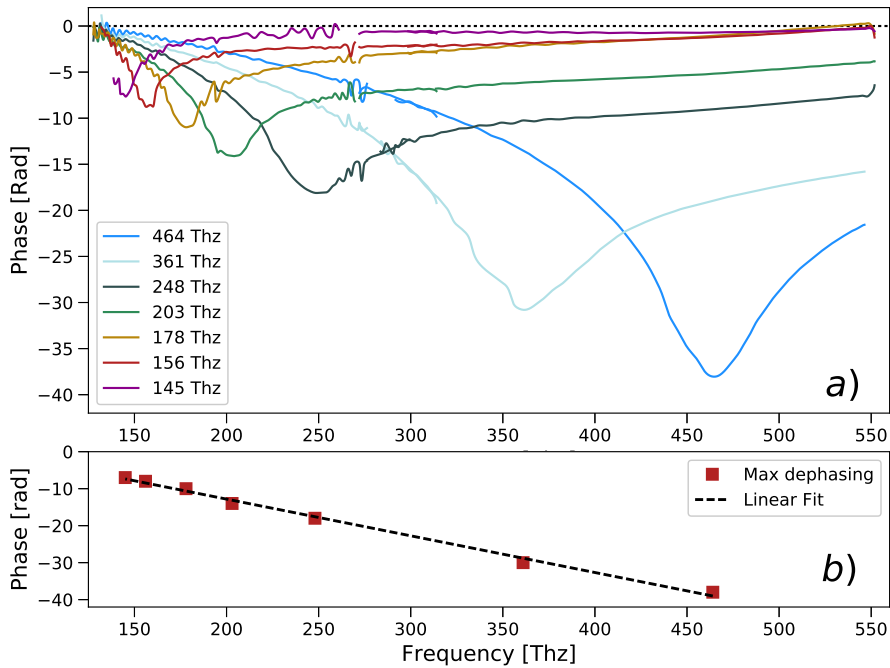


Figure 83: THOR-SLM Calibration: a) spectral phase-shift with a lateral displacement of the addressing beam. b) Maximum introduced phase shift as a function of the central frequency. The dashed line indicates a linear fit.

( $\Delta n = 0.1$ ) over the full spectral bandwidth( Figure 83b) ), according to:

$$\Delta\varphi = \frac{2\pi L}{c}\nu\Delta n \quad (6.4)$$

Finally, the spectral profile of the phase shift indicates a Lorentzian-like profile of the thermal gradient, in agreement with the results of section 6.3.1.

## 6.5 Targeted phase and associated spatial profiles

### 6.5.1 Phase shaping algorithm

In order to have an arbitrary control of the spectral phase, the DLP writing configuration is necessary. The goal of this section is to present the developed algorithm in order to correlate a targeted phase profile to a DLP pattern.

The algorithm is briefly summarized in Figure 84, and it is composed of different steps:

1. **Definition of the targeted spectral phase  $\varphi(\nu)$ .**
2. **Birefringence excursion calculation  $\Delta n(\nu)$ :**  
The first step consists in calculating the thermo-optically induced birefringence excursion from the targeted phase profiles  $\varphi(\nu)$  using eq.6.4.
3. **Refractive index spatial profile  $\Delta n(x)$  determination:**  
From this  $\Delta n(\nu)$ , the spatial variation of the refractive index along the  $x$  axis can be calculated ( $\Delta n(\nu, x)$ ) by the calibration performed in section 6.4.3.

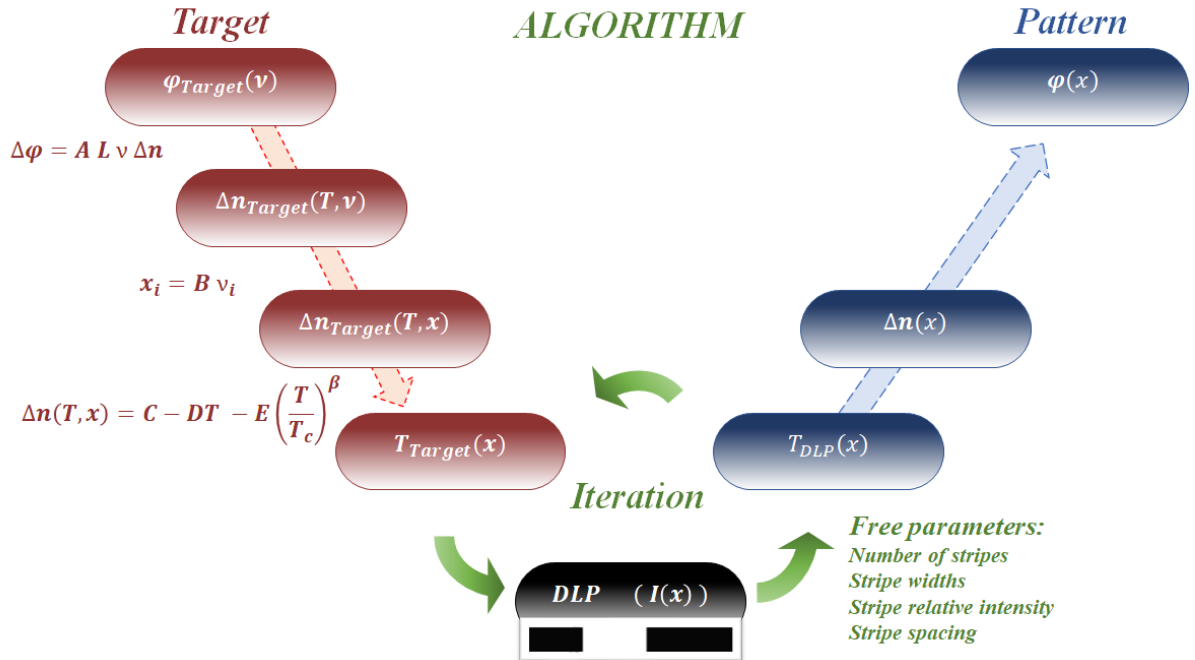


Figure 84: DLP retrieving algorithm. A is a fundamental constant, B is a calibration constant. C,D,E are constants specific to a LC employed.

4. **Thermal gradient estimation  $T(x)$ :**  
To get the targeted spatial distribution of the temperature function, the E7 thermotropicy has to be introduced. As already studied, it can be expressed as:

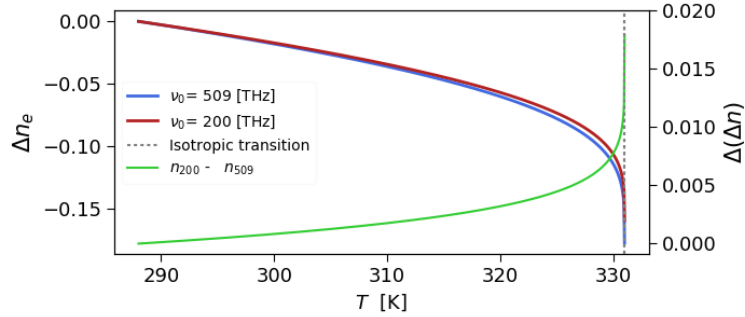


Figure 85:  $\Delta n_e(T)$  for E7, calculated according to eq. 6.5 and Tab. 19 for two different frequencies (blue and red lines).  $T_c$  is also indicated. The green line is the difference between the two curves (right scale) (Li, 2005).

	$A$	$B$	$T_c$	$\beta$	$\Delta n_0$
$\nu = 509 THz$	1.7546	$5.36 \cdot 10^{-4}$	331	0.2391	0.3768
$\nu = 200 THz$	1.723	$5.24 \cdot 10^{-4}$	331	0.2542	0.3485

Table 19: Fitting coefficients of E7 thermotropy (eq. 6.5) for two frequencies.

$$n_e(T) = A - BT + \frac{2\Delta n_0}{3} \left(1 - \frac{T}{T_c}\right)^\beta \quad (6.5)$$

with A, B,  $\Delta n_0$ , and  $T_c$  some fitting parameters, subject to change with the spectral range, as recalled in table 19.

The induced birefringence  $\Delta n_e(T)$  is then calculated for the two spectral ranges and plotted in Figure 84. Up to 325 K, that is  $\Delta n_e = 0.07$ ,  $\Delta n_e(T)$  is considered as spectrally invariant.

### 5. Computation of the DLP pattern $F(x)$ :

To compute  $F(x)$ , the particular shapes of the thermal gradients, as calculated in section 6.3.1, are fully exploited to reach the target temperature profile with only a few control points on the DLP. The temperature elevation is assumed to evolve linearly with the flux and the control points coupling is taken as the linear combination of individual gradients. The control points are simple stripes with four tunable parameters: Number of stripes, stripe width, stripe relative intensity, stripe spacing. The DLP pattern is retrieved through an iterative method:

- **First DLP pattern loading  $F_0(x)$ :**  
The initial pattern is composed by 2 stripes spaced by 6 mm (dispersed spectrum extension)
- **Estimation of DLP temperature spatial profile ( $T_{DLP}$ ):**  
The simulation code used in section 6.3.1 estimates the temperature profile corresponding to the loaded pattern.
- **Estimation of the error term ( $\epsilon = T_{targeted} - T_{DLP}$ ):**  
The difference between the estimated targeted temperature profile ( $T_{targeted}(x)$ ) and DLP simulated one ( $T_{DLP}(x)$ ) is then measured.
- **Minimization of the error term ( $\epsilon = T_{targeted} - T_{DLP}$ ):**  
A new DLP pattern loading  $I_i(x)$  is loaded by changing the free parameters in order to minimize  $\epsilon$ .

## 6. Final Pattern:

The final pattern is ready to be loaded into the DLP.

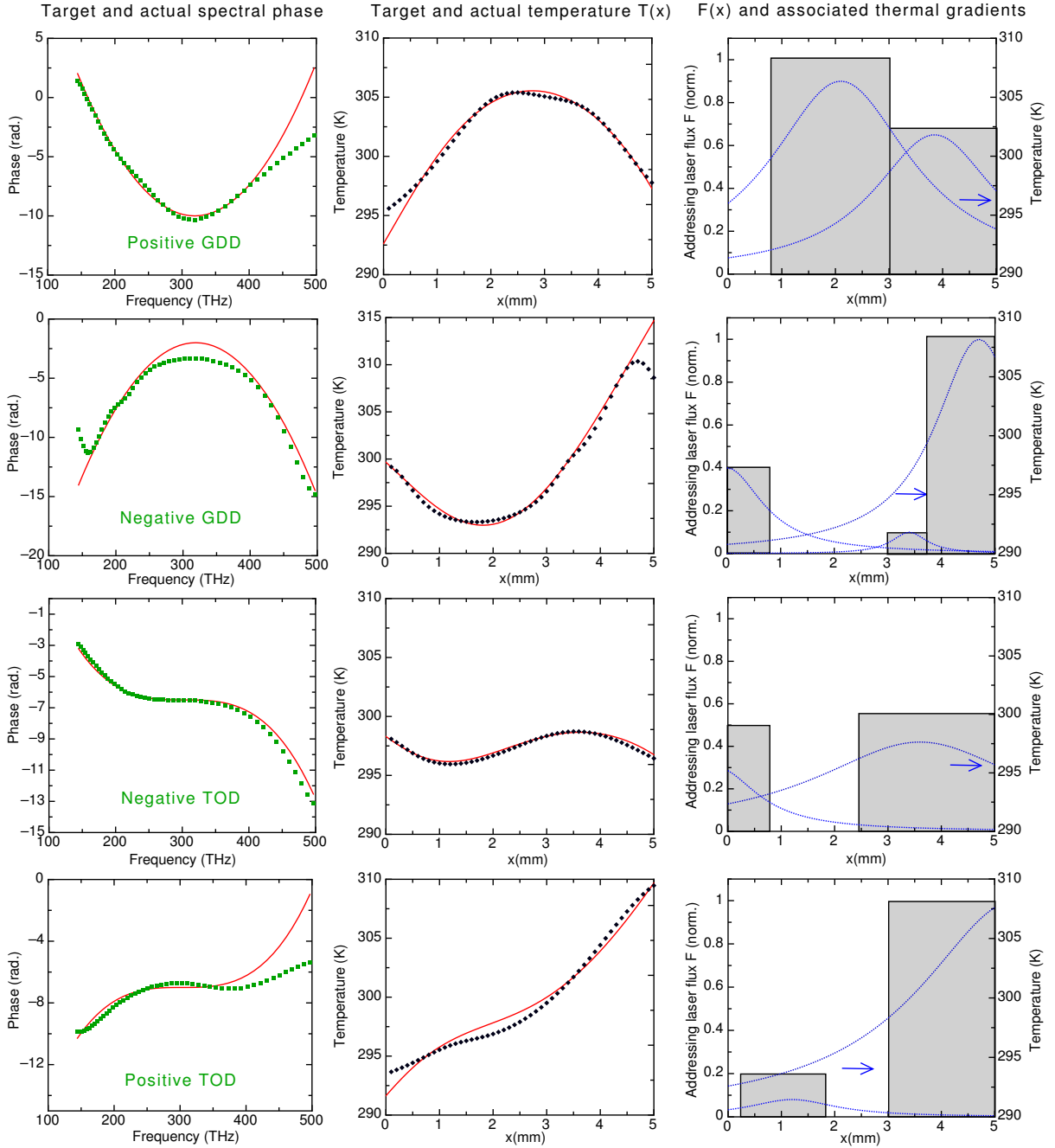


Figure 86: Algorithm for the determination of the blue light spatial profiles loaded on the DLP. Each row refers to a target spectral phase (positive GDD, negative GDD, negative TOD, positive TOD). The target spectral phase is plotted in the first column (green dots). The deduced target spatial evolution of the temperature,  $T_{target}(x)$ , is plotted in column 2 (black dots). Column 3 shows a suggestion of normalized spatial flux of the addressing beam onto THOR-SLM plane (light gray) and the calculated thermal gradients (dotted blue). Induced temperature (resp. spectral phase) is then shown in red in column 2 (resp. column 1).

Figure 86 quantifies this algorithm: targeted phase and relative birefringence excursion are plotted in the first column, temperature spatial profiles in the second one and, finally the retrieved DLP pattern on the last one. Each row corresponds to a different desired phase. 4 distinct cases are shown: pure quadratic positive (first row) and negative (second row), pure cubic negative

(third row) and positive (last row). Therefore, these patterns can be finally used to induce the targeted phase. After this algorithm two or three steps should be enough to induce quadratic or cubic spectral phase

To conclude, a dedicated simulation code is developed to get the DLP pattern from the targeted phase. The approximation ( $\Delta n(T)$  does not depend on the frequency) is valid since the refractive index variation is smaller than 0.07 ( $T < 325K$ ), which is the case in the present experiments. Above that, the chromatic contribution of  $\Delta n(T)$  will have to be taken into account.

## 6.6 Phase shaping experimental results

### 6.6.1 Spatial sensitivity

Although the required patterns to introduce quadratic or cubic phase are already known, the optimal writing beam position has still to be experimentally determined. Indeed, as shown during the calibration, THOR-SLM is sensitive to the writing-reading overlap, and even a small mismatch can affect the phase shaping. To demonstrate and, at the same time, quantify this effect, an x-scan is performed: an arbitrary DLP pattern is kept constant meanwhile the whole writing arrangement (Figure 77) is transversally displaced along  $x$ . Figure 87a) pictures the introduced spectral phase when moving the writing arrangement with a step of  $500\mu\text{m}$  (DLP profile in the inset).

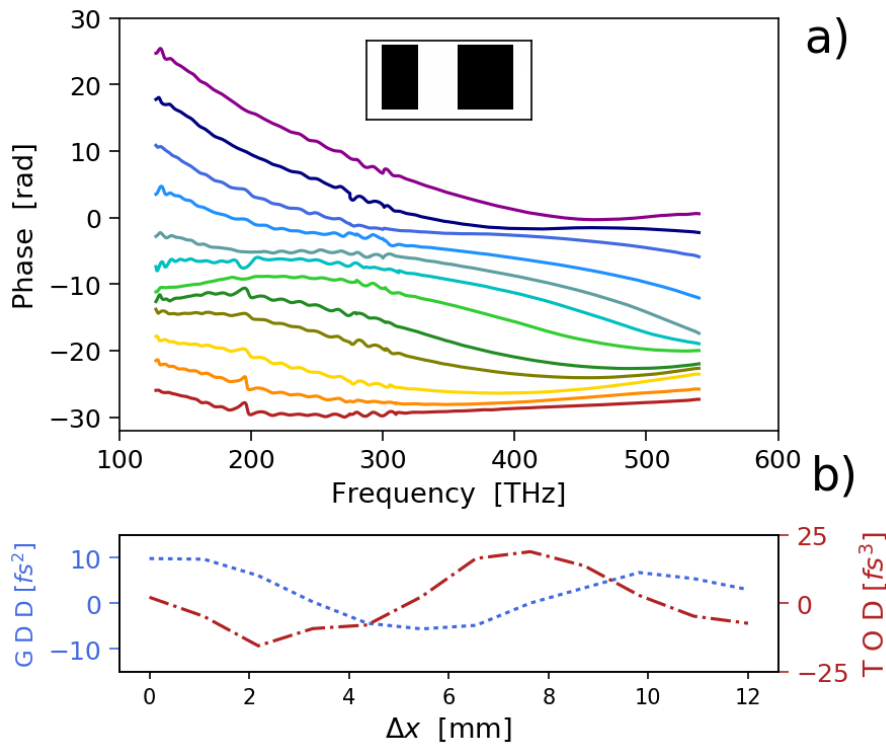


Figure 87: a): Spectral phase during the X scan (0.5mm step). In the top, the uploaded DLP pattern is pictured. b) GDD and TOD from (a) as a function of  $\Delta x$  at 330 THz.

Several phase profiles are achieved for the same DLP pattern, combining second and third phase order coefficients. Figure 87b) quantifies this variation plotting the GDD and the TOD for each writing arrangement position. As matter of fact just displacing the same DLP pattern a phase span of  $20 \text{ fs}^2$  and  $40 \text{ fs}^3$  are possible (330 THz). This effect can be exploited, e.g. with the same DLP pattern several phase profiles can be achieved just displacing the writing arrangement. At the same time, a high sensitivity ( $< 500\mu\text{m}$ ) to the writing-reading overlap is shown.

### 6.6.2 Pure quadratic or cubic phase

In this section, THOR-SLM shaping capabilities are demonstrated to induce a pure quadratic or cubic phase shift. The pattern uploaded are the ones retrieved by the algorithm and an x-scan is first performed in order to find the correct writing-reading overlap.

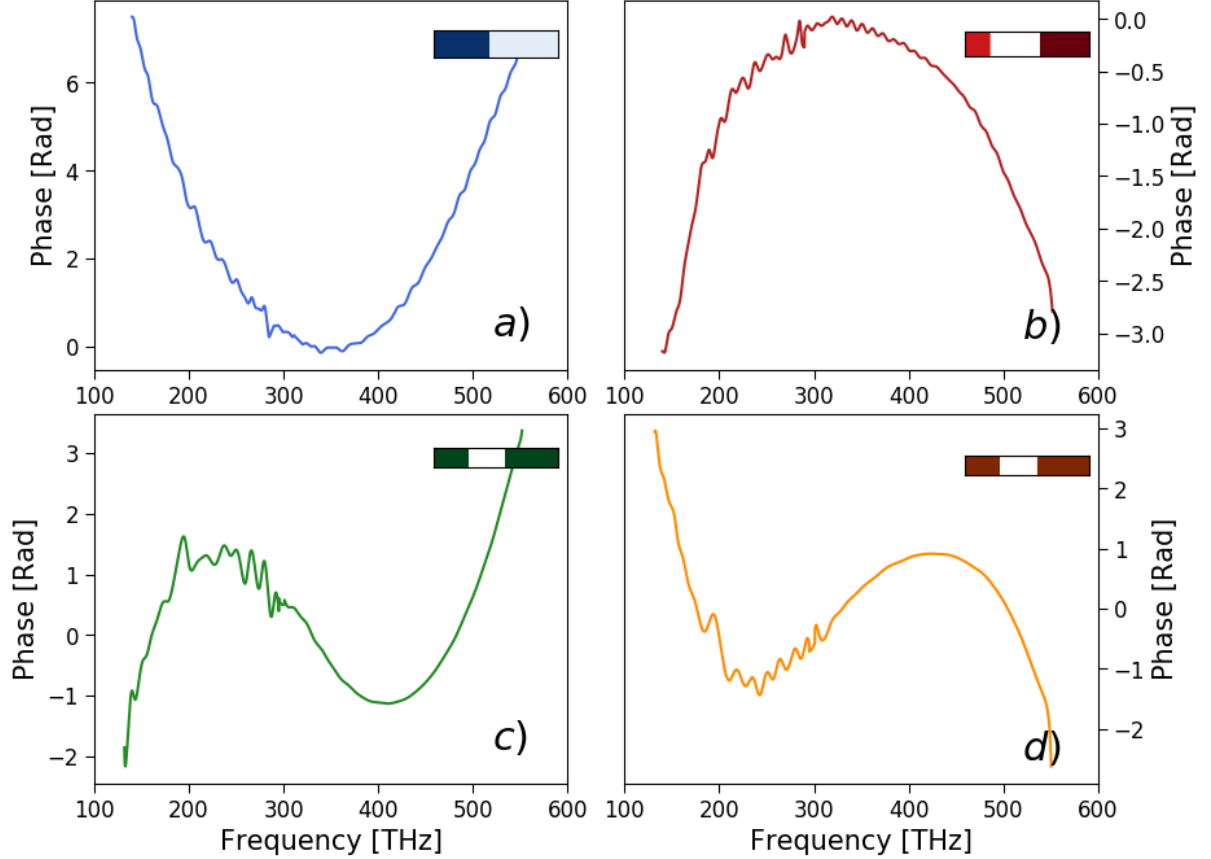


Figure 88: Introduced spectral phase for the 50  $\mu\text{m}$ -thick E7-Gold THOR-SLM: a) Positive quadratic phase ( $+8.2 fs^2$ ), b) negative quadratic phase ( $-2.5 fs^2$ ), c) negative cubic phase ( $-13 fs^3$ ), d) positive cubic phase ( $+13 fs^3$ ). The spatial pattern loaded on the DLP is shown in the top right corner.

A gallery of experimental results is shown in Figure 88. Arbitrary and smooth second or third-order spectral phase is applied over the full 450 THz spectral bandwidth. Therefore, it is possible to introduce a pure positive (resp. negative) quadratic phase with more than 8 rad (resp. 2.5 rad) (Figure 88 a),b). Relative uploaded profiles are shown in the inset. The difference in amplitude between the positive and negative phase shift is due to the smaller energy deposited on the SLM by the related pattern. However the total chirp span ( $> 10 fs^2$ ) is large enough to triple the pulse duration of a single-cycle Fourier-Transform limited pulse at 1  $\mu\text{m}$  (3 fs). Pure positive (resp. negative) cubic phase shift is also possible with  $\pm 5 rad$ , corresponding to  $\pm 13 fs^3$  (Figure 88 c),d).

It is demonstrated that THOR-SLM can handle a spectral phase larger than 450 THz (2000 nm) introducing both positive and negative values. In addition, arbitrary and independent control of the GDD and TOD is achievable. To the best of my knowledge, these performances exceed the current state of the art of the existing multi-octave pulse shaper, e.g. wedges, bulk plates, and chirped mirrors have never modulated such spectral bandwidth arbitrarily.



### 6.6.3 Influence of the writing beam power

The writing light energy considerably affects the induced phase shift as already demonstrated in the previous chapters. Therefore, a power scan (P-scan) is also performed: starting from the maximum, the writing laser power is progressively decreased. In Figure 89, the P-scan results, uploading the former 4 patterns, are pictured. Each of these deposes a distinct writing beam power on the rear of THOR-SLM, so it is more convenient to compare them in terms of normalized power. In Figure 89a),b) the spectral phases are plotted for the pure quadratic

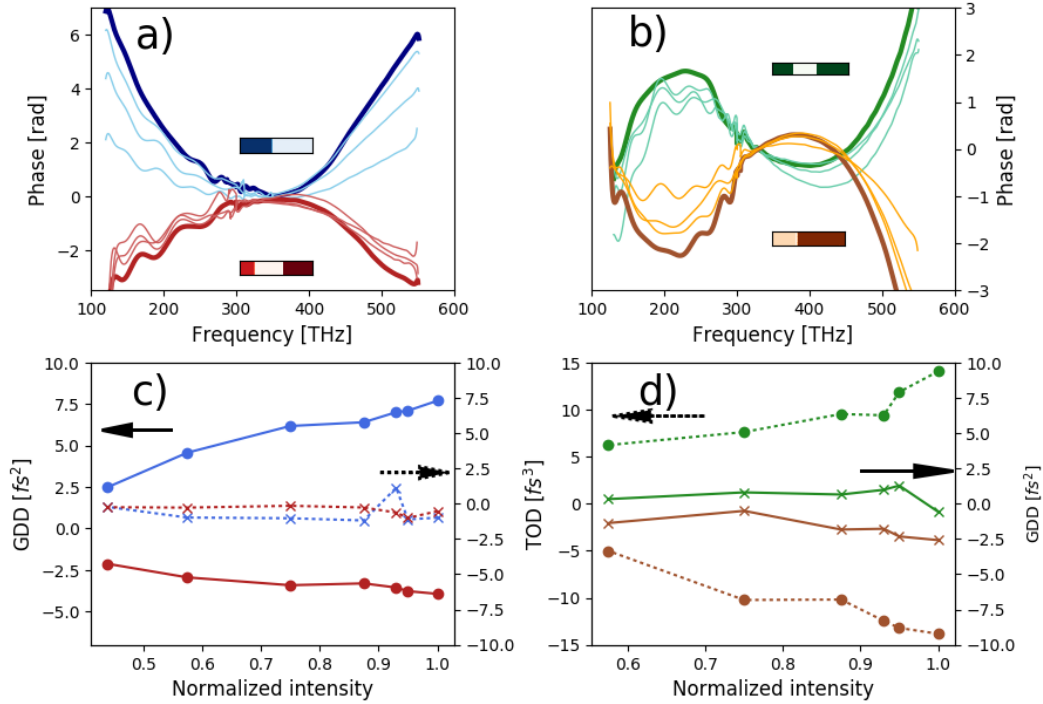


Figure 89: P-scan results: a) positive (in blue) and negative (in red) quadratic spectral phases changing the blue power. b) positive (in green) and negative (in brown) cubic phases. Relative DLP patterns are pictured as an inset with the same colour. c), d)  $\varphi^2$  (solid lines) and  $\varphi^3$  (dotted lines) coefficients as a function of the normalized writing beam power for all the patterns.

(positive and negative) and pure cubic (positive and negative) targeted phase. The corresponding DLP patterns are pictured with the same colours than their relative phase. In this way, in Figure 89c), the GDD coefficients for positive and negative excursion are plotted as a function of the normalized power. At the same time, the third-order coefficient is shown (dotted) and it is found almost constant during the full scan. Symmetric results are achieved changing the TOD, e.g. the GDD is not affected by the power variation (Figure 89d). To conclude, the blue writing beam power is a simple tuning parameter, enabling to adjust a single spectral phase order without involving the other ones.

### 6.6.4 Influence of the LC layer thickness

To improve the phase span, two distinct ways are possible according to eq. 6.4, e.g. increase the  $\Delta n$  or the LC thickness ( $L$ ). Increasing the  $\Delta n$  is possible using MLC2132, however, shown in the previous chapters, it requires more writing beam power which is not available currently. More accessible is to increase the LC thickness. As mentioned in chapter 5, a E7-Gold prototype of  $110 \mu\text{m}$  has been already fabricated. In that analysis is demonstrated although the heating process is less efficient in thick layers, the phase-shift can be considerably increased. Therefore  $110\mu\text{m}$  prototype is tested using again the same 4 patterns for GDD and TOD control. The

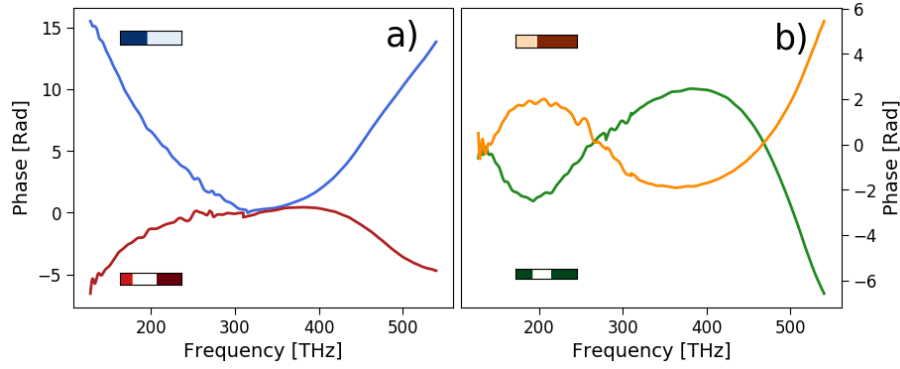


Figure 90: Introduced spectral phase for the  $110\mu\text{m}$ -thick THOR-SLM: a) Positive quadratic phase in blue ( $+19 fs^2$ ), negative quadratic phase in red ( $-7 fs^2$ ), b) negative cubic phase in green ( $-19 fs^3$ ), and positive cubic phase in orange ( $18 fs^3$ ).

results are plotted in Figure 90. The chirp span is then  $25 fs^2$ , therefore it provides a 7 fold-increase of the duration of a single-cycle Fourier-Transform limited pulse at  $1 \mu\text{m}$ . This is a significant step forward compared to the thinner former prototype. In addition, the TOD span variation is increased as well:  $\pm 18 fs^3$  can be continuously introduced.

## 6.7 Prospectives

### 6.7.1 Experimental arrangement improvements

#### Dispersive wedge compensation

As explained earlier, for this proof of concept experiment, the wedge thickness used to spatially disperse the spectrum was not taken into account in the phase measurements. In order to exploit THOR-SLM shaping capabilities over the multi-octave bandwidth, a more adapted dispersion element and its compensation has to be proposed. Spatial dispersion of such bandwidth will only

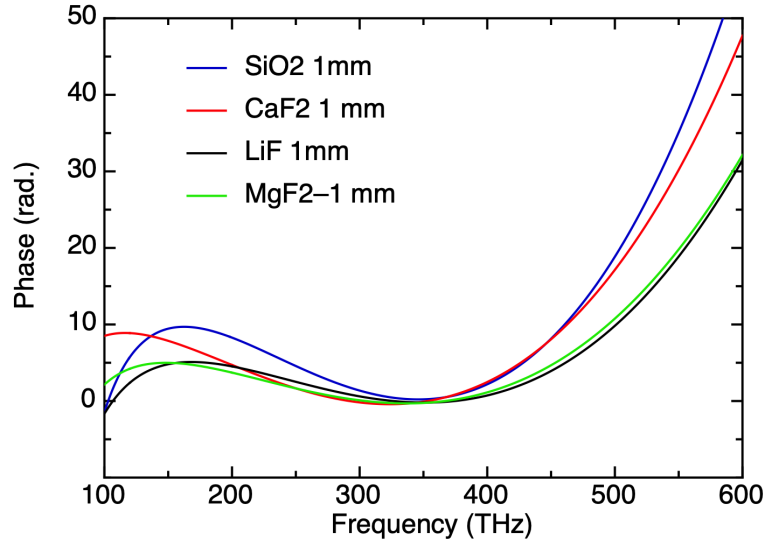


Figure 91: Spectral dispersion of 1mm of different glasses  $SiO_2$ ,  $CaF_2$ ,  $LiF$ , and  $MgF_2$ .

be achieved with a prism, or ultra-thin wedge made with a low dispersion material. Working close to the apex can also reduce the path length. Figure 91 summarizes the spectral phase induced by 1mm of several glasses ( $SiO_2$ ,  $CaF_2$ ,  $LiF$ , and  $MgF_2$ ).  $LiF$  appears like a good compromise because of its rather low spectral phase in the visible range.

To verify the ability to compensate for it, some simulations are performed as explained in section 6.5.1. E7-Gold 100  $\mu\text{m}$ -thick prototype is selected in order to maximize the pulse shaping

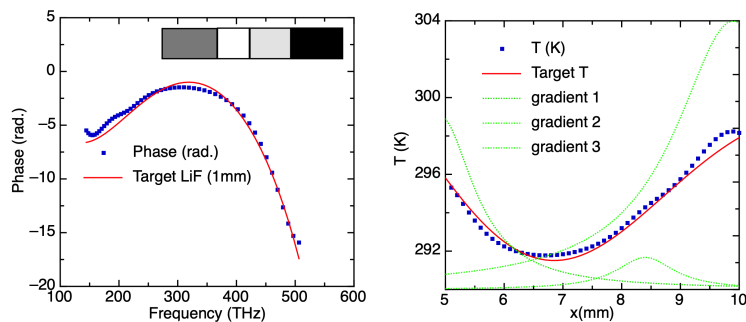


Figure 92: a) Phase introduced by a 1mm of  $LiF$  and the needed phase compensation by THOR-SLM. The DLP pattern is pictured in the corner of a), and the relative temperature spatial profile is plotted in b).

capabilities of the device.

As shown in Figure 92, the algorithm makes possible  $LiF$  compensation with a 3-stripes DLP profile, corresponding to a maximum increase of temperature of 8K and a refractive index excursion of 0.012. This value is four times lower than the  $\Delta n$  addressed in the experiment with the current laser diode power. Therefore, shaping capabilities beyond the prism compensation

should be preserved and will naturally be extended using a more powerful addressing laser.

### Reading beam laser

The demonstrated phase modulation is spectrally limited only by the source used in the experiment. Indeed, an even larger spectrum can be phase shaped even with those first, not-optimized, prototypes. Thus, tests with spectrally broader lights have to be performed to define the actual working spectral span of THOR-SLM.

Phase management of a narrowband femtosecond laser is presented in the annex (D.4.1) using the first, not-optimized, writing beam configuration (see 5.4.1). However, a demonstration using the DLP configuration must be performed as a final validation. Eventually, a few-cycle or single-cycle pulse will definitely prove the unprecedented THOR-SLM phase shaping capabilities.

### Writing beam laser

The writing beam power is actually the largest limitation of THOR-SLM. Even when using a more powerful diode, compared to the one used in chapter 5, only 600 *mW* are finally deposited with the new arrangement in the best of case. Therefore, the rise of temperature and the consequent phase shift are limited. In the latest experiments, less than 25% of the maximum temperature elevation has been reached, while THOR-SLM can be addressed up to the LC transition temperature, which is 331 *K* for E7-based prototypes (386 *K* for MLC2132 ones). Hence, THOR-SLM phase shaping capabilities are not completely exploited and still partially unknown.

Another possibility is to take advantage of the multi-layer configuration and completely change the writing beam laser. Indeed, blue diodes were chosen for their compatibilities with the gold layer the single-layer prototype. Nevertheless, the multi-layer configuration makes possible to spectrally change the writing beam laser. Indeed, Chrome-based devices could be potentially addressed with green or 800nm laser diode and, eventually broadband white light sources with a possible gain in absorption efficiency.

## 6.7.2 THOR-SLM conception improvements

### Motivation

Despite the unprecedented results shown in this chapter, some THOR-SLM design improvements can be done. Indeed, the materials involved and their spatial dimensions can be optimized in order to improve:

- Spatial resolution
- Spectral acceptance
- Phase shift

### Spatial resolution

The first improvement of THOR-SLM overall geometry concerns the BK7 glass substrate. As simulated in section 6.3.1, the temperature in the 6mm-thick BK7 substrate is high enough to participate to the LC heating process. Its thermal conductivity (1.14 *W/mK*) is probably too low to correctly spread the heat and it might also absorb part of the writing beam. Thus, a narrowing of this layer could reduce this effect and maybe increase the THOR-SLM spatial resolution. Hence, some simulations following the model developed in section 6.3.1 are performed

considering a 1 mm-thick BK7 layer (Figure 93). A small reduction of the thermal gradient is actually visible, demonstrating this thickness influence.

To further reduce the thermal gradient, the BK7 can be replaced by another glass with higher thermal conductivity. Sapphire seems suitable for this,  $\kappa_m = 30 \text{ W/mK}$ . In Figure 93a), it is visible how the induced thermal gradient with a substrate of 1mm of sapphire is narrower (10%) using the same writing beam conditions, e.g.  $R_S = 1.5 \text{ mm}$ .

Finally, the size of the writing beam is tuned ( $R_S$  from 1.5 mm to 0.1 mm) to study its effect on the thermal gradient. The evolution of the spatial distribution (at the  $1/e^2$ ) is plotted for the three substrates (BK7-6mm, BK7-1mm, sapphire-1mm).

The expected narrowing of the thermal gradient and the reduction of the maximum  $\Delta K$  are theoretically confirmed for all the writing beam radius.

Thus, it is reasonable to think that higher spatial, and so spectral, resolution can be achieved reducing the glass substrate thickness or replacing the BK7 with more conductive materials. At the same time, this narrowing is accompanied by a reduction in the rise of temperature. Thus, a compromise between the spectral resolution and the maximum of the phase shift must be reached.

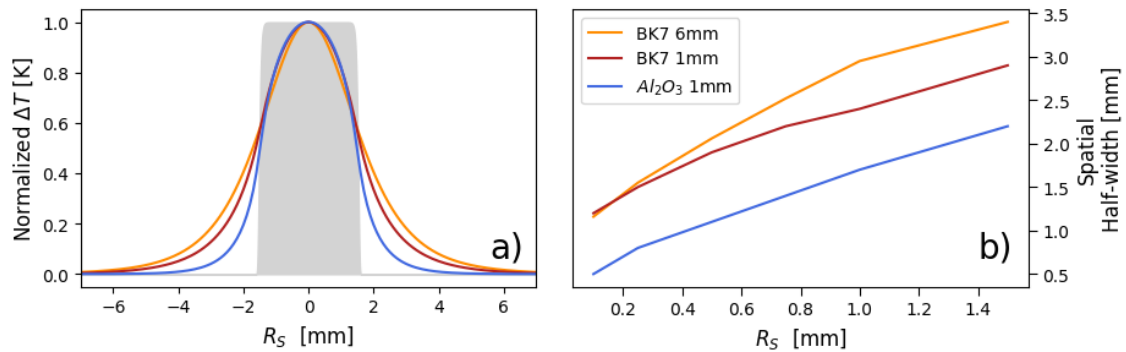


Figure 93: Simulated normalized thermal gradient for three different substrates (6 mm of BK7 in orange, 1mm of BK7 in red, 1mm of sapphire in blue) considering a source of 1.5 mm (showed in grey). b) Spatial width of the thermal gradients (at  $1/e^2$ ) as function of the radius source for the the same substrates.

### Spectral acceptance

The BK7 window substrate also affects the phase shaping capabilities. The spectral acceptance is partially restricted to the infrared light (until 200 THz, e.g. 1.7 nm). Hence, Sapphire or  $CaF_2$  seem suitable to replace it in the future, because of their larger spectral transparency (see Figure94).

### Phase shift

THOR-SLM phase shift depends also on the LC thickness, in this thesis E7-Gold- 110  $\mu\text{m}$  is the thickest prototype used. Nevertheless, the process to fabricate THOR-SLM is the same as the common LC-cell explained in detail in Chapter 1. This procedure has already fabricated LC-cells of more than 200  $\mu\text{m}$  in the past (Jullien et al., 2017). Thus, it is reasonable to expect that such layer can be also obtained even with THOR-SLM. If verified, this could be a remarkable gain in terms of spectral phase shift.

Another possibility is to replace E7 and MLC2132 liquid crystal mixtures. The new mixture must have a large birefringence excursion, and at the same time, a low enough clearing point temperature. Nevertheless, the research and development of liquid crystal mixtures are so fast that realistically upcoming mixtures will present better characteristics than E7 and MLC2132.

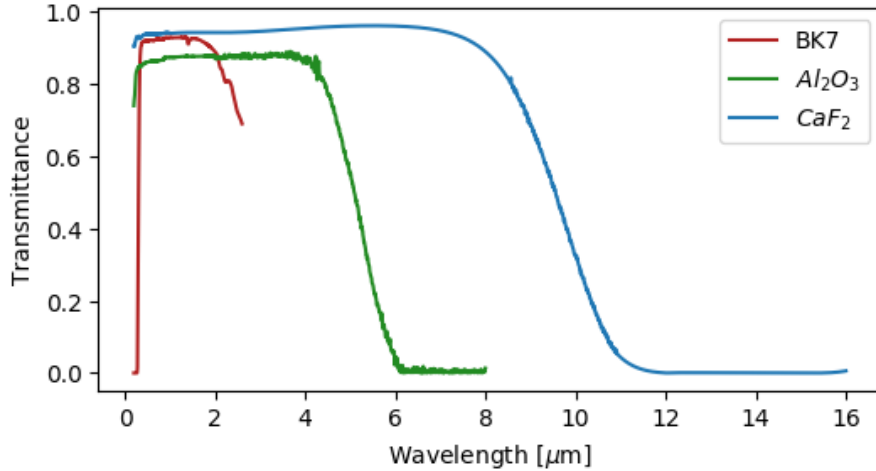


Figure 94: Transmission of common glasses (BK7, Sapphire and  $\text{CaF}_2$ ).

## 6.8 Conclusions

In this chapter, the phase addressed by the THOR-SLM is extended to the IR light. Some numerical simulations about the inner thermal gradient are performed in order to estimate the temperature profiles and, as a consequence, the spatial/spectral resolution. The writing laser arrangement is improved involving a more powerful diode and a digital processing mirror (DLP) to increase THOR-SLM phase shaping capabilities. Dedicated python code is developed to find the optimal patterns to upload on the DLP. Finally, an ultra-broadband interferometer is installed to measure the spectral phase from 550 to 2500 nm ( $> 450\text{THz}$ ) using the FTSI technique. The achromaticity of the device is first confirmed and then an interferometer calibration is performed.

A pure quadratic or cubic phase is applied over a multi-octave spectral bandwidth ( $> 2500\text{nm}$ ). The total chirp span is large enough to provide a seven-fold increase in the duration of a single-cycle Fourier-Transform-Limited pulse at  $\sim 1\ \mu\text{m}$  ( $3\text{fs}$ ). The influence of the addressing power is also reported as it also demonstrated the control of a single-phase term (GDD or TOD) without affecting the other one. SLM based on thicker LC layer ( $110\ \mu\text{m}$ ) presents an even larger phase span ( $> 25\text{fs}^2$ ) with a smaller birefringence excursion ( $\Delta n = 0.04$ ) due to the volume effect of the LC.

None of the existing pulse shaper combines at the same time this spectral acceptance with this phase tunability. These results open the way to unprecedented temporal shaping capabilities of few-cycle and single-cycle femtosecond pulses.



# Conclusions

The main goal of this thesis is to develop innovative LC-based devices for ultrafast optics applications with a particular attention to thick nematic layers. In more details, the growth of the tunable birefringence and the extension of the working spectral range towards mid-infrared spectral range of the LC-based phase shapers are required.

Before any applications, a characterization of the optical properties of the liquid crystal is necessary, especially for the latest ones. In this work, the broadband spectral interferometry is for the first time used to measure the chromatic dispersion of liquid crystal mixtures. The technique is first validated measuring the well-known E7 mixture. Afterwards, the completely unknown MLC2132 mixture is spectrally characterized proposing also the coefficients for the Extended Cauchy equation. A new method is then presented to evaluate the actual refractive index at one specific wavelength.

The interferometry is able as-well to evaluate the liquid crystal thermotropy measuring the refractive index variation when it is heated up. Thus, the coefficients for the *4 parameter parabolic* equation are also proposed for the MLC2132 mixture.

Therefore, now a new powerful instrument is available in the laboratory for upcoming LC mixtures characterizations.

The improvement of the already existing ultrafast group delay line is one of the starting point of this work. In particular, other ways to electrically address the molecules are investigated in order to reduce the huge time necessary to fulfil the birefringence excursion. The proposed transient relaxation is experimentally confirmed to be invariant in time to the voltage step. However, more than 2 minutes are still needed for the molecular commutation and some back reflections affects the signal. Hence, the switching-on is preferred despite the presence of starting voltage threshold (Fréedericksz transition). An unexpected dependence of this threshold with the LC thickness is discovered and, through the definition of the transient transition, two distinct regimes are determined. Thick cells ( $> 75 \mu\text{m}$ ) show a rounding of the transition, unlike the common step-like functions of the thin ones. So,  $180 \mu\text{m}$ -cells can be addressed even with a starting voltage lower than the Fréedericksz transition, with a remarkable gain in birefringence excursion.

Nevertheless, only the thickness-effect is taken into account, but some other LC-cell parameters could affect the transition. Among the others, anchoring condition and molecular geometry are suspected to affect as-well the molecules commutation.

Another central goal of this thesis is the spectral extension of the LC-based optical devices. In particular, to solve some of the electrode issues that prevent shaping mid-IR laser pulses. Thus, IR-optimized cells have been fabricated to work at  $1.5 \mu\text{m}$ . But, once tested, even those cells show a laser absorption of  $< 20\%$ . The LC thermotropy is large enough to drive a change of the LC refractive indices. The induced phase shift generates a spatial ring-pattern (spatial phase modulation, SPM) that becomes visible after long propagation. According to the literature, it is possible to estimate this phase shift and, consequently the birefringence excursion, through the ring-pattern. Through the *4 parameter parabolic* equation, already verified and used in this



work, the LC-cell inner temperature is also estimated up to the nematic-to-isotropic transition (331 K for E7 mixture). However, the ring counting analysis suffers from some limitations. Therefore a more precise measurement of the wavefront has still to be performed to solve some of those uncertainties. Moreover, some theoretical and numerical analysis of the ITO absorption and thermal gradient spread into the cell have to be implemented.

This analysis demonstrates that even the IR-optimized electrodes still have issues in the infrared spectral range, so the electrical addressing is still awkward. Nevertheless, such large non-linear effects without beam collapsing are rare in ultrafast optics and the measured birefringence excursion is close to the one electrically achievable. Therefore, a thermo-optical strategy can be contemplated for LC molecules control.

The LC thermotropicity combined with the electrode-related issues have driven to research new ways to address the LC molecules: in particular they have brought to an original thermo-optical address. This innovative strategy is based on light absorption of a writing beam that heats up the LC, while a second one (reading beam) is phase modulated passing through the LC layer. In this way, the remarkable LC optical properties can be finally exploited. For instance, a phase shaper that covers the full spectral acceptance bandwidth of the LC can be contemplated. Moreover, it can induce a phase shift larger than  $2\pi$  without any pixelization.

Thereby, a new LC-based optical device is developed and patented: THOR-SLM (Thermo-Optically Reflective Spatial Light modulator). Three first prototypes are fabricated in order to find the best performing configuration. The spatial, the spectral and the temporal phase shifts of these prototypes are measured through interferometry with three distinct experimental set-ups and at different wavelengths, from 500 nm to 1000 nm. After some set-up upgrades and some theoretical simulations, THOR-SLM is inserted in a multi-octave spectral interferometer. An unprecedented arbitrary shape is demonstrated over a spectral bandwidth of 450 THz, spanning from 540 nm to 2500 nm, introducing positive or negative values of group delay dispersion and third-order dispersion. The total introduced chirp span ( $> 25 fs^2$ ) is large enough to provide a seven-fold increase in duration to a single-cycle Fourier-transform-limited pulse at  $1 \mu m$  (3 fs). Even if these results open the way to unprecedented temporal shaping capabilities of few-cycle and single-cycle femtosecond pulses, further improvements in both experimental set-up, such-as THOR-SLM design, can be achieved. In more details, some upgrades should involve the reading beam, as replacing the thick-wedge of the 4f-line with other less dispersive optical components. But also the writing process can be improved using more powerful diodes to increase the birefringence excursion. Finally, also the architecture itself of THOR-SLM can be optimized to have a better spatial resolution or to further extend the spectral bandwidth acceptance.

In the end, this carefully characterization of optical properties of thick nematic liquid crystal cells has enabled to disclose new applications for ultrafast optics, in particular for multi-octave phase shaping.

# Chapter 7

## Annex

### A.1 Scientific Production

#### A.1.1 List of Publications

- **Highly stable, 15 W, few-cycle, 65 mrad CEP-noise mid-IR OPCPA for statistical physics.**  
Nicolas Thiré, Raman Maksimenka, Bálint Kiss, Clement Ferchaud, Gregory Gitzinger, Thomas Pinoteau, Hervé Joussetin, Sebastian Jarosch, Pierre Bizouard, Vittorio Di Pietro, Eric Cormier, Karoly Osvay, and Nicolas Forget.  
Optics Express 26, 26907-26915 (2018).
- **Dynamical optical response of nematic liquid crystal cells through electrically driven Fredericksz transition: influence of the nematic layer thickness.**  
Vittorio Maria Di Pietro, Aurélie Jullien, Umberto Bortolozzo, Nicolas Forget, and Stefania Residori.  
Optics Express 26, 10716-10728 (2018).
- **Thermally-induced nonlinear spatial shaping of infrared femtosecond pulses in nematic liquid crystals.**  
Vittorio Maria Di Pietro, Aurélie Jullien, Umberto Bortolozzo, Nicolas Forget, and Stefania Residori.  
Laser Physics Letters, 16.1: 015301. (2018).
- **A phase-only pulse shaper for multi-octave light sources.**  
Vittorio Maria Di Pietro, Simone Bux, Nicolas Forget, and Aurélie Jullien.  
Submitted in Optica (2019).

#### A.1.2 Patents

**MODULATEUR SPATIAL DE LUMIERE ADRESSE THERMO-OPTIQUEMENT**  
(FR1910894, registered October, 1st, 2019. )

Inventors: Nicolas Forget, Vittorio Maria di Pietro, Aurélie Jullien.

#### A.1.3 List of conferences

- **MEDEA 2017**, Nice,  
Oral presentation
- **UFDIM 2018**, Ayios Nikolaos, Greece.  
Oral presentation & Poster

- **CAMEL 2019**, Nessabar, Bulgaria.  
Oral presentation
- **CLEO Europe 2019**, Munich, Germany.  
Oral presentation
- **UFO 2019**, Bol, Croatia.  
Poster presentation awarded as *Best student poster*

#### B.2.4 HICONO activities

- **1st mini school and soft skill seminar**, Technical University of Darmstadt, Germany (2016).  
Basic concepts of high-intensity light-matter interactions
- **2nd mini school and career planning seminar**, Weizman Institute, Israel (2017).  
High-intensity enabling technologies
- **Secondment**, Institute of Photonic Sciences (ICFO), Castelldefels, Barcelona (2018).  
During this secondment, it has been demonstrated the extension towards longer wavelengths of some already existing devices. In particular, the possible combination of a mid-infrared spectrometer (Mozza, Fastlite) with a scanning, frequency-resolved, second-order auto-correlator (FROZZER, Fastlite). Through those devices, the OPCPA laser system installed at ICFO laboratory has been characterized in the mid-infrared spectral range (3.2  $\mu\text{m}$ ). MOZZA (Fastlite) and FROZZER (Fastlite) combination for mid-infrared pulse characterization.
- **Laboratory and technology course at Fastlite**, Sophia Antipolis, France (2018):  
Measurement and shaping of ultra-short laser pulses
- **3rd mini school and industry seminar**, Agios Nikolaos, Crete, Greece (2018).  
Applications of high-intensity nonlinear optics
- **Laboratory and technology course at Ametek, Darmstadt, Germany (2019)**:  
Non-linear high-precision microscopy and distance measurement

## D.4 THOR-SLM applications

### D.4.1 First applications to femtosecond pulses

In these annexes, THOR-SLM is applied to shape the phase of an ultrafast pulse laser. A first demonstration is performed shaping the spectral phase of a femtosecond pulse (400 fs) at  $1\ \mu\text{m}$ . Afterward, the spatial phase shift is exploited to produce a tunable defocusing lens at  $1.5\ \mu\text{m}$

#### Phase correction of a femtosecond pulse in the NIR range

The control of the spectral phase can be exploited for compression or stretching of an ultrafast pulse laser. In this section, it is qualitatively demonstrated that THOR-SLM can compress a narrowband femtosecond laser in the Near-Infrared spectral range.

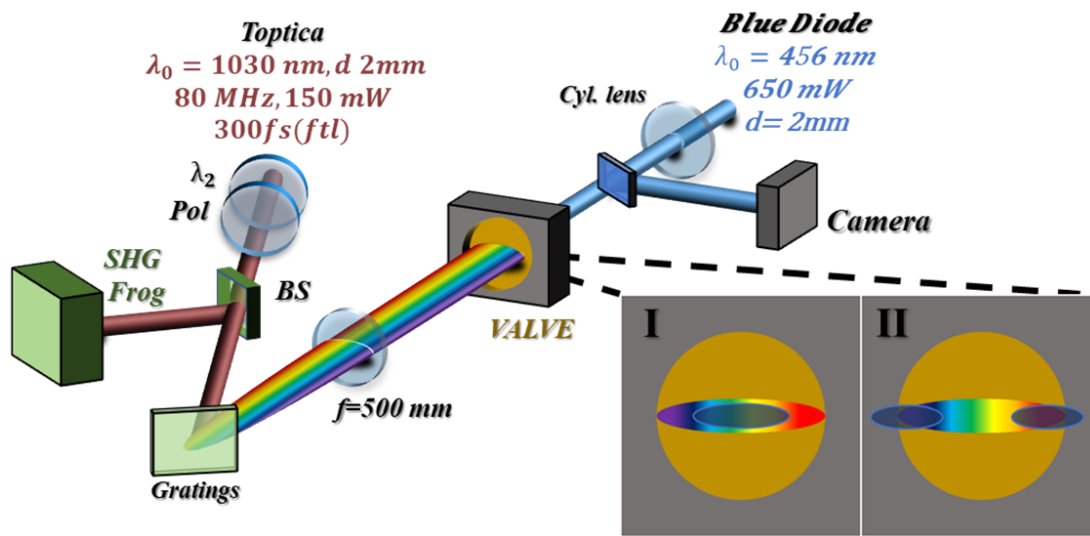


Figure 95: Experimental set-up: a fs laser (400 fs FTL,  $\lambda_0 = 1\ \mu\text{m}$ , 150 mW of average power and a high repetition rate of 80 MHz) is polarized parallel with the respect of the nematic director of the LC cell. A gratings ( $24.8^\circ$  Groove Angle, 1200 Grooves/mm) disperses the spectrum. THOR-SLM is inserted in the Fourier plane of a 4f-line ( $f=500\ \text{mm}$ ). The reflection is then analyzed by a SHG FROG (FROZZER). The blue fibre diode ( $d = 2\ \text{mm}$ ,  $650\ \text{mW}$ ,  $\lambda = 465\ \text{nm}$ , by Thorlabs) is focusing on the rear of the LC-SLM with a cylindrical lens ( $f=150\ \text{mm}$ ). The two different focusing strategies are pictured as well.

The experimental set-up is shown in (Figure 95): a polarizer sets the polarization state parallel with the respect of the liquid crystal nematic director. A femtosecond laser 400 fs (FTL) centered at  $1\ \mu\text{m}$  (150 mW of average power and a high repetition rate of 80 MHz) is dispersed using a reflective grating ( $24.8^\circ$  Groove Angle,  $1200\ \text{Gr}/\text{mm}$ ) and is then imaged onto the LC-SLM placed in the Fourier plane in a 4f-line of a folded configuration ( $f=500\ \text{mm}$ ,  $d=2\ \text{mm}$ ). Spatial extension of fs pulse is about 4mm. A D-shape mirror selects the reflected beam (not included in Figure 95 for the sake of visibility) and it is sent to a SHG FROG (Trebino, 2012) for spectral phase measurements.

A blue writing fibre diode ( $d = 2\ \text{mm}$ ,  $650\ \text{mW}$ ,  $\lambda = 465\ \text{nm}$ ) is focused using a cylindrical lens ( $f=150\ \text{mm}$ ), but in 2 different configurations (as in the previous section):

1. Cylindrical lens with writing laser focusing on the center of the dispersed reading beam spectrum.
2. The blue writing laser is split in 2 (BS 50:50) and both ways are focusing (cylindrical lens  $f=150\ \text{mm}$ ) on the edges of the femtosecond laser.

FROG results of the reference unaddressed pulse are shown in figure Figure 96: measured (resp. retrieved) spectral map is plotted in a (resp. b), while spectral (resp. temporal) intensity and phase are plotted in d (resp. c).

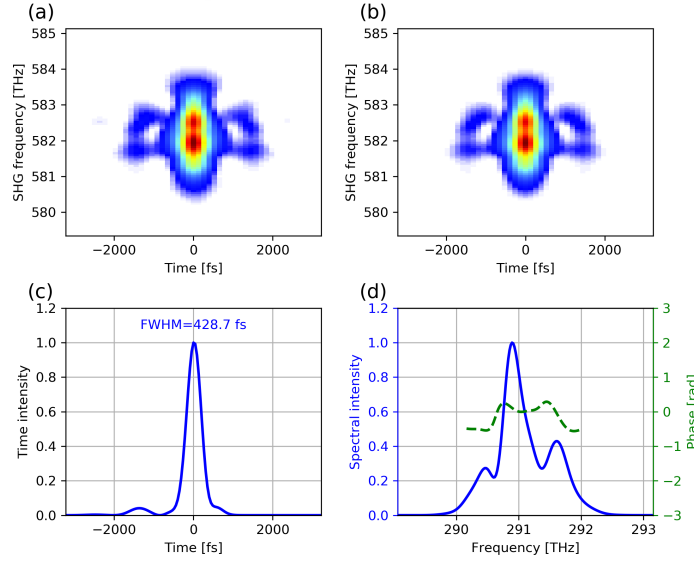


Figure 96: FROG traces for the reference pulse. a) Measured spectrum map. b) Retrieved spectrum map. c) Temporal profile. d) Retrieved spectrum intensity (blue) and phase (green).

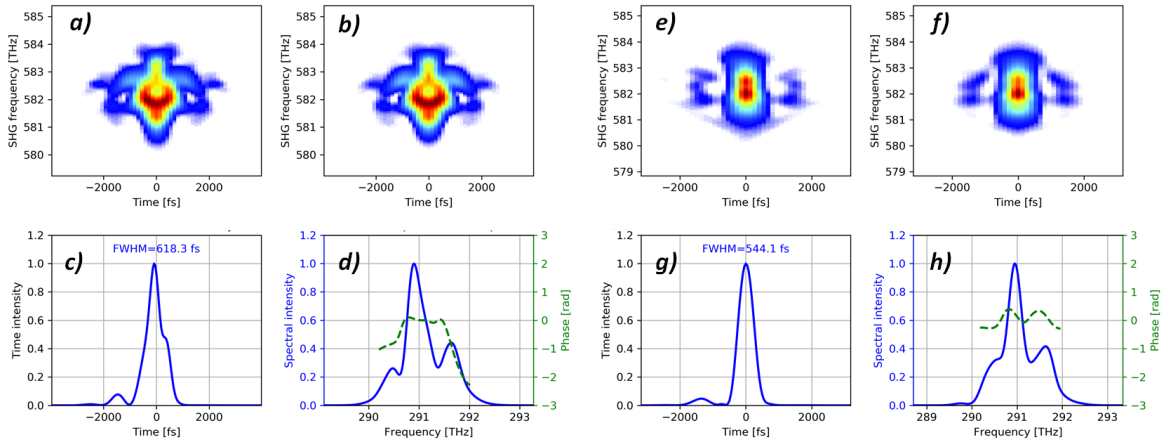


Figure 97: FROG traces for the first configuration positive chirp (a,b,c,d) and for the second one (e,f,g,h) negative chirp introduced.

Both configurations are used to address the whole spectral phase of the femtosecond laser. Indeed with a centered Gaussian spot, the central wavelengths components are encountering smaller refractive indices values compared to the boundaries ones. Therefore a positive phase shift (positive GDD) is introduced, e.g. the pulse is temporally stretched. Increasing the input power, the chirp introduced increases as-well. The maximum pulse duration reached is 3500 fs applying 650mW.

Using the second configuration (focusing on both spectrum edges at the same time), a negative GDD is introduced. Again, the retrieved pulse duration is 544 fs applying 300 mW. As for the section (5.5.3), the negative chirp configuration is strongly limited by the writing arrangement

hand control. In particular, the intensity distribution of the two spots, the relative distance and the position with respect to the femtosecond laser hamper the possibility of large and precise phase control. Nevertheless, the ability of the LC-SLM to stretch, compress and arbitrary shape the spectral phase of an ultrashort laser pulse has been qualitatively demonstrated in the Near-Infrared spectral range ( $1\ \mu\text{m}$ ).

FROG	Pulse Duration	GDD	RMS Error
Reference	430 $fs$	16270	0.23%
Positive Chirp	618 $fs$	61756 $fs^2$	0.5%
Negative Chirp	460 $fs$	45557 $fs^2$	0.5%

Table 20: Summary table of the phase control capabilities of THOR-SLM of an infrared ultrafast pulse laser.

### D.4.2 Defocusing tunable lens for IR light

The thermo-optically induced negative and non-linear refractive index variation on the extraordinary axis can be used for really interesting applications: among the others, adaptive optics as a tunable defocusing lens can be contemplated. The absence of electrodes removes all the chromatic limitations, therefore experiments can be performed at  $\lambda_0 = 1.5\mu\text{m}$ .

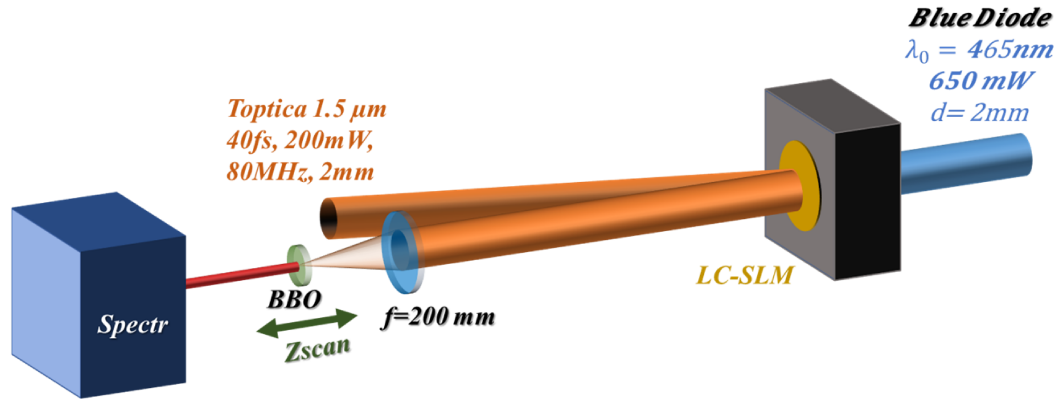


Figure 98: A femtosecond oscillator 40 fs, 150 mW, 80 MHz at  $\lambda_0 = 1.55\mu\text{m}$  is reflected by the THOR-SLM and focused ( $f=200$ ) in a BBO crystal placed on a translation stage (z-scan). The SHG generate signal is acquired by a spectrometer (Ocean Optics). The device is addressed from the rear with a fibre diode by Thorlabs ( $d = 2\text{mm}$ ,  $650\text{mWmax}$ ,  $\lambda = 465\text{nm}$ ).

The employed source is a femtosecond laser (TOPTICA) delivering 40 fs pulses train with an average power of 150 mW and a high repetition rate of 80 MHz. The spectral bandwidth is centered at  $\lambda_0=1.55\mu\text{m}$  ( $=1.3\mu\text{m}-1.7\mu\text{m}$ ). The proposed experimental set-up is shown in Figure 98. The IR reading laser is reflected by the THOR-SLM with a small angle, while the writing laser is spatially reduced in order to match the fs reading one ( $2\text{mm}$ ). Therefore, if the writing and reading lasers are perfectly coaxially overlapped on the THOR-SLM plane, the reading beam undergoes all the spatially induced OPD shown in Figure64a. This effect is equivalent to a defocusing lens and therefore, turning-on the writing laser, a shift of the focal plane is induced. Increasing the addressing blue power, the refractive index difference increases as well with a progressive translation of the focal plane. This displacement can be registered and measured using the second harmonic generation (SHG) of the BBO crystal. Indeed, SHG efficiency changes considerably with the focal conditions, so even a small deviation can be easily detected. Thus, the reading laser is then focused ( $f = 200\text{mm}$ ) onto a BBO SHG crystal (type I) placed on a translation stage, after long propagation ( $> 2\text{m}$ ). The generated second harmonic signal is acquired by a spectrometer (Ocean Optics 450 nm-850 nm, 0.3 nm of resolution). To quantify this shift a z-scan is performed around the focal plane in the rest position. When the writing beam is turned on, the focal position moves and with it the position of SHG has the maximum efficiency (Figure 99). The writing flux is limited by the Spatial phase modulation (SPM) that modifies the far-field spatial reading pattern and affects the non-linear generation on the BBO. Therefore the full birefringence excursion is not achievable in this experiment. The experiment is performed with E7-Gold and MLC-Gold, MLC-chrome is not taken into account because of its low blue absorption. Figure 99 represents the BBO z-scan at different writing flux: E7-Gold in the first column, MLC-Gold in the second one.  $> 7\text{mm}$  of focal plane shift is measured for the E7-Gold SLM at  $0.7\text{W}/\text{cm}^2$ , while MLC-Gold has a smaller displacement ( $5\text{mm}$ ) but a higher threshold  $0.95\text{W}/\text{cm}^2$ . Both effects come from the lower phase introduced

by the MLC2132 mixture due to its higher isotropic phase transition temperature.

From this focal shift is possible to deduce the equivalent focal length (EFL) in THOR-SLM:

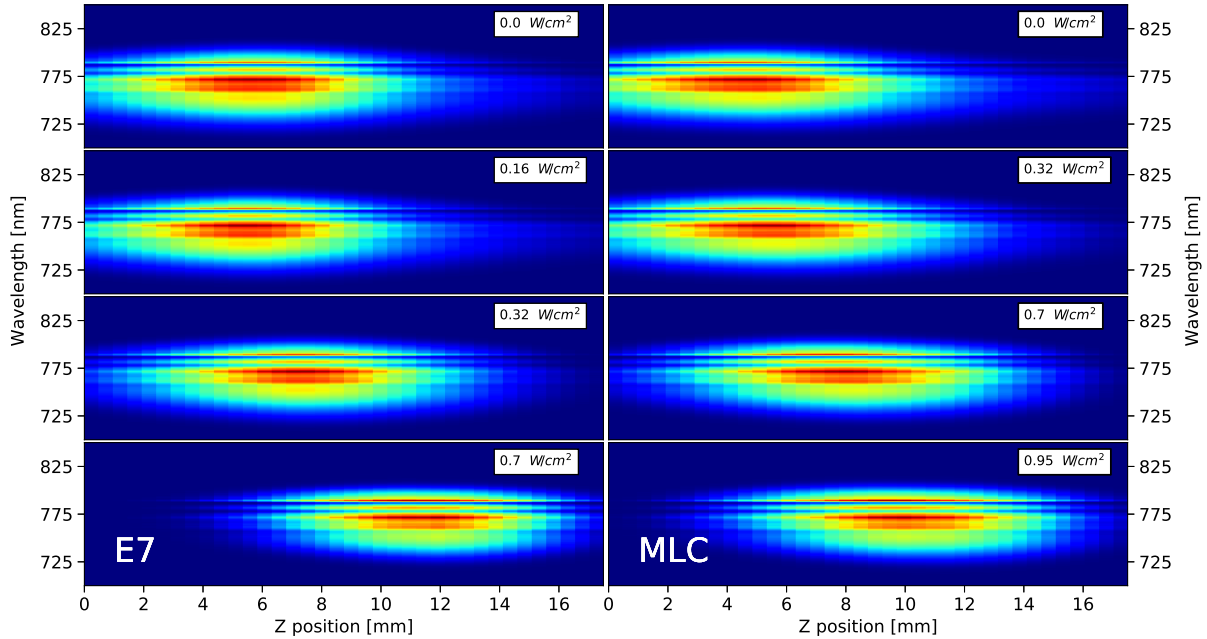


Figure 99: SHG generation spectra at different BBO position for E7-Gold (left) and for MLC-Gold (right). Each graph shows represents different writing power.

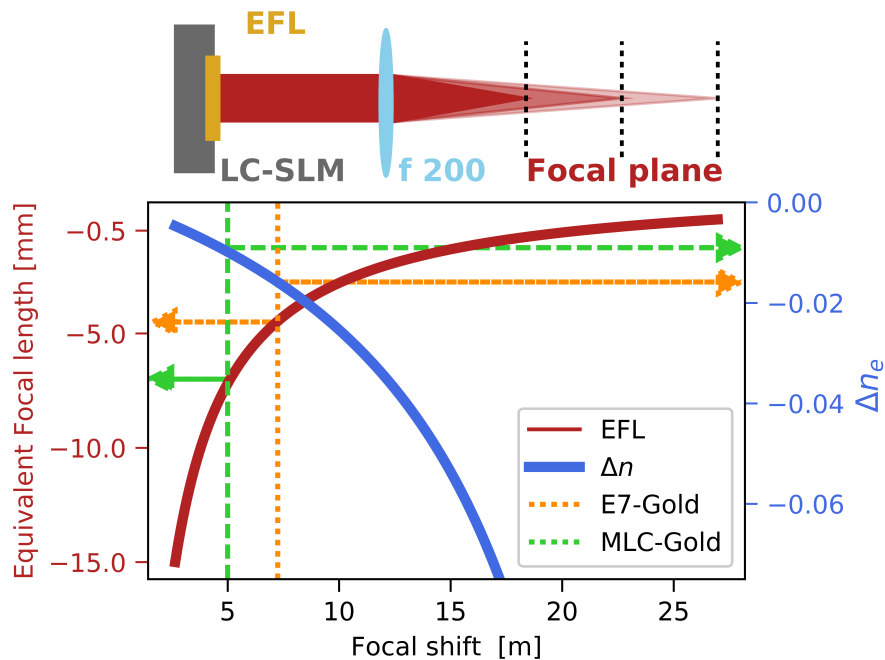


Figure 100: Sketch of the focal plane shifting and Equivalent focal length (red curve) and relative birefringence excursion (blue curve) as function of the focal shift. E7-Gold is plotted in orange and MLC-Gold in green.

$$B = f\left(\frac{EFL - d}{EFL + f - d}\right) \quad (\text{D.1})$$

where  $f = 200$  mm (lens used to focusing into the BBO),  $d$  and  $B$  the distances THOR-SLM-lens and lens-EFL focus respectively (see sketch in Figure 100). An EFL of  $-4.5\text{m}$  (resp  $-7\text{m}$ ) is



found for a focal shift of  $7mm$  (resp.  $5mm$ ) induced by E7-Gold (resp. MLC-Gold). Therefore THOR-SLM can de-focus a laser beam from  $-\infty$  to  $-4.5m$  or  $-7m$  continuously, depending on the prototype.

EFL enables to estimate also the spatial refractive index variation inside the LC layer. Knowing the beam diameter  $d$  ( $2mm$ ), the LC thickness  $L$  ( $100\mu m$ ,  $50\mu m$  double pass) the birefringence excursion can be estimated using:

$$\frac{d^2}{EFL} = \frac{\Delta n_e}{n_e} L \quad (D.2)$$

In E7-Gold the  $\Delta n_e$  is estimated equal to 0.016, while in the case of MLC-Gold it is 0.01. For the same flux ( $0.7W/cm^2$ ), the birefringence excursion is almost two times smaller compared to what was found in the previous section. This difference is mainly due to the size of the writing beam, here three times smaller. Thus, it can be assumed that a smaller writing laser eases the heat dissipation, making the local heating process less efficient.

# List of Figures

1	Spectral and temporal representation of a Gaussian ultrashort pulse. . . . .	2
2	Effect of the first three phase components on the pulse temporal profile. . . . .	3
3	Angular dispersion induced by a dispersive glass prism. . . . .	4
4	Principle of spectral interferometry. . . . .	4
5	FTSI algorithm: a) Original spectral and its interference pattern. b) AC component filtering, c) Retrieved spectral phase. . . . .	5
6	The FTSI technique in self-referenced Michelson configuration. . . . .	6
7	Scheme of a typical experimental SHG FROG setup with a typical spectral map. . . . .	7
8	Basic set-up of a phase shaper based on gratings. . . . .	8
9	Basic set-up of a phase shaper based on chirped mirrors and dispersive wedges. . . . .	8
10	AOPDF principle: by diffraction on the acoustic grating through an acousto-optic interaction, the different spectral components can be diffracted to the extraordinary axis at different positions of the crystal. . . . .	9
11	Basic set-up of a 4f-line shaper system. . . . .	10
12	Schematic representation of the mesophases of rod-like molecules (Image from (Yang, 2014)). . . . .	12
13	Alignment, chemical components and global texture of E7 Nematic liquid crystal from Merck (Images from Wikipedia). . . . .	13
14	Sketches of the different nematic geometries: Homeotropic, Planer splay, Planar twisted. . . . .	13
15	Sketches of the different director axis deformations: (a) splay; (b) twist; and (c) bend (image from (Yang, 2014)). . . . .	14
16	Isotropic and uniaxial index ellipsoids. a) Spherical isotropic index ellipsoid with refractive index $n$ . b) Uniaxial positive, refractive indices $n_e > n_o$ . c) Uniaxial negative, refractive indices $n_e < n_o$ . . . . .	15
17	a) LC cell in the steady state. b) Molecular re-orientation induced by the external electric field. c) Tilt angle at the middle plane as function of the external electric field, where $E_c$ is the threshold. . . . .	16
18	Schematic diagram showing the states with different orientational order parameters (Image from (Yang, 2014)). . . . .	19
19	The Four liquid crystal chemical components of the E7 by Merck. . . . .	20
20	a) E7 transmission on the extraordinary axes and birefringence as function of the wavelength (images from (I. Khoo, 2006)). . . . .	21
21	Assembly of the cell: a) first step with positioning of the spacers and polymerization of four glue dots and a second step with sealing the lateral edges. b) lateral view of the finished cell. c) and e) Molecules alignment due to the anchoring induced by the rubbing roll (d). 3D view (f) and photo (g) of the final cell. . . . .	22
22	Sketch of a common LC-based SLM. . . . .	23
23	Summary table of the 3 different experimental set-ups (first row, LC cell is highlighted in yellow) with their own interference spectra (second row), the thicknesses of the used cells (third row), with their own results (fourth row), and their own objectives (fifth row). . . . .	31

24	a) Experimental Set Up: a super-continuum fiber laser source from Leukos is used as a source of Michelson interferometer for referenced spectral phase interferometry (FTSI). A polarizer sets the polarization state in order to study both LC axis. The LC cell is placed in one arm, and eventually inside a oven for thermotropy analysis. Figure legend (F: long-pass filter (cut-off: 530 nm), D: short-pass dichroic mirror (cut-off: 950 nm), M: mirror, BS: beam splitter, C: compensator) . b) Input raw spectrum (blue curve) and the interference pattern (green curve) acquired by the Ocean Optics 450 nm-850 nm spectrometers (the other is an Avantes 550 nm-1000 nm). c) Fourier Transform of the acquired spectrum in blue and the Super Gaussian profile used as a filter in green. d) Recovered spectral phase from the FTSI analysis. . . . .	32
25	E7 measured spectral phase (dotted lines) and their fit (solid lines) for the 2 different wavelength ranges (0.45 $\mu\text{m}$ -0.7 $\mu\text{m}$ and 0.65 $\mu\text{m}$ -0.9 $\mu\text{m}$ ) and for the 2 LC axis. . . . .	34
26	MLC2132 measured spectral phase (dotted lines) and their fit (solid lines) for the 2 spectral ranges (0.45 $\mu\text{m}$ -0.7 $\mu\text{m}$ and 0.65 $\mu\text{m}$ -0.9 $\mu\text{m}$ ) and for the 2 LC axis. . . . .	35
27	Refractive index as function of wavelength: E7 (dotted lines) and MLC (solid lines) in both polarization directions (Extraordinary axis in blue and Ordinary axis in red). Purple crosses are the official data from the manufacturer. . . . .	35
28	MLC2132 (blue) and E7 (red) acquired interference spectra for different position of the delays stage. The excursion of $\lambda_0 \pm \delta\lambda$ shows the index shift between the two mixtures. .	36
29	MLC2132 Group indices $\Delta n_g$ measured (solid lines) and calculated from section 2.3.4 (dashed lines) for both polarization states. An uncertainty of 2 $\mu\text{m}$ on $\Delta z$ is considered (grey span). b) Absolute error. . . . .	37
30	a) Interference spectra for MLC2132 at different values of temperature approaching the isotropic phase transition. b) FFT at different temperature. The temperature increase leads a decrease of $\Delta n_g$ . . . . .	38
31	Refractive index variation with the temperature. The E7 theoretical curves $n_{e,o}$ (solid lines) is in agreement with the $\Delta n_{g_{e,o}}$ experimental data (dots). The MLC2132 $\Delta n_{g_{e,o}}$ data are also plotted (squares) with the coefficient determined in this work for $n_{e,o}$ (dashed lines). The phase transition temperatures for both mixture are also indicated. The spectral range is 550-1050 nm. . . . .	40
32	a) Principle of the ultrafast LC (group) delay line. Green : LC cell, blue: molecular orientation. . . . .	44
33	Illustration of the considered three driving options and associated experimental tunable parameters. . . . .	45
34	Experimental set-ups: a) A femtosecond laser (30 fs, repetition rate 80 MHz, spectrum centered at 770 nm) produces a 30mW beam. A half-wave plate and a polarizer orientate the input polarization at 45° with respect to the initial director of the LC-cell (L=180 $\mu\text{m}$ fixed) to generate two cross-polarized sub-pulses delayed by $\Delta\tau_g = \Delta n_g \frac{L}{c}$ after the propagation in the LC. A polarizer placed at the output of the cell projects the two polarization components onto the same polarization direction in order to generate a spectral interference pattern. A spectrometer acquires the dynamical spectral map. (b) The dynamical characterization of the FT. A 5mW light beam from a Helium-Neon laser ( $\lambda = 633 \text{ nm}$ ) is sent onto the LC-cell after a half-wave plate and a polarizer that orientate its polarization direction at 45° with respect to the initial nematic director $\vec{n}$ . The cube beam-splitter separates the two components of polarization at the output of the cell, each component is, then, sent to a photodiode. The photodiodes and the voltage generator are connected to the oscilloscope to acquire the polarization signals and a copy of the applied voltage. . . . .	46

35	a) Retrieved group delay (points) and corresponding molecular tilt angle $\theta$ (solid line) averaged over the cell thickness as a function of the applied voltage. b) Interference spectrum map measured as a function of the voltage, for a 88 $\mu\text{m}$ -thick LC cell. Image from (Jullien et al., 2016). . . . .	47
36	a) Group index variation as a function of time for different LC thicknesses ( $L= 14, 50, 110, 180, 250 \mu\text{m}$ ). b) Spectrogram of 180 $\mu\text{m}$ thick cell during the transient nematic relaxation. c) Time coefficient ( $\tau_{off}$ ) as a function of effective LC thickness (crosses) which slightly differs from the size of the spacers (see chapter 1), and its quadratic fit (green curve). . . . .	49
37	Spectrogram as a function of time for the 180 $\mu\text{m}$ LC cell under a constraint bias voltage of 2V. The relative group index is plotted below (note the narrow scale). . . . .	49
38	a) Refractive index (orange curve) and Reflectivity at ITO-E7 boundaries (red curve) are plotted as a function of time. b) The related oscillations. c) Group delay excursion of a 50 $\mu\text{m}$ cell: raw data (blue solid curve), exponential fit (black solid curve), and exponential fit with oscillations (red dotted curve). . . . .	50
39	a) Voltage step applied to the LC-cells during the switch-on dynamics. $V_0$ varies from 0V to 2V, while the final voltage is fixed at 10V. b) Transmitted signals along with the extraordinary (A, blue and red) and ordinary (B, light blue and orange) axis, acquired for a voltage step $V_0 = 0V - 10V$ and a voltage step $V_0 = 1.3V - 10V$ ( $L=14 \mu\text{m}$ ). An artificial offset (0.5V) is added between the two sets of data for a better visibility. c) Transmitted signal from photodiode A (extraordinary axis) for the same cell ( $L=14 \mu\text{m}$ ) and for different starting voltages $V_0$ . All the measurements start from the same $t_0$ (not indicated in the plot for the sake of better visibility). . . . .	53
40	a) Transmitted signal along the extraordinary axis (photodiode A) acquired during the cell switch-on for the same voltage step (0V - 10V) and for different LC thickness. Data are normalized and presented with an arbitrary temporal offset in order to compare the maximum losses (lowest value of the transmission dip). b) Transient transmission (see definition in the text) measured along the extraordinary axis during the cell switch-on for an applied voltage step $V_0-10V$ by changing the starting voltage $V_0$ and for different cell thicknesses. The area beyond $V_{th}$ (1.2V) is highlighted in blue. . . . .	54
41	Transient transmission (color-coded) as function of $L$ and $V_0$ , extrapolated from our experimental data. The dotted white line features $T = 50\%$ . . . . .	55
42	Transmitted signal along the extraordinary axis from a $L=9\mu\text{m}$ cell at $V_0 = 0V$ (blue line). Grey line represents the electric field applied. $\tau_{min}$ and $\tau_{prec}$ are indicated. . . . .	56
43	Temporal dynamical features of the Fréedericksz transition. $\tau_{min}$ evolution as a function of $V_0$ and thickness (a, b), $\tau_{prec}$ as a function of $V_0$ and thickness (c, d). The area beyond the $V_{th}$ (1.2V) is highlighted in blue (a,c) and the red line (b,d) indicates a quadratic fit of the data. . . . .	56
44	Dynamical spectral maps obtained by using the experimental setup shown in Figure 34b); data are acquired at $t = t_0$ for different $V_0-10 \text{ V}$ voltage steps $V_0=(0 \text{ V}-1 \text{ V}-1.3 \text{ V}-1.5 \text{ V})$ . . . . .	58
45	a) $\Delta n_g$ and $\Delta \tau_g$ plotted as a function of acquisition time for different $V_0$ (0V, 1V, 1.3V, 1.5V); the blue area is associated to the $V_0 = 0$ measurement and indicates that for this voltage step the Fourier Transform is not possible in this time interval. b) Comparison between $\Delta n_g$ normalized and the transient transmission $T$ as a function of $V_0$ (the curve is extrapolated from the experimental data). In gray the condition of $T = 50\%$ . . . . .	58
46	a) Retrieved group delay as a function of time for E7 (blue curve) and MLC (red curve) using 180 $\mu\text{m}$ . Starting voltage is 1V and final one is 10V. b) Transient transition (T) as function of the starting voltage $V_0$ for a thin-25 $\mu\text{m}$ (orange curve) and thick-180 $\mu\text{m}$ MLC2132-based cells. . . . .	60
47	ITO spectral transmission and reflectivity for optimized-AR-ITO layer (Image from Thorlabs). . . . .	62

48	A half-wave plate and a polarizer set the laser polarization and pulse energy. The laser is collimated and an iris selects the central part of the beam after propagation in the LC cell. In the inset the laser spectrum is plotted. . . . .	63
49	a) Transmitted beam profile after $> 10$ cm of propagation for an average input power of $5W/cm^2$ . b) Signal transmitted through a central iris in different configurations (O.A. = ordinary axis, E.A. = extraordinary axis, see text). c) Characteristic decay rate $\gamma$ ( $s^{-1}$ ) of an exponential fit of the signal decreases as a function of laser average power. The dashed line indicates a linear fit. . . . .	64
50	The laser is focused onto the LC cell and the beam profile is acquired after propagation (Goldeye ALLIED vision P-008 SWIR). Maximum peak intensity is $2.5e^9 W/cm^2$ while the maximum average flux is $7.6e^3 W/cm^2$ . . . . .	65
51	Typical multiple-ring pattern when the laser is polarized along the LC ordinary axis in a) and along the extraordinary axis in b). . . . .	66
52	MIRO simulations of the spatial profile after long propagation induced by a Gaussian pulse encountering a phase change with the same spatial extension: a) positive phase shift ( $+10rad$ ) and b) negative phase shift ( $-10rad$ ). . . . .	67
53	a) Acquired multiple-ring pattern (laser polarized along EA). b) Horizontal spatial distribution as a function of time for a pattern composed by 15 rings. c) Horizontal spectral distribution. Each sub-plot is related to one-ring. The last image on the right represents to reference laser spectrum. . . . .	68
54	a) Typical multiple-ring pattern on the extraordinary axis induced by a cw laser. Normalized intensity horizontal profiles (for $N \sim 10$ ) for the femtosecond laser (dark red curve) and cw laser (orange curve). . . . .	68
55	Ring pattern formation. First line: the laser is extraordinary polarized (a= $150mW$ , b= $132mW$ , c= $108mW$ ). Second line: the laser is ordinary polarized (d= $150mW$ , e= $143mW$ , f= $108mW$ ). . . . .	69
56	Refractive index $n$ variation as a function of the average power and the position around the focus (a, b respectively). The red (resp. orange) line refers to an extraordinary (resp. ordinary) laser polarization direction. In a), the labels refer to Figure 55. The beam as a function of $z$ appears in gray in panel b). In c), d) are plotted the maximum LC temperature $T$ as function of the average power (c) and the position (d), deduced from a) and b) (see text). Again, the red (resp. orange) line refers to an extraordinary (resp. ordinary) laser polarization direction. Critical temperature ( $T_c = 331K$ ) is indicated. Arrows show the $z$ -scan direction. . . . .	70
57	a) Experimental Set-up: self-diffraction experiment in a two-wave configuration with a $500 mW$ cw laser at ( $\lambda_0 = 1.06 \mu m$ ): red beams are the diffracted beams. b) Image of the fringes with a period of $140 \mu m$ . c) The spatial pattern when blocking one beam: the image is taken as reference. d) Diffraction pattern when the two beams interfere onto the LC: the generated diffracted beams are highlighted by arrows. . . . .	72
58	Group Delay Dispersion ( $fs^2$ ) introduced by a $180\mu m$ thick NLC. In red, GDD as a function of time following a $10v-0v$ voltage step in an electrically-driven Lc-cell. In blue, GDD variation as a function of the inner temperature. Note the decreasing temperature scale. . . . .	73
59	Common LC based light modulators (LC-SLM, LCOS, LCLV, LLCDD). . . . .	76
60	Evolution of the LC devices used in this thesis: from the transmissive LC cells (left) to the retro-reflective multilayer THOR-SLM (center) until the final single-layer THOR-SLM (right). . . . .	78

61	Spatial Interferometer: a half-wave plate and a polarizer set the He-Ne laser polarization and energy. The THOR-SLM is placed on the transmitted arm of a and its spatial profile is imaged onto a camera (2f-2f). The rear of the device is illuminated by a blue fibre diode by Thorlabs ( $d = 2 \text{ mm}$ , $650 \text{ mW max}$ , $\lambda = 465 \text{ nm}$ ). The number and position of the fringes are set by the reference mirror. The green arrow indicates the extraordinary axis of THOR-SLM. . . . .	84
62	Acquired interference patterns increasing the writing laser flux for the E7-Gold. The blue light spatial profile is plotted close to the reference on the top of the graph. The chaotic transition pattern is visible on the last two graphs ( $2.1\text{-}2.25 \text{ W/cm}^2$ ). . . . .	85
63	Fringes patterns addressed with the maximum writing flux $2.25 \text{ (W/cm}^2\text{)}$ : E7-Gold on the left, MLC-Gold on the center, MLC-Chrome on the right. . . . .	86
64	a) Introduced spatial phase shift on the extraordinary axis for E7-Gold: each plot represents a different writing flux. b) Maximum phase shift (left black scale), $\Delta n_e$ (right black scale) and $OPD$ (right blue scale) as a function of the writing laser flux ( $\text{W/cm}^2$ ) for the three THOR-SLM prototypes. E7-Gold isotropic phase transition is plotted in grey and an exponential fit of the experimental points in blue (dotted) to indicate non-linearity of $\Delta n_e$ with the writing laser flux. c) (orange frame in b) Zoom of MLC-Gold and MLC-Chrome phase-shift. . . . .	87
65	Experimental Set-up: a broadband Michelson interferometer is installed with a super-continuum white light source (LEUKOS, $200 \text{ mW}$ , $450\text{-}850 \text{ nm}$ ). A long-pass filter (cut-off: $500 \text{ nm}$ ) with a short-pass dichroic mirror (cut-off: $950 \text{ nm}$ ) select the spectral range. The polarization state is set using a polarizer. Bulk materials are added on one interferometer arm to compensate the THOR-SLM dispersion placed in the other one. The device is imaged ( $f = 150 \text{ mm}$ ) into a spectrometer (Ocean Optics $450\text{-}850 \text{ nm}$ ). The extraordinary axis of the LC molecules is indicated with a green arrow. The fibre diode ( $d = 6 \text{ mm}$ , $650 \text{ mW max}$ , $\lambda = 465 \text{ nm}$ by Thorlabs) is the addressing writing laser. The two gaussian spatial profiles are also plotted: reading beam (orange curve; $d=2 \text{ mm}$ ) and writing beam (blue curve, $d=6 \text{ mm}$ ). The raw spectrum (orange) and the interference one (blue) are also plotted. . . . .	90
66	a) E7-Gold refractive group indices $n_{g_e}$ (green spots) and $n_{g_o}$ (orange spots) as a function of the addressing flux ( $\text{W/cm}^2$ ). b) Same graph but for MLC2132-Gold (squared) and MLC2132-Chrome (stars). The relative introduced group delay scale is plotted on the right axis. . . . .	91
67	E7-Gold (red curve) and MLC-Gold (blue curve) inner temperature as a function of applied writing flux. E7 isotropic transition temperature is also plotted. Writing beam size of $6 \text{ mm}$ . . . . .	92
68	Refractive group index as a function of the writing beam flux on the extraordinary axis. Different LC thicknesses are plotted, E7-Gold: $25 \text{ }\mu\text{m}$ (Green spots), $50 \text{ }\mu\text{m}$ (Red spots) and $110 \text{ }\mu\text{m}$ (Blue spots). In the legend are shown the relative max group delay excursions $\Delta\tau$ . . . . .	93
69	Interferogram as a function of acquisition time for E7-Gold (a,b) and MLC-Gold (c): approaching the nematic-to-isotropic transition the signal drops suddenly in (a). At lower flux ( $1.75 \text{ W/cm}^2$ ) the full excursion is visible (b). MLC-Gold shows a smaller fringes shift due to the lower dephasing (c). (d) Recovered $\Delta n_g$ excursion during the turning-on (E7-Gold in blue and green, MLC-Gold in orange) and turning off (MLC-Gold in red). . . . .	94
70	a) Experimental Set-up: a broadband Michelson interferometer is installed with a super-continuum white light source (LEUKOS, $200 \text{ mW}$ , $450\text{-}950 \text{ nm}$ ). A grating ( $300 \text{ Grooves/mm}$ , $31.7^\circ$ blaze angle) disperses the spectrum and the SLM is placed in the Fourier plane of $4f$ -line in a folded configuration ( $f=75\text{mm}$ ). Writing laser is a blue fibre diode $650 \text{ mW}$ , $\lambda_0 = 465 \text{ nm}$ , $d = 6 \text{ mm}$ . The three spatial addressing configurations (different focusing conditions) are shown in b). c) Raw spectra: one arm in orange, fringed spectrum in blue. . . . .	96

71	<p>Estimation of the introduced phase resolution: a) Reference (gold) and addressed spectrum (green) with the relative phase shift (blue). The arrows indicates the phase amplitude peak (light blue) and its width (red). Spectral phase map as function of wavelength and writing flux for E7-Gold (b) and MLC-Gold (c). d) The maximum phase introduced for both SLMs (in blue) and the relative width (in red). . . . .</p>	97
72	<p>Phase maps for all the prototypes and for both configurations: MLC-Chrome in the first row (a,b,c), MLC-Gold in the second one (d,e,f) and E7-Gold in the last one (g,h,i). The first column (a,d,g) is related to a positive group delay excursion (second focusing arrangement), the second column (b,e,h) shows the spectral maps introducing a negative phase shift (third focusing arrangement). Some positive and negative spectral phase variation are plotted in the third column (c,f,i) for each prototype. In the last row, the relative spatial writing beam intensity profiles are plotted for the second configuration (j) and for the third one (k). Dotted black curves are the gaussian fit (<math>\sigma = 1mm.</math>) The colorbar features the chromatic reading beam spatial repartition. In the last graph (l), the GDD coefficients are plotted as a function of the blue writing power. In blue scale the positive variation, in red scale the negative one. The same mark is used to identify the prototype (spot E7-Gold, Squares MLC-Gold, Crosses MLC-Chrome). . . . .</p>	99
73	<p>Scheme of the common ultrafast pulse shaper in terms of spectral phase tunability and spectral acceptance. . . . .</p>	104
74	<p>State of art of the best chirped mirrors in terms of spectral acceptance: left continuous Group delay control by (Chia et al., 2014), right discontinuous phase control over <math>&gt; 3</math>-octave span by (Razskazovskaya et al., 2017) . . . . .</p>	105
75	<p>Scheme of the THOR-SLM for thermal calculations. Grey area refer to the glass substrates, yellow to Gold layer, and green to LC layer. <math>r</math> is the radial coordinate and <math>R_m</math> the maximum source diameter. <math>z</math> is the propagation direction and <math>z_i</math> delimits the thickness of medium <math>i</math>. . . . .</p>	106
76	<p>a) Temperature profile along <math>z</math> direction crossing THOR-SLM layers for <math>r=0</math>, and <math>R_S = 0.5</math> mm. b) Increase of the temperature <math>\Delta T</math> at <math>z = z_{Au}</math> as a function of <math>r</math> (orange) for <math>R = 0.5mm</math> (illumination source spatial profile indicated in grey). c) Normalized Increase of the temperature <math>\Delta T</math> at <math>z = z_{Au}</math> as a function of <math>r</math> for various <math>R</math> values. d) Thermal gradient width (at <math>1/e^2</math>) as a function of the writing beam radius. . . . .</p>	107
77	<p>New writing arrangement: a blue diode is passing through a polarizer, a half-wave plate and is focused into a square-core fiber. The writing beam is then reflected on a Digital mirror (DLP) and imaged onto the rear of THOR-SLM. Fiber output, DLP and lenses are all placed on a translation stage. A sketch of the blue spatial profile over the DLP is also shown. . . . .</p>	108
78	<p>Addressing patterns (first column), measured fringes shift (second column) and spectral map (third column) changing the period step of the stripes. Each row represents a different number and periodic step: from 1 stripe of <math>3.75</math> mm, to 8 stripes of <math>0.5</math> mm thick (last row). . . . .</p>	109
79	<p>a) Horizontal cut of the phase map for different periodic steps (blue = <math>7.44</math> mm, orange = <math>5.58</math> mm, green = <math>3.72</math> mm, light-blue = <math>1.86</math> mm , red = <math>0.93</math> mm). b) Introduced phase of <math>3.72</math> mm (black curve) with its multi-gaussian fit (light blue dotted curve). The arrows refers to the maximum phase introduced (<math>\varphi</math> blue), the phase width (<math>\sigma</math> orange) plotted with the same colour in c) as function of the step period. The modulation depth (<math>\Phi</math> red arrow in b) ) is plotted in d). . . . .</p>	110

80	Experimental setup: a) the ultra-broadband light source seeds a Michelson interferometer for referenced phase shaping measurement. The THOR-SLM is inserted in a 4f-line in a folded configuration ( $f=500\text{ mm}$ ). Yellow arrow indicates the laser polarization direction and the extraordinary axis of the LC layer. b) Typical acquired spectra. Different color lines refer to the three different spectrometers. . . . .	112
81	THOR-SLM spectral reflectivity. In blue E7-Gold prototype, in black the MLC-Chrome one. . . . .	113
82	4f-line calibration through X-scan: in a) the acquired spectra are pictured displacing along $x$ the optical fiber. b) Retrieved central frequencies $\nu_0$ as function of the lateral position. . . . .	114
83	THOR-SLM Calibration: a) spectral phase-shift with a lateral displacement of the addressing beam. b) Maximum introduced phase shift as a function of the central frequency. The dashed line indicates a linear fit. . . . .	114
84	DLP retrieving algorithm. A is a fundamental constant, B is a calibration constant. C,D,E are constants specific to a LC employed. . . . .	115
85	$\Delta n_e(T)$ for E7, calculated according to eq. 6.5 and Tab. 19 for two different frequencies (blue and red lines). $T_c$ is also indicated. The green line is the difference between the two curves (right scale) (Li, 2005). . . . .	116
86	Algorithm for the determination of the blue light spatial profiles loaded on the DLP. Each row refers to a target spectral phase (positive GDD, negative GDD, negative TOD, positive TOD). The target spectral phase is plotted in the first column (green dots). The deduced target spatial evolution of the temperature, $T_{target}(x)$ , is plotted in column 2 (black dots). Column 3 shows a suggestion of normalized spatial flux of the addressing beam onto THOR-SLM plane (light gray) and the calculated thermal gradients (dotted blue). Induced temperature (resp. spectral phase) is then shown in red in column 2 (resp. column 1). . . . .	117
87	a): Spectral phase during the X scan (0.5mm step). In the top, the uploaded DLP pattern is pictured. b) GDD and TOD from (a) as a function of $\Delta x$ at 330 THz. . . . .	118
88	Introduced spectral phase for the 50 $\mu\text{m}$ -thick E7-Gold THOR-SLM: a) Positive quadratic phase ( $+8.2\text{ fs}^2$ ), b) negative quadratic phase ( $-2.5\text{ fs}^2$ ), c) negative cubic phase ( $-13\text{ fs}^3$ ), d) positive cubic phase ( $+13\text{ fs}^3$ ). The spatial pattern loaded on the DLP is shown in the top right corner. . . . .	119
89	P-scan results: a) positive (in blue) and negative (in red) quadratic spectral phases changing the blue power. b) positive (in green) and negative (in brown) cubic phases. Relative DLP patterns are pictured as an inset with the same colour. c), d) $\varphi^2$ (solid lines) and $\varphi^3$ (dotted lines) coefficients as a function of the normalized writing beam power for all the patterns. . . . .	120
90	Introduced spectral phase for the 110 $\mu\text{m}$ -thick THOR-SLM: a) Positive quadratic phase in blue ( $+19\text{ fs}^2$ ), negative quadratic phase in red ( $-7\text{ fs}^2$ ), b) negative cubic phase in green ( $-19\text{ fs}^3$ ), and positive cubic phase in orange ( $18\text{ fs}^3$ ). . . . .	121
91	Spectral dispersion of 1mm of different glasses $\text{SiO}_2, \text{CaF}_2, \text{LiF}$ , and $\text{MgF}_2$ . . . . .	122
92	a) Phase introduced by a 1mm of LiF and the needed phase compensation by THOR-SLM. The DLP pattern is pictured in the corner of a), and the relative temperature spatial profile is plotted in b). . . . .	122
93	Simulated normalized thermal gradient for three different substrates (6 mm of BK7 in orange, 1mm of BK7 in red, 1mm of sapphire in blue) considering a source of 1.5 mm (showed in grey). b) Spatial width of the thermal gradients (at $1/e^2$ ) as function of the radius source for the the same substrates. . . . .	124
94	Transmission of common glasses (BK7, Sapphire and $\text{CaF}_2$ ). . . . .	125



95	Experimental set-up: a fs laser (400 fs FTL, $\lambda_0 = 1\mu\text{m}$ , 150 mW of average power and a high repetition rate of 80 MHz) is polarized parallel with the respect of the nematic director of the LC cell. A gratings (24.8° Groove Angle, 1200 Grooves/mm) disperses the spectrum. THOR-SLM is inserted in the Fourier plane of a 4f-line (f=500 mm). The reflection is then analyzed by a SHG FROG (FROZZER). The blue fibre diode ( $d = 2\text{mm}$ , 650mW, $\lambda = 465\text{nm}$ , by Thorlabs) is focusing on the rear of the LC-SLM with a cylindric lens (f=150 mm). The two different focusing strategies are pictured as well. . . . .	131
96	FROG traces for the reference pulse. a) Measured spectrum map. b) Retrieved spectrum map. c) Temporal profile. d) Retrieved spectrum intensity (blue) and phase (green). . .	132
97	FROG traces for the first configuration positive chirp (a,b,c,d) and for the second one (e,f,g,h) negative chirp introduced. . . . .	132
98	A femtosecond oscillator 40 fs, 150 mW, 80 MHz at $\lambda_0 = 1.55\mu\text{m}$ is reflected by the THOR-SLM and focused (f=200) in a BBO crystal placed on a translation stage (z-scan). The SHG generate signal is acquired by a spectrometer (Ocean Optics). The device is addressed from the rear with a fibre diode by Thorlabs ( $d = 2\text{mm}$ , 650mWmax, $\lambda = 465\text{nm}$ ). . . . .	134
99	SHG generation spectra at different BBO position for E7-Gold (left) and for MLC-Gold (right). Each graph shows represents different writing power. . . . .	135
100	Sketch of the focal plane shifting and Equivalent focal length (red curve) and relative birefringence excursion (blue curve) as function of the focal shift. E7-Gold is plotted in orange and MLC-Gold in green. . . . .	135

---

## References

- Agez, G., Clerc, M. G., Louvergneaux, E., & Rojas, R. G. (2013). Bifurcations of emerging patterns in the presence of additive noise. *Physical Review E*, *87*(4), 042919.
- Akturk, S., Gu, X., Gabolde, P., & Trebino, R. (2005). The general theory of first-order spatio-temporal distortions of gaussian pulses and beams. *Optics express*, *13*(21), 8642–8661.
- Alam, M. Z., De Leon, I., & Boyd, R. W. (2016). Large optical nonlinearity of indium tin oxide in its epsilon-near-zero region. *Science*, *352*(6287), 795–797.
- Ara, M. M., Bahramian, R., Mousavi, S., & Abolhasani, M. (2009). Self-phase modulation and ring pattern observation by applying electrical field on dye-doped nematic liquid crystal. *Journal of Molecular Liquids*, *149*(1-2), 18–21.
- Aubourg, P., Huignard, J. P., Hareng, M., & Mullen, R. A. (1982, Oct). Liquid crystal light valve using bulk monocrystalline bi12sio20 as the photoconductive material. *Appl. Opt.*, *21*(20), 3706–3712. Retrieved from <http://ao.osa.org/abstract.cfm?URI=ao-21-20-3706>
- Backus, S., Durfee, C. G., Mourou, G., Kapteyn, H. C., & Murnane, M. M. (1997). 0.2-tw laser system at 1 khz. *Optics letters*, *22*(16), 1256–1258.
- baron Fourier, J. B. J. (1822). *Théorie analytique de la chaleur*. F. Didot.
- Blake, G., Mullin, T., & Tavener, S. (1999). The freedericksz transition as a bifurcation problem. *Dynamics and Stability of Systems*, *14*(3), 299–331.
- Bock, M., Kumar Das, S., Grunwald, R., Osten, S., Staudt, P., & Stibenz, G. (2008). Spectral and temporal response of liquid-crystal-on-silicon spatial light modulators. *Applied Physics Letters*, *92*(15), 151105. Retrieved from <https://doi.org/10.1063/1.2909115>
- Bohman, S., Suda, A., Kanai, T., Yamaguchi, S., & Midorikawa, K. (2010, Jun). Generation of 5.0fs, 5.0mj pulses at 1khz using hollow-fiber pulse compression. *Opt. Lett.*, *35*(11), 1887–1889. Retrieved from <http://ol.osa.org/abstract.cfm?URI=ol-35-11-1887>
- Bortolozzo, U., Montina, A., Arecchi, F. T., Huignard, J. P., & Residori, S. (2007, Jul). Spatiotemporal pulses in a liquid crystal optical oscillator. *Phys. Rev. Lett.*, *99*, 023901. Retrieved from <https://link.aps.org/doi/10.1103/PhysRevLett.99.023901>
- Bortolozzo, U., Residori, S., & Howell, J. C. (2013, Aug). Precision doppler measurements with steep dispersion. *Opt. Lett.*, *38*(16), 3107–3110. Retrieved from <http://ol.osa.org/abstract.cfm?URI=ol-38-16-3107>
- Bortolozzo, U., Residori, S., & Huignard, J. P. (2007, Apr). Self-pumped phase conjugation in a liquid crystal light valve with a tilted feedback mirror. *Opt. Lett.*, *32*(7), 829–831. Retrieved from <http://ol.osa.org/abstract.cfm?URI=ol-32-7-829>
- Bortolozzo, U., Residori, S., & Huignard, J.-P. (2010, Jun). Slow-light birefringence and polarization interferometry. *Opt. Lett.*, *35*(12), 2076–2078. Retrieved from <http://ol.osa.org/abstract.cfm?URI=ol-35-12-2076>
- Bortolozzo, U., Residori, S., & Huignard, J.-P. (2013). Transmissive liquid crystal light-valve for near-infrared applications. *Applied optics*, *52*(22), E73–E77.
- Bortolozzo, U., Residori, S., Petrosyan, A., & Huignard, J. (2006). Pattern formation and direct measurement of the spatial resolution in a photorefractive liquid crystal light valve. *Optics communications*, *263*(2), 317–321.
- Borzsonyi, A., Kovacs, A., & Osvay, K. (2013). What we can learn about ultrashort pulses by linear optical methods. *Applied Sciences*, *3*(2), 515–544.
- Boughdad, O., Eloy, A., Mortessagne, F., Bellec, M., & Michel, C. (2019). Anisotropic nonlinear refractive index measurement of a photorefractive crystal via spatial self-phase modulation. *arXiv preprint arXiv:1907.09865*.
- Brabec, T., & Krausz, F. (2000, Apr). Intense few-cycle laser fields: Frontiers of nonlinear optics. *Rev. Mod. Phys.*, *72*, 545–591. Retrieved from <https://link.aps.org/doi/10.1103/RevModPhys.72.545>
- Brignon, A., Bongrand, I., Loiseaux, B., & Huignard, J.-P. (1997). Signal-beam amplification by two-wave mixing in a liquid-crystal light valve. *Optics letters*, *22*(24), 1855–1857.

- Brixner, T., & Gerber, G. (2001, Apr). Femtosecond polarization pulse shaping. *Opt. Lett.*, *26*(8), 557–559. Retrieved from <http://ol.osa.org/abstract.cfm?URI=ol-26-8-557>
- Brugioni, S., Faetti, S., & Meucci, R. (2003). Mid-infrared refractive indices of the nematic mixture e7. *Liquid crystals*, *30*(8), 927–930.
- Callen, W., Huth, B., & Pantell, R. (1967). optical patterns of thermally self-defocused light. *Applied Physics Letters*, *11*(3), 103–105.
- Castellano, J. A. (2005). *Liquid gold: the story of liquid crystal displays and the creation of an industry*. World Scientific.
- Cattaneo, L., Savoini, M., Muševič, I., Kimel, A., & Rasing, T. (2015). Ultrafast all-optical response of a nematic liquid crystal. *Optics express*, *23*(11), 14010–14017.
- Chandrasekhar, S., Sadashiva, B., & Suresh, K. (1977). Liquid crystals of disc-like molecules. *pramana*, *9*(5), 471–480.
- Chia, S.-H., Cirmi, G., Fang, S., Rossi, G. M., Mücke, O. D., & Kärtner, F. X. (2014). Two-octave-spanning dispersion-controlled precision optics for sub-optical-cycle waveform synthesizers. *Optica*, *1*(5), 315–322.
- Choon Khoo, I. (2009, 02). Nonlinear optics of liquid crystalline materials. *Physics Reports-review Section of Physics Letters - PHYS REP-REV SECT PHYS LETT*, *471*, 221–267.
- Ciesielski, A., Skowronski, L., Trzcinski, M., Górecka, E., Trautman, P., & Szoplik, T. (2018). Evidence of germanium segregation in gold thin films. *Surface Science*, *674*, 73–78.
- Clarke, D. (2004). Interference effects in single wave plates. *Journal of Optics A: Pure and Applied Optics*, *6*(11), 1036.
- Dabby, F., Gustafson, T., Whinnery, J., Kohanzadeh, Y., & Kelley, P. (1970). thermally self-induced phase modulation of laser beams. *Applied Physics Letters*, *16*(9), 362–365.
- De Gennes, P.-G., & Prost, J. (1995). *The physics of liquid crystals* (Vol. 83). Oxford university press.
- De Luca, A., Nersisyan, S., & Umeton, C. (2003). Observation of cancellation and second light-induced fréedericksz transition in nematic liquid crystals. *Optics letters*, *28*(2), 108–110.
- Derfel, G. (1988). Field effects in nematic liquid crystals in terms of catastrophe theory. *Liquid Crystals*, *3*(10), 1411–1424.
- Dewey, A. (1984). Laser-addressed liquid crystal displays. *Optical Engineering*, *23*(3), 230–1.
- di Pietro, V. M., Jullien, A., Bortolozzo, U., Forget, N., & Residori, S. (2018). Thermally-induced nonlinear spatial shaping of infrared femtosecond pulses in nematic liquid crystals. *Laser Physics Letters*, *16*(1), 015301.
- Dorrer, C., Salin, F., Verluise, F., & Huignard, J. (1998). Programmable phase control of femtosecond pulses by use of a nonpixelated spatial light modulator. *Optics letters*, *23*(9), 709–711.
- Dorrer, C., Wei, S.-H., Leung, P., Vargas, M., Wegman, K., Boulé, J., ... Chen, S. (2011). High-damage-threshold static laser beam shaping using optically patterned liquid-crystal devices. *Optics letters*, *36*(20), 4035–4037.
- Dou, T. H., Tautz, R., Gu, X., Marcus, G., Feurer, T., Krausz, F., & Veisz, L. (2010). Dispersion control with reflection grisms of an ultra-broadband spectrum approaching a full octave. *Optics express*, *18*(26), 27900–27909.
- Dubietis, A., Couairon, A., & Genty, G. (2019, Feb). Supercontinuum generation: introduction. *J. Opt. Soc. Am. B*, *36*(2), SG1–SG3. Retrieved from <http://josab.osa.org/abstract.cfm?URI=josab-36-2-SG1>
- Dugan, M., Tull, J., & Warren, W. (1997). High-resolution acousto-optic shaping of unamplified and amplified femtosecond laser pulses. *JOSA B*, *14*(9), 2348–2358.
- Durbin, S., Arakelian, S., & Shen, Y. (1981). Laser-induced diffraction rings from a nematic-liquid-crystal film. *Optics letters*, *6*(9), 411–413.
- Ericksen, J. L. (1961). Conservation laws for liquid crystals. *Transactions of the Society of Rheology*, *5*(1), 23–34.

- Ericksen, J. L. (1969). Continuum theory of liquid crystals of nematic type. *Molecular crystals and liquid crystals*, 7(1), 153–164.
- Fattahi, H., Barros, H. G., Gorjan, M., Nubbemeyer, T., Alsaif, B., Teisset, C. Y., ... others (2014). Third-generation femtosecond technology. *Optica*, 1(1), 45–63.
- Feurer, T., Vaughan, J. C., Koehl, R. M., & Nelson, K. A. (2002, Apr). Multidimensional control of femtosecond pulses by use of a programmable liquid-crystal matrix. *Opt. Lett.*, 27(8), 652–654. Retrieved from <http://ol.osa.org/abstract.cfm?URI=ol-27-8-652>
- Forget, N., Crozatier, V., & Tournois, P. (2012). Transmission bragg-grating grisms for pulse compression. *Applied Physics B*, 109(1), 121–125.
- Frank, F. C. (1958). I. liquid crystals. on the theory of liquid crystals. *Discussions of the Faraday Society*, 25, 19–28.
- Froehly, C., Colombeau, B., & Vampouille, M. (1983). Li shaping and analysis of picosecond light pulses. In *Progress in optics* (Vol. 20, pp. 63–153). Elsevier.
- Froehly, C., Lacourt, A., & Vienot, J. C. (1973). Time impulse response and time frequency response of optical pupils.: Experimental confirmations and applications. *Nouvelle Revue d'Optique*, 4(4), 183.
- Gerritsma, C., Van Doorn, C., & Van Zanten, P. (1974). Transient effects in the electrically controlled light transmission of a twisted nematic layer. *Physics Letters A*, 48(4), 263–264.
- Gires, F., & Tournois, P. (1964). Interferometre utilisable pour la compression d'impulsions lumineuses modulees en frequence. *COMPTES RENDUS HEBDOMADAIRES DES SEANCES DE L ACADEMIE DES SCIENCES*, 258(25), 6112.
- Grabielle, S. (2011). *Manipulation et caractérisation du champ électrique optique: applications aux impulsions femtosecondes* (Unpublished doctoral dissertation). Ecole Polytechnique X.
- Haller, I. (1975). Thermodynamic and static properties of liquid crystals. *Progress in solid state chemistry*, 10, 103–118.
- Harrison, R., Dambly, L., Yu, D., & Lu, W. (1997). A new self-diffraction pattern formation in defocusing liquid media. *Optics communications*, 139(1-3), 69–72.
- Hauri, C., Kornelis, W., Helbing, F., Heinrich, A., Couairon, A., Mysyrowicz, A., ... Keller, U. (2004). Generation of intense, carrier-envelope phase-locked few-cycle laser pulses through filamentation. *Applied Physics B*, 79(6), 673–677.
- He, X., Wang, X., Wu, L., Tan, Q., Li, M., Shang, J., ... Huang, Z. (2017). Theoretical modeling on the laser induced effect of liquid crystal optical phased beam steering. *Optics Communications*, 382, 437–443.
- Huang, S.-W., Cirimi, G., Moses, J., Hong, K.-H., Bhardwaj, S., Birge, J. R., ... others (2011). High-energy pulse synthesis with sub-cycle waveform control for strong-field physics. *Nature photonics*, 5(8), 475.
- Humar, M., & Mušević, I. (2010). 3d microlasers from self-assembled cholesteric liquid-crystal microdroplets. *Optics express*, 18(26), 26995–27003.
- Hussain, A., Martínez, J., & Campos, J. (2013). Holographic superresolution using spatial light modulator. *Journal of the European Optical Society-Rapid publications*, 8.
- Hussain, A., Martínez, J., Lizana, A., & Campos, J. (2013). Super resolution imaging achieved by using on-axis interferometry based on a spatial light modulator. *Optics express*, 21(8), 9615–9623.
- Jakeman, E., & Raynes, E. (1972). Electro-optic response times in liquid crystals. *Physics Letters A*, 39(1), 69–70.
- Johnson, P. B., & Christy, R.-W. (1972). Optical constants of the noble metals. *Physical review B*, 6(12), 4370.
- Jullien, A., Bortolozzo, U., Grabielle, S., Huignard, J.-P., Forget, N., & Residori, S. (2016). Continuously tunable femtosecond delay-line based on liquid crystal cells. *Optics express*, 24(13), 14483–14493.

- Jullien, A., Pascal, R., Bortolozzo, U., Forget, N., & Residori, S. (2017). High-resolution hyperspectral imaging with cascaded liquid crystal cells. *Optica*, *4*(4), 400–405.
- Jullien, A., Scarangella, A., Bortolozzo, U., Residori, S., & Mitov, M. (2019). Nanoscale hyperspectral imaging of tilted cholesteric liquid crystal structures. *Soft matter*, *15*(15), 3256–3263.
- Kasprzack, M. (2014). *Thermally deformable mirrors: a new adaptive optics scheme for advanced gravitational wave interferometers* (Unpublished doctoral dissertation).
- Kelker, H., & Scheurle, B. (1969). A liquid-crystalline (nematic) phase with a particularly low solidification point. *Angewandte Chemie International Edition in English*, *8*(11), 884–885. Retrieved from <https://onlinelibrary.wiley.com/doi/abs/10.1002/anie.196908841>
- Kerr, J. (1875). Liv. a new relation between electricity and light: Dielectrified media birefringent (second paper). *The London, Edinburgh, and Dublin Philosophical Magazine and Journal of Science*, *50*(333), 446–458.
- Khoo, I. (1995). *Liquid crystals: Physical properties and nonlinear optical phenomena*. Wiley. Retrieved from <https://books.google.fr/books?id=sgnwAAAAAAAJ>
- Khoo, I. (2006, 05). Wiley series in pure and applied optics. In (p. 369-369).
- Khoo, I., Hou, J., Liu, T., Yan, P., Michael, R., & Finn, G. (1987). Transverse self-phase modulation and bistability in the transmission of a laser beam through a nonlinear thin film. *JOSA B*, *4*(6), 886–891.
- Khoo, I. C. (2014). Nonlinear optics, active plasmonics and metamaterials with liquid crystals. *Progress in Quantum Electronics*, *38*(2), 77–117.
- Kondilis, A., Aperathitis, E., & Modreanu, M. (2008). Derivation of the complex refractive index of ito and iton films in the infrared region of the spectrum by the analysis of optical measurements. *Thin Solid Films*, *516*(22), 8073–8076.
- Krausz, F., & Ivanov, M. (2009). Attosecond physics. *Reviews of Modern Physics*, *81*(1), 163.
- Laberdesque, R., Jullien, A., Bortolozzo, U., Forget, N., & Residori, S. (2017). Tunable angular shearing interferometer based on wedged liquid crystal cells. *Applied optics*, *56*(31), 8656–8662.
- Landau, L. (1980). Em lifshitz statistical physics. *Course of Theoretical Physics*, *5*, 396–400.
- Lavenu, L., Natile, M., Guichard, F., Délen, X., Hanna, M., Zaouter, Y., & Georges, P. (2019). High-power two-cycle ultrafast source based on hybrid nonlinear compression. *Optics express*, *27*(3), 1958–1967.
- Lavenu, L., Natile, M., Guichard, F., Zaouter, Y., Delen, X., Hanna, M., . . . Georges, P. (2018). Nonlinear pulse compression based on a gas-filled multipass cell. *Optics letters*, *43*(10), 2252–2255.
- Lee, S., Lee, S., & Kim, H. (1998). Electro-optic characteristics and switching principle of a nematic liquid crystal cell controlled by fringe-field switching. *Applied physics letters*, *73*(20), 2881–2883.
- Lenzini, F., Residori, S., Arecchi, F. T., & Bortolozzo, U. (2011, Dec). Optical vortex interaction and generation via nonlinear wave mixing. *Phys. Rev. A*, *84*, 061801. Retrieved from <https://link.aps.org/doi/10.1103/PhysRevA.84.061801>
- Lepetit, L., Chériaux, G., & Joffre, M. (1995). Linear techniques of phase measurement by femtosecond spectral interferometry for applications in spectroscopy. *JOSA B*, *12*(12), 2467–2474.
- Leslie, F. M. (1968). Some constitutive equations for liquid crystals. *Archive for Rational Mechanics and Analysis*, *28*(4), 265–283.
- Li, J. (2005). Refractive indices of liquid crystals and their applications in display and photonic devices.
- Li, J., Gauza, S., & Wu, S.-T. (2004). Temperature effect on liquid crystal refractive indices. *Journal of applied physics*, *96*(1), 19–24.

- Li, J., Gauzia, S., & Wu, S.-T. (2004). High temperature-gradient refractive index liquid crystals. *Optics express*, *12*(9), 2002–2010.
- Li, J., & Wu, S.-T. (2004). Extended cauchy equations for the refractive indices of liquid crystals. *Journal of applied physics*, *95*(3), 896–901.
- Lin, P.-T., Wu, S.-T., Chang, C.-Y., & Hsu, C.-S. (2004). Uv stability of high birefringence liquid crystals. *Molecular Crystals and Liquid Crystals*, *411*(1), 243–253.
- Lureau, F., Laux, S., Casagrande, O., Chalus, O., Pellegrina, A., Matras, G., ... others (2016). Latest results of 10 petawatt laser beamline for eli nuclear physics infrastructure. In *Solid state lasers xxv: Technology and devices* (Vol. 9726, p. 972613).
- Maine, P., Strickland, D., Bado, P., Pessot, M., & Mourou, G. (1988). Generation of ultrahigh peak power pulses by chirped pulse amplification. *IEEE Journal of Quantum electronics*, *24*(2), 398–403.
- Malacara, D. (2007). *Optical shop testing* (Vol. 59). John Wiley & Sons.
- Manneville, P. (1981). The transition to turbulence in nematic liquid crystals. *Molecular crystals and liquid crystals*, *70*(1), 223–250.
- Marcus, S. (2019). *A new generation of high-power, waveform controlled, few-cycle light sources*. Springer Theses Series.
- McConville, S., Laurent, D., Guarino, A., & Residori, S. (2005). Measurement of the giant nonlinear response of dye-doped liquid crystals. *American journal of physics*, *73*(5), 425–432.
- Melnyk, O., Garbovskiy, Y., Bueno-Baques, D., & Glushchenko, A. (2019). Electro-optical switching of dual-frequency nematic liquid crystals: Regimes of thin and thick cells. *Crystals*, *9*(6), 314.
- Mercuri, F., Marinelli, M., Zammit, U., & Scudieri, F. (1998). Thermal conductivity and thermal diffusivity anisotropy in a liquid crystal. *Journal of thermal analysis and calorimetry*, *52*(3), 739–744.
- Miranda, M., Arnold, C. L., Fordell, T., Silva, F., Alonso, B., Weigand, R., ... Crespo, H. (2012). Characterization of broadband few-cycle laser pulses with the d-scan technique. *Optics express*, *20*(17), 18732–18743.
- Monmayrant, A., Weber, S., & Chatel, B. (2010). A newcomer’s guide to ultrashort pulse shaping and characterization. *Journal of Physics B: Atomic, Molecular and Optical Physics*, *43*(10), 103001.
- Morice, O. (2003). Miró: complete modeling and software for pulse amplification and propagation in high-power laser systems. *Optical Engineering*, *42*(6), 1530–1542.
- Moss, F., & McClintock, P. V. (1989). *Noise in nonlinear dynamical systems* (Vol. 2). Cambridge University Press.
- Moulton, P. F. (1986, Jan). Spectroscopic and laser characteristics of ti:al<sub>2</sub>o<sub>3</sub>. *J. Opt. Soc. Am. B*, *3*(1), 125–133. Retrieved from <http://josab.osa.org/abstract.cfm?URI=josab-3-1-125>
- Mourou, G. A., Tajima, T., & Bulanov, S. V. (2006). Optics in the relativistic regime. *Reviews of modern physics*, *78*(2), 309.
- Mysyrowicz, A., Couairon, A., & Keller, U. (2008). Self-compression of optical laser pulses by filamentation. *New Journal of Physics*, *10*(2), 025023.
- Nabekawa, Y., Kuramoto, Y., Togashi, T., Sekikawa, T., & Watanabe, S. (1998). Generation of 0.66-tw pulses at 1?? khz by a ti: sapphire laser. *Optics letters*, *23*(17), 1384–1386.
- Napoli, G. (2005). Weak anchoring effects in electrically driven freedericksz transitions. *Journal of Physics A: Mathematical and General*, *39*(1), 11.
- Neradovskiy, M., Scarangella, A., Jullien, A., & Mitov, M. (2019). Dispersion of 20 fs pulses through band edges of cholesteric liquid crystals. *Optics Express*, *27*(15), 21794–21809.
- Nespoulous, M., Blanc, C., & Nobili, M. (2010). Orientational quenched disorder of a nematic liquid crystal. *Physical review letters*, *104*(9), 097801.

- Oh-e, M., & Kondo, K. (1996). Response mechanism of nematic liquid crystals using the in-plane switching mode. *Applied physics letters*, *69*(5), 623–625.
- Ono, H., Igarashi, Y., & Harato, Y. (1998). Self-diffraction pattern formation in liquid crystals on dye-doped polymer surfaces. *Molecular Crystals and Liquid Crystals Science and Technology. Section A. Molecular Crystals and Liquid Crystals*, *325*(1), 137–144.
- Onokhov, A., Berenberg, V., Beresnev, L., Chaika, A., Feoktistov, N., Isaev, M., & Konshina, E. (2000, 07). Reflective optically addressed flc slms for dynamic holography. *Proceedings of SPIE - The International Society for Optical Engineering*.
- Orihara, H., Sakai, A., & Nagaya, T. (2001). Direct observation of the orientational fluctuations in a nematic liquid crystal with a high-speed camera. *Molecular Crystals and Liquid Crystals Science and Technology. Section A. Molecular Crystals and Liquid Crystals*, *366*(1), 143–149.
- Ouillé, M., Vernier, A., Boehle, F., Bocoum, M., Lozano, M., Rousseau, J.-P., ... others (2019). Relativistic near-single-cycle optics at 1 khz. *arXiv preprint arXiv:1907.01239*.
- Papadopoulos, D., Zou, J., Le Blanc, C., Chériaux, G., Georges, P., Druon, F., ... others (2016). The apollon 10 pw laser: experimental and theoretical investigation of the temporal characteristics. *High Power Laser Science and Engineering*, *4*.
- Peigné, A., Bortolozzo, U., Residori, S., Molin, S., Nouchi, P., Dolfi, D., & Huignard, J.-P. (2015, Dec). Adaptive holographic interferometer at 1.55 $\mu\text{m}$  based on optically addressed spatial light modulator. *Opt. Lett.*, *40*(23), 5482–5485. Retrieved from <http://ol.osa.org/abstract.cfm?URI=ol-40-23-5482>
- Pervak, V., Ahmad, I., Trubetskov, M., Tikhonravov, A., & Krausz, F. (2009). Double-angle multilayer mirrors with smooth dispersion characteristics. *Optics express*, *17*(10), 7943–7951.
- Pervak, V., Naumov, S., Krausz, F., & Apolonski, A. (2007, Oct). Chirped mirrors with low dispersion ripple. *Opt. Express*, *15*(21), 13768–13772. Retrieved from <http://www.opticsexpress.org/abstract.cfm?URI=oe-15-21-13768>
- Petrossian, A., & Residori, S. (2002). Surfactant enhanced reorientation in dye-doped nematic liquid crystals. *EPL (Europhysics Letters)*, *60*(1), 79.
- Ramirez, E. G., Carrasco, M. A., Otero, M. M., Cerda, S. C., & Castillo, M. I. (2010). Far field intensity distributions due to spatial self phase modulation of a gaussian beam by a thin nonlocal nonlinear media. *Optics express*, *18*(21), 22067–22079.
- Raynes, E. P., Brown, C. V., & Strmer, J. F. (2003). Method for the measurement of the  $k_{22}$  nematic elastic constant. *Applied Physics Letters*, *82*(1), 13-15. Retrieved from <https://doi.org/10.1063/1.1534942>
- Razskazovskaya, O., Krausz, F., & Pervak, V. (2017). Multilayer coatings for femto-and attosecond technology. *Optica*, *4*(1), 129–138.
- Reichelt, S., Häussler, R., Fütterer, G., Leister, N., Kato, H., Usukura, N., & Kanbayashi, Y. (2012). Full-range, complex spatial light modulator for real-time holography. *Optics letters*, *37*(11), 1955–1957.
- Reinitzer, F. (1888). Beiträge zur kenntniss des cholesterins. *Monatshefte für Chemie/Chemical Monthly*, *9*(1), 421–441.
- Residori, S., & Petrossian, A. (2003). Light induced reorientation in azo-dye doped liquid crystals: The relative role of surface and bulk effects. *Molecular Crystals and Liquid Crystals*, *398*(1), 137–156.
- Robertson, B., Yang, H., Redmond, M. M., Collings, N., Moore, J. R., Liu, J., ... others (2013). Demonstration of multi-casting in a  $1 \times 9$  lcos wavelength selective switch. *Journal of Lightwave Technology*, *32*(3), 402–410.
- Robertson, B., Zhang, Z., Redmond, M. M., Collings, N., Liu, J., Lin, R., ... Chu, D. (2012). Use of wavefront encoding in optical interconnects and fiber switches for cross talk mitigation. *Applied optics*, *51*(5), 659–668.

- Robertson, B., Zhang, Z., Yang, H., Redmond, M. M., Collings, N., Liu, J., ... others (2012). Application of the fractional fourier transform to the design of lcos based optical interconnects and fiber switches. *Applied optics*, 51(12), 2212–2222.
- Sanner, N., Huot, N., Audouard, E., Larat, C., Huignard, J.-P., & Loiseaux, B. (2005, Jun). Programmable focal spot shaping of amplified femtosecond laser pulses. *Opt. Lett.*, 30(12), 1479–1481. Retrieved from <http://ol.osa.org/abstract.cfm?URI=ol-30-12-1479>
- Singh, S. (2000). Phase transitions in liquid crystals. *Physics Reports*, 324(2-4), 107–269.
- Song, L., Fu, S., Liu, Y., Zhou, J., Chigrinov, V. G., & Khoo, I. C. (2013, Dec). Direct femtosecond pulse compression with miniature-sized bragg cholesteric liquid crystal. *Opt. Lett.*, 38(23), 5040–5042. Retrieved from <http://ol.osa.org/abstract.cfm?URI=ol-38-23-5040>
- Spence, D. E., Kean, P. N., & Sibbett, W. (1991). 60-fsec pulse generation from a self-mode-locked ti: sapphire laser. *Optics letters*, 16(1), 42–44.
- Stibenz, G., Zhavoronkov, N., & Steinmeyer, G. (2006, Jan). Self-compression of millijoule pulses to 7.8 fs duration in a white-light filament. *Opt. Lett.*, 31(2), 274–276. Retrieved from <http://ol.osa.org/abstract.cfm?URI=ol-31-2-274>
- Strickland, D., & Mourou, G. (1985). Compression of amplified chirped optical pulses. *Optics communications*, 55(6), 447–449.
- Sung, J. H., Lee, H. W., Yoo, J. Y., Yoon, J. W., Lee, C. W., Yang, J. M., ... Nam, C. H. (2017). 4.2 pw, 20 fs ti: sapphire laser at 0.1 hz. *Optics letters*, 42(11), 2058–2061.
- Tajalli, A., Chanteau, B., Kretschmar, M., Kurz, H. G., Zuber, D., Kovačev, M., ... Nagy, T. (2016). Few-cycle optical pulse characterization via cross-polarized wave generation dispersion scan technique. *Optics letters*, 41(22), 5246–5249.
- Takatoh, K., Sakamoto, M., Hasegawa, R., Koden, M., Itoh, N., & Hasegawa, M. (2005). *Alignment technology and applications of liquid crystal devices*. CRC Press.
- Tavella, F., Marcinkevičius, A., & Krausz, F. (2006, Dec). 90 mj parametric chirped pulse amplification of 10 fs pulses. *Opt. Express*, 14(26), 12822–12827. Retrieved from <http://www.opticsexpress.org/abstract.cfm?URI=oe-14-26-12822>
- Tavella, F., Nomura, Y., Veisz, L., Pervak, V., Marcinkevičius, A., & Krausz, F. (2007, Aug). Dispersion management for a sub-10-fs, 10 tw optical parametric chirped-pulse amplifier. *Opt. Lett.*, 32(15), 2227–2229. Retrieved from <http://ol.osa.org/abstract.cfm?URI=ol-32-15-2227>
- Thiré, N., Maksimenka, R., Kiss, B., Ferchaud, C., Gitzinger, G., Pinoteau, T., ... Forget, N. (2018, Oct). Highly stable, 15 w, few-cycle, 65 mrad cep-noise mid-ir opcpa for statistical physics. *Opt. Express*, 26(21), 26907–26915. Retrieved from <http://www.opticsexpress.org/abstract.cfm?URI=oe-26-21-26907>
- Tian, P., Bedrov, D., Smith, G. D., Glaser, M., & MacLennan, J. E. (2002). A molecular-dynamics simulation study of the switching dynamics of a nematic liquid crystal under an applied electrical field. *The Journal of chemical physics*, 117(20), 9452–9459.
- Tkachenko, V., Abbate, G., Marino, A., Vita, F., Giocondo, M., Mazzulla, A., ... Stefano, L. D. (2006). Nematic liquid crystal optical dispersion in the visible-near infrared range. *Molecular Crystals and Liquid Crystals*, 454(1), 263–665.
- Tournois, P. (1997, 08). Acousto-optic programmable dispersive filter for adaptive compensation of group delay time dispersion in laser systems. *Optics Communications*, 140, 245–249.
- Träger, F. (2012). *Springer handbook of lasers and optics*. Springer Science & Business Media.
- Trebino, R. (2012). *Frequency-resolved optical gating: the measurement of ultrashort laser pulses*. Springer Science & Business Media.
- Vargas, A., del Mar Sánchez-López, M., García-Martínez, P., Arias, J., & Moreno, I. (2014). Highly accurate spectral retardance characterization of a liquid crystal retarder including fabry-perot interference effects. *Journal of Applied Physics*, 115(3), 033101.
- Vasilyev, S., Moskalev, I., Smolski, V., Peppers, J., Mirov, M., Muraviev, A., ... Gapontsev,



- V. (2019, May). Multi-octave visible to long-wave ir femtosecond continuum generated in cr:zns-gase tandem. *Opt. Express*, *27*(11), 16405–16412. Retrieved from <http://www.opticsexpress.org/abstract.cfm?URI=oe-27-11-16405>
- Vaz, N., Smith, G., Montgomery Jr, G., Marion, W., Percec, V., & Lee, M. (1991). Refractive indices of a methylstilbene polymer liquid crystal. *Molecular Crystals and Liquid Crystals*, *198*(1), 305–321.
- Vena, C., Versace, C., Strangi, G., DELia, S., & Bartolino, R. (2007). Light depolarization effects during the freedericksz transition in nematic liquid crystals. *Optics Express*, *15*(25), 17063–17071.
- Vettese, D. (2010). Microdisplays: Liquid crystal on silicon. *Nature Photonics*, *4*(11), 752.
- Vuks, M. (1966). Determination of the optical anisotropy of aromatic molecules from the double refraction of crystals. *Optics and Spectroscopy*, *20*, 361.
- Walmsley, I., Waxer, L., & Dorrer, C. (2001). The role of dispersion in ultrafast optics. *Review of Scientific Instruments*, *72*(1), 1-29. Retrieved from <https://doi.org/10.1063/1.1330575>
- Wang, Q., Zhang, J., Kessel, A., Nagl, N., Pervak, V., Pronin, O., & Mak, K. F. (2019, May). Broadband mid-infrared coverage (2&#x2013;17&#x2009;&#x2009;&#x03bc;m) with few-cycle pulses via cascaded parametric processes. *Opt. Lett.*, *44*(10), 2566–2569. Retrieved from <http://ol.osa.org/abstract.cfm?URI=ol-44-10-2566>
- Warengem, M., & Joly, G. (1991). Liquid crystals refractive indices behavior versus wavelength and temperature. *Molecular Crystals and Liquid Crystals*, *207*(1), 205–218.
- Wefers, M. M., & Nelson, K. A. (1995). Generation of high-fidelity programmable ultrafast optical waveforms. *Optics letters*, *20*(9), 1047-1049.
- Weiner, A. M. (2000). Femtosecond pulse shaping using spatial light modulators. *Review of Scientific Instruments*, *71*(5), 1929-1960. Retrieved from <https://doi.org/10.1063/1.1150614>
- Weiner, A. M., Heritage, J. P., & Kirschner, E. (1988). High-resolution femtosecond pulse shaping. *JOSA B*, *5*(8), 1563–1572.
- Weiner, A. M., Leaird, D. E., Patel, J., & Wullert, J. R. (1992). Programmable shaping of femtosecond optical pulses by use of 128-element liquid crystal phase modulator. *IEEE Journal of Quantum Electronics*, *28*(4), 908–920.
- Weiner, A. M., Leaird, D. E., Patel, J. S., & Wullert, J. R. (1990). Programmable femtosecond pulse shaping by use of a multielement liquid-crystal phase modulator. *Optics letters*, *15*(6), 326–328.
- Wittenbecher, L., & Zigmantas, D. (2019, Aug). Correction of fabry-p&#x00e9;rot interference effects in phase and amplitude pulse shapers based on liquid crystal spatial light modulators. *Opt. Express*, *27*(16), 22970–22982. Retrieved from <http://www.opticsexpress.org/abstract.cfm?URI=oe-27-16-22970>
- Wolfram, S. (1999). The mathematica book. *Assembly Automation*.
- Wu, S.-T. (1986). Birefringence dispersions of liquid crystals. *Physical Review A*, *33*(2), 1270.
- Wu, S.-T. (1987). Infrared properties of nematic liquid crystals: an overview. *Optical Engineering*, *26*(2), 262120.
- Yan, X., Mont, F. W., Poxson, D. J., Schubert, M. F., Kim, J. K., Cho, J., & Schubert, E. F. (2009). Refractive-index-matched indium–tin-oxide electrodes for liquid crystal displays. *Japanese Journal of Applied Physics*, *48*(12R), 120203.
- Yang, D.-K. (2014). *Fundamentals of liquid crystal devices*. John Wiley & Sons.
- Zeek, E., Maginnis, K., Backus, S., Russek, U., Murnane, M., Mourou, G., . . . Vdovin, G. (1999). Pulse compression by use of deformable mirrors. *Optics letters*, *24*(7), 493–495.
- Zeng, X., Bai, J., Hou, C., & Yang, G. (2011). Compact optical correlator based on one phase-only spatial light modulator. *Optics letters*, *36*(8), 1383–1385.

Zhang, Z., You, Z., & Chu, D. (2014). Fundamentals of phase-only liquid crystal on silicon (lcos) devices. *Light: Science & Applications*, 3(10), e213.